Thermodynamic Variables for Active Brownian Particles

Pressure, Surface Tension and Chemical Potential

Jeroen Rodenburg

Thermodynamic Variables for Active Brownian Particles

Pressure, Surface Tension, and Chemical Potential

Jeroen Rodenburg

PhD thesis, Utrecht University, April 2020.
ISBN: 978-94-6380-756-2.
Printed by ProefschriftMaken.nl.
A catalogue record of this thesis is available from the Utrecht University Library.

Thermodynamic Variables for Active Brownian Particles

Pressure, Surface Tension, and Chemical Potential

Thermodynamische Variabelen

voor

Actieve Brownse Deeltjes

Druk, Oppervlaktespanning
en Chemische Potentiaal

(met een samenvatting in het Nederlands)

Proefschrift

ter verkrijging van de graad van doctor aan de Universiteit Utrecht op gezag van de rector magnificus, prof. dr. H. G. B. M. Kummeling, ingevolge het besluit van het college voor promoties in het openbaar te verdedigen op woensdag 15 april 2020 des middags te 12.45 uur

door

Anne Jeroen Rodenburg

geboren op 27 april 1991 te Amersfoort

Promotor: Prof. dr. R. H. H. G. van Roij

Roads go ever ever on,
Over rock and under tree,
By caves where never sun has shone,
By streams that never find the sea:
Over snow by winter sown,
And through the merry flowers of June,
Over grass and over stone,
And under mountains in the moon.

- J. R. R. Tolkien, *The Hobbit*

Contents

List of publications

This thesis is based on the following publications.

- Chapter 2
  Robin van Damme, Jeroen Rodenburg, René van Roij and Marjolein Dijkstra, *Interparticle torques suppress motility-induced phase separation for rodlike particles*, J. Chem. Phys. **150**, 164501 (2019).

- Chapter 3
  Jeroen Rodenburg, Marjolein Dijkstra and René van Roij, *Van't Hoff's law for active suspensions: the role of the solvent chemical potential*, Soft Matter **13**, 8957 (2017).

- Chapter 4
  Jeroen Rodenburg, René van Roij and Liesbeth Janssen, *Interfacial properties of ideal active Brownian particles in a motility gradient*, in preparation.

- Chapter 5
  Siddharth Paliwal, Jeroen Rodenburg, René van Roij and Marjolein Dijkstra, *Chemical potential in active systems: predicting phase equilibrium from bulk equations of state?*, New J. Phys. **20**, 015003 (2018).

- Chapter 6
  Jeroen Rodenburg, Siddharth Paliwal, Marjolein de Jager, Peter G. Bolhuis, Marjolein Dijkstra and René van Roij, *Ratchet-induced variations in bulk states of an active ideal gas*, J. Chem. Phys. **149**, 174901 (2018).

1

Introduction

In this chapter, we pose the questions that this thesis aims to answer in the field of active matter. To this end, first, we introduce thermodynamic variables, and explain why they are valuable tools. Next, we give background information on active matter, and introduce active Brownian particles as a model system. Subsequently, we describe the phenomenon of motility-induced phase separation, and explain how it leads to the research questions of this thesis. Finally, we outline how these questions are addressed in the remainder of the thesis.

1.1 From individual to collective behavior

Have you ever stopped to watch a flock of starlings in the winter months (Fig. 1.1)? These flocks, that can consist of as many as 100.000 birds, tend to form patterns that are truly mesmerizing to watch. If you have, then perhaps you have also wondered *why* these patterns form. The behavior is *not* coordinated by one, or a few, leader bird(s). Instead, the patterns form *spontaneously*, and result, somehow, from the way that every individual bird flies, and interacts with its neighbours.

Suppose that one is very determined to find out how this happens. Then one could first study how a bird flies in isolation, and subsequently how it responds to nearby birds as a function of their positions and velocities. Suppose that one then knows this 'individual' behavior perfectly. One then proceeds to study the behavior of large groups of birds. By using different types of birds, one finds that different types of collective behavior can emerge. Perhaps a certain type of bird always flocks in one large group, whereas another tends to split up into smaller subgroups. The question is then: *why* do the different types of birds show different these collective behaviors? Admittedly, it may not be entirely clear when one completely *understands* the reason, but, arguably, part of it is to be able to *predict* the collective behavior of a certain type of bird from its individual behavior. Phrased more generally, the question is then:

Figure 1.1: Photograph of a starling murmuration, taken by Paul Goldstein in Suffolk, UK, 16 Feb 2018. Credit: Paul Goldstein/Cover Images. Taken from `https://komonews.com/news/offbeat/gallery/its-birds-its-a-plane-its-photographer-captures-stunning-starling-murmuration#photo-9`

"Given a large number of units (or: particles) whose individual dynamics and interaction rules are specified, is it possible to predict and characterize the behavior of the collective?"

One approach would be to perform a computer simulation that uses the individual behavioral rules to compute how the positions of all particles evolve from any timestep to the next. While this is a very useful method, it can be very time and resource consuming. Moreover, the output is a sequence of *all* subsequent positions and velocities of *all* particles, which is a huge number of variables, and it is not a priori clear how the different collective behaviors are to be distinguished from those.

Therefore, instead, would it not be convenient if we could have only *a few* variables that completely characterize the collective? Variables that can, moreover, be calculated from the individual behavior rules? Such variables are called *thermodynamic variables*, and are at the core of this thesis.

While finding such variables may sound elusive, systems that are in thermodynamic equilibrium *can* be described by them. For these systems, knowledge of the interaction potential between the individual particles allows one, in principle, to calculate the system's free energy, and derive any collective property - such as the pressure, heat capacity, etc. - from there [1]. This has far-reaching consequences: it allows one, for example, to predict the temperature at which water boils at the top of Mt. Everest, but ultimately also underlies the engines that power our cars and airplanes [1]. Admittedly, calculating the thermodynamic variables from the interaction potential may not be *easy*, but a formal route (via partition functions and free energies) *does* exist, a route that moreover allows for systematic approximations [2]. In addition, the thermodynamic variables can be determined from computer simulations *without* using any approximation [3].

So when is a system in thermodynamic equilibrium, such that all of this is possible? Different authors give different definitions [4–7]; here, we paraphrase R. Haase [6]. A system is in thermodynamic equilibrium if it satisfies the following two conditions.

1. The system does not change over time, i.e., the system is in *steady state*.
2. If the system is cut off from all external influences, except from static external potential energy fields, the system remains unchanged.

As the reader may have guessed, a flock of birds is *not* in thermodynamic equilibrium, but before discussing why, we first place the example in a broader context.

1.2 Active Matter

The behavior of a group of birds falls into a class of systems nowadays known as *active matter* [8]. Although the term is sometimes used more broadly, here I define active matter as *systems that consist of a large number of units (or: particles) that continuously consume energy and convert it into motion.* The term "active" refers to the inherent motion of the particles; the term "matter" is perhaps less intuitive, and is discussed below. The

definition includes a very diverse range of systems. Not only can one think of schools of fish, or crowds of people, but also of granular rods that are being vibrated on a table, or of the kinetics of the cytoskeleton of a human cell [8, 9].

The experimental systems known as *microswimmers* [10, 11] deserve special attention. They are particles of micrometer-ranged size that "swim" in a solvent. Their value lies in the fact that their individual behavior can be manipulated to a relatively large extent, while also the particle movement can be accurately tracked under the microscope. We distinguish *biological* and *synthetic* microswimmers. Biological microswimmers are mostly swimming bacteria, such as *E. Coli* [12]. By appropriately choosing the species, or by manipulating its DNA, the swimming behavior can be controlled to a surprisingly large extent. For example, some species swim in intervals interrupted by tumbles [13], whereas others swim only when illuminated by light [14]. Synthetic microswimmers are nonliving particles whose swimming is made possible by some ongoing physical process, typically the chemical reaction of a solute taking place on (part of) the surface of the swimmer. The resulting processes that make the particle swim go by names as self-diffusiophoresis, self-electrophoresis, and self-thermophoresis. Often, but not always [15], these particles have a built-in asymmetry that dictates the direction of swimming. Synthetic swimmers, too, can be manipulated by exernal fields, such as light intensity, solute concentration, or magnetic fields [10, 11].

The last few decades have known a surge of interest in active matter in general, and microswimmers in particular. The interest partly comes from the prospect of applications, for example in self-assembly [16, 17], microsurgery [18] or targeted drug delivery [18–20].

Another reason is of fundamental nature. Indeed, the term "matter" suggests that these systems could be described in ways analogous to their passive counterparts. However, to which extent this is possible, is a priori not clear, because active matter systems are not in thermodynamic equilibrium. To see this, let us go back to the two conditions stated in Sec. 1.1. As for condition 1: it is perfectly possible to consider active steady states. In fact, in this thesis we focus *only* on steady states in order to be 'as close to equilibrium as possible'. However, *keeping* the system in steady state requires a steady flux of some kind of fuel into the system. Cutting off this external influence would make it impossible to sustain the particles' motion, and would therefore violate condition 2. So, indeed, active matter systems are by definition out of equilibrium.

But then why have hope that these systems can be described by a few collective thermodynamic variables? Well, active matter systems do *resemble* equilibrium systems in that they allow for steady states that are *homogeneous*. This contrasts with systems that are driven out of equilibrium 'from the outside'. An example of the latter is a system with two opposing boundaries that are kept at different temperatures. Clearly, this system will go to a steady state that has a temperature gradient, and is therefore not homogeneous. On the other hand, active matter systems are driven at the single-particle level, and therefore *can* have homogeneous steady states. In this sense, active matter steady states seem to be 'the closest thing to equilibrium'.

Moreover, several simple active matter models can undergo a motility-induced phase

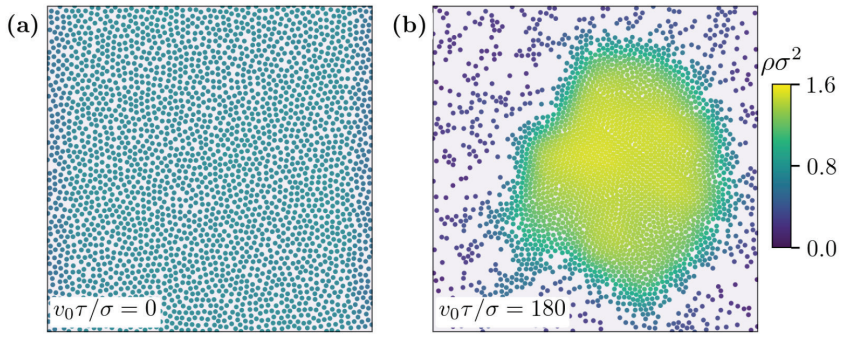

Figure 1.2: Figure taken and caption adapted from S. Paliwal's PhD thesis [21]. Typical configurations of two-dimensional (a) passive and (b) active Brownian particles with purely repulsive interactions. The particles' propulsion speed v_0, reorientation time τ and diameter σ are related as indicated. The coloring of the particles shows the local particle density ρ. Whereas the passive system shows a homogeneous distribution, the active system shows a dense cluster phase surrounded by a dilute gas phase.

separation, which, when one sees it, inevitably reminds one (or at least the author of this thesis) of an equilibrium gas-liquid, or gas-solid, phase separation.

1.3 Motility-induced phase separation

To investigate the use of thermodynamic variables for active matter, in this thesis we focus on a simple theoretical model: the model of active Brownian particles (ABPs). While later chapters specify their dynamics in full detail, here we point out the crucial ingredients. They are Brownian particles, whose steady-state behavior is that of an equilibrium system, except for the extra ingredient of *activity*: every particle feels a constant propulsion force - giving rise to propulsion speed v_0 - in a direction that changes on a timescale τ by rotational diffusion.

Let us assume that the particles interact via a purely repulsive interaction potential, e.g. a Weeks-Chandler-Andersen potential (the repulsive part of a Lennard-Jones potential) with particle diameter σ [22]. Also, let us assume that the overall density is fixed, and below the equilibrium freezing transition. Then *passive* particles ($v_0 = 0$) form a simple homogeneous fluid phase, as depicted in Fig. 1.2(a). However, when the particles are made sufficiently active, they separate into a dense cluster phase and a dilute gas phase, as depicted in Fig. 1.2(b) for $v_0\tau/\sigma = 180$. This phenomenon is known as *motility-induced phase separation* (MIPS), and is discussed in much more detail in chapter 2. Note that MIPS is a *non-equilibrium* phase coexistence of *repulsive* particles. Yet, it resembles the *equilibrium* phase coexistence of *attractive* particles, in the following senses:

- The coexistence forms a steady state in which the dense cluster does not significantly move.
- The bulk of both the dense and dilute phase is homogeneous and isotropic.
- The lever rule is satisfied. This means that if one adds particles to (or: removes particles from) the coexistence of Fig. 1.2(b), then the dense cluster will simply grow (shrink) while the *densities* of the bulk phases do not change [23].

The last observation suggests that the system somehow *'likes'* to have the particular densities that the dense and dilute phase attain.

For an equilibrium phase coexistence (at fixed temperature), this 'liking' is expressed by the statement that the total Helmholtz free energy of the system is minimized. This minimization boils down to performing a common tangent construction on the free energy density of a bulk state of density ρ (at fixed temperature) [1, 24]. This construction then selects out the gas density ρ_g and liquid density ρ_l. An equivalent way to minimize the free energy is to demand that both bulk phases have equal pressure $P(\rho)$ and chemical potential $\mu(\rho)$ [1, 24]. The two equalities $P(\rho_g) = P(\rho_l)$ and $\mu(\rho_g) = \mu(\rho_l)$ can then be solved for the two unknowns ρ_g and ρ_l. The latter approach is especially useful since, as emphasized in section 1.1, the pressure $P(\rho)$ and $\mu(\rho)$ have microscopic expressions that can be determined in computer simulations, in principle without needing any approximations[a] [3]. Thus, for an equilibrium phase coexistence, knowing the thermodynamic variables $P(\rho)$ and $\mu(\rho)$ for *bulk* states of density ρ allows one to determine the densities ρ_g and ρ_l of the *phase-separated* state.

This naturally leads to the question: can we also define a pressure and chemical potential for *active* steady states, preferably as microscopic expressions? And can they be utilized to find the coexisting densities of the MIPS phases of Fig. 1.2(b)? These questions are central to this thesis.

Another intriguing aspect of MIPS is the interface between the dense and the dilute phase. Any movie of MIPS readily shows that the interface fluctuates wildly (see e.g. movies supplementary to [25]). In equilibrium, the key property that determines the behavior of the interface - including its fluctuations - is the *interfacial tension*[b]. This has led to studies on the surface tension of MIPS [25–31], and while the *magnitude* of the surface tension could be related to the fluctuations [25, 26], its *sign* turned out to be surprising: Bialké et al. [26] found it to be negative! This immediately leads to the question: how can an interface with a negative tension be stable? This question - as well as the sign of the surface tension - is curently heavily debated in the literature [25, 27, 29, 31].

This has been a motivation to study the thermodynamic variable surface tension in this thesis as well. In particular, we focus on the question how to define surface tension out of equilibrium, and how it relates to the stability of the interface.

[a] The attentive reader may wonder how a computer simulation can produce a *bulk* state of a density $\rho_g < \rho < \rho_l$ for which the system wants to phase separate. The answer is: there are tricks [3]. The relevant simulations in this thesis, performed by collaborators R. van Damme and S. Paliwal, used systems that are too small to phase separate. The inherent finite-size effects can be estimated by doing this for various (small) sizes, and turn out to be insignificant. See e.g. section 2.C.

[b] Or *surface tension*. I shall use the words interchangeably.

1.4 Scope and outline of the thesis

In this thesis, we study the definition and usefulness of thermodynamic variables for ABPs. Motivated by the questions posed in section 1.3, we focus on the variables pressure, chemical potential and surface tension.

One may wonder whether temperature is a suitable thermodynamic variable for ABPs as well. Indeed, many studies have focused on this question, see e.g. [32] and references therein. This thesis, however, simply focuses on other variables. A temperature T *does* enter our equations, but it is not the temperature of the ABPs themselves. Instead, we think of the ABPs as microswimmers, and of T as the temperature of the solvent they are immersed in[c]. It enters the equations as follows. The ABPs - being Brownian - exhibit Brownian motion. When other driving forces, such as activity, are absent, this motion leads to translational diffusion with diffusion constant D_t. At the same time, any movement of the particle through the solvent leads to a drag force with (translational) friction constant γ_t. Throughout this thesis, the constants D_t and γ_t are assumed to be related by the Einstein relation $D_t\gamma_t = k_BT$, where k_B is the Boltzmann constant. This is how the temperature T enters. Actually, the Einstein relation assumes equipartition [24], and therefore only holds in equilibrium. Yet we assume it for active particles out of equilibrium also. This assumption is undoubtedly false, but it is made *only* to obtain expressions that *look* familiar, and that are therefore more reader friendly. By no means is the assumed Einstein relation essential to any of our results: one can simply replace any k_BT one encounters by $D_t\gamma_t$.[d] In fact, this is probably the best way to think about the temperature T that appears in this thesis: it is the quantity that sets the strength of the passive Brownian motion, and thereby the diffusion constant D_t.

The outline of this thesis is as follows.

In **chapter 2**, we introduce MIPS. We present phase diagrams, and rationalize the onset of MIPS by performing a stability analysis of the homogeneous isotropic phase. As interesting phenomenology, we show that MIPS disappears if one changes perfectly spherical particles into slightly elongated rods.

In **chapter 3**, we study the thermodynamic variable pressure. In particular, we take

[c]Strictly speaking, the solvent temperature is not constant in time: since the microswimmers dissipate energy, the solvent heats up. The rate at which this happens can be estimated as follows. A swimmer with speed v_0 experiences a drag force of magnitude $\gamma_t v_0$, where the friction coefficient can be estimated from the Stokes relation $\gamma_t = 3\pi\eta\sigma$, with η the dynamic viscosity of the solvent. Consequently, a single swimmer dissipates the power $\gamma_t v_0^2$, such that N swimmers dissipate the power $P = N\gamma_t v_0^2$. This dissipation leads to an increase in solvent temperature ΔT per time interval Δt via $P = c_v \Delta T \rho_s V/\Delta t$, where c_v is the specific heat of the solvent, ρ_s the mass density of the solvent, and V the volume. If we assume that the swimmers have (effective) diameter $\sigma = 1\,\mu$m, swimming speed $v_0 = 1\,\mu$m/s, and packing fraction $\phi = N\pi\sigma^3/(6V) = 0.01$, and assume that the solvent is water at room temperature, such that $\rho_s = 1\cdot 10^3\,\mathrm{kg/m^3}$, $\eta = 1\cdot 10^{-3}\,\mathrm{Pa\cdot s}$, and $c_v = 4\cdot 10^3\,\mathrm{J/(K\,kg)}$, we can calculate that the time it takes the solvent to heat up $\Delta T = 1\,\mathrm{K}$ is given by $\Delta t \approx 3\cdot 10^2$ years. Therefore, we can safely assume that the solvent temperature T is constant in time.

[d]Actually, in chapter 3 the Einstein relation is assumed to hold for rotational motion also, i.e. it is assumed that $D_r\gamma_r = k_BT$, with D_r and γ_r the rotational diffusion and friction coefficients, respectively. In this case, one should replace k_BT by $D_t\gamma_t$ in the first line of Eq. (3.2) and by $D_r\gamma_r$ in its second line, and work these modifications through in the rest of the chapter.

the role of the solvent into account, which allows to define and calculate the *osmotic* pressure.

In **chapter 4**, we switch back to a colloids-only description. In addition to the pressure, we study the other thermodynamic variable that can be defined mechanically: the surface tension. We do not consider the surface tension of MIPS directly, but examine a system that can - to some extent - be regarded as a toy model for MIPS: an active ideal gas in between two bulks with different propulsion speeds. We give two possible definitions for its interfacial tension, and show that the stability of the interface is not determined by their sign, but is instead guaranteed by tangential currents. These tangential currents are caused by the Marangoni effect, which is the effect that lateral inhomogeneities in the interfacial tension lead to mass transfer along the interface from low to high tension [33]. We show that these tangential currents restore any (slightly) perturbed interface to its original state.

In **chapter 5**, we address the next thermodynamic variable: the chemical potential. We define a chemical potential-like quantity and test whether it can be used together with the pressure to find the densities of active phase coexistences. While this works for a coexistence of weakly active Lennard-Jones particles, it does not correctly predict the densities of the highly active MIPS. We show this to be due to the highly nonlocal dependence of the chemical potential.

Finally, in **chapter 6**, we address a related effect. Where the previous chapter studied the definition of a *chemical* potential, this chapter focuses on the effect of applying an *external* potential. In particular, we show that applying an external potential in the shape of a sawtooth leads to an active steady state whose density profile depends on the details of the sawtooth, even arbitrarily far away. We aim to characterize, and understand, this 'long-range effect'. We conclude that both this effect and the chemical potential's nonlocal dependence make the statistical physics of ABPs a challenging affair.

Chapter 7 concludes the thesis by summarizing the main findings, discussing what we have learnt from the research as a whole, and providing directions for further research.

2

Motility-Induced Phase Separation

In this chapter, we introduce motility-induced phase separation (MIPS). We construct its phase diagram, and explain its formation from a stability analysis of the homogeneous isotropic phase.

As interesting phenomenology, we allow for the possibility of orientation-dependent interactions (torque) between the particles. This is done by considering rodlike particles of varying aspect ratio. Surprisingly, we find that MIPS disappears if one changes the particle shape from spherical to only slightly elongated. We propose a suppression mechanism based on the duration of collisions, and argue that this mechanism can explain both the suppression of MIPS found here for rodlike particles, but also the enhancement of MIPS found for particles with Vicsek interactions.

This chapter is based on the publication *"Interparticle torques suppress motility-induced phase separation for rodlike particles"* [34], and has been part of a collaboration with Robin van Damme, René van Roij and Marjolein Dijkstra. Robin van Damme performed all the simulations and their analysis, whereas the author of this thesis developed the stability analysis of the homogeneous isotropic phase.

2.1 Introduction

Active 2D disks or 3D spheres, two well-studied model systems, often have a parameter regime in which the system demixes into a dense and a dilute region. This phase separation closely resembles the well-known gas-liquid coexistence found in, for instance, water or Lennard-Jones systems. Unlike the gas-liquid phase separation, however, the clustering in active matter occurs because of the motility rather than the particle-particle attractions. Hence, the phenomenon has been coined motility-induced phase separation (MIPS). Recently, MIPS has been studied extensively [35–45]. For example, it has been identified for both active Brownian [36–38, 42] and run-and-tumble particles [35], its nucleation has been studied [43], and it has been derived from several theoretical models [40, 41, 45, 46].

All of the above studies logically constrained themselves to the simplest possible model systems, in which particles interact either through hard-particle excluded-volume interactions or through (softer) short-range repulsions. Importantly, these studies did not consider any torque interactions between the particles. Studies that do include torques typically fall into two categories. The first uses particles with Vicsek-like alignment interactions [47, 48], which mimic a visual alignment mechanism, such as for birds or fish. The second uses particles with an anisotropic, typically rodlike shape [49–53]. This most closely mimics bacteria, whose alignment arises simply from bumping into one another. While studies of active rods reveal a zoo of nonequilibrium phases, they do not exhibit MIPS; there seems to be no parameter regime for which there is a separation into dense and dilute regions without strong alignment. Naturally, this raises questions such as: why does MIPS occur for 2D disks and 3D spheres, but not for 2D and 3D rods? How anisotropic or rod-like must a particle be for MIPS to disappear? In this chapter, we will address these questions by both simulations and theory.

To address these questions numerically, we need a model system which exhibits MIPS, and a means to identify MIPS when it occurs. Section 2.2 describes both the Active Brownian Particle model we use, and the modified cluster algorithm that was developed to identify MIPS. In Section 2.3 we present an analytical criterion for the onset of MIPS, on the basis of a stability analysis of density fluctuations in the homogeneous isotropic phase. Section 2.4.1 discusses the phase diagrams for the 2D disks, 3D spheres and 2D and 3D rods, showing unambiguously that MIPS indeed disappears for increasing aspect ratio. Subsequently, the mechanism behind this suppression is discussed in Section 2.4.2. Section 2.5 then concludes this chapter by discussing the influence of torque on MIPS in a more general context.

2.2 Computational methods

2.2.1 Active Brownian Particles

Using Brownian Dynamics (BD) simulations, we study a system of N spherocylinder-shaped active Brownian particles (ABP) of head-to-tail length l and diameter $\sigma \leq l$ in a periodic area A. The spherocylinders self-propell by a mechanism that we leave unspecified, such that their velocity (at infinite dilution) is v_0 along their long axis $\hat{\boldsymbol{e}}$.

The particles are subject to rotational and translational noise, with rotational diffusion constant D_r and translational diffusion tensor $\boldsymbol{D}_t = D_\parallel \hat{\boldsymbol{e}}\hat{\boldsymbol{e}} + D_\perp(\boldsymbol{\mathcal{I}} - \hat{\boldsymbol{e}}\hat{\boldsymbol{e}})$, with parallel and perpendicular components $D_\parallel$ and $D_\perp$, respectively. For such a 2D system, shown schematically in Fig. 2.1, the overdamped Langevin equations are given by

$$\partial_t \boldsymbol{r}_i = v_0 \hat{\boldsymbol{e}}_i + \beta \boldsymbol{D}_{t,i} \cdot \sum_{i \neq j} \boldsymbol{\mathcal{F}}_{ij} + \sqrt{2\boldsymbol{D}_{t,i}} \cdot \boldsymbol{\Lambda}_i^t, \tag{2.1}$$

$$\partial_t \theta_i = \beta D_r \sum_{i \neq j} \mathcal{T}_{ij} + \sqrt{2D_r}\Lambda_i^r, \tag{2.2}$$

where $i = 1, ..., N$ is the particle label, $\boldsymbol{r}_i$ is the center-of-mass position of particle i, $\hat{\boldsymbol{e}}_i = (\cos\theta_i, \sin\theta_i)$ the particle orientation, and $\beta = 1/k_BT$. The force $\boldsymbol{\mathcal{F}}_{ij}$ and torque $\mathcal{T}_{ij}$ are due to particle-particle interactions. We assume fluctuation-dissipation to hold on the scale of individual particles, such that the translational and rotational noise terms $\Lambda_i^{t,\alpha}$ and Λ_i^r, respectively, are Gaussian distributed random numbers with zero mean and unit variance, i.e.

$$\langle \Lambda_i \rangle = 0, \qquad \langle \Lambda_i^\alpha(t)\Lambda_j^\beta(t')\rangle = \delta_{ij}\delta_{\alpha\beta}\delta(t-t'). \tag{2.3}$$

To describe excluded-volume interaction between particles i and j, we let the forces $\boldsymbol{\mathcal{F}}_{ij} = (\partial u_{WCA}(r_{s,ij})/\partial r_{s,ij})\hat{\boldsymbol{r}}_{s,ij}$ be the result of a short-range pairwise repulsive WCA potential $u_{WCA}(r_{s,ij})$ acting on the shortest distance $r_{s,ij}$ between particle cores:

$$u_{WCA}(r_{s,ij}) = \begin{cases} 4\epsilon\left[\left(\frac{\sigma}{r_{s,ij}}\right)^{12} - \left(\frac{\sigma}{r_{s,ij}}\right)^{6}\right] + \epsilon & \text{if } \; r_{s,ij} < 2^{1/6}\sigma; \\ 0 & \text{if } \; r_{s,ij} \geq 2^{1/6}\sigma. \end{cases}$$

For disks ($l/\sigma = 1$), the distance $r_{s,ij}$ is simply the distance between their centers. For $l/\sigma > 1$ the cores of the particles are no longer points, but lines. The distance $r_{s,ij}$ then corresponds to the shortest distance between these two line segments. The torques $\boldsymbol{\mathcal{T}}$ are calculated from the forces by $\boldsymbol{\mathcal{T}}_{ij} = \boldsymbol{a}_{ij} \times \boldsymbol{\mathcal{F}}_{ij}$, where $\boldsymbol{a}_{ij}$ is the lever arm for the applied force $\boldsymbol{\mathcal{F}}_{ij}$ on rod i by rod j (see Fig. 2.1). For each pair of particles, both the shortest distance $r_{s,ij}$ and the lever arms $\boldsymbol{a}_{ij}$ are calculated using the algorithm described in Ref. [54]. In 2D this torque always points out of plane, so we only need to consider its out-of-plane component $\mathcal{T}$ in the equations of motion.

This 2D model easily generalizes to 3D: aside from vectorial quantities now being three- rather than two-dimensional, we must now also consider the direction of the torque. For convenience, we also switch to vector notation in the orientational equation of motion. The equations of motion in 3D are thus:

$$\partial_t \boldsymbol{r}_i = v_0 \hat{\boldsymbol{e}}_i + \beta \boldsymbol{D}_{t,i} \cdot \sum_{i \neq j} \boldsymbol{\mathcal{F}}_{ij} + \sqrt{2\boldsymbol{D}_{t,i}} \cdot \boldsymbol{\Lambda}_i^t \tag{2.4}$$

$$\partial_t \hat{\boldsymbol{e}}_i = \beta D_r \sum_{i \neq j} \boldsymbol{\mathcal{T}}_{ij} \times \hat{\boldsymbol{e}}_i + \sqrt{2D_r}(\hat{\boldsymbol{e}}_i \times \boldsymbol{\Lambda}_i^r). \tag{2.5}$$

We nondimensionalize the 2D and 3D system by expressing all distances in units of the particle diameter σ, all energies in terms of the thermal energy k_BT, and all units of time in terms of $\tau = 1/D_r$.

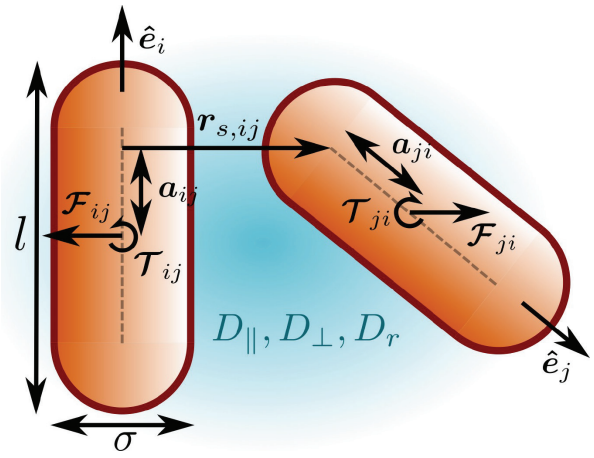

Figure 2.1: Schematic representation of the model. Particles are 2D or 3D spherocylinders of diameter σ and head-to-tail length l, self-propelled with a velocity v_0 in their forward direction $\hat{\boldsymbol{e}}$. They interact based on their core-to-core distance $\boldsymbol{r}_{\boldsymbol{s},\boldsymbol{ij}}$, causing repulsive forces $\boldsymbol{\mathcal{F}}_{ij}$ and torques $\boldsymbol{\mathcal{T}}_{ij}$. Additionally, they diffuse rotationally with diffusion constant D_r, and translationally along their long and short axis with diffusion constants $D_\parallel$ and $D_\perp$, respectively.

2.2.2 Choice of model parameters and additional assumptions

Our investigation studies the influence of four parameters: the dimensionality $d = 2$ or $d = 3$, the aspect ratio $p = l/\sigma$, the packing fraction $\phi = N((\pi/4)\sigma^2 + (l-\sigma)\sigma)/A$ (or $\phi = N((\pi/6)\sigma^3 + (\pi/4)(l-\sigma)\sigma^2)/V$ in 3D) and the Péclet number[a] $\mathrm{Pe} = v_0/\sigma D_r$. The diffusion constants $D_\parallel$ and $D_\perp$ for rodlike particles can be calculated from simulations including hydrodynamics as in e.g. Ref. [55] or, for short spherocylinders, approximated by the exact results for ellipsoids [56], see also appendix 2.B. We found that the influence of this change of diffusion constants is negligible for the aspect ratio range we look at, so for simplicity we will set $D_\parallel = D_\perp = D_t = \sigma^2 D_r/3$ from now on. This choice corresponds to the correct ratio between translational and rotational diffusion for 3D spheres (see footnote a).

Some care is required in the way the Péclet number is varied. The most straightforward way is to simply vary it by changing the self-propulsion velocity v_0. However, if we do this and keep the pair interaction strength fixed, the ratio between active and interaction forces will depend on the Péclet number. The result of changing this ratio is that the particle interaction effectively becomes softer as the Péclet number increases. In the

[a] We warn the reader that this definition of Pe agrees with the definition used in chapter 5, but not with the definition used in chapters 3, 4 and 6. The latter chapters use the slightly different convention $\mathrm{Pe} = v_0/\sqrt{D_t D_r}$, with D_t the translational diffusion coefficient of the spherical particles considered in those chapters. Since for spherical particles we assume the Stokes-Einstein relations $k_B T = D_t 3\pi\eta\sigma$ and $k_B T = D_r \pi\eta\sigma^3$ to hold (with η the viscosity of the solvent), D_t and σ are related as $D_t = \sigma^2 D_r/3$. Consequently, the difference between the two conventions for the definition of Pe is the proportionality factor $\sqrt{3}$.

extreme case, MIPS may even disappear for high enough Péclet numbers. Earlier work has remarked on this subtlety of varying the Péclet number [57, 58]. As our aim is not to provide quantitative but only qualitative data on the phase behaviour, we nevertheless use the straightforward approach by fixing $\epsilon = 24k_BT$ and changing the Péclet number by varying v_0.

2.2.3 Identifying motility-induced phase separation by clustering regions of similar density

MIPS is a separation of a system of self-propelled particles into a dense and a dilute region. While it can be identified quite readily from visual inspection of particle configurations, it is also useful to have a more quantitative method. Two of these methods are common. The first is to measure the distribution of the local density: for a homogeneous system, such a distribution is unimodal, while for a phase-separated system it is bimodal [59–61]. However, such a distribution can not tell us whether the system has separated into one or into multiple domains, which means it cannot distinguish between micro- and macrophase separation. This distinction becomes important for rods.

The other method is to group particles together into clusters based on a distance cutoff and to determine the fraction f_{cl} of particles in the largest cluster [36, 62, 63]. Since MIPS eventually forms one large, dense cluster in a very dilute background gas, $f_{\mathrm{cl}} \to 1$ for MIPS for large enough systems, while for a homogeneous fluid $f_{\mathrm{cl}} \to 0$. This latter method requires a cutoff distance that specifies whether particles are close enough to belong to the same cluster. In practice, we found that there is no single cutoff distance that yielded reasonable results for the resulting cluster fraction across all shapes and densities we wish to study.

To solve this problem, a slightly different clustering method was developed, shown schematically in Fig. 2.2. From the particle positions (Fig. 2.2a), we make a Voronoi construction. This provides us not only with a parameter-free way to define neighbouring particles, but also with a means of measuring the local packing fraction: $\phi_l = ((\pi/4)\sigma^2 + (l-\sigma)\sigma)/A_v$ or $((\pi/6)\sigma^3 + (\pi/4)(l-\sigma)\sigma^2)/V_v$, with A_v and V_v the area (2D) or volume (3D) of the Voronoi cell (colors in Fig. 2.2b). Our requirements for two particles to belong to the same cluster are then that (a) their Voronoi cells are connected and (b) they both have a local packing fraction that is either lower or higher than the mean packing fraction ϕ by a certain cutoff $\Delta\phi$. Using this method, we create clusters of similar local density (Fig. 2.2c). We choose $\Delta\phi = 0.025$, as we found through trial and error that this cutoff allows us to meaningfully distinguish between homogeneous states with $f_{\mathrm{cl}} < 0.5$ and phase-separated states with $f_{\mathrm{cl}} \geq 0.5$ for all aspect ratios and Péclet numbers of interest and for nearly all densities, both in $d = 2$ and $d = 3$. Note that f_{cl} is not guaranteed to go to zero in the homogeneous phase when using this definition of clusters due to density fluctuations, but $f_{\mathrm{cl}} = 0.5$ still offers a reasonable threshold.

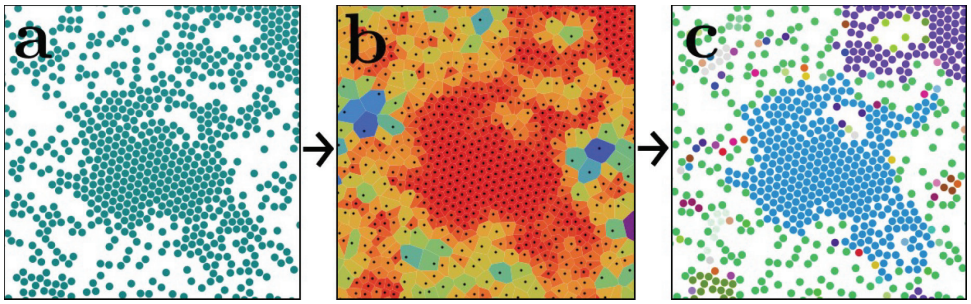

Figure 2.2: Representation of our clustering algorithm. From unlabeled coordinates (a), construct a Voronoi tesselation and obtain local densities (b), then use these to create clusters of particles with similar density (c).

2.3 An analytical criterion for the onset of MIPS

Having described the means to obtain and identify MIPS numerically in simulations, we now describe an analytical criterion for the onset of MIPS. We are aware of three ways to obtain such a criterion: by considering the particle flux balance between a dense cluster and a dilute gas phase [37, 64], by constructing an effective free energy and proceeding as in equilibrium [40, 65], and by a stability analysis of density fluctuations of the homogeneous isotropic phase [58, 66]. All three methods have previously been used for torque-free systems.

In this section, we extend the mean-field-like third method laid out in [66] to 3D systems with torque. The method consists of the following steps. In section 2.3.1, we map our system to an active ideal gas, where the effect of the many-body forces and torques is subsumed into a modified, *effective* swim speed v^{eff}, effective translation diffusion D_t^{eff}, and - due to the present of torques - also a modified rotational diffusion D_r^{eff}. By doing this mapping, we effectively make two approximations: the only effect of the interparticle forces $\boldsymbol{\mathcal{F}}$ is to slow particles down, and the only effect of the torques $\boldsymbol{\mathcal{T}}$ is to change the rate at which particles change their orientation. The former is a good approximation in the absence of structural order, the latter in the absence of orientational order. Both approximations become poorer at higher densities, where structure and alignment become important. In section 2.3.2, we perform a stability analysis of the homogeneous isotropic phase of the active ideal gas, which allows to obtain an analytical criterion for the onset of MIPS. This criterion involves the effective coefficients v^{eff}, D_r^{eff}, and D_t^{eff}, which are still a function of the the mean density $\bar{\rho}$ and input swimming speed v_0. Section 2.3.3 discusses how this dependence of the effective coefficients on $\bar{\rho}$ and v_0 can be determined.

2.3.1 Effective Smoluchowski equation

To render the problem analytically tractable, our first goal is to simplify the effect of the pairwise forces and torques. We will do this using a mean-field-like approximation. Following the same procedure as Refs. [58, 66], we start from the Smoluchowski equation

for the one-particle probability density $\psi(\boldsymbol{r}, \hat{\boldsymbol{e}}, t)$, given by

$$\partial_t \psi = -\boldsymbol{\nabla} \cdot (v_0 \hat{\boldsymbol{e}} \psi + \beta D_t \boldsymbol{\mathcal{F}} - D_t \boldsymbol{\nabla} \psi) - \boldsymbol{\mathcal{R}} \cdot (\beta D_r \boldsymbol{\mathcal{T}} - D_r \boldsymbol{\mathcal{R}} \psi), \tag{2.6}$$

where $\boldsymbol{\nabla}$ are the 2D and 3D gradient operators and $\boldsymbol{\mathcal{R}}$ is the rotation operator, defined as $\mathcal{R} = \partial_\theta$ in 2D and $\boldsymbol{\mathcal{R}} = \hat{\boldsymbol{e}} \times \boldsymbol{\nabla}_{\hat{\boldsymbol{e}}}$ in 3D. Note that similar to our numerical model we neglect the influence of particle shape anisotropy on the translational diffusion and simply set $\boldsymbol{D}_t = D_t \boldsymbol{\mathcal{I}}$. $\boldsymbol{\mathcal{F}}$ and $\boldsymbol{\mathcal{T}}$ are pairwise force and torque *densities*, respectively, and not to be confused with the interparticle force $\boldsymbol{\mathcal{F}}_{ij}$ and interparticle torque $\boldsymbol{\mathcal{T}}_{ij}$. They are defined in terms of the pair potential $V_{\hat{\boldsymbol{e}}_1, \hat{\boldsymbol{e}}_2}(\boldsymbol{r}_1, \boldsymbol{r}_2)$ and the two-body probability density $\psi^{(2)}_{\hat{\boldsymbol{e}}_1, \hat{\boldsymbol{e}}_2}(\boldsymbol{r}_1, \boldsymbol{r}_2, t)$ as

$$\boldsymbol{\mathcal{F}}(\boldsymbol{r}_1, \hat{\boldsymbol{e}}_1, t) \equiv \int \mathrm{d}\boldsymbol{r}_2 \mathrm{d}\hat{\boldsymbol{e}}_2 \left(-\nabla_1 V_{\hat{\boldsymbol{e}}_1, \hat{\boldsymbol{e}}_2}(\boldsymbol{r}_1, \boldsymbol{r}_2)\right) \psi^{(2)}_{\hat{\boldsymbol{e}}_1, \hat{\boldsymbol{e}}_2}(\boldsymbol{r}_1, \boldsymbol{r}_2, t), \tag{2.7}$$

$$\boldsymbol{\mathcal{T}}(\boldsymbol{r}_1, \hat{\boldsymbol{e}}_1, t) \equiv \int \mathrm{d}\boldsymbol{r}_2 \mathrm{d}\hat{\boldsymbol{e}}_2 \left(-\mathcal{R}_1 V_{\hat{\boldsymbol{e}}_1, \hat{\boldsymbol{e}}_2}(\boldsymbol{r}_1, \boldsymbol{r}_2)\right) \psi^{(2)}_{\hat{\boldsymbol{e}}_1, \hat{\boldsymbol{e}}_2}(\boldsymbol{r}_1, \boldsymbol{r}_2, t). \tag{2.8}$$

In order to close Eq. (2.6), the force and torque densities $\boldsymbol{\mathcal{F}}$ and $\boldsymbol{\mathcal{T}}$ need to be expressed in terms of the one-body PDF. To do so, we first use the identity

$$\psi^{(2)}_{\hat{\boldsymbol{e}}_1 \hat{\boldsymbol{e}}_2}(\boldsymbol{r}_1, \boldsymbol{r}_2, t) = \psi(\boldsymbol{r}_1, \hat{\boldsymbol{e}}_1, t) \psi(\boldsymbol{r}_2, \hat{\boldsymbol{e}}_2, t) g_{\hat{\boldsymbol{e}}_1 \hat{\boldsymbol{e}}_2}(\boldsymbol{r}_1, \boldsymbol{r}_2, t) \tag{2.9}$$

to rewrite Eq. (2.7) as $\boldsymbol{\mathcal{F}} = \tilde{\boldsymbol{\mathcal{F}}} \psi$, where

$$\tilde{\boldsymbol{\mathcal{F}}}(\boldsymbol{r}_1, \hat{\boldsymbol{e}}_1, t) \equiv \int \mathrm{d}\boldsymbol{r}_2 \mathrm{d}\hat{\boldsymbol{e}}_2 \left(-\nabla_1 V_{\hat{\boldsymbol{e}}_1, \hat{\boldsymbol{e}}_2}(\boldsymbol{r}_1, \boldsymbol{r}_2)\right) \psi(\boldsymbol{r}_2, \hat{\boldsymbol{e}}_2, t) g_{\hat{\boldsymbol{e}}_1, \hat{\boldsymbol{e}}_2}(\boldsymbol{r}_1, \boldsymbol{r}_2, t). \tag{2.10}$$

To obtain a closure, we make the following assumptions. First, we assume that the force $\boldsymbol{\mathcal{F}}$ acts along the direction of self-propulsion, i.e. $\boldsymbol{\mathcal{F}} = (\boldsymbol{\mathcal{F}} \cdot \hat{\boldsymbol{e}}) \hat{\boldsymbol{e}}$. Whereas this is exact in a homogeneous, isotropic bulk as dictated by symmetry, in general we neglect a possible second component that is perpendicular to $\hat{\boldsymbol{e}}$. In Ref. [66], Speck et al. assume this second component to act along the gradient of the one-particle PDF, i.e. $\boldsymbol{\mathcal{F}} = (\boldsymbol{\mathcal{F}} \cdot \hat{\boldsymbol{e}}) \hat{\boldsymbol{e}} + a \nabla \psi$. This additional assumption leads to a modified translational diffusion $D_t^{\mathrm{eff}} = (1 - \beta a) D_t$. We measured the magnitude of this modification for 3D spheres and rods, and found that the modification provided by βa is of negligible influence on the location of the phase boundaries. Therefore, we do not consider this additional component here and simply set $a = 0$, such that $D_t^{\mathrm{eff}} = D_t$. We did not explicitly check the validity of this assumption in the 2D case, but see no reason to assume a difference.

To continue our derivation, we make the second assumption that $\tilde{\boldsymbol{\mathcal{F}}} \cdot \hat{\boldsymbol{e}}$ is linear in the local density $\rho(\boldsymbol{r}, t) = \int \mathrm{d}\hat{\boldsymbol{e}} \psi(\boldsymbol{r}, \hat{\boldsymbol{e}}, t)$ and has no further dependence on $(\boldsymbol{r}, \hat{\boldsymbol{e}}, t)$:

$$\tilde{\boldsymbol{\mathcal{F}}}(\boldsymbol{r}, \hat{\boldsymbol{e}}, t) \cdot \hat{\boldsymbol{e}} = -\rho(\boldsymbol{r}, t) \zeta(\bar{\rho}, v_0). \tag{2.11}$$

Here the constant ζ is independent of $(\boldsymbol{r}, \hat{\boldsymbol{e}}, t)$, but can still depend on the mean density $\bar{\rho} = N/A$ (or N/V in 3D) and the self-propulsion strength v_0. In this way, the effect of

the interaction forces in Eq. (2.6) can be absorbed into a modified self-propulsion velocity v^{eff}, which is given by

$$v^{\text{eff}} = v_0 - \beta D_t \rho(\boldsymbol{r}, t)\zeta(\bar{\rho}, v_0). \tag{2.12}$$

For the torques, we make the approximation that its only influence is to modify the rotational diffusion, i.e.

$$\boldsymbol{\mathcal{T}}(\boldsymbol{r}, \hat{\boldsymbol{e}}, t) \approx b\boldsymbol{\mathcal{R}}_1\psi(\boldsymbol{r}, \hat{\boldsymbol{e}}, t). \tag{2.13}$$

We assume the constant b to be homogeneous and isotropic, such that it can only depend on the mean density and self-propulsion: $b = b(\bar{\rho}, v_0)$. With these approximations, Eq. (2.6) simplifies and becomes the Smoluchowski equation of an active ideal gas:

$$\partial_t\psi = -\boldsymbol{\nabla}\cdot\left(v^{\text{eff}}\hat{\boldsymbol{e}}\psi - D_t\boldsymbol{\nabla}\psi\right) + D_r^{\text{eff}}\boldsymbol{\mathcal{R}}\cdot\boldsymbol{\mathcal{R}}\psi, \tag{2.14}$$

where v^{eff} and D_r^{eff} are now the *effective* self-propulsion and rotational diffusion constant, respectively.

2.3.2 Stability analysis of the homogeneous isotropic phase

Now that we have reduced the full Smoluchowski Eq. (2.6) into the ideal-gas form of Eq. (2.14), we can perform a linear stability analysis on the homogeneous isotropic phase. We start by defining the relevant moments of the one-particle PDF $\psi(\boldsymbol{r}, \hat{\boldsymbol{e}}, t)$,

$$\rho(\boldsymbol{r}, t) = \int \mathrm{d}\hat{\boldsymbol{e}}\psi(\boldsymbol{r}, \hat{\boldsymbol{e}}, t) \quad \text{(density)}, \tag{2.15}$$

$$m_\alpha(\boldsymbol{r}, t) = \int \mathrm{d}\hat{\boldsymbol{e}}e_\alpha\psi(\boldsymbol{r}, \hat{\boldsymbol{e}}, t) \quad \text{(polarization)}, \tag{2.16}$$

$$S_{\alpha\beta}(\boldsymbol{r}, t) = \int \mathrm{d}\hat{\boldsymbol{e}}(e_\alpha e_\beta - \frac{1}{d}\delta_{\alpha\beta})\psi(\boldsymbol{r}, \hat{\boldsymbol{e}}, t) \quad \text{(nematic alignment tensor)}. \tag{2.17}$$

Here, the Greek indices label the Cartesian vector- or tensor components, and in the following we shall employ the Einstein summation convention. Considering the same moments of the ideal gas Smoluchowski equation (2.14) yields the following evolution equations:

$$\partial_t\rho = -\boldsymbol{\nabla}\cdot\left(v^{\text{eff}}\boldsymbol{m} - D_t\boldsymbol{\nabla}\rho\right), \tag{2.18}$$

$$\partial_t m_\alpha = -\partial_\beta[v^{\text{eff}}(S_{\alpha\beta} + \frac{1}{d}\rho\delta_{\alpha\beta}) - D_t\partial_\beta m_\alpha] - (d-1)D_r^{\text{eff}}m_\alpha, \tag{2.19}$$

$$\partial_t S_{\alpha\beta} = -\partial_\gamma[v^{\text{eff}}(B_{\alpha\beta\gamma} - \frac{1}{d}m_\gamma\delta_{\alpha\beta\gamma}) - D_t\partial_\gamma S_{\alpha\beta}] - d(d-1)D_r^{\text{eff}}S_{\alpha\beta}. \tag{2.20}$$

Here $B_{\alpha\beta\gamma}$ is the next (third) order moment. The structure of this hierarchy of time-evolution equations (2.18)-(2.20) is such that the time-derivative of each moment depends linearly on itself and lower order ones, and on the next one. However, as we shall see, moments beyond m are irrelevant for the instability we wish to consider.

A steady-state solution to Eq. (2.14) is the homogeneous isotropic phase: $\psi(\boldsymbol{r}, \hat{\boldsymbol{e}}, t) \propto \bar{\rho}$. Expressed in terms of the angular moments (2.15)-(2.17), this gives $\rho(\boldsymbol{r}, t) = \bar{\rho}$ and

$\boldsymbol{m}(\boldsymbol{r},t) = \boldsymbol{S}(\boldsymbol{r},t) = 0$. To obtain a criterion for the stability of this solution, we investigate the behaviour of small perturbations to the homogeneous state:

$$\rho(\boldsymbol{r},t) = \bar{\rho} + \delta\rho(\boldsymbol{r},t), \tag{2.21}$$
$$\boldsymbol{m}(\boldsymbol{r},t) = \delta\boldsymbol{m}(\boldsymbol{r},t), \tag{2.22}$$
$$\boldsymbol{S}(\boldsymbol{r},t) = \delta\boldsymbol{S}(\boldsymbol{r},t). \tag{2.23}$$

Since MIPS is a macroscopic phase separation, we study the instability with respect to long-range perturbations, i.e. perturbations with small spatial gradients. In this limit, the dynamics are dominated by the terms in Eqs. (2.18)-(2.20) that have the fewest spatial gradients. Of the three moments, it is ρ whose time evolution is slowest. Its timescale is of order ∇^{-1}, while $\boldsymbol{m}$ and $\boldsymbol{S}$ evolve at the timescale $(D_r^{\text{eff}})^{-1} \sim \nabla^0$. As we are interested in the evolution of the density perturbations, i.e. of the slow variable, we can assume that at any given time the higher moments $\boldsymbol{m}$ and $\boldsymbol{S}$ are given by their steady-state solutions that correspond to the density profile $\rho(\boldsymbol{r},t)$ at that instant. Solving Eq. (2.20) for its steady-state solution $\delta S_{\alpha\beta}$ reveals that it scales as $\mathcal{O}(\nabla^1)$. Therefore, its contribution to the evolution of polarization perturbations (Eq. (2.19)) is of higher order. To leading order, the evolution of polarization perturbations is then given by

$$\delta\boldsymbol{m}(\boldsymbol{r},t) = -\frac{1}{d(d-1)D_r^{\text{eff}}}\boldsymbol{\nabla}\left(v^{\text{eff}}(\boldsymbol{r},t)\rho(\boldsymbol{r},t)\right). \tag{2.24}$$

Recalling that $v^{\text{eff}} = v_0 - \beta D_t \rho(\boldsymbol{r},t)\zeta(\bar{\rho},v_0)$, we can evaluate the gradient explicitly and obtain

$$\delta\boldsymbol{m}(\boldsymbol{r},t) = -\frac{1}{d(d-1)D_r^{\text{eff}}}\left(v_0 - 2\beta D_t\rho(\boldsymbol{r},t)\zeta\right)\boldsymbol{\nabla}\rho(\boldsymbol{r},t). \tag{2.25}$$

Using this result, the equation for the time evolution of density perturbations becomes

$$\partial_t\delta\rho(\boldsymbol{r},t) = \mathcal{D}_{\delta\rho}(\bar{\rho},v_0)\boldsymbol{\nabla}^2\delta\rho(\boldsymbol{r},t), \tag{2.26}$$

which is a diffusion equation with diffusion constant

$$\mathcal{D}_{\delta\rho}(\bar{\rho},v_0) = D_t + \frac{(v_0 - \beta D_t\bar{\rho}\zeta)(v_0 - 2\beta D_t\bar{\rho}\zeta)}{d(d-1)D_r^{\text{eff}}} = D_t + \frac{v^{\text{eff}}(2v^{\text{eff}} - v_0)}{d(d-1)D_r^{\text{eff}}}. \tag{2.27}$$

Importantly, values exist of the effective coefficients $v^{\text{eff}}(\bar{\rho},v_0)$ and $D_r^{\text{eff}}(\bar{\rho},v_0)$ for which the diffusion constant $\mathcal{D}_{\delta\rho}(\bar{\rho},v_0)$ of Eq. (2.27) is negative. When this happens, density perturbations $\delta\rho(\boldsymbol{r},t)$ *grow*. Therefore, the condition $\mathcal{D}_{\delta\rho}(\bar{\rho},v_0) < 0$ maps out a region in $(\bar{\rho},v_0)$-space where the homogeneous isotropic phase is unstable. The line that separates the stable from the unstable regions in $(\bar{\rho},v_0)$-space is called the *spinodal* - it is the line that corresponds to $\mathcal{D}_{\delta\rho}(\bar{\rho},v_0) = 0$ in the phase diagrams that are to be discussed in Sec. 2.4. The lowest point of the spinodal in $(\bar{\rho},v_0)$-space occurs when the propulsion speed v_0 equals the critical threshold $v^* = 2\sqrt{2}\sqrt{d(d-1)}\sqrt{D_t D_r^{\text{eff}}}$. Indeed, it follows from Eq. (2.27) that $v_0 > v^*$ is a necessary condition for the inequality $\mathcal{D}_{\delta\rho}(\bar{\rho},v_0) < 0$ to occur.

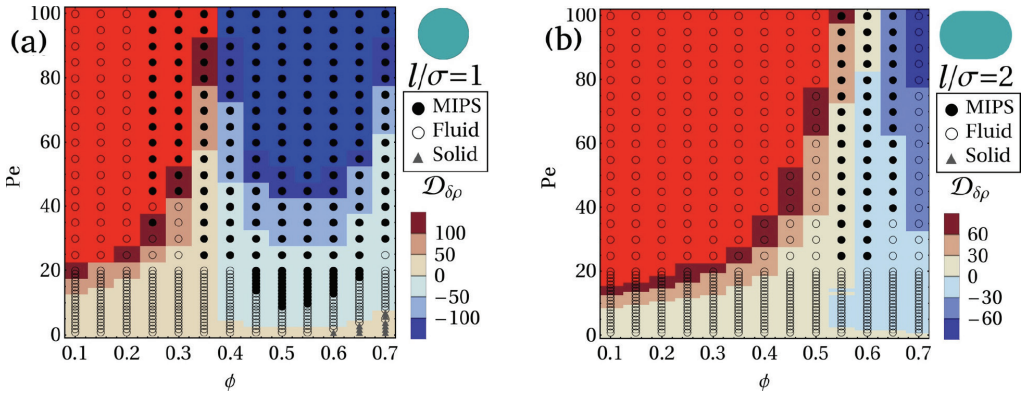

Figure 2.3: Phase diagram of 2D self-propelled disks (a) and rods of aspect ratio $l/\sigma = 2.0$ (b), for different Péclet numbers Pe and packing fractions ϕ. Data points indicate the resulting phase of $N = 10^4$ particles as obtained from Brownian dynamics simulations, in which we distinguished MIPS, fluid and solid phases. The colors indicate the diffusion constant of density fluctuations $\mathcal{D}_{\delta\rho}$. Spinodal decomposition to a MIPS state is then predicted where $\mathcal{D}_{\delta\rho} < 0$.

2.3.3 Determination of the effective coefficients

The effective coefficients v^{eff} and D_r^{eff} can be found in two ways: either by formulating closed-form equations for these effective constants, or by measuring them in some way. Here the latter method is used, and their values are determined from the correlation functions

$$\langle \dot{\boldsymbol{r}}_i(t) \cdot \hat{\boldsymbol{e}}_i(t) \rangle = v^{\text{eff}}, \tag{2.28}$$

$$\langle \hat{\boldsymbol{e}}_i(t) \cdot \hat{\boldsymbol{e}}_i(0) \rangle = \exp(-(d-1)D_r^{\text{eff}} t), \tag{2.29}$$

which measure the effective velocity in the direction of self-propulsion, and how quickly a particle loses its orientation, respectively. Thus, the effective coefficients v^{eff} and D_r^{eff} are determined in a simulation of a (small) system in the homogeneous isotropic phase.

2.4 Results & Discussion

To explore the MIPS-related phase behaviour, within a collaboration we performed Brownian Dynamics simulations with $N = 10^4$ particles in the packing-fraction range $0.1 \leq \phi \leq 0.7$, and the Péclet-number range $1 \leq \text{Pe} \leq 100$ (2D) and $1 \leq \text{Pe} \leq 150$ (3D). This spans the entire density range from the fluid regime to just below the hexatic/solid regimes [67, 68]. The Péclet range spans from below the MIPS critical point to high enough Péclet that the MIPS region attains a near-constant width in density [57, 69]. We also performed smaller simulations to measure the effective constants v^{eff} and D_r^{eff}. The initial state for all simulations was one with random positions and orientations. Using only a limited number of particles ($N = 100$) ensures that the system remains in the homogeneous isotropic phase regardless of density or activity. Of course, these smaller

simulations suffer from finite-size effects. Appendix 2.C contains a more detailed analysis of these finite-size effects.

We now turn to answer the questions posed in the introduction. How elongated do particles have to be to not display MIPS? And what is the mechanism that suppresses MIPS for rods?

2.4.1 Phase diagrams of self-propelled disks, spheres and rods

Before we can appreciate how the phase behaviour changes with aspect ratio, we must first establish the relevant features of MIPS for isotropic particles. Let us start in 2D.

The phase boundaries of MIPS for disks have been studied by a number of authors [37, 45, 66, 69, 70], and report a U-shaped MIPS region in the density-activity plane. Recently, a comprehensive study appeared that also includes the high-density hexatic and solid phases [68]. However, an in-depth comparison of the high-density phase boundaries falls outside the scope of this chapter. Instead, we will merely identify the solid-like phases by looking at where the effective velocity v^{eff} becomes vanishingly small ($v^{\text{eff}} < 0.1\sigma D_r$). Although this is not a very accurate measure, it serves to crudely distinguish the solid or hexatic phase from the fluid and MIPS phases, at least at low self-propulsion. We use this criterion for all phase diagrams throughout this chapter. With this information in mind, let us consider the phase diagrams in Figure 2.3.

Figure 2.3 shows phase diagrams in the Péclet number Pe - packing fraction ϕ representation for 2D disks and rods that show both the MIPS region predicted on the basis of the stability analysis (blue-tinted region, $\mathcal{D} < 0$), and the MIPS region found in the simulations using $N = 10^4$ (black points). Both methods seem to indicate MIPS in roughly the same region, but there are a few notable differences. On the low density side, we also find MIPS outside of the predicted spinodal region. Making the analogy with the gas/liquid phase separation, we would expect MIPS in this region to then occur through nucleation and growth. Is this also the case?

A simple way to see if MIPS forms through a nucleation process is to look at domain growth, which we can track using a time series of cluster fraction f_{cl} defined in Section 2.2.3. If the system immediately decays from an isotropic to a MIPS state, this fraction will likewise increase immediately. If, on the other hand, the system stays in the fluid state for a prolonged period of time, only to later transition into MIPS through a nucleation process, f_{cl} will retain the value corresponding to the fluid for a finite time.

Figure 2.4 compares the time evolution of the fraction f_{cl} of particles in the largest cluster for a number of Péclet numbers at two different densities: one on the low density side of the MIPS regime at $\phi = 0.25$ and one on the high density side at $\phi = 0.7$. On the low density side and outside of the predicted spinodal region, the cluster fraction can stay constant for a significant amount of time ($t > 30\tau$) before transitioning to a MIPS state. On the high density side of the MIPS region, such a delay is absent. The stability analysis predicts spinodal decomposition in this regime, and the cluster growth agrees. This asymmetry is consistent with the findings of Speck et al. [66], who report that the MIPS transition is discontinuous at low densities, but continuous at high densities.

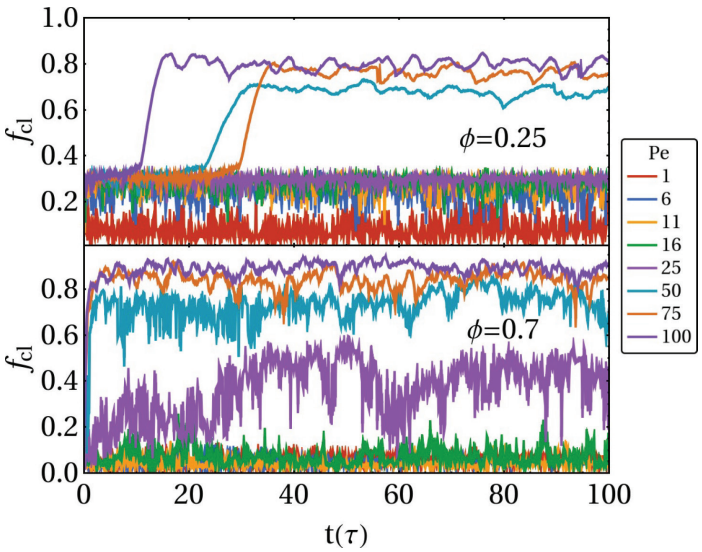

Figure 2.4: Time series of the largest cluster fraction f_{cl} for active disks ($l/\sigma = 1$). At low density $\phi = 0.25$, the system occasionally only clusters after a significant amount of time ($t > 10\tau$), suggesting that the transition is triggered by a rare nucleation event. At high density $\phi = 0.7$, this is never the case—only spinodal decomposition is observed.

There is also a discrepancy between the stability analysis and the large-scale simulation at low Péclet numbers. This is to be expected: in this region the fluid-MIPS transition is continuous, and the difference in density between the coexisting phases is small when we close to a critical point. Consequently, distinguishing between clusters of particles is difficult, and the exact choice of cluster fraction threshold f_{cl} can shift the boundary quite a bit in this region.

Having identified the most important features of the phase diagram for active disks, let us now turn to rods and see how these features change. Figure 2.3b shows the phase diagram in the density-activity representation for rods with an aspect ratio of $l/\sigma = 2$, using the same density and activity ranges as for the disks. The most obvious difference with the rods is that the MIPS region is now both shifted to higher densities and much narrower. The predictions of the stability analysis are worse for the rods: the predicted spinodal now lies in the middle of the simulated MIPS region. We find that the transition from fluid to MIPS now appears to be completely continuous—the system always starts clustering immediately, without any nucleation-like transient period. As can be seen from Figure 2.5a, the suppression is continuous with increasing aspect ratio, and it eventually pushes the fluid-MIPS transition into the regime where solid phases typically emerge.

Let us now see whether the 3D case is similar. Figure 2.6 displays phase diagrams in the (ϕ, Pe) representation, in Fig. 2.6a for 3D spheres and in Fig. 2.6b for 3D rods with

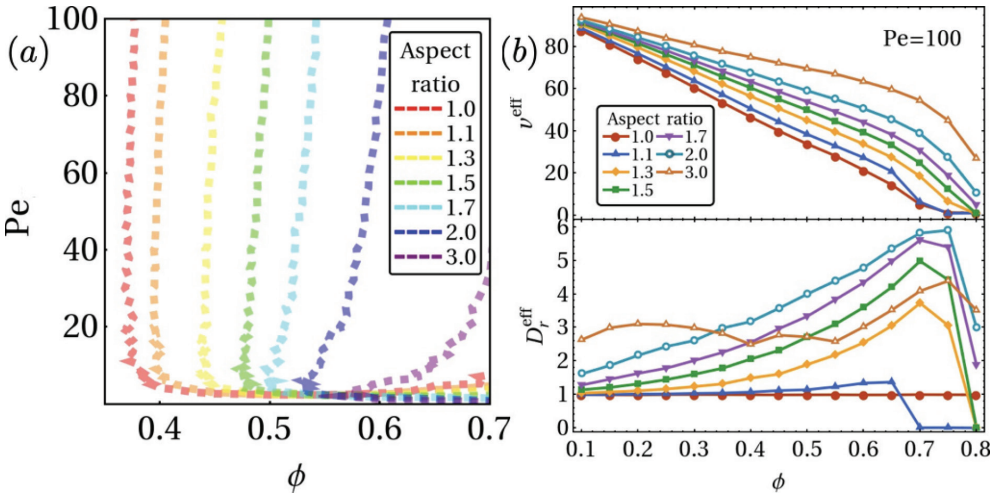

Figure 2.5: Spinodal lines for 2D active rods as predicted from Eq. 2.27, as a function of aspect ratio (a), and the corresponding effective self-propulsion velocity v^{eff} and rotational diffusion D_r^{eff} at Péclet number $\text{Pe} = 100$ as a function of packing fraction (b). At high activity, the effective self-propulsion decreases more slowly with density, while the rotational diffusion is enhanced.

$l/\sigma = 2$. Somewhat unsurprisingly, they are similar to their 2D counterparts. The most important feature is retained: MIPS disappears when the aspect ratio is increased. The fluid gap we found in between the solid and MIPS phases is also present for the active spheres. However, there are notable differences between the 2D and 3D cases.

In contrast to the 2D case, we observe no region for the active spheres where the MIPS transition is discontinuous. All simulations that form MIPS appear to undergo immediate spinodal decomposition. This does not necessarily mean that there is no binodal region: it may simply be quite small or have low nucleation barriers. The density regime of the metastable region for 3D active spheres is not well understood. We are only aware of one comparable simulation study by Stenhammar et al. [57], who looked at 2D and 3D active disks/spheres to study the influence of dimensionality. However, their binodal lines were defined as the density at which a high-Péclet system phase separated, which is not directly comparable to the metastable region we define here. Hence, further studies are needed to explain the difference in the width of the metastable region between $d = 2$ and $d = 3$.

Another difference is at high Péclet number, where the predicted MIPS region for the spheres continues to shift towards higher density, instead of moving towards a constant one. We believe this to be the behaviour that we discussed in Section 2.2.2: for higher Péclet numbers the particles can approach each other closer due to the active forces, causing the effective diameter of the particles to decrease. This effect appears to be stronger in 3D than in 2D, presumably due to the increased coordination of each particle.

The final difference between the 2D and 3D cases is perhaps the most notable one: for the rods, MIPS has disappeared completely. Whatever mechanism suppresses MIPS,

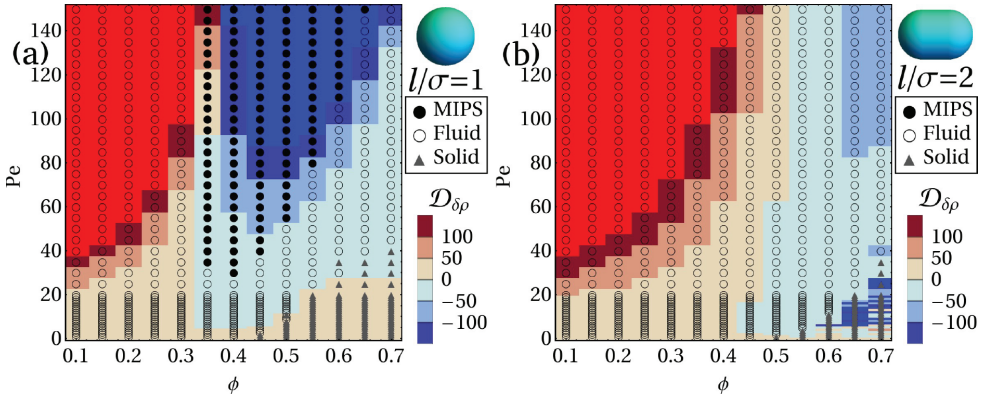

Figure 2.6: Phase diagram of 3D self-propelled spheres (a) and rods of aspect ratio $l/\sigma = 2.0$ (b), in the Péclet number Pe-packing fraction ϕ representation. Data points indicate the resulting phase of $N = 10^4$ particles as obtained from Brownian dynamics simulations, in which we distinguished MIPS, fluid and solid phases. The colors indicate the diffusion constant of density fluctuations $\mathcal{D}_{\delta\rho}$. Spinodal decomposition to a MIPS state is then predicted to occur in the blue region where $\mathcal{D}_{\delta\rho} < 0$. The small region of predicted instability in (b) under the points indicated as solid is an artefact of the fluid-solid transition there, where $D_{\delta\rho}$ fluctuates strongly as both v^{eff} and D_r^{eff} go to zero.

it appears to be stronger in 3D than in 2D. Curiously enough, the stability analysis still predicts MIPS in a significant portion of the phase diagram. This discrepancy, combined with its 2D counterpart, suggests that our theoretical approach breaks down for longer aspect ratios. We will see why this is the case in the next section, where we discuss the suppression mechanism.

Armed with the knowledge of these phase diagrams, we now turn to the first question posed in the introduction: "How rodlike must a particle be for MIPS to disappear?" Unfortunately, we can answer this question only partially. Determining the exact aspect ratio where MIPS disappears turns out to be quite difficult. We now know that the nature of the suppression stems from the fluid-MIPS transition shifting to higher densities, but unfortunately our methods to identify MIPS are less reliable at higher densities. More importantly, however, when the particle interactions are not isotropic, MIPS is no longer defined unambiguously and multiple types of clustered phases are possible which all fit the present criteria. When we identify MIPS according to a) the system phase-separating into a single dense cluster in a background gas and b) this cluster having no net orientational order, there are still multiple realizations of such a system (see Fig. 2.D.2 of appendix 2.D), such as a dense cluster with large domains of oppositely oriented particles ($l/\sigma = 1.1$) or a percolating cluster with low orientational order and many voids ($l/\sigma = 1.3,\ 2.0$). Therefore, establishing the boundaries of MIPS at these higher densities requires a more careful consideration of both hexatic [68] and orientational order [71]. We leave this investigation to future work and instead, having established *that* MIPS is

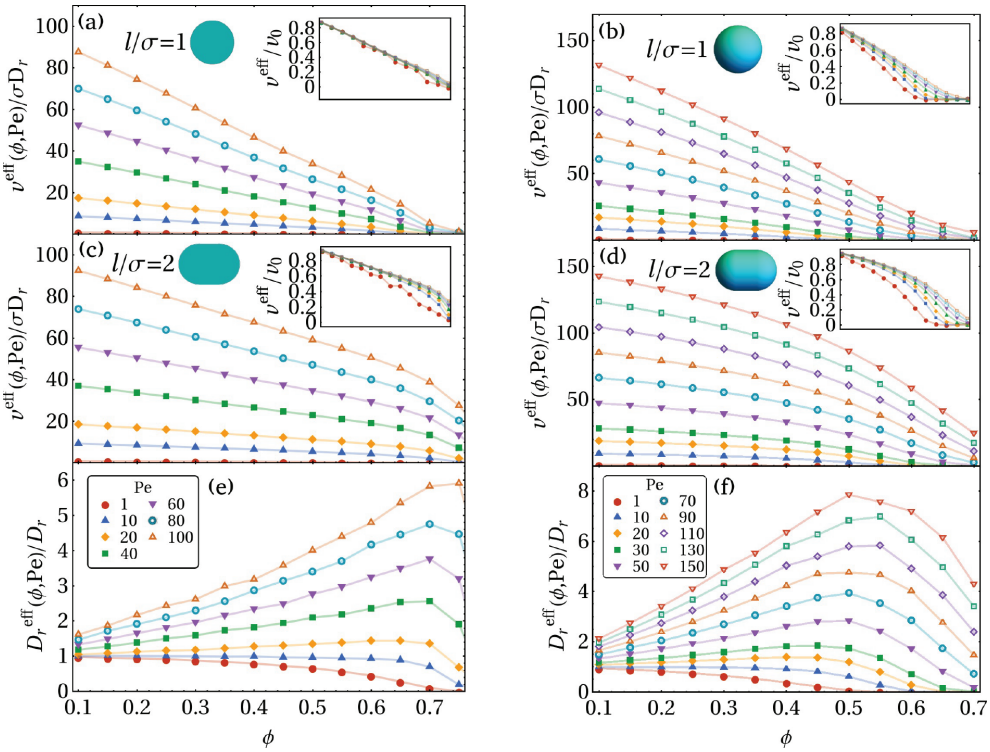

Figure 2.7: Simulation results for the effective self-propulsion speed v^{eff} of 2D act ive disks and 3D active spheres (a,b), effective self-propulsion speed v^{eff} for 2D and 3D active rods (c,d), and effective rotational diffusion D_r^{eff} for 2D and 3D rods with an aspect ratio $l/\sigma = 2.0$ (e,f). All insets show effective velocity divided by input velocity, for comparison with $v^{\text{eff}} = v_0(1 - \phi/\phi_{cp})$ with ϕ_{cp} the close packing density.

suppressed when particles become elongated, we now turn to finding out *why*.

2.4.2 Torque-induced suppression of motility-induced phase separation

Since the main difference between the disk and rod systems is the presence of torque, it is likely that the suppression of MIPS must arise there. In our stability analysis, the only effect of torques is to modify the rotational diffusion. Looking at Eq. (2.27), it might be possible to suppress MIPS if D_r^{eff} is increased enough to make the second term on the right-hand side smaller than D_t. Is this the case? Is the rotational diffusion perhaps enhanced so much that we effectively end up with a thermal system again?

A closer inspection of Eq. (2.27) shows that this is not the case. Due to the large

values of v^{eff} (see Figs. 2.7(a-d)), the second term on the right-hand-side of Eq. (2.27) dominates over D_t^{eff}. Therefore, the sign of $\mathcal{D}_{\delta\rho}$ is almost completely determined by the sign of the second term, which, in turn, is determined by the value of v^{eff}, and *not* by the value of D_r^{eff}. Consequently, it is v^{eff} that contains the key information that allows us to predict MIPS or its suppression[b]. Comparing the effective swimming speeds of different aspect ratios (Figs. 2.7a and 2.7c, or 2.7b and 2.7d), we see that the rods slow down less with increasing density than the disks. In other words, the rods hinder each other's movement less than the disks do. Why is this? Again we must look to the main difference between the two systems: torque.

For disks, one can derive the linear decrease of the velocity with increasing density $v^{\text{eff}} = v_0(1 - \rho/\rho^*)$ from mean-field theory and kinetic arguments [61, 72, 73]. This is done by assuming that particles slow down at low density due to time spent in binary collisions, which leads to $v^{\text{eff}}(\rho) \simeq v_0(1 - \tau_c/\tau_f)$, where τ_c is the time spent in a collision and $\tau_f = 1/(\sigma v_0 \rho)$ the mean free time between collisions. At low density, we expect the mean free time τ_f to be mostly unaffected by the presence of torques as long as there are no significant short-range orientational correlations. The duration of collisions τ_c, however, can change significantly when torques are involved. For disks, the duration of their collision—of their hindrance—is determined by how long it takes for them to slide around each other. Rods, however, will rotate to reorient their swimming directions away from the combined center of mass of the collision. This will decrease the collision duration. Since collisions are now shorter, the rods spend more time moving freely: less hindered. Furthermore, this reorientation leads to an enhanced rotational diffusion—exactly what we find.

Interestingly, this suggests that an inverse mechanism might also exist. If the torques between two colliding particles cause the particles to rotate towards their center of mass, collisions would be prolonged and MIPS would be enhanced. Precisely this inverse effect was reported earlier in Refs. [47, 48]: MIPS is enhanced for self-propelled particles that align through Vicsek interactions. In binary collisions, the Vicsek torques always rotate particles towards the combined center of mass, increasing the duration of collisions, increasing hindrance and thus enhancing MIPS.

Is the changing density dependence of v^{eff} with increasing anisotropy enough to completely describe the suppression of MIPS? If we would have a system of self-propelled particles with some arbitrary shape and we would know how the effective swim speed depends on density, could we then predict whether and where it will undergo MIPS? Unfortunately, no. As we can see from the rod phase diagrams in Figs. 2.3b and 2.6b, our stability analysis predicts the right qualitative trend, but its quantitative prediction is poor. This is probably due to neglecting alignment effects in the stability analysis. As the rod length increases, nematic and polar alignment of the particles start playing a more significant role in their phase behaviour, which is not captured by our theory. For instance consider

[b]Note that this argument uses Eq. (2.27), which is the result of the stability analysis of Sec. 2.3.2. Even though - as discussed in Sec. 2.4.1 - this analysis does not does predict the phase diagrams quantitavely, it *does* predict the MIPS suppression for high aspect ratios, and therefore we believe this argumentation to be sound.

Fig. 2.8, where we show a snapshot of rods at $\phi = 0.5$, Pe $= 100$, just outside the MIPS region, and colour particles according to nematic orientation. The clusters formed by the rods have significant short-range nematic order. Incorporating the dynamics of the polarization and nematic fields using theory developed for active nematics [74, 75] might allow for more accurate predictions for the onset of MIPS for longer rods.

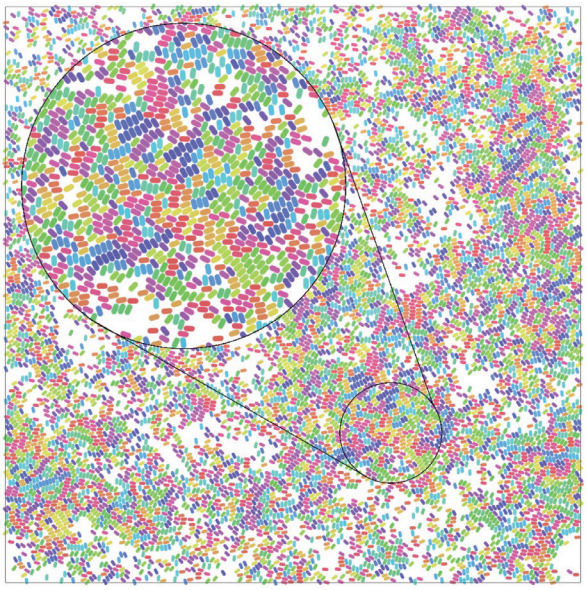

Figure 2.8: Simulation snapshot of 2D rods with aspect ratio $l/\sigma = 2$ at a packing fraction of $\phi = 0.5$ and a Péclet number of Pe $= 100$. Particles are coloured according to their orientation. Dense clusters display significant short-range orientational order, and no large-scale phase separation can be seen.

2.5 Conclusions & outlook

In this chapter, we showed that motility-induced phase separation does not occur for rod-like particles when they become sufficiently anisotropic. This disappearance is observed both from many-particle simulations and from a stability analysis of the homogeneous isotropic phase. The latter provides a simple criterion for the onset of MIPS by considering the effective swimming speed of the particles and their effective rotational diffusion. Both methods agree qualitatively in that MIPS is pushed to higher densities for increasing rod aspect ratio, and they agree quantitatively for short rods that deviate only slightly from disks or spheres. For larger aspect ratios the quantitative agreement is lost, presumable due to alignment interactions that are present, but not taken into account in the stability analysis.

We also propose a more intuitive explanation for the suppression mechanism. MIPS

relies on particles slowing down sufficiently with increasing density [40]. This hindrance is closely linked to the duration of collisions between particles [61, 72, 73]. Excluding torques, the duration of collisions is determined by how long it takes for them to slide along one another. Including torques can dramatically decrease the duration of collisions by rotating the forward axes of the self-propelled particles away from each other. Formulated in this way, we can also explain the results of Refs. [47, 48], where MIPS is enhanced for particles with Vicsek interactions. Simply put, Vicsek torques prolong particle collisions, while rodlike excluded volume torques shorten them. Intriguingly, this provides us with a particle design tool to enhance or suppress MIPS. MIPS is enhanced for Vicsek-like interactions [47, 48], for faceted, concave and/or rough particles [63, 76, 77], while we expect to be suppressed for smooth particles and rodlike shapes [71]. In addition to steric interactions, hydrodynamic interactions between active particles also play an important role in whether or not MIPS can form. While hydrodynamics seems to usually suppress MIPS [78–80], the details depend on whether particles are "pushers" or "pullers" and on the dimensionality [81, 82].

Despite recent advancements, the role of torque in active systems is still not well understood. Much of the developed theory has been restricted to the torque-free regime, but recent numerical studies suggest that torque interactions [47, 48] can have a significant effect on the structure and dynamics of active matter systems. In order to understand active matter beyond torque-free model systems, more theoretical work is needed to elucidate the influence of torques in active systems.

2.6 Acknowledgements

This chapter is part of a collaboration with Robin van Damme, René van Roij and Marjolein Dijkstra. Robin van Damme developed the simulations of Sec. 2.2, and obtained and analysed all results presented in Sec. 2.4. The author of this thesis derived the analytical criterion presented in Sec. 2.3. René van Roij and Marjolein Dijkstra helped by critically examining all results and identifying future directions throughout the research process. We acknowledge Bram Bet for useful discussions and information on the friction coefficients of short spherocylinders.

Appendices

These appendices present an analysis of the significance of the effective translational diffusion D_t^{eff}, the hydrodynamic friction coefficients for short spherocylinders, a finite-size analysis of the effective self-propulsion velocity v^{eff} and effective rotational diffusion D_r^{eff}, and additional simulation snapshots.

Appendix 2.A Insignificance of effective translational diffusion

In the stability analysis we have mapped the effect of interparticle forces into an effective swim speed v^{eff} and an effective translational diffusion D_t^{eff}. Previous literature with similar stability analyses has assumed that this effective translational diffusion is equal to the bare translational diffusion i.e. $D_t^{\text{eff}} = D_t$, usually as an approximation or closure [58, 66]. We opted to check this whether such an assumption is reasonable for 3D spheres and rods as well by measuring it from the 3D mean square displacement (MSD)

$$\langle |\boldsymbol{r}_i(t) - \boldsymbol{r}_i(0)|^2 \rangle = \frac{(v^{\text{eff}})^2}{2(D_r^{\text{eff}})^2} \left(e^{-2D_r^{\text{eff}} t} - 1 \right) + 6 \left(D_t^{\text{eff}} + \frac{(v^{\text{eff}})^2}{6D_r^{\text{eff}}} \right) t. \tag{2.30}$$

Similar to Ref. [66], we associate D_t^{eff} with the long-time diffusion constant of a passive system. For a passive system, the MSD becomes

$$\langle |\boldsymbol{r}_i(t) - \boldsymbol{r}_i(0)|^2 \rangle = 6D_t^{\text{eff}} t. \tag{2.31}$$

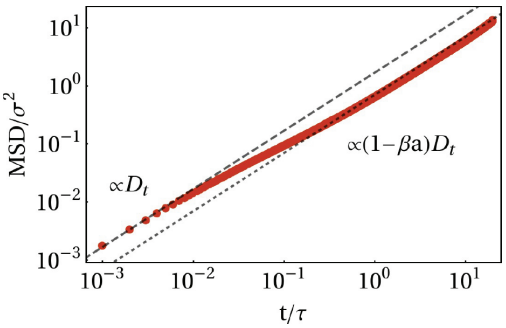

Figure 2.A.1: Mean square displacement of $N = 200$ 3D passive spheres (Pe $= 0$) at a packing fraction of $\phi = 0.3$. At very small times, there is free diffusion i.e. $\text{MSD}/\sigma^2 \approx 6D_t t$, while at long times the particle interactions lead to a decrease of the diffusion coefficient i.e. $\text{MSD}/\sigma^2 \approx 6D_t^{\text{eff}} t$.

Figure 2.A.1 shows the MSD measured for a system of passive spheres at a packing fraction of $\phi = \pi\sigma^3 N/6V = 0.3$. At short times, diffusion is essentially free and $D_t^{\text{eff}} = D_t$. At long times the particle interactions lead to an effective decrease of the diffusion coefficient. This decrease depends on the density of the system. For $\phi = 0.3$, we find that $D_t^{\text{eff}}/D_t \approx 0.34$. While this decrease is significant in terms of the diffusion of passive particles, it is entirely *in*significant when considering the stability of the homogeneous isotropic phase for self-propelled particles, as long as the Péclet number is higher than roughly $\text{Pe} \sim 1$. Thus, we just approximate $D_t^{\text{eff}} = D_t$.

Appendix 2.B Hydrodynamics friction coefficients for 3D spherocylindrical particles

In Figure 2.B.1 we show the hydrodynamic friction factors of short ($1 \leq l/\sigma < 2.5$) spherocylinders and ellipsoids in 3D, defined with respect to a sphere of the same volume as detailed in Ref. [55]. For these aspect ratios the difference between ellipsoids and spherocylinders is minimal, so one can safely use the exact friction factors that were determined by Perrin in Ref. [56].

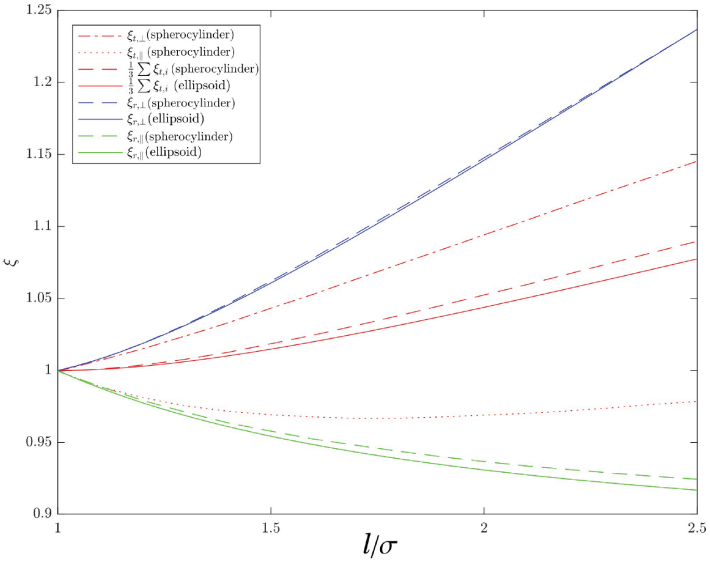

Figure 2.B.1: Hydrodynamic friction coefficients for ellipsoids and spherocylinders for small aspect ratios $1 < l/\sigma < 2.5$, defined with respect to a sphere of the same volume [55]. The red long-short dashed and dotted lines indicate the translational friction coefficients of spherocylinders, while the red solid and dashed lines indicate the total friction coefficient of ellipsoids and spherocylinders, respectively. The green and blue lines indicate the rotational friction coefficients around and perpendicular to the long axis, respectively. The difference between any of the curves in this aspect ratio regime are $< 5\%$, so we can safely approximate the translational and rotational friction coefficients of spherocylinders by those of ellipsoids.

Appendix 2.C Finite-size effects when measuring effective swim speed and rotational diffusion

Measuring the effective swim speed v^{eff} and rotational diffusion D_r^{eff} from simulations with only few particles ($N \sim 100$) means these constants will suffer from finite-size effects. Here we show the magnitude of this effect. Figure 2.C.1 shows the scaling of (a) the effective swim speed v^{eff} and (b) the fraction of particles in the largest cluster f_{cl} with the inverse of the number of particles N for 3D active spheres, at a packing fraction $\phi = 0.44$ and a Péclet number of $\text{Pe} = 100$. A clear kink can be seen in both graphs at roughly the same system size ($N \sim 4000$), which after visual inspection of the corresponding snapshots (Fig. 2.D.1) can be associated with MIPS. As our small-N simulations take place well below this threshold and v^{eff} does not scale strongly with the number of particles in this regime, we assume that they provide a reasonable estimate of the effective swim speed even when a larger system would phase-separate.

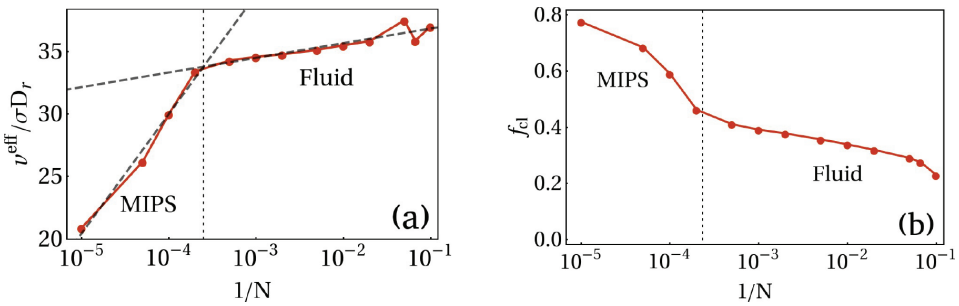

Figure 2.C.1: Effective swim speed v^{eff} (a) and fraction of particles in the largest cluster f_{cl} (b) for 3D active spheres as a function of the inverse of the number of particles N, at a packing fraction $\phi = 0.44$ and a Péclet number of $\text{Pe} = 100$. Both v^{eff} and f_{cl} display a clear kink around $N \sim 4000$ that denotes MIPS. The dashed lines are drawn to show the transition in scaling from the fluid to the MIPS regime, and the dotted line denotes the intercept at $N \approx 4000$.

Appendix 2.D Additional simulation snapshots

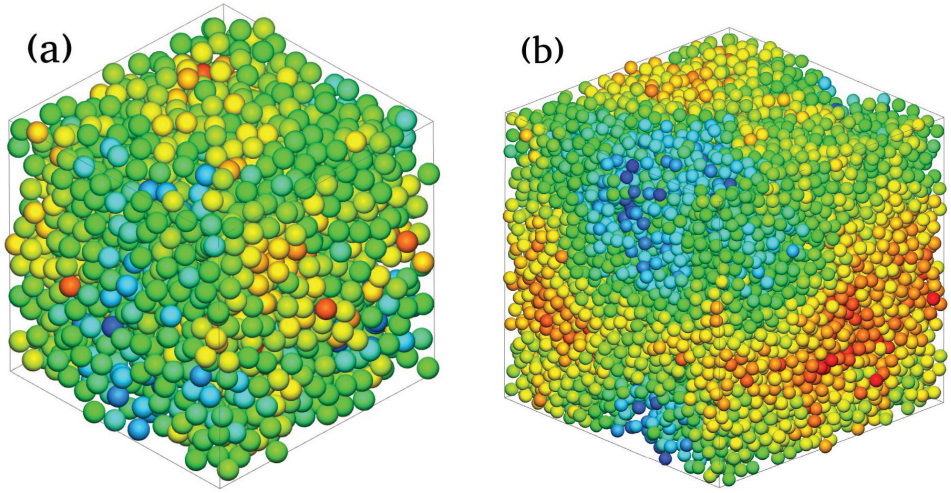

Figure 2.D.1: Two representative snapshots of the simulated system of Fig. 2.C.1 for (a) $N = 2000$ in the fluid regime, and (b) $N = 10000$ in the MIPS regime. Particles are coloured according to their local density. While no large-scale phase separation can be seen for (a), (b) has clearly separated into a dense and a dilute region.

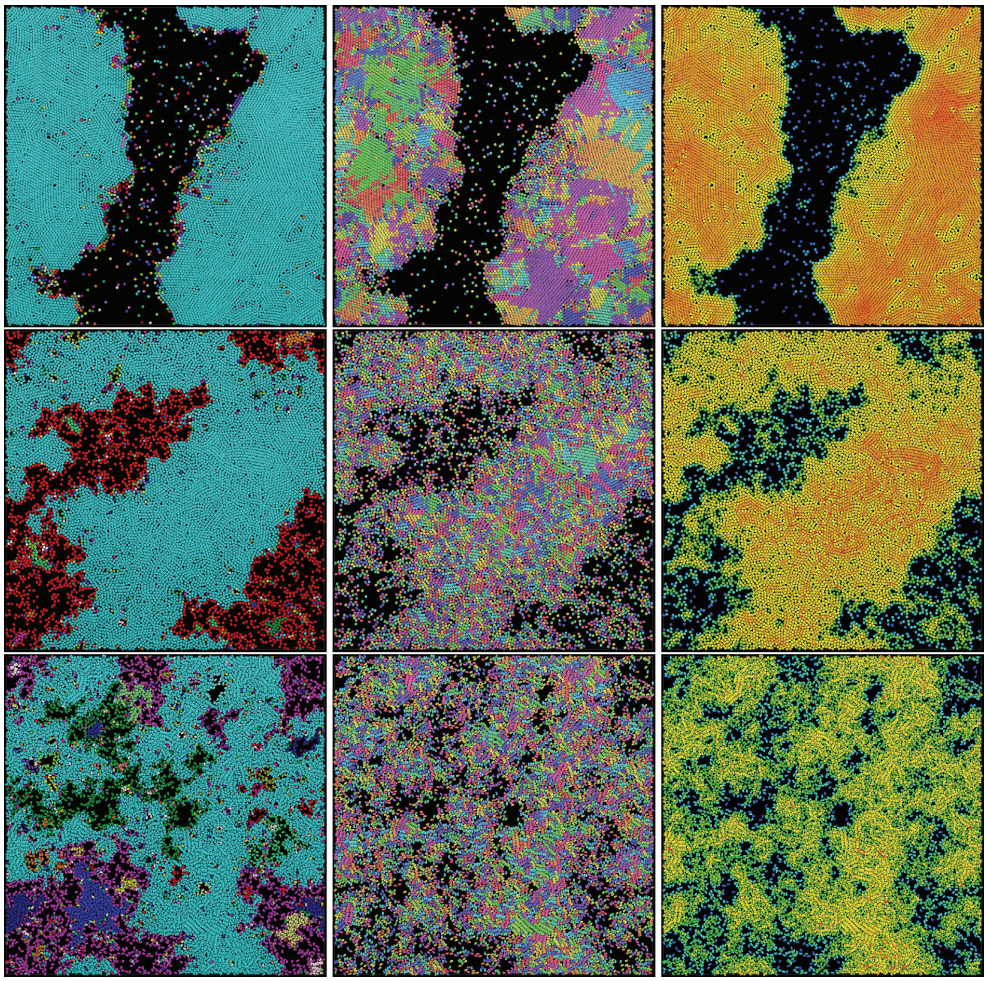

Figure 2.D.2: 2D Simulation snapshots for $N = 10000$ rods with aspect ratios $l/\sigma = 1.1$ (top), $l/\sigma = 1.3$ (middle) and $l/\sigma = 2.0$ (bottom), at $\phi = 0.6$, $\mathrm{Pe} = 100$, deep within the MIPS region. The columns depict the same snapshot three times with various color maps. The left column shows the distribution of clusters, where each cluster is assigned a unique color. In the middle column the color is indicative of the particle orientation, with nematic symmetry. Zooming in also shows black stripes that indicate the polar orientations. In the right column the color represents the local density. Even though all three snapshots show a separation into dense and dilute regions, form a single connected cluster and have no global orientational order (and are thus classified as MIPS), the three cases are clearly different.

3

Van't Hoff's law for active suspensions

In this chapter, we focus on the thermodynamic variable pressure. In contrast to the rest of this thesis, we take into account the fact that the ABPs swim in a solvent. Hence, we study their *osmotic* pressure.

We show that the osmotic pressure increases with the activity of the swimmers. We calculate this increase for ABPs, and find that it can be measured as a rise in the height of the suspension as large as micrometers for experimentally realized microswimmers described in the literature. Moreover, we show that the increase in osmotic pressure is due to an increase in the pressure of the *solvent*. We rationalize this finding by arguing that the background solvent is, in contrast to passive suspensions, no longer at the chemical potential of the solvent reservoir.

This chapter is based on the publication *"Van't Hoff's law for active suspensions: the role of the solvent chemical potential"* [83], written in collaboration with Marjolein Dijkstra and René van Roij.

3.1 Introduction

In this chapter, we study the thermodynamic variable pressure for active Brownian particles (ABPs). The first studies on their pressure [84–86] focussed on *isotropic* particles, and extended the virial theorem (for equilibrium systems [87]) to show that activity makes the particles exert an additional pressure onto the walls of the container that confines them. This additional pressure is usually known as the *"swim pressure"*, or the *"active pressure"*, and was attributed to the increased long-time diffusion constant of the active particles. Later, Solon et al. [88] studied the pressure of *anisotropic* particles, and found a surprising result: the pressure that *these* particles exert onto a container wall depends on the details of the particle-wall interaction! This is in sharp contrast to systems in thermodynamic equilibrium, whose pressure is a function *only* of the variables that characterize the system state, e.g. of the system's density and temperature, and *not* of the particle-wall interaction potential. In other words, Solon et al. showed that the pressure that anisotropic particles exert onto a surrounding wall is not a state function. Not only is this surprising, it is also problematic: if one wishes to predict the densities of two coexisting phases by equating their pressure (and chemical potential), then what should one use for the pressure of a particular phase?

Importantly, these and most other studies on the pressure [26, 45, 84–86, 88–104] consider a model that consists of active particles *only*. Thereby, they model self-propelled particles *on a substrate*. For active particles *in a solvent*, such as the self-propelled colloidal particles used in many experiments, they represent an effective "colloids-only" picture that models the solvent only implicitly via the Brownian motion of the ABPs. However, since the propulsion force is an internal force [8], the solvent *itself* - and in particular its pressure - is affected by the opposite reaction force [94], and this effect is not present in a colloids-only picture. The solvent *is* explicitly modelled in Ref. [105], but only as a passive species that is unaffected by the propulsion force. The only work we know of that *does* study the influence of the reaction force on the solvent is Ref. [94], but it remains unclear how the reaction force affects the conclusion of [88] that the pressure of ABPs is not a state function.

In this chapter, we take the reaction force on the solvent explicitly into account, and study the pressure of an active suspension of particles *and* solvent. In particular, we study the *osmotic* pressure of (anisotropic) ABPs, and ask whether it is a state function or not.

To this end, first we review the following basic knowledge about the osmotic pressure of *passive* Brownian particles in thermodynamic equilibium. These systems obey Van't Hoff's law, which states that the osmotic pressure Π of a dilute suspension equals the pressure $\rho k_B T$ of a dilute gas of the same concentration ρ and temperature T [106–108]. In Van't Hoff's interpretation, the total pressure of the suspension $P_{\text{tot}}(\rho, \mu_s) = \rho k_B T + P_s(\mu_s)$ decomposes into the sum of the effective colloid-only pressure $\rho k_B T$ and a 'background' pressure $P_s(\mu_s)$ of the solvent at chemical potential μ_s. In the typical experimental setup to measure osmotic pressure (Fig. 3.1), μ_s is set by a solvent reservoir that connects to the suspension via a membrane permeable to solvent only. The net force per unit area exerted on the membrane defines the osmotic pressure, and results from the difference in suspension pressure $P_{\text{tot}}(\rho, \mu_s)$ and reservoir pressure $P_s(\mu_s)$. As this pressure difference induces a height difference H between the two menisci, the osmotic pressure $\Pi \sim H$ can

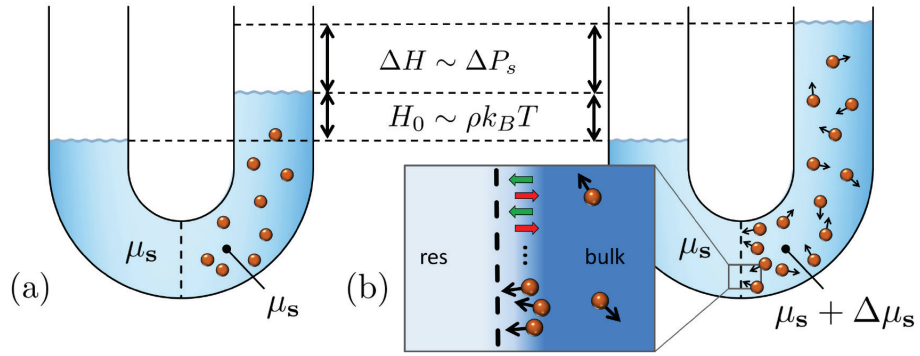

Figure 3.1: Schematic setup to measure the osmotic pressure Π from the height difference $H = H_0 + \Delta H$ between the two menisci. (a) For a passive system, the solvent chemical potential of the suspension equals the reservoir chemical potential μ_s, such that $\Pi = \rho k_B T$ and $H = H_0 \sim \rho k_B T$. (b) For an active system, colloids tend to 'propel into' the membrane (green arrows), thereby exerting the opposite reaction force on the solvent (red arrows). As a result, the solvent pressure and solvent chemical potential in the bulk suspension increase by ΔP_s and $\Delta\mu_s$, respectively, indicated by the darker blue background, such that Π and H increase by ΔP_s and $\Delta H \sim \Delta P_s$, respectively, as we will see in this chapter.

be directly inferred.

In this chapter, we extend Van't Hoff's law to active suspensions. We show that the osmotic pressure increases with activity due to a difference in *solvent* pressure that develops between the suspension and the reservoir. We predict the effect of this solvent pressure difference to be experimentally measurable, either as an additional meniscus rise ΔH (Fig. 3.1), or as a solvent flow through a semipermeable membrane towards the active particles in an open system (Fig. 3.2). The solvent pressure difference implies also a difference in solvent chemical potential, that, remarkably, depends on the details of the colloid-membrane interactions. We will conclude that the osmotic pressure is a state function of a state that itself, however, is affected by the colloid-membrane interaction potential.

3.2 Model

We model the effective one-component system of suspended particles as overdamped active Brownian particles (ABPs) [109, 110]. Every particle is characterized by a three-dimensional position $\mathbf{r}$ and an orientation $\hat{\mathbf{e}}$. It is well known that the probability density $\psi(\mathbf{r}, \hat{\mathbf{e}}, t)$ satisfies the continuity equation

$$\partial_t \psi(\mathbf{r}, \hat{\mathbf{e}}, t) = -\boldsymbol{\nabla} \cdot \mathbf{j}(\mathbf{r}, \hat{\mathbf{e}}, t) - \boldsymbol{\nabla}_{\hat{\mathbf{e}}} \cdot \mathbf{j}_{\hat{\mathbf{e}}}(\mathbf{r}, \hat{\mathbf{e}}, t), \tag{3.1}$$

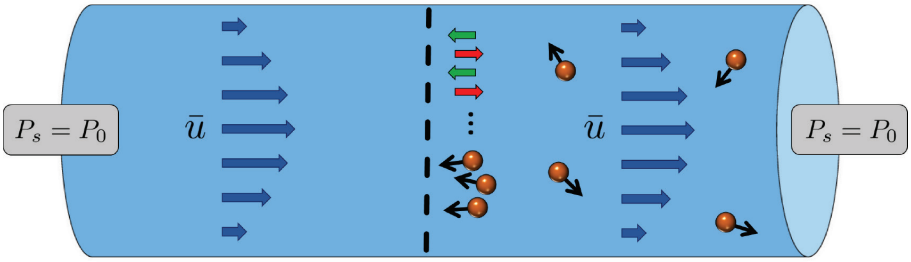

Figure 3.2: Schematic setup to measure how active colloids confined to one side of a semipermeable membrane in an open pipe affect the solvent, viewed in the lab frame. As the colloids tend to 'propel into' the membrane (green arrows), they exert the opposite reaction force on the solvent (red arrows). Under boundary conditions of equal solvent pressure P_s on either side of the pipe, the reaction force drives a parabolic solvent flow profile of mean velocity $\bar{u}$, as indicated by the blue arrows.

and that the translational flux $\mathbf{j}$ and rotational flux $\mathbf{j}_{\hat{\mathbf{e}}}$ follow from the force and torque balance,

$$\begin{aligned} 0 &= -\gamma_t \mathbf{j} \; - \psi \boldsymbol{\nabla} V(\mathbf{r}, \hat{\mathbf{e}}) + \gamma_t v_0 \psi \hat{\mathbf{e}} - k_B T \boldsymbol{\nabla} \psi \quad \text{and} \\ 0 &= -\gamma_r \mathbf{j}_{\hat{\mathbf{e}}} - \psi \boldsymbol{\nabla}_{\hat{\mathbf{e}}} V(\mathbf{r}, \hat{\mathbf{e}}) - k_B T \boldsymbol{\nabla}_{\hat{\mathbf{e}}} \psi, \end{aligned} \tag{3.2}$$

respectively, between (i) the frictional force and torque, with friction coefficients γ_t and γ_r, (ii) an external force and torque generated by the external potential $V(\mathbf{r}, \hat{\mathbf{e}})$ acting on every particle, (iii) a constant self-propulsion force, corresponding to propulsion speed v_0, acting along each particle's orientation $\hat{\mathbf{e}}$, and (iv) Brownian forces and torques giving rise to translational and rotational diffusion. In order to focus on the essential physics, we follow Van't Hoff and consider the dilute limit, where effective colloid-colloid interactions can be ignored, and where also hydrodynamic colloid-colloid interactions are expected to be nonessential. Furthermore, we assume a steady state, i.e. $\partial_t \psi = 0$. We analyse the force balance by taking the zeroth moment of Eq. (3.2), which upon defining the density $\rho(\mathbf{r}) \equiv \int \mathrm{d}\hat{\mathbf{e}} \psi(\mathbf{r}, \hat{\mathbf{e}})$, the polarization $\mathbf{m}(\mathbf{r}) \equiv \int \mathrm{d}\hat{\mathbf{e}} \psi(\mathbf{r}, \hat{\mathbf{e}}) \hat{\mathbf{e}}$, and the colloid flux $\mathbf{J}(\mathbf{r}) \equiv \int \mathrm{d}\hat{\mathbf{e}} \mathbf{j}(\mathbf{r}, \hat{\mathbf{e}})$, yields the balance

$$\begin{aligned} \mathbf{0} &= -\gamma_t \mathbf{J}(\mathbf{r}) - \int \mathrm{d}\hat{\mathbf{e}} \psi \boldsymbol{\nabla} V(\mathbf{r}, \hat{\mathbf{e}}) + \gamma_t v_0 \mathbf{m}(\mathbf{r}) - k_B T \boldsymbol{\nabla} \rho(\mathbf{r}) \\ &\equiv \mathbf{f}^f(\mathbf{r}) + \mathbf{f}^e(\mathbf{r}) + \mathbf{f}^p(\mathbf{r}) - \boldsymbol{\nabla} P(\mathbf{r}) \end{aligned} \tag{3.3}$$

between the frictional body force $\mathbf{f}^f$, the external body force $\mathbf{f}^e$, the propulsion body force $\mathbf{f}^p$, and the pressure gradient force $-\boldsymbol{\nabla} P$. The form of the propulsion body force,

$$\mathbf{f}^p(\mathbf{r}) \equiv \gamma_t v_0 \mathbf{m}(\mathbf{r}), \tag{3.4}$$

is easily understood as the sum of propulsion forces $\gamma_t v_0 \hat{\mathbf{e}}$ acting on individual colloids. Just like the frictional force $\mathbf{f}^f$, the propulsion force $\mathbf{f}^p$ is an *internal* force.

We now turn our attention to the solvent, that we assume to be incompressible and at small Reynolds number. On a scale coarse-grained over the colloids - i.e. the same scale

Eq. (3.3) applies to - the local solvent velocity $\mathbf{u}(\mathbf{r})$ is governed by the Stokes equation

$$\mathbf{f}_s^e(\mathbf{r}) - \mathbf{f}^f(\mathbf{r}) - \mathbf{f}^p(\mathbf{r}) - \boldsymbol{\nabla} P_s(\mathbf{r}) + \eta \boldsymbol{\nabla}^2 \mathbf{u}(\mathbf{r}) = 0, \tag{3.5}$$

as derived in appendix 3.A. Eq. (3.5) is simply the solvent force balance equipped with a possible external body force $\mathbf{f}_s^e(\mathbf{r})$, and the opposite internal body forces $-\mathbf{f}^f(\mathbf{r})$ and $-\mathbf{f}^p(\mathbf{r})$ as reaction forces, in accordance with Newton's third law. Furthermore, η is the dynamic viscosity of the solvent, and $P_s(\mathbf{r})$ is the (coarse-grained) solvent pressure. For the present purposes, one can regard the solvent pressure $P_s(\mathbf{r})$ and velocity $\mathbf{u}(\mathbf{r})$ as being defined by Eq. (3.5) together with the incompressibility condition $\boldsymbol{\nabla} \cdot \mathbf{u}(\mathbf{r})$ - for a more careful definition, see appendix 3.A.

3.3 Osmotic pressure

To represent the setting of Fig. 3.1, we assume an external potential due to a semipermeable membrane that is planar and normal to the Cartesian unit vector $\hat{\mathbf{z}}$, i.e. $V(\mathbf{r}, \hat{\mathbf{e}}) = V(z, \theta)$, with $\cos\theta \equiv \hat{\mathbf{e}} \cdot \hat{\mathbf{z}}$. This implies $\psi(\mathbf{r}, \hat{\mathbf{e}}) = \psi(z, \theta)$, $\mathbf{J}(\mathbf{r}) = J_z(z)\hat{\mathbf{z}}$ etc. The potential $V(z, \theta)$ is assumed to decay from ∞ in an infinitely large reservoir, located at $z < 0$ and containing z-coordinate $z_{\text{res}} \ll 0$ in bulk, to 0 in the suspension, located at $z > 0$ and containing $z_b \gg 0$ in bulk. The zeroth moment of Eq. (3.1), $\partial_z J_z(z) = 0$, together with a no-flux boundary condition, then implies $J_z(z) = 0$, and hence the frictional body force $\mathbf{f}^f(z) = 0$. For a state without any solvent flow ($\mathbf{u} = \mathbf{0}$), and for a membrane perfectly invisible to the solvent ($\mathbf{f}_s^e = \mathbf{0}$), Eq. (3.5) then simplifies to $-f_z^p(z) - \partial_z P_s(z) = 0$.

For a passive system, where the propulsion body force $f_z^p(z) = 0$, this solvent force balance guarantees equal solvent pressures in the bulk suspension and solvent reservoir, i.e. $\Delta P_s \equiv P_s(z_b) - P_s(z_{\text{res}}) = 0$. In an active system, however, the existence of a nonzero propulsion force $f_z^p(z)$ results in a difference in these solvent pressures, derived in the supplementary information (SI) to be

$$\begin{aligned} \Delta P_s &= -\int_{z_{\text{res}}}^{z_b} \mathrm{d}z f_z^p(z) \\ &= \frac{\gamma_t \gamma_r v_0^2}{6 k_B T} \rho \; - \frac{\gamma_t v_0}{2 k_B T} \int_{z_{\text{res}}}^{z_b} \mathrm{d}z \int \mathrm{d}\hat{\mathbf{e}} \psi(z, \theta) \sin(\theta) \partial_\theta V(z, \theta). \end{aligned} \tag{3.6}$$

The first term on the right-hand side of Eq. (3.6) corresponds to what is known as the swim pressure [84–86], which we thus actually identify as a difference in solvent pressure. The second term on the right-hand side of Eq. (3.6), present for particles experiencing a torque $-\partial_\theta V(z, \theta)$, is of special interest because it turns out to lead to the conlusion that ΔP_s depends on the potential $V(z, \theta)$. This issue will be discussed later.

The force balance of the total suspension simply follows as the sum of the colloid force balance (3.3) and the solvent force balance (3.5), yielding in the planar and flow-free geometry of interest

$$f_z^e(z) - \partial_z P_{\text{tot}}(z) = 0, \tag{3.7}$$

where $P_{\text{tot}}(z) \equiv P(z) + P_s(z)$. From the total force balance (3.7), the osmotic pressure $\Pi \equiv \int_{z_{\text{res}}}^{z_b} \mathrm{d}z f_z^e(z)$, defined as the magnitude of the force per unit area exerted on the

membrane, follows as $P_{\rm tot}(z_b) - P_s(z_{\rm res})$. As the total bulk pressure decomposes into colloid and solvent contributions as $P_{\rm tot}(z_b) = \rho k_B T + P_s(z_b)$, the osmotic pressure reads

$$\Pi = \rho k_B T + \Delta P_s. \tag{3.8}$$

In equilibrium, Eq. (3.8) reduces to Van't Hoff's result $\Pi = \rho k_B T$ on account of $\Delta P_s = 0$. Activity increases the osmotic pressure by increasing the solvent pressure with respect to the reservoir by ΔP_s, which is the key result of this chapter. Together, Eq. (3.8) and (3.6) generalize Van't Hoff's law to active suspensions.

To clarify these concepts further, we have solved the Smoluchowski equation (3.1) numerically for a system of spheres subject to a propulsion force, characterized by Péclet number $\mathrm{Pe} \equiv (\gamma_t \gamma_r)^{\frac{1}{2}} v_0 / k_B T$, in the planar geometry modelling the setting of Fig. 3.1. The membrane, felt by the colloids only, is modelled by the soft potential $V(z) = \lambda k_B T (z/\ell)^2$ for $z < 0$ and $V(z) = 0$ for $z \geq 0$ (Fig. 3.3(a)), i.e. there is no torque. Here $\lambda = 1$ is the strength of the potential, and $\ell \equiv (\gamma_r/\gamma_t)^{\frac{1}{2}}$ is the appropriate unit of length, which is of the order of the (effective) particle size upon using Stokes relations for γ_t and γ_r. Fig. 3.3(b) shows the profile of the propulsion body force $f_z^p(z)$. Whereas $f_z^p(z) = 0$ for a passive system ($\mathrm{Pe} = 0$), an active system displays a nonzero polarization $m_z(z)$, and thus by Eq. (3.4) a propulsion body force $f_z^p(z)$, in the vicinity of the membrane directed towards the membrane. This well-known effect [111–116] is in this case caused by colloids persistently propelling 'into' the repulsive membrane. Fig. 3.3(c), for $\mathrm{Pe} = 0$, shows the pressure profiles $P(z)$ of the passive colloids, $P_s(z)$ of the solvent, and $P_{\rm tot}(z)$ of the total passive suspension. Here the reaction body force $-f_z^p(z) = 0$, and hence the solvent pressure $P_s(z)$ is constant, as argued before. It is only due to the bulk colloid pressure $P(z_b) = \rho k_B T$ that the total bulk pressure $P_{\rm tot}(z_b)$ is higher than the total reservoir pressure $P_{\rm tot}(z_{\rm res})$. The osmotic pressure $\Pi = P_{\rm tot}(z_b) - P_{\rm tot}(z_{\rm res})$ is therefore equal to $\rho k_B T$. The profiles for an active system ($\mathrm{Pe} = 3$), displayed in Fig. 3.3(d), show that the solvent bulk pressure $P_s(z_b)$ exceeds the solvent reservoir pressure $P_s(z_{\rm res})$. This is caused by the reaction body force $-f_z^p(z)$, that pushes solvent towards the bulk, as pictured in Fig. 3.1(b). As a result, both the total bulk pressure $P_{\rm tot}(z_b)$ and the osmotic pressure Π exceed their passive counterparts by $\Delta P_s = \gamma_t \gamma_r v_0^2 \rho / 6 k_B T$ on account of Eq. (3.6) for the torque-free potential of interest here.

3.4 Experimental predictions

The experiments that have addressed the pressure of active systems [91, 98, 103] are few in number. In particular, the osmotic pressure has never been measured directly. Despite the simplicity of the ABP model, that neglects e.g. hydrodynamic interactions, our expression for the osmotic pressure does allow to estimate the order of magnitude of the meniscus height difference $H = \Pi/(\rho_s^m g)$ that is to be expected in the experiment sketched in Fig. 3.1. Here we focus on an aqueous dispersion (mass density $\rho_s^m = 1$ kg/dm^3) of active hard spheres of radius a, with friction coefficients given by the Stokes relations $\gamma_t = 6\pi\eta a$ and $\gamma_r = 8\pi\eta a^3$, subject to Earth's gravitational acceleration g, at room temperature, and at packing fraction 0.01 that should mimic the ideal (non-interaction) conditions.

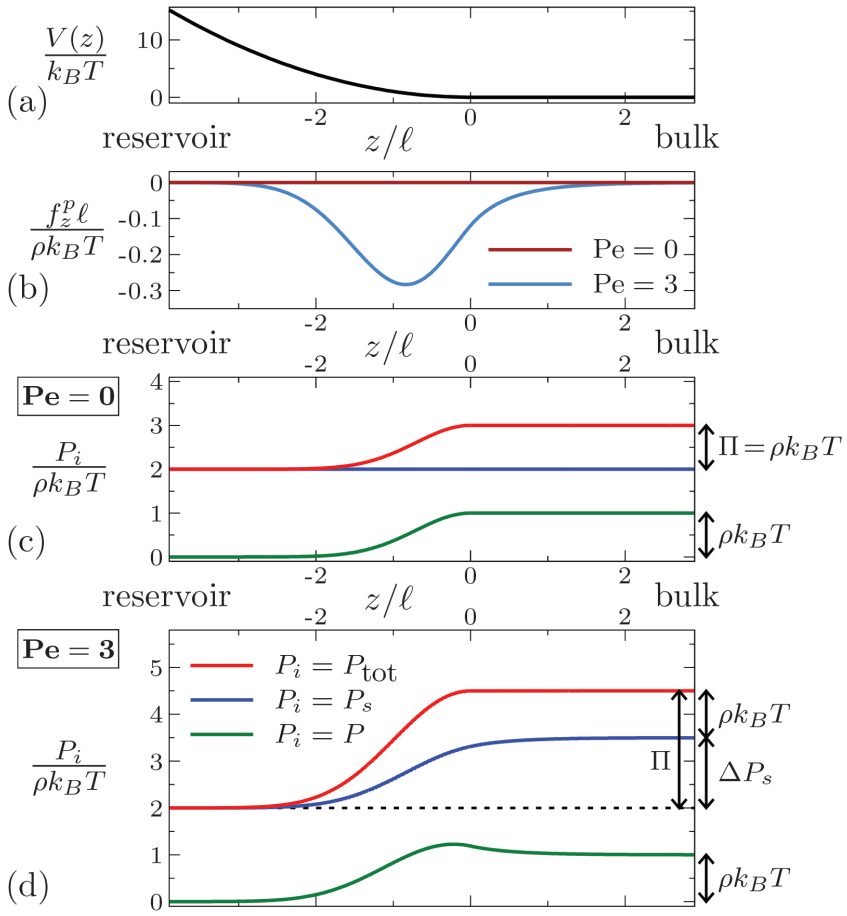

Figure 3.3: (a) External potential $V(z)$ modelling the planar membrane of Fig. 3.1 that separates the reservoir at $z_{\rm res} = -4\ell$ from the bulk suspension at $z_b = 3\ell$. (b) The steady state propulsion body force $f_z^p(z)$, at activity Pe. Passive (c) and active (d) pressure profiles of the colloids $P(z)$, the solvent $P_s(z)$, and the total suspension $P_{\rm tot}(z) = P(z) + P_s(z)$. For the passive system (Pe = 0), $P_s(z)$ is constant, such that the osmotic pressure $\Pi = P_{\rm tot}(z_b) - P_{\rm tot}(z_{\rm res})$ equals the bulk colloid pressure $P(z_b) = \rho k_BT$. For the active system (Pe = 3), the reaction body force $-f_z^p(z)$ increases the bulk solvent pressure $P_s(z_b)$, as well as $P_{\rm tot}(z_b)$ and Π, by ΔP_s.

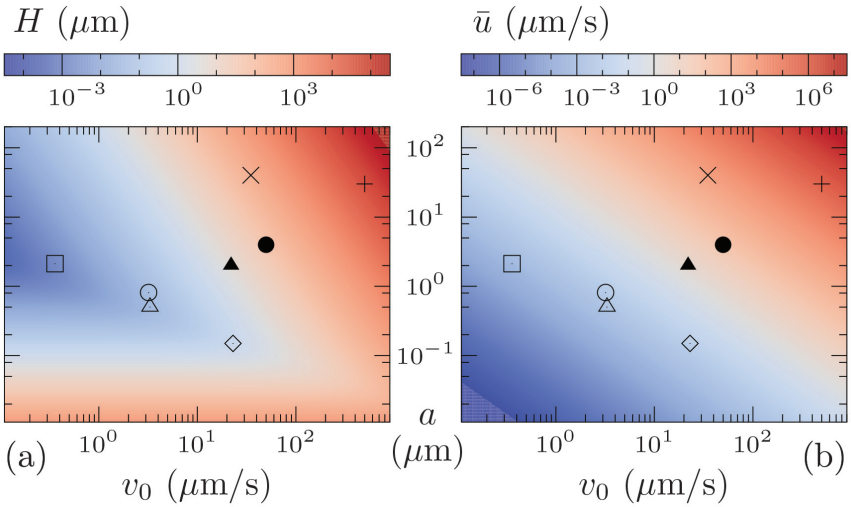

Figure 3.4: (a) Predicted rise $H = H_0 + \Delta H$ in Fig. 3.1, for spherical particles of radius a at propulsion speed v_0 at packing fraction 0.01 in water. (b) Predicted mean solvent velocity $\bar{u}$ in Fig. 3.2, for a cylindrical pipe of radius $5a$ and length $100a$. Symbols denote literature values of (v_0,a) combinations of experimentally realized self-propelled colloids + [15], × [117], ⋄ [118], ∘ [119], △ [120], □ [121]; and motile bacteria • [122], ▲ [123].

The predicted height differences H are shown in Fig. 3.4(a). Whereas the passive osmotic pressure $\rho k_B T$ induces a passive rise $H_0 \sim a^{-3}$ too small to measure for colloidal particles, activity induces an additional rise $\Delta H \sim \Delta P_s \sim a v_0^2$ that brings $H = H_0 + \Delta H$ up to the regime of micrometers [117, 122, 123] or even millimeters [15] for the larger values of propulsion speed v_0 and particle size a of experimentally realized microswimmers.

To determine experimentally that the activity-induced increase in osmotic pressure results from the increase in *solvent* pressure ΔP_s, we propose to confine active particles by a membrane to one half of an open, horizontal pipe, for which gravity plays no role, as illustrated in Fig. 3.2. Applying *equal* solvent pressures to either side of the pipe, rather than the no-flux boundary condition before, results in a steady state where the reaction body force near the membrane $-\mathbf{f}^p$ drives a steady solvent flow $\mathbf{u}(\mathbf{r})$ through the pipe (as seen in the lab frame), according to Eq. (3.5). In the limit $|\mathbf{u}(\mathbf{r})| \ll v_0$, and for a cylindrical pipe, this flow velocity is identical to the Poisseuile flow that would be generated in a pipe filled with only solvent upon applying the solvent pressure difference ΔP_s of Eq. (3.6) between either end of the pipe. For a derivation see the SI. The predicted mean solvent velocity $\bar{u} \sim a^2 v_0^2$ is shown in Fig. 3.4(b) as a function of the propulsion speed v_0 and colloid radius a, for a pipe of radius $5a$ and length $100a$. For the larger values of v_0 and a of experimentally realized swimmers [15, 117, 122, 123], the solvent velocity $\bar{u}$ (although not satisfying $\bar{u} \ll v_0$ in all cases) is predicted to be on the

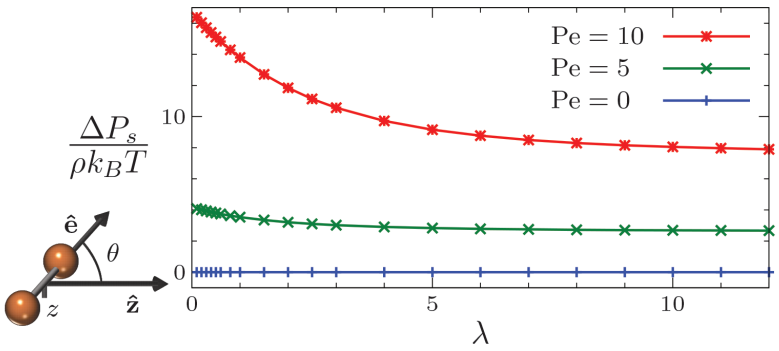

Figure 3.5: Increase in bulk solvent pressure ΔP_s as a function of the strength λ of the soft colloid-membrane interaction potential in the setting of Fig. 3.1 for active dumbells at varying activity Pe. For active systems (Pe>0) ΔP_s depends on λ.

order of micrometers per second, and hence easily detectable, e.g. by using tracer particles.

3.5 The solvent chemical potential

We now return to the the original setting of Fig. 3.1 to interpret the solvent pressure difference ΔP_s between the suspension and the reservoir. Even though the active suspension is out of equilibrium, the solvent pressure $P_s(z)$ can still be used to define a meaningful intrinsic solvent chemical potential $\mu_s^{\rm int}(z)$ by the (Gibbs-Duhem like) relation $\rho_s(z)\partial_z\mu_s^{\rm int}(z) = \partial_z P_s(z)$, with $\rho_s(z)$ the number density of the solvent (see the SI for details). Hence, the solvent pressure difference ΔP_s is accompanied by a difference in the intrinsic solvent chemical potential

$$\Delta\mu_s \equiv \mu_s^{\rm int}(z_b) - \mu_s^{\rm int}(z_{\rm res}) = \int_{z_{\rm res}}^{z_b} {\rm d}z \frac{\partial_z P_s(z)}{\rho_s(z)}. \tag{3.9}$$

We can thus rephrase our findings as follows. Activity increases the solvent chemical potential of the bulk of the suspension from the reservoir value μ_s to $\mu_s + \Delta\mu_s$. The total bulk pressure $P_{\rm tot}(\rho, \mu_s + \Delta\mu_s) = \rho k_B T + P_s(\mu_s + \Delta\mu_s)$ increases accordingly, such that the osmotic pressure $\Pi = P_{\rm tot}(\rho, \mu_s + \Delta\mu_s) - P_s(\mu_s)$, which is the difference between the total bulk pressure and the reservoir pressure, now equals $\Pi = \rho k_B T + \Delta P_s$, where $\Delta P_s = P_s(\mu_s + \Delta\mu_s) - P_s(\mu_s)$ is the difference in solvent pressures accompanying the difference in solvent chemical potentials.

In this light, we address the second term of Eq. (3.6), present for anisotropic colloids experiencing a torque $-\partial_\theta V(z,\theta)$. To investigate the implications of this term, we have solved the Smoluchowski equation (3.1) for active dumbells, consisting of two point particles with separation $\ell = (\gamma_r/\gamma_t)^{\frac{1}{2}}$. Both point particles are subject to the same membrane potential $V(z) = \lambda k_B T (z/\ell)^2$ for $z < 0$ as before, where the strength parameter λ can now be varied. The resulting potential acting on a dumbell, $V(z,\theta) =$

$V(z+\frac{\ell}{2}\cos\theta)+V(z-\frac{\ell}{2}\cos\theta)$, exerts a nonzero torque $-\partial_\theta V(z,\theta)$, that tends to align dumbells parallel to the wall. Fig. 3.5 shows the resulting increase in solvent pressure ΔP_s, calculated from Eq. (3.6), for different activities Pe as a function of the strength λ of the colloid-membrane interaction potential. For Pe > 0, ΔP_s decreases with λ. The reason for this decrease is that the torque generated by the potential rotates the particles that propel 'into' the membrane, and thereby influences the shape of the polarization profile $m_z(z)$. As it turns out, the torque reduces the total polarization near the membrane $-\int_{z_{\rm res}}^{z_b} \mathrm{d}z m_z(z)$, and by that also the integrated reaction body force $-\int_{z_{\rm res}}^{z_b} \mathrm{d}z f_z^p(z)$ that pushes solvent towards the suspension, see Eq. (3.4). Consequently, the increase in solvent pressure ΔP_s decreases as the strength of the colloid-membrane interaction potential increases. The same dependence was found in Ref. [88] for ellipsoidal particles under the assumptions that the distribution $\psi(z,\theta)$ attains its bulk value already at $z=0$, and that the effect of ellipses that only feel the potential partially is negligible. We thus confirm the conclusion of Ref. [88] that the second term of Eq. (3.6) depends on the precise form of the colloid-membrane interaction potential $V(z,\theta)$, by a numerical solution $\psi(z,\theta)$ that does not require any further assumptions.

Whereas in Ref. [88] this finding was reason to question whether the osmotic pressure is a state function, we emphasize it is the bulk state of the suspension itself that depends on the colloid-membrane potential. To appreciate its consequences, we note that in equilibrium the ensemble of reservoir *and* suspension is specified by the state variables (μ_s,ρ,T), since the solvent chemical potential of the reservoir μ_s sets the same chemical potential in the suspension. The fact that for an active system the solvent pressure difference ΔP_s - and thereby also the chemical potential difference $\Delta\mu_s$ - generally depends on the colloid-membrane interaction potential, implies that a complete specification of the ensemble requires an additional state variable, e.g. the bulk solvent chemical potential $\mu_s^b \equiv \mu_s + \Delta\mu_s$. In fact, upon including effective colloid-colloid interactions, the activity is also required as a state variable, e.g. in terms of v_0 (see SI). A complete set of (intensive) state variables therefore reads $(\mu_s,\mu_s^b,\rho,T,v_0)$. All the mentioned pressures, including the osmotic pressure, *are* state functions of these variables. In other words, they are *not* a direct function of the strength λ of the colloid-membrane interaction potential, but can only depend on λ *via* the bulk solvent chemical potential $\mu_s^b(\lambda)$.

3.6 Conclusions

We have generalized Van't Hoff's law to active suspensions. We have shown that the active particles exert a net reaction force on the solvent, an effect that we predict to be experimentally measurable either as a solvent flow through a semipermeable membrane confining the active suspension to one side of an open pipe, or as a macroscopic rise of the suspension meniscus in a U-pipe experiment. In the latter case, the reaction force increases the solvent pressure of the suspension, and thereby the solvent chemical potential. Remarkably, this increase, and thereby the bulk state of the suspension *itself*, depends on the details of the colloid-membrane interactions. The osmotic pressure *is* a

state function of (amongst others) the solvent chemical potential; it *does* depend on the details of the colloid-membrane interactions, but only *via* the solvent chemical potential.

3.7 Discussion

The predictions of Eq. (3.6) and of Fig. 3.4 are made for active particles whose orientation changes only by rotational diffusion with a rate that follows from the Stokes-Einstein relations for spherical particles. The corresponding typical reorientation time τ_r, equal to γ_r/k_BT in this case, is shown by Eq. (3.6) to be proportional to the excess solvent pressure ΔP_s. In fact, the result $\Delta P_s \sim \tau_r$ is more general[85], because the typical time τ_r that a particle spends propelling 'into' the membrane determines the magnitude of the time-averaged reaction force it exerts on the solvent, and thus of the excess solvent pressure ΔP_s. In general, this reorientation time τ_r depends on more factors, for instance on the details of the propulsion mechanism of the active particle, and on its (hydrodynamic) interaction with the membrane [112, 124]. An interesting example of the latter type occurs for the square-shaped particles simulated in Ref. [125]. These particles tend to form a crystal phase next to the membrane, with the majority of particles facing the membrane [126]. This effect increases τ_r, and thereby the excess solvent pressure ΔP_s, dramatically.

In the SI, we generalize the framework presented here to include interactions. The active version of Van't Hoff's law (3.8) then generalizes to $\Pi = P(\rho, \mu_s^b, v_0) + \Delta P_s$, where $P(\rho, \mu_s^b, v_0)$ now denotes the full pressure (ideal gas plus virial contributions) of the effective colloids-only system that is characterized by (ρ, μ_s^b, v_0). Hence, the functional form of the osmotic pressure Π differs from its passive expression only by the excess solvent pressure ΔP_s. This excess pressure ΔP_s again depends on the membrane potential, except in the absence of any torque interactions between either the particles and the membrane, or between the particles themselves. In the absence of such torques, ΔP_s again reduces to the known swim pressure. While this swim pressure is a linear function of ρ at low colloid densities, cf. Eq. (3.6), it typically becomes a decreasing function of ρ at high densities [84, 92, 127, 128]. For general interactions, it remains true that the difference in solvent pressure ΔP_s is accompanied by a difference in solvent chemical potential $\Delta\mu_s$, and that the osmotic pressure *is* a state function of the variables $(\mu_s, \mu_s^b, \rho, T, v_0)$.

Crucial in our approach is that activity enters the colloid force balance (3.3) as the body force $\mathbf{f}^p(\mathbf{r})$, cf. Ref. [94], whereas the local pressure $P(\mathbf{r}) = \rho(\mathbf{r})k_BT$ is of the same form as in equilibrium. Our approach follows Speck and Jack [97], who showed that the bulk colloid pressure ρk_BT represents momentum flux of non-interacting colloids. In the interacting case, the local pressure tensor $P(\mathbf{r})$ generalizes to a local pressure tensor, that consists of both momentum flux and a term accounting for interaction forces (see Sec. 1 of the SI), as the conventional local pressure tensor does [129]. Representing activity by a body force contrasts the approach that we present in chapter 4, where activity is accounted for (in a colloid-only picture) as a contribution to the local pressure tensor, known as the "swim pressure". The latter approach is also followed by Refs. [26, 101, 130, 131].

Whereas the approach presented in this chapter is valid for general particle-particle and particle-wall interactions (see SI), this 'activity-modified' local pressure has only been defined for isotropic particles, and indeed its derivation [102, 132] does not seem to be extendable to systems with torque interactions.

The generalizations of the force balances (3.3), (3.5) and (3.7) to an interacting suspension (see Sec. 3 of the SI) can readily be applied to other typical phenomena exhibited by active systems, such as the motility-induced phase separation that we encountered in chapter 2. Strikingly, the interface of the phase coexistence generated by MIPS was found to have a negative interfacial tension, defined in the colloid-only picture in terms of the activity-modified pressure tensor [26]. This begs the question what this negative interfacial tension - and its interpretation [26, 27] - translate into in the picture presented here, both in the colloid-only sense and upon taking the solvent into account. This question - in the colloid-only sense - is the subject of chapter 4.

3.8 Acknowledgements

This chapter came into being in collaboration with Marjolein Dijkstra and René van Roij, who helped by critically examining all results and identifying future directions throughout the research process. We acknowledge Bram Bet and Bob Evans for useful discussions.

3.9 Supplementary Information

See the supplementary information (SI) of the article on which this chapter is based [83] for the following information - numbered according to section number in the SI.

1. A derivation of the overdamped Smoluchowski Eq. (3.1) and colloid momentum balance (3.3) from the underdamped case. This includes a proof that the local pressure tensor $P(\mathbf{r})$ represents momentum flux in the non-interacting case, as well as the generalizations to interacting systems.

2. A slightly more extended version of the derivation (of the solvent force balance (3.5)) presented in appendix 3.A.

3. A generalization to interacting systems of the osmotic pressure presented in Sec. 3.3 and of the solvent chemical potential presented in Sec. 3.5.

4. A derivation of the solvent pressure difference (3.6), as well as its generalization to interacting systems.

5. Details of the numerical solution (to the Smoluchowski equation (3.1)) that underlies Figs. 3.3 and 3.5.

6. A calculation that shows that the polarization of colloids near the semi-permeable membrane can also lead to solvent flow through an open pipe.

Appendices

Appendix 3.A Derivation of the solvent force balance

In this section we derive that Eq. (3.5) of the main text is the force balance governing the solvent flow on a scale where the colloids can be regarded as a continuum. To this end, we start from the hydrodynamic problem that governs the solvent flow around a single swimmer, and coarse-grain this problem to the desired larger scale. As done throughout this Electronic Supplementary Information, Latin indices i, j, k shall label particles, whereas Greek indices α, β, γ shall refer to the Cartesian components x, y, z. We apply the Einstein summation convention *only* to the latter Greek indices, and only in this section. Furthermore, we use the notation $A_{(\alpha\beta)} \equiv \frac{1}{2}(A_{\alpha\beta} + A_{\alpha\beta})$ to denote the symmetrization of a tensor $\mathbf{A}$ with respect to its Greek indices *only*.

To describe the solvent flow around a single swimmer, we consider a model in which the swimming is generated by a nonzero slip-velocity at the surface of the single particle. This models for example biological swimmers - so-called 'squirmers' - that move by the beating motion of small flagella at their body surface, or by small body deformations [133], but also the swimming of active colloidal particles [134, 135]. The hydrodynamic problem is as follows. The swimmer/particle i, occupying a volume V_i enclosed by the surface S_i, is assumed to have a fixed overall shape, such that it can only undergo rigid body motion, with center-of-mass velocity $\mathbf{v}_i$ and angular velocity $\boldsymbol{\omega}_i$ around its center-of-mass position $\mathbf{r}_i$. It swims in an ambient flow $\mathbf{u}^\infty(\mathbf{r})$ that is assumed to solve the Stokes equation for all $\mathbf{r}$ in the absence of any particles. In the fluid region V_f, bounded by S_i and by a spherical surface S_∞ with radius R that we plan to take towards ∞, the fluid velocity $\mathbf{u}^{\text{out}}(\mathbf{r})$ and pressure $p^{\text{out}}(\mathbf{r})$ satisfy

$$\left.\begin{aligned} \boldsymbol{\nabla}\cdot\mathbf{u}^{\text{out}} &= 0 \\ -\boldsymbol{\nabla}p^{\text{out}} + \eta\boldsymbol{\nabla}^2\mathbf{u}^{\text{out}} &= \mathbf{0} \end{aligned}\right\} \quad \text{with b.c.'s} \quad \begin{cases} \mathbf{u}^{\text{out}}(\mathbf{r}) = \mathbf{u}_i^{\text{RBM}}(\mathbf{r}) + \mathbf{u}_i^s(\mathbf{r}), & \text{for } \mathbf{r}\in S_i, \\ \mathbf{u}^{\text{out}}(\mathbf{r}) = \mathbf{u}^\infty(\mathbf{r}), & \text{for } \mathbf{r}\in S_\infty, \end{cases} \tag{3.10}$$

where η is the dynamic solvent viscosity, where $\mathbf{u}_i^{\text{RBM}}(\mathbf{r}) \equiv \mathbf{v}_i + \boldsymbol{\omega}_i \times (\mathbf{r} - \mathbf{r}_i)$ is the surface velocity of particle i due to its rigid body motion, and where $\mathbf{u}_i^s(\mathbf{x})$ is the additional slip velocity satisfying $\mathbf{u}_i^s(\mathbf{x})\cdot\hat{\mathbf{n}}_i = 0$, $\hat{\mathbf{n}}_i$ being the normal vector pointing from particle i into V_f. The stress tensor $\boldsymbol{\sigma}^{\text{out}}$ of the solvent is given as $\sigma_{\alpha\beta}^{\text{out}} = -p^{\text{out}}\delta_{\alpha\beta} + 2\eta\partial_{(\alpha}u_{\beta)}^{\text{out}}$; the second equation of (3.10), known as the Stokes equation, can thus also be written as $\boldsymbol{\nabla}\cdot\boldsymbol{\sigma}^{\text{out}} = \mathbf{0}$. Note that we assume that no external body force acts on the solvent. This assumption is made for simplicity only, and the derivation can be extended to include a nonzero external body force.

It is not Eqs. (3.10) that we shall coarse-grain, but an integral representation of these differential equations. This integral representation is derived in e.g. the book of Kim and Karilla [136] for a rigid, non-swimming particle, i.e. for $\mathbf{u}_i^s(\mathbf{r}) = \mathbf{0}$. Here, we extend this result to a finite swimming velocity $\mathbf{u}_i^s(\mathbf{r})$. It is important to realize that Eqs. (3.10) are equations for the solvent velocity *outside* the particle; to emphasize this, we have called this velocity $\mathbf{u}^{\text{out}}(\mathbf{x})$. Of course, no solvent is present inside the particle, yet it shall be convenient to formally consider an 'extended' solvent velocity profile defined on both V_f *and* V_i as

$$\mathbf{u}(\mathbf{r}) = \begin{cases} \mathbf{u}^{\text{out}}(\mathbf{r}), & \text{if } \mathbf{r} \in V_f, \\ \mathbf{u}_i^{\text{in}}(\mathbf{r}), & \text{if } \mathbf{r} \in V_i, \end{cases} \tag{3.11}$$

where $\mathbf{u}_i^{\text{in}}(\mathbf{r})$ is defined as the velocity field solving the Stokes equation *inside* particle i (i.e. in V_i) subject to the boundary condition

$$\mathbf{u}_i^{\text{in}}(\mathbf{r}) = \mathbf{u}_i^{\text{RBM}}(\mathbf{r}) \text{ for } \mathbf{r} \in S_i. \tag{3.12}$$

This velocity profile inside the particle is easily solved as

$$\mathbf{u}_i^{\text{in}}(\mathbf{r}) = \mathbf{v}_i + \boldsymbol{\omega}_i \times (\mathbf{r} - \mathbf{r}_i), \tag{3.13}$$

which means that $\mathbf{u}_i^{\text{in}}(\mathbf{r})$ has the same functional form as $\mathbf{u}_i^{\text{RBM}}(\mathbf{r})$, yet is defined on V_i rather than only on S_i. As such, it is clear that the solution (3.13) indeed satisfies the boundary condition (3.12). One can check that the solution (3.13) also solves the Stokes equations by noting that $\boldsymbol{\nabla} \cdot \mathbf{u}_i^{\text{in}}(\mathbf{r}) = 0$ and $\boldsymbol{\nabla}^2 \mathbf{u}_i^{\text{in}} = 0$. The corresponding stress tensor reads $\boldsymbol{\sigma}_i^{\text{in}}(\mathbf{r}) = -p_i^0 \mathbb{I}$, where p_i^0 is a spatially constant pressure. In order to find an integral representation for the solvent velocity profile $\mathbf{u}(\mathbf{r})$ as defined by (3.11), we follow the procedure followed in [136], but for a nonzero $\mathbf{u}_i^s(\mathbf{r})$. The resulting integral representation for $\mathbf{u}(\mathbf{r})$ makes use of the Green's functions that correspond to equations (3.10). These Green's functions, $\mathcal{G}_{\alpha\beta}$, $\mathcal{P}_\alpha$, and $\Sigma_{\alpha\beta\gamma}$, are defined by

$$\begin{cases} \partial_\alpha \mathcal{G}_{\alpha\beta}(\mathbf{r}) = 0, \\ 8\pi\eta \partial_\gamma \Sigma_{\alpha\beta\gamma}(\mathbf{r}) = -\partial_\alpha \mathcal{P}_\beta(\mathbf{r}) + \eta \boldsymbol{\nabla}^2 \mathcal{G}_{\alpha\beta}(\mathbf{r}) = -8\pi\eta \delta_{\alpha\beta} \delta(\mathbf{r}). \end{cases} \tag{3.14}$$

Physically, they represent the solvent response to a point force $f_\alpha = 8\pi\eta\delta_{\alpha\beta}\delta(\mathbf{r})$ that acts in direction β; the resulting velocity profile $u_\alpha(\mathbf{r})$ is $\mathcal{G}_{\alpha\beta}(\mathbf{r})$, the resulting pressure profile is $\mathcal{P}_\beta(\mathbf{r})$, and the resulting stress tensor $\sigma_{\alpha\gamma}(\mathbf{r})$ is $\Sigma_{\alpha\beta\gamma}(\mathbf{r})$. The integral formulation for the velocity field $\mathbf{u}(\mathbf{r})$ then reads

$$\mathbf{u}(\mathbf{r}) = \mathbf{u}^\infty(\mathbf{r}) - \frac{1}{8\pi\eta} \oint_{S_i} \mathrm{d}S(\boldsymbol{\xi}) (\boldsymbol{\sigma}^{\text{out}}(\boldsymbol{\xi}) \cdot \hat{\mathbf{n}}_i) \cdot \boldsymbol{\mathcal{G}}(\mathbf{r} - \boldsymbol{\xi}) - \oint_{S_i} \mathrm{d}S(\boldsymbol{\xi}) \mathbf{u}_i^s(\boldsymbol{\xi}) \cdot \boldsymbol{\Sigma}(\mathbf{r} - \boldsymbol{\xi}) \cdot \hat{\mathbf{n}}_i. \tag{3.15}$$

For $\mathbf{u}_i^s(\mathbf{r}) = \mathbf{0}$, Eq. (3.15) shows that the solvent flow can be understood as resulting from a collection of force monopoles $-\boldsymbol{\sigma}^{\text{out}}(\boldsymbol{\xi}) \cdot \hat{\mathbf{n}}_i$ distributed over the surface of the particle. For nonzero $\mathbf{u}_i^s(\mathbf{r})$, the effect of the last term in (3.15) is that an additional surface distribution

of force *dipoles* comes into play. To see that the last term indeed represents force dipoles, we use $\Sigma_{\alpha\beta\gamma} = (8\pi\eta)^{-1}(-\mathcal{P}_\beta\delta_{\alpha\gamma} + 2\eta\partial_{(\gamma}\mathcal{G}_{\alpha)\beta})$ to rewrite this term as

$$\begin{aligned}
&-\oint_{S_i} \mathrm{d}S(\boldsymbol{\xi}) u^s_{i\alpha}(\boldsymbol{\xi})\Sigma_{\alpha\beta\gamma}(\mathbf{r}-\boldsymbol{\xi})\hat{n}_{i\gamma} \\
&\quad = \frac{1}{8\pi\eta}\oint_{S_i} \mathrm{d}S(\boldsymbol{\xi})\mathcal{P}_\beta(\mathbf{r}-\boldsymbol{\xi})\mathbf{u}^s_i(\boldsymbol{\xi})\cdot\hat{\mathbf{n}}_i - \frac{1}{4\pi}\oint_{S_i}\mathrm{d}S(\boldsymbol{\xi})\partial_{(\gamma}\mathcal{G}_{\alpha)\beta}(\mathbf{r}-\boldsymbol{\xi})u^s_{i\alpha}(\boldsymbol{\xi})\hat{n}_{i\gamma} \\
&\quad = -\frac{1}{4\pi}\oint_{S_i}\mathrm{d}S(\boldsymbol{\xi})\lim_{\epsilon\downarrow 0}\left\{\left[\mathcal{G}_{\alpha\beta}\left(\mathbf{r}-(\boldsymbol{\xi}-\epsilon\hat{\boldsymbol{\gamma}})\right)-\mathcal{G}_{\alpha\beta}(\mathbf{r}-\boldsymbol{\xi})\right]\frac{u^s_{i(\alpha}(\boldsymbol{\xi})\hat{n}_{i\gamma)}(\boldsymbol{\xi})}{\epsilon}\right\}, \qquad (3.16)
\end{aligned}$$

where in the last line we used $\mathbf{u}^s_i(\boldsymbol{\xi})\cdot\hat{\mathbf{n}}_i(\boldsymbol{\xi}) = 0$, wrote out the definition of the derivative ∂_γ, with $\hat{\boldsymbol{\gamma}}$ denoting the unit vector in the γ-direction, and used $A_{(\alpha\beta)}B_{\alpha\beta} = A_{(\alpha\beta)}B_{(\alpha\beta)} = A_{\alpha\beta}B_{(\alpha\beta)}$ for any tensors $\mathbf{A}$ and $\mathbf{B}$. A summation over γ is implied in the last line of (3.16), and will be implied in similar terms that arise from this term. The last line of Eq. (3.16) indeed represents the solvent flow $u_\alpha(\mathbf{r})$ that arises as a result of a collection of force dipoles distributed over the surface S_i. The combination of Eqs. (3.15) and (3.16) shows that the solvent velocity profile $\mathbf{u}(\mathbf{r})$ satisfies the problem

$$\begin{aligned}
\boldsymbol{\nabla}\cdot\mathbf{u}(\mathbf{r}) &= 0, \\
-\partial_\alpha p(\mathbf{r}) + \eta\boldsymbol{\nabla}^2 u_\alpha(\mathbf{r}) &= \sum_i \oint_{S_i}\mathrm{d}S(\boldsymbol{\xi})\sigma^{\mathrm{out}}_{\alpha\beta}(\boldsymbol{\xi})\hat{n}_{i\beta}(\boldsymbol{\xi})\delta^3(\mathbf{r}-\boldsymbol{\xi}) \qquad (3.17) \\
&\quad + 2\eta\sum_i\oint_{S_i}\mathrm{d}S(\boldsymbol{\xi})\lim_{\epsilon\downarrow 0}\left\{\frac{u^s_{i(\alpha}(\boldsymbol{\xi})\hat{n}_{i\gamma)}(\boldsymbol{\xi})}{\epsilon}\Big[\delta^3\left(\mathbf{r}-(\boldsymbol{\xi}-\epsilon\hat{\boldsymbol{\gamma}})\right)-\delta^3(\mathbf{r}-\boldsymbol{\xi})\Big]\right\},
\end{aligned}$$

where we now account for many possible particles i present, and where $\mathbf{u}(\mathbf{r})$ is subject to the boundary condition $\mathbf{u}(\mathbf{r}) = \mathbf{u}^\infty(\mathbf{r})$ for $\mathbf{r}\in S_\infty$ (with $R\to\infty$). Eq. (3.17) indeed shows that the velocity profile $\mathbf{u}(\mathbf{r})$ can be thought of as resulting from a distribution of force monopoles, *and*, for $\mathbf{u}^s_i(\mathbf{r})\neq\mathbf{0}$, force dipoles distributed over the surfaces of the particles.

It is equation (3.17) that we shall coarse-grain. In order to do so, we define a window $w(\mathbf{r})$ around $\mathbf{r}$, that satisfies $\int\mathrm{d}\mathbf{r}w(\mathbf{r}) = 1$, and whose 'width' determines the coarse-graining scale L. For definiteness, we shall take

$$w(\mathbf{r}) = \frac{1}{L^3}\prod_{\alpha=x,y,z}\Theta(\frac{L}{2}-|r_\alpha|), \qquad (3.18)$$

such that $w(\mathbf{r})$ is only nonzero (and equal to L^{-3}) inside a cube with ribbons of length L centered at $\mathbf{r}$, that we shall refer to as $\mathcal{C}(\mathbf{r},L)$. We assume the window to 'contain' many colloids; for our cubical window (3.18) we thus assume $L\gg a,b$, where a is the particle radius and b the typical particle separation. We define the coarse-grained version of any solvent property $f(\mathbf{r})$ as

$$\langle f\rangle(\mathbf{r}) = \int_{V_f^+}\mathrm{d}\mathbf{r}'w(\mathbf{r}-\mathbf{r}')f(\mathbf{r}') = \frac{1}{L^3}\int_{\mathcal{C}(\mathbf{r},L)\cap V_f^+}\mathrm{d}\mathbf{r}'f(\mathbf{r}'), \qquad (3.19)$$

where V_f^+ denotes the fluid volume V_f, plus, for every particle i, a thin shell of width δ enclosing the particle surface S_i [a]. Note that the integration is *not* over the volume *inside* the particles, while we *do* divide by the entire window volume L^3. Consequently, the coarse-grained solvent velocity $\langle \mathbf{u} \rangle(\mathbf{r})$ is the *physical* velocity $\mathbf{u}^{\text{out}}(\mathbf{r})$ *volume-averaged* over $\mathcal{C}(\mathbf{r}, L)$. It is related to the average velocity *per solvent particle* $\mathbf{u}^{\text{av}}(\mathbf{r})$ as $\langle \mathbf{u} \rangle(\mathbf{r}) = (1 - \phi(\mathbf{r}))\mathbf{u}^{\text{av}}(\mathbf{r})$, where $\phi(\mathbf{r})$ is the local volume fraction of colloids.

We now coarse-grain Eq. (3.17), i.e. we calculate $\langle (3.17) \rangle(\mathbf{r})$. First, we note that any distribution $f(\mathbf{r})$ satisfies

$$\begin{aligned}\langle \boldsymbol{\nabla} f \rangle(\mathbf{r}) &= \int_{V_f^+} \mathrm{d}\mathbf{r}' w(\mathbf{r} - \mathbf{r}') \boldsymbol{\nabla}' f(\mathbf{r}') = -\int_{V_f^+} \mathrm{d}\mathbf{r}' \boldsymbol{\nabla}' w(\mathbf{r} - \mathbf{r}') f(\mathbf{r}') = \boldsymbol{\nabla} \int_{V_f^+} \mathrm{d}\mathbf{r}' w(\mathbf{r} - \mathbf{r}') f(\mathbf{r}') \\ &= \boldsymbol{\nabla} \langle f \rangle(\mathbf{r}). \end{aligned} \tag{3.20}$$

Using this property, the coarse-grained version of the first equality of Eq. (3.17) becomes $\boldsymbol{\nabla} \cdot \langle \mathbf{u} \rangle(\mathbf{r}) = 0$, whereas the left-hand side of the second equality of Eq. (3.17) becomes

$$-\partial_\alpha \langle p \rangle(\mathbf{r}) + \eta \boldsymbol{\nabla}^2 \langle u_\alpha \rangle(\mathbf{r}). \tag{3.21}$$

We adress the right-hand-side terms of the second equality of Eq. (3.17) one by one. The coarse-grained version of the first right-hand-side term is

$$\begin{aligned}\sum_i \oint_{S_i} \mathrm{d}S(\boldsymbol{\xi}) w(\mathbf{r} - \boldsymbol{\xi}) \sigma^{\text{out}}_{\alpha\beta}(\boldsymbol{\xi}) \hat{n}_{i\beta}(\boldsymbol{\xi}) &\approx \frac{1}{L^3} \sum_{i \in \mathcal{C}(\mathbf{r}, L)} \oint_{S_i} \mathrm{d}S(\boldsymbol{\xi}) \sigma^{\text{out}}_{\alpha\beta}(\boldsymbol{\xi}) \hat{n}_{i\beta}(\boldsymbol{\xi}) \\ &= \frac{1}{L^3} \sum_{i \in \mathcal{C}(\mathbf{r}, L)} F^H_{i,\alpha}, \end{aligned} \tag{3.22}$$

where $\mathbf{F}_i^H = \oint_{S_i} \mathrm{d}S \boldsymbol{\sigma}^{\text{out}} \cdot \hat{\mathbf{n}}$ is the hydrodynamic force exerted on particle i, and where we neglected any contributions from particles contained only partially in $\mathcal{C}(\mathbf{r}, L)$, which is justified by virtue of the assumption $L \gg a, b$. The coarse-grained version of the second right-hand-side term of the second equality of Eq. (3.17) is

$$\begin{aligned} &2\eta \int_{V_f^+} \mathrm{d}\mathbf{r}' w(\mathbf{r} - \mathbf{r}') \sum_i \oint_{S_i} \mathrm{d}S(\boldsymbol{\xi}) \lim_{\epsilon \downarrow 0} \left\{ \frac{u^s_{i(\alpha}(\boldsymbol{\xi}) \hat{n}_{\gamma)}(\boldsymbol{\xi})}{\epsilon} \left[\delta^3(\mathbf{r}' - (\boldsymbol{\xi} - \epsilon \hat{\boldsymbol{\gamma}})) - \delta^3(\mathbf{r}' - \boldsymbol{\xi}) \right] \right\} \\ &\quad = 2\eta \sum_i \oint_{S_i} \mathrm{d}S(\boldsymbol{\xi}) \lim_{\epsilon \downarrow 0} \left\{ \frac{w(\mathbf{r} - (\boldsymbol{\xi} - \epsilon \hat{\boldsymbol{\gamma}})) - w(\mathbf{r} - \boldsymbol{\xi})}{\epsilon} \right\} u^s_{i(\alpha}(\boldsymbol{\xi}) \hat{n}_{i\gamma)}(\boldsymbol{\xi}) \\ &\quad = 2\eta \sum_i \oint_{S_i} \mathrm{d}S(\boldsymbol{\xi}) \frac{\partial w(\mathbf{r} - \boldsymbol{\xi})}{\partial r_\gamma} u^s_{i(\alpha}(\boldsymbol{\xi}) \hat{n}_{i\gamma)}(\boldsymbol{\xi}) \\ &\quad \overset{(3.18)}{=} -\frac{2\eta}{L^3} \sum_i \oint_{S_i} \mathrm{d}S(\boldsymbol{\xi}) \left(\prod_{\beta \neq \gamma} \Theta(\frac{L}{2} - |r_\beta - \xi_\beta|) \right) \\ &\qquad\qquad \left\{ \delta\Big(r_\gamma - (\xi_\gamma + \frac{L}{2})\Big) - \delta\Big(r_\gamma - (\xi_\gamma - \frac{L}{2})\Big) \right\} u^s_{i(\alpha}(\boldsymbol{\xi}) \hat{n}_{i\gamma)}(\boldsymbol{\xi}) \\ &\quad = -\frac{2\eta}{L^3} \sum_i \left(\oint_{\delta \mathcal{C}_\gamma^+(\mathbf{r}, L) \cap S_i} \mathrm{d}l(\boldsymbol{\xi}) - \oint_{\delta \mathcal{C}_\gamma^-(\mathbf{r}, L) \cap S_i} \mathrm{d}l(\boldsymbol{\xi}) \right) u^s_{i(\alpha}(\boldsymbol{\xi}) \hat{n}_{i\gamma)}(\boldsymbol{\xi}), \end{aligned} \tag{3.23}$$

[a] Formally we take $\delta \to 0$, while ensuring that $\delta > \epsilon$ at all times. All the monopoles *and* dipoles appearing in Eq. (3.17) are thus entirely contained in V_f^+.

where in the last line $\delta\mathcal{C}_\gamma^\pm(\mathbf{r},L)$ denotes the face of the $\mathcal{C}(\mathbf{r},L)$ cube with outward normal $\pm\hat{\boldsymbol{\gamma}}$. The integrations in the last line thus run over the intersection of the $\delta\mathcal{C}_\gamma^\pm(\mathbf{r},L)$-face with the surface S_i of any particle i that intersects it. For any particle i, the integration domain is thus an intersection between two surfaces, which forms a line. The magnitude of the contributions (3.22) and (3.23) can now be estimated. Denoting the magnitude of F_i^H by F, and the colloid density by ρ such that the number of colloids inside $\mathcal{C}(\mathbf{r},L)$ approximately equals ρL^3, the magnitude of the contribution (3.22) is estimated as $L^{-3}(\rho L^3)F = \rho F \approx F\phi a^{-3}$, where ϕ denotes the packing fraction of the colloids, and where a denotes the particle size. To estimate the contribution of either integral in (3.23), we note that i) the number of particles intersecting $\delta\mathcal{C}_\gamma^\pm(\mathbf{r},L)$ has as approximate upper bound $(\rho L^3)^{\frac{2}{3}}$ (in fact, the number of intersecting particles is much less for a dilute suspension), ii) for any particle intersecting $\delta\mathcal{C}_\gamma^\pm(\mathbf{r},L)$, the length of the intersection line is of the order a, and iii) $\eta u_i^s \approx a\sigma^{\text{out}} \approx F/a$. Therefore, the contribution of either integral in (3.23) is approximated as $L^{-3}(\rho L^3)^{\frac{2}{3}}a(F/a) = F\rho^{2/3}L^{-1} \approx F\phi^{\frac{2}{3}}a^{-2}L^{-1}$. Since $L^{-1} \ll a^{-1}$, the contribution of (3.23) is negligible as compared to the contribution of (3.22). Therefore, the coarse-grained version of the second equation in (3.17) reads

$$-\partial_\alpha\langle p\rangle(\mathbf{r}) + \eta\boldsymbol{\nabla}^2\langle u_\alpha\rangle(\mathbf{r}) = \frac{1}{L^3}\sum_{i\in\mathcal{C}(\mathbf{r},L)} F_{i,\alpha}^H. \tag{3.24}$$

The hydrodynamic force $\mathbf{F}_i^H$ experienced by a spherical particle i can be decomposed as $\mathbf{F}_i^H = -\gamma_t\mathbf{v}_i + \gamma_t v_0\hat{\mathbf{e}}_i$, where $\mathbf{v}_i$ is the velocity of particle i and $\hat{\mathbf{e}}_i$ its orientation [94]. The evolution of $\mathbf{v}_i(t)$ and $\hat{\mathbf{e}}_i(t)$ are governed by the Langevin dynamics of the particles [b]. Consequently, even though it was left implicit so far, the solvent pressure $\langle p\rangle(\mathbf{r},t)$ and velocity $\langle\mathbf{u}\rangle(\mathbf{r},t)$ actually depend on time, via Eq. (3.24). To relate the right-hand side of Eq. (3.24) to the probability distribution function $\psi(\mathbf{r},\mathbf{e},t)$ of the particles - whose time evolution is governed by the Smoluchowski equation (3.1) - we assume that the dynamics of the particles does not to change significantly throughout a window, which means that e.g. the external potential $V^{\text{ext}}(\mathbf{r})$ must not vary significantly under $r_\alpha \to r_\alpha + L$ [c]. This implies that ψ is approximately constant within any window, i.e. $\psi(\mathbf{r}',\mathbf{e},t) \approx \psi(\mathbf{r},\mathbf{e},t)$ with $\mathbf{r}' \in \mathcal{C}(\mathbf{r},L)$ for any $\mathbf{r}$. In this case, the sum over all particles in $\mathcal{C}(\mathbf{r},L)$ (which are many) coincides with a sum over different realizations of the noise appearing in the Langevin equation. As shown in Sec. 2 of the SI, the coarse-grained Stokes equation (3.24) then becomes

$$\begin{aligned}-\boldsymbol{\nabla}\langle p\rangle(\mathbf{r},t) + \eta\boldsymbol{\nabla}^2\langle\mathbf{u}\rangle(\mathbf{r},t) &= -\gamma_t\mathbf{J}(\mathbf{r},t) + \gamma_t v_0\mathbf{m}(\mathbf{r},t)\\ &\equiv \mathbf{f}^f(\mathbf{r},t) + \mathbf{f}^p(\mathbf{r},t),\end{aligned} \tag{3.25}$$

where in the first equality we used that the polarization is defined as $\mathbf{m}(\mathbf{r},t) = \int \mathrm{d}\hat{\mathbf{e}}\psi(\mathbf{r},\hat{\mathbf{e}},t)\hat{\mathbf{e}}$, and in the second equality we used the definitions of the the frictional body force $\mathbf{f}^f(\mathbf{r},t) =$

[b] This is under the assumption that the effect of the slip velocity $\mathbf{u}_i^s$ is to displace particle i only translationally; if it also rotates the particle an additional 'self-torque' has to be added to the Langevin equations.

[c] In the main text we *do* consider a membrane potential that changes on the scale $a \ll L$. However, this is in a planar geometry; if one employs a window that is thin in the direction perpendicular to the membrane, and elongated in the parallel direction(s), it can still contain many colloids, yet have an approximately constant $V(\mathbf{r})$ inside.

$-\gamma_t \mathbf{J}(\mathbf{r},t)$ and the propulsion body force density $\mathbf{f}^p(\mathbf{r},t) = \gamma_t v_0 \mathbf{m}(\mathbf{r},t)$, which are the internal body forces appearing in the colloidal force balance (3.3) of the main text. This derivation can be extended to also include a nonzero body force that acts on the solvent, in which case the result is simply Eq. (3.25) with the coarse-grained version of this body force $\mathbf{f}_s^e(\mathbf{r},t)$ additionally appearing on the left-hand side of Eq. (3.25). Eq. (3.25) then forms the solvent force balance (3.5) of the main text, where we simply denoted $\langle \mathbf{u}(\mathbf{r},t) \rangle$ by $\mathbf{u}(\mathbf{r},t)$ and $\langle p(\mathbf{r},t) \rangle$ by $P_s(\mathbf{r},t)$.

4

Interfacial properties of ideal active Brownian particles in a motility gradient

In this chapter, we switch back to a picture that considers the active colloids without making the solvent explicit. We review the definition of pressure for such a colloids-only system, but mainly focus on the other thermodynamic variable that can be defined mechanically: the interfacial tension.

Rather than MIPS, we study what could well be the simplest active system that admits an interface: an active ideal gas in two half-spaces with different propulsion speeds. We show that this system gives rise to an interface that qualitatively resembles the interface of MIPS. We propose two possibilities for the definition of an interfacial tension, and find microscopic expressions - and thus the signs - for both. Related to this, we investigate the stability of the interface. Remarkably, the normal force on a piece of perturbed interface acts in the same direction as the perturbation, and thus seems to have a destabilizing effect. Nonetheless, the interface is stable, owing to a Marangoni-like effect that leads to tangential currents which restore the interface to its original state.

This chapter is part of a collaboration with Liesbeth Janssen (Eindhoven University of Technology), who performed particle-based computer simulations on the same system (whose results are not shown).

4.1 Remarks on notation

In contrast to the other chapters, where σ denotes the particle diameter, throughout this chapter σ is used for the interfacial tension.

Furthermore, while the setting of this chapter (a colloids-only picture, isotropic particles and an inhomogeneous propulsion speed) differs from the setting in chapter 3 (an explicit solvent, anisotropic particles and a homogeneous propulsion speed), the various pressures that appear in both chapters are related. The pressure P that was associated with the colloids in chapter 3 equals the bare pressure P defined in this chapter. For isotropic particles with homogeneous propulsion, and in a flux-free steady state[a] - which is considered throughout most of this thesis - the solvent pressure P_s of chapter 3 equals the swim pressure P^{swim} defined in this chapter. Under the same conditions, the total pressure P_{tot} of the suspension of chapter 3 equals the total pressure P^{tot} defined in this chapter.

4.2 Introduction

An intriguing aspect of MIPS, that we have not discussed in chapter 2, is its interface. Any movie of MIPS shows that active particles continuously attach to and detach from the dense phase, and that the interface fluctuates wildly (see e.g. movies supplementary to [25]).

For phase coexistences in thermodynamic equilibrium, these fluctuations are controlled by the stiffness κ, which, in turn, is set by the surface tension σ via $\kappa = \sigma/k_BT$. Here k_BT can be thought of as the energy scale of the interface perturbations. Previous studies [25, 26, 137] showed that a similar relation holds for active phase coexistences when one adopts a mechanical definition for the surface tension, provided that one replaces the temperature T by an effective temperature T_{eff}. Then $\kappa = \sigma/k_BT_{\text{eff}}$ [137]. At large activity Pe, the effective temperature $T_{\text{eff}} \propto \text{Pe}^2$ is also large, which is consistent with the wild fluctuations of the MIPS interface. Intuitively, the fact that the fluctuations are so large can be understood from the fact that the energy scale k_BT_{eff} of interface perturbations is simply much larger for active than for passive systems [27].

Thus, the *magnitude* of the surface tension σ seems to be understood reasonably well. However, in the case of MIPS, its *sign* turned out to be surprising: Bialké et al. [26] found it to be negative! Since in equilibrium the surface tension is also the tensile force (per unit length) that restores the interface when it is perturbed [138], it would seem that a negative interfacial tension would *enhance* perturbations and thus lead to an unstable interface. But then why is the MIPS interface nonetheless stable?

This question is being debated in the literature [25, 27, 29, 31]. On one hand, Patch et al. [25] propose that while the surface tension is indeed negative, it is also curvature-dependent, which leads to a "Marangoni-like effect". The Marangoni effect is the effect that lateral inhomogeneities in the interfacial tension lead to tangential currents from low to high interfacial tension [33]. Patch et al. propose that these tangential currents

[a] where, moreover, the pressure profiles are not affected by any external force $\mathbf{f}_s^e$ that acts on the solvent.

restore the perturbed interface to its original state. On the other hand, Lee [29] argues that the stability of the interface is controlled by an effective surface tension that is positive, and also Hermann et al. [31] argue that the stability is controlled by a non-negative surface tension. The surface tensions proposed by Lee [29] and Hermann et al. [31] are distinct from each other, and also from the mechanical surface tension[b] first proposed by Refs. [25, 26, 137].

In this chapter, we focus on a simpler system that can - to some extent - be regarded as a toy model for MIPS. In chapter 2, we explained that MIPS forms because particles in denser regions undergo more collisions and therefore effectively slow down, which increases the density further. Formally, this explanation came in the form of a mapping from the interacting system to an active ideal gas with an effective velocity profile[c]. We employ the same analogy here: rather than considering the interface of MIPS, we consider the interface that is formed by an active ideal gas in two neighbouring regions with different propulsion speeds. While the interface of this toy model does not map quantitavely to the MIPS interface, we will show that it *does* share some of its qualitative features. Moreover, this toy model is arguably the simplest active system that admits an interface. And precisely because it is a simple active ideal gas, issues concerning the interfacial tension can be rather easily understood.

One important issue that we address is: how to define an interfacial tension for this non-equilibrium system in the first place? We propose two definitions, from pure mechanical arguments that do not make reference to any free energy. We discuss when these definitions coincide, and also find their signs. Finally, we ask: what makes the interface stable against small perturbations?

The outline of this chapter is as follows. In section 4.3 we introduce the model, and in section 4.4 we characterize the interface that forms. Then, in section 4.5, we discuss the various forces and pressures at play in the interface, such that in section 4.6 we can give our first definition of the interfacial tension: the *mechanical* interfacial tension, defined in terms of the work required for deforming the system in such a way that the area of the interface changes while the volume of the system remains constant. In section 4.7, we give our second definition: the interfacial tension as the tensile force in the interface. In this section we also discuss the stability of the interface.

4.3 Model

In order to describe self-propelled particles in a minimal way, we model them as active Brownian particles [109]. For simplicity, we consider non-interacting, isotropic particles that live in only two spatial dimensions [d], characterized by the Cartesian coordinates x and y. Every particle undergoes overdamped motion driven by a number of forces. The most important driving force is the self-propulsion force. Usually, its magnitude is taken to be spatially constant, such that it gives rise to a constant propulsion speed v_0. In this

[b] Actually, the surface tension proposed by Hermann et al. [31] is defined mechanically, but only from the structural force components.

[c] and, for anisotropic particles, an effective rotational diffusion constant. Here, however, we only consider isotropic particles.

[d] All of our results are easily generalizable to three dimensions.

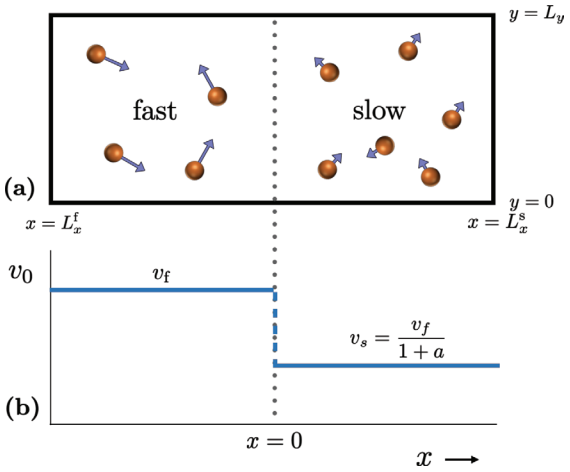

Figure 4.1: (a) Pictorial representation of the considered setting: active Brownian particles with (b) a position-dependent self-propulsion speed $v_0(x)$ that represents a fast bulk with propulsion speed v_{f} at $x < 0$ connected with a slow bulk with self-propulsion speed $v_{\mathrm{s}} < v_{\mathrm{f}}$ at $x > 0$.

chapter, however, we consider a spatially varying propulsion speed $v_0(x)$, that we specify below. The direction of the propulsion force defines a particle's orientation $\hat{\mathbf{e}}$, a unit vector that can also be expressed by the angle θ with the x-axis as $\hat{\mathbf{e}}(\theta) = \cos(\theta)\,\hat{\mathbf{x}} + \sin(\theta)\,\hat{\mathbf{y}}$. The orientation $\hat{\mathbf{e}}$ undergoes rotational diffusion with diffusion constant D_r. An additional driving force is the external force, generated by the potential $V(\mathbf{r})$ of the walls[e] of the system that we specify below. The final effect that can change a particle's position $\mathbf{r} = (x, y)$ is translational diffusion, with an associated diffusion constant D_t. The probability density $\psi(\mathbf{r}, \theta, t)$ to find a particle at time t with orientation θ at position $\mathbf{r}$ then evolves according to the Smoluchowski equation

$$\partial_t \psi = -\boldsymbol{\nabla} \cdot \mathbf{j} - \partial_\theta j_\theta, \tag{4.1}$$

where $\mathbf{j} = (j_x, j_y)$ and j_θ are components of the probability flux in $(\mathbf{r}, \theta)$-space. They are given by

$$\mathbf{j} \equiv v_0(x)\hat{\mathbf{e}}\psi - \frac{1}{\gamma}\psi \boldsymbol{\nabla} V(\mathbf{r}) - D_t \boldsymbol{\nabla}\psi, \quad j_\theta \equiv -D_r \partial_\theta \psi. \tag{4.2}$$

Here γ is the friction coefficient associated with the overdamped motion.

The setting we consider consists of two adjacent bulks with *different* propulsion speeds, separated by an interface that is taken to be parallel to the y-axis and in the vicinity of $x = 0$. A 'fast' bulk is located at negative x-values, and contains the bulk coordinate $(x_{\mathrm{b}}^{\mathrm{f}}, y_{\mathrm{b}})$, with $x_{\mathrm{b}}^{\mathrm{f}} \ll 0$. A 'slow' bulk is located at positive x-values, and contains the coordinate $(x_{\mathrm{b}}^{\mathrm{s}}, y_{\mathrm{b}})$, with $x_{\mathrm{b}}^{\mathrm{s}} \gg 0$. The propulsion speed $v_0(x)$ is a function of x in such a way that for $x \ll 0$ it equals $v_0(x_{\mathrm{b}}^{\mathrm{f}}) \equiv v_{\mathrm{f}}$, while for $x \gg 0$ it equals $v_0(x_{\mathrm{b}}^{\mathrm{s}}) \equiv v_{\mathrm{s}} \leq v_{\mathrm{f}}$.

[e] and not $V(\mathbf{r}, \theta)$, since the particles are isotropic.

In principle, $v_0(x)$ can interpolate between these bulk values in any way, but for most of this chapter we assume the simple stepwise velocity profile

$$v_0(x) = v_\mathrm{f} + (v_\mathrm{s} - v_\mathrm{f})\Theta(x), \tag{4.3}$$

where $\Theta(x)$ is the Heaviside step function. This propulsion speed profile is depicted in Fig. 4.1(b). Rather than specifying both v_f and v_s, in most of the chapter we shall specify the velocity v_f through the dimensionless Péclet number $\mathrm{Pe} \equiv v_\mathrm{f}/\sqrt{D_t D_r}$, while v_s then follows from the specified asymmetry in propulsion speeds

$$a \equiv (v_\mathrm{f} - v_\mathrm{s})/v_\mathrm{s} \geq 0. \tag{4.4}$$

The external potential $V(\mathbf{r})$ represents the hard walls of a rectangular box that surrounds the whole ensemble of two bulks, as depicted in Fig. 4.1(a). The vertical walls of the box are at $x = -L_x^\mathrm{f}$ and $x = L_x^\mathrm{s}$, while the horizontal walls are at $y = 0$ and $y = L_y$. The box is assumed to be large, such that there are two bulk states; the bulk coordinates $(x_\mathrm{b}^\mathrm{f}, y_\mathrm{b})$ and $(x_\mathrm{b}^\mathrm{s}, y_\mathrm{b})$ are located far from the walls. We are mostly interested in the region where the presence of the walls is not felt, and therefore we mostly consider x-coordinates $x_\mathrm{b}^\mathrm{f} \leq x \leq x_\mathrm{b}^\mathrm{f}$ at fixed $y = y_\mathrm{b}$. This region is invariant in the y-direction, such that Eq. (4.1) simplifies to

$$\partial_t \psi = -\partial_x j_x - \partial_\theta j_\theta \tag{4.5}$$

Throughout this chapter, whenever we discuss the solution far from any walls, we shall display the spatial x-dependence of functions and leave the considered $y = y_\mathrm{b}$ implicit, e.g. we write $\psi(x, \theta, t)$ rather than $\psi(x, y_\mathrm{b}, \theta, t)$.

Rather than considering the full probability density $\psi(\mathbf{r}, \theta, t)$, one can also decompose its orientation dependence into angular moments. The lowest order moments are

$$\begin{aligned}
\rho(\mathbf{r}, t) &= \int \mathrm{d}\theta \psi(\mathbf{r}, \theta, t) \quad \text{(density)}, \\
m_\alpha(\mathbf{r}, t) &= \int \mathrm{d}\theta e_\alpha \psi(\mathbf{r}, \theta, t) \quad \text{(polarization)}, \\
S_{\alpha\beta}(\mathbf{r}, t) &= \int \mathrm{d}\theta (e_\alpha e_\beta - \frac{1}{2}\delta_{\alpha\beta})\psi(\mathbf{r}, \theta, t) \quad \text{(nematic)}.
\end{aligned} \tag{4.6}$$

Here $\alpha, \beta \in (x, y)$ label Cartesian components. These angular moments follow a set of coupled differential equations that follow by taking the angular moments of Eq. (4.1). The evolution equations for the density and polarization read

$$\partial_t \rho = -\boldsymbol{\nabla} \cdot \mathbf{J}, \tag{4.7a}$$

$$\partial_t m_\alpha = -\partial_\beta \mathcal{J}^m_{\beta\alpha} - D_r m_\alpha, \tag{4.7b}$$

where the particle current $\mathbf{J}(\mathbf{r}, t)$ and orientation current $\boldsymbol{\mathcal{J}}^m(\mathbf{r}, t)$ are given by

$$\mathbf{J} = v_0(x)\mathbf{m} - \frac{1}{\gamma}(\boldsymbol{\nabla} V)\rho - D_t \boldsymbol{\nabla}\rho, \tag{4.8a}$$

$$\mathcal{J}^m_{\beta\alpha} = v_0(x)\left(S_{\alpha\beta} + \frac{\rho}{2}\delta_{\alpha\beta}\right) - \frac{1}{\gamma}(\partial_\beta V)m_\alpha - D_t \partial_\beta m_\alpha, \tag{4.8b}$$

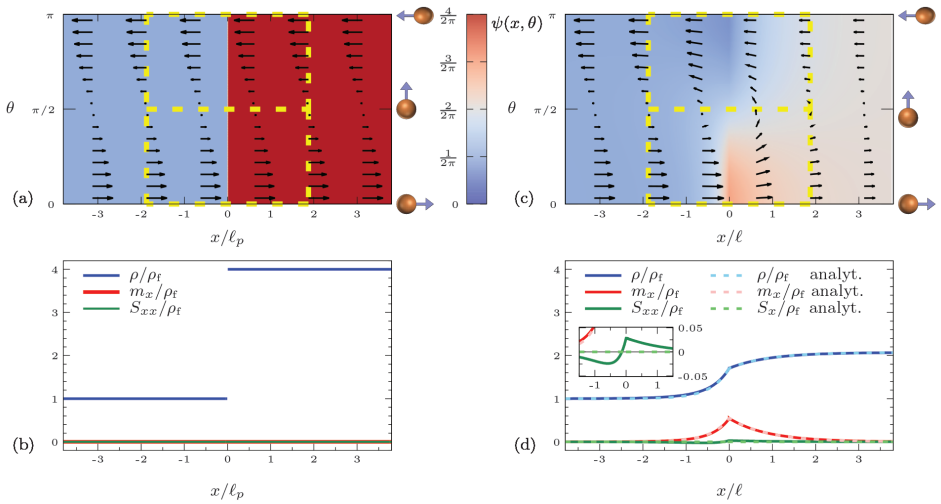

Figure 4.2: (a) Steady state probability density $\psi(x,\theta)$ in the absence of translational diffusion ($D_t = 0$), for a propulsion speed asymmetry $a = 3$. Arrows represent the probability flux $\mathbf{j}^{\text{prob}}$. (b) Corresponding profiles of density ρ, polarization m_x, and nematic order S_{xx}, as a function of position x in units of the persistence length ℓ_p. (c) Probability density *with* translational diffusion ($D_t > 0$), as obtained numerically from Eqs. (4.5) and (4.2), for the same asymmetry $a = 3$ and for Péclet number $\text{Pe} = 3$. The finite translational diffusion results in a lower slow bulk density as for the $D_t = 0$ case. Consequently, the probability flux in the slow bulk is also smaller. In order to guarantee equal in- and outfluxes in the marked phase-space regions, a polarization and associated rotational current form in the interface. (d) Corresponding profiles of density ρ, polarization m_x, and nematic order S_{xx}, both numerically and analytically (under the closure $S_{xx} = 0$), as a function of x now measured in units of the diffusive length scale ℓ. (d-inset) Zoom around the origin of the graph.

respectively. Note that if one wants to solve the two relations of Eqs. (4.7) and (4.8) for the three unknowns ρ, $\mathbf{m}$ and $\mathbf{S}$ one needs an additional closure relation. We shall use the closure $S_{\alpha\beta} = 0$ in the next section to obtain analytical solutions.

4.4 Characterization of the interface

In this section we show that non-interacting particles in the velocity profile of Fig. 4.1 give rise to nontrivial steady-state profiles. To this end, we study the solution to our system away from any walls, i.e. the steady-state solution to Eq. (4.5). We shall see that the obtained interface profiles qualitatively resemble the interface profiles found in MIPS.

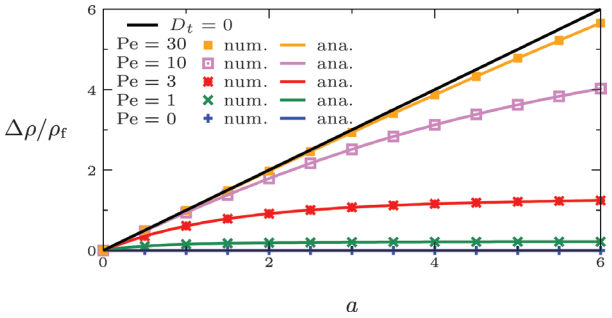

Figure 4.3: Normalized difference in bulk densities $\Delta\rho/\rho_f$ as a function of the asymmetry in propulsion speeds a, for several activities Pe as indicated. The symbols denote numerical solutions; the correspondingly colored lines are analytical solutions; and the black line shows the solution in the absence of translational diffusion $\Delta\rho/\rho_f = a$.

4.4.1 No translational diffusion

In order to better understand the general solution to Eq. (4.5), we first discuss a limiting case that has a simple, intuitive solution: the case of no translational diffusion, i.e. $D_t = 0$. In this case, Eq. (4.5) is easily solved by $v_0(x)\psi(x,\theta) = \text{constant}$. Using as a boundary condition that the density in the left bulk equals ρ_f, i.e. $\rho(x_b^f) = \rho_f$, yields

$$\psi(x,\theta) = \frac{v_f}{v_0(x)}\frac{\rho_f}{2\pi}. \tag{4.9}$$

Eq. (4.3) then implies that $\psi(x,\theta) = \rho_f/2\pi$ for $x < 0$, and $\psi(x,\theta) = (1+a)\rho_f/2\pi$ for $x > 0$, where a is asymmetry between the two velocities given in Eq. (4.4). Note that a is the only system parameter (aside from the imposed density ρ_f) the solution depends on. For $a = 3$, the solution (4.9) is by the heat map of Fig. 4.2(a). The arrows in the figure represent the (dimensionless) probability flux in (x,θ)-space

$$\mathbf{j}^{\text{prob}}(x,\theta) \equiv (\rho_f v_f)^{-1} j_x \hat{\mathbf{x}} + (D_r)^{-1} j_\theta \hat{\boldsymbol{\theta}} = \frac{v_0(x)}{v_f}\cos(\theta)\frac{\psi}{\rho_f}\hat{\mathbf{x}} - \frac{\partial_\theta \psi}{\rho_f}\hat{\boldsymbol{\theta}}, \tag{4.10}$$

which, according to Eq. (4.5), has to be divergence free in steady state in the sense that $\ell_p \partial_x j_x + \partial_\theta j_\theta = 0$. Here $\ell_p \equiv v_f/D_r$ denotes the persistence length of particles in the fast bulk, i.e. the typical length they travel by their propulsion force before rotating by one radian. Note that ℓ_p is the only internal length scale of (the fast side of) the system when $D_t = 0$. Fig. 4.2(a) also shows the probability current (4.10), which, by Eq. (4.9), simply reads $j_x = \cos(\theta)/2\pi$ and $j_\theta = 0$. This current is indeed divergence free. In particular, note that the marked phase-space region of particles near the interface $(-2\ell_p < x < 2\ell_p)$ with positive x-orientation $(-\pi/2 < \theta < \pi/2)$ has equal in- and outflux of probability, such that the number of particles in this phase-space region does indeed remain constant. The same is true for particles near the interface with negative x-orientation. Fig. 4.2(b) shows the density profile, which simply jumps from $\rho(x) = \rho_f$ for $x < 0$ to $\rho(x) = (1+a)\rho_f$ for $x > 0$. The slow bulk density $\rho_s \equiv \rho(x \gg 0)$ is thus given by $\rho_s = (1+a)\rho_f$, and the difference in bulk densities $\Delta\rho \equiv \rho_s - \rho_f$ satisfies $\Delta\rho/\rho_f = a$. This normalized

density difference is plotted as the black line in Fig. 4.3. Finally, since the solution (4.9) is independent of the angle θ, the polarization $\mathbf{m}$ and nematic order $\mathbf{S}$ are zero everywhere, as also displayed in Fig. 4.2(b).

4.4.2 Nonzero translational diffusion

We now consider the general case with a nonzero translational diffusion constant $D_t > 0$. This introduces the additional length scale $\ell = \sqrt{D_t/D_r}$, which we call the diffusive length scale, as it is the typical distance a particle diffuses before rotating by one radian. To completely specify the problem, one must now not only specify the velocity asymmetry a, but also the ratio $\mathrm{Pe} = \ell_p/\ell$ of the persistence and diffusive lengths. This ratio is known as the Péclet number, and provides a dimensionless measure of the activity of the system.

To obtain the probabilty density $\psi(x, \theta)$ we solve Eq. (4.5) numerically. We use the boundary conditions

1. that $x \ll -\ell$ represents a fast bulk with density ρ_f, i.e. $\psi(x_\mathrm{b}^\mathrm{f}, \theta) = \rho_\mathrm{f}/2\pi$,
2. that $x \gg \ell$ represents a homogeneous bulk (whose density is to follow from the solution of the equations), i.e. $\partial_x \psi(x_\mathrm{b}^\mathrm{s}, \theta) = 0$, and
3. periodic boundary conditions for the angle θ, i.e. $\psi(x, -\pi) = \psi(x, \pi)$ and $\partial_\theta \psi(x, -\pi) = \partial_\theta \psi(x, \pi)$.

Fig. 4.2(c) shows the solution $\psi(x, \theta)$ for the same velocity asymmetry $a = 3$ used for the $D_t = 0$ solutions of Figs. 4.2(a-b), and for activity $\mathrm{Pe} = 3$. Note that boundary condition 1 dictates that the density in the fast bulk ρ_f is the same as for the $D_t = 0$ solution, but that the density in the slow bulk is now lower. The reason is that the probability current

$$\mathbf{j}^\mathrm{prob} = \left(\frac{v_0(x)}{v_\mathrm{f}} \cos\theta \frac{\psi}{\rho_\mathrm{f}} - \frac{1}{\mathrm{Pe}} \frac{\ell \partial_x \psi}{\rho_\mathrm{f}} \right) \hat{\mathbf{x}} - \frac{\partial_\theta \psi}{\rho_\mathrm{f}} \hat{\boldsymbol{\theta}} \tag{4.11}$$

now includes an additional diffusive flux from the higher density in the slow bulk towards the lower density in the fast bulk. The lowering of the slow bulk density distorts the flux balance in the interface region. Indeed, the same phase-space region of right-pointing particles in the interface now has an outflux towards the slow bulk that is smaller than the influx from the fast bulk. Conversely, the phase-space region of *left*-pointing particles in the interface now has an *influx from* the slow bulk that is smaller than the *outflux towards* the fast bulk. Therefore, as Fig. 4.2(c) illustrates, the resulting steady state has an interface with an excess of right-pointing particles, as well as a deficit of left-pointing particles. This asymmetry leads to a rotational diffusive flux from right- to left-pointing particles. This rotational flux restores the flux balance in the interface.

Fig. 4.2(d) shows the corresponding density, polarization and nematic order profile. The polarization profile indeed shows that particles in the interface preferentially point towards the slow bulk. A similar polarization in between two bulks with different propulsion was found in Ref. [139]. In their case, the polarization was developed by self-propelled rods that form a membrane-like structure in the interface. Here, we show that no aligning interactions are required: the polarization already forms for non-interacting spherical

particles. The inset of Fig. 4.2(d) also shows that there is small nematic order $S_{xx}(x)$, which demonstrates that particles preferentially point tangential to the interface on the fast side of the interface, and preferentially normal to the interface on the slow side of the interface. All these profiles agree qualitatively with the profiles found for MIPS. For MIPS, too, the density is highest on the side where the particles move slowest [140], while also the interfacial profiles are similar: the polarization points towards the dense phase [141], and there is nematic alignment parallel to the interface on the dilute side, and perpendicular to the interface on the dense side [25].

The normalized difference in bulk densities $\Delta\rho/\rho_\mathrm{f}$ is represented by the symbols in Fig. 4.3 for a range of Péclet numbers as a function of the asymmetry in propulsion speeds a. For $\mathrm{Pe} = 0$, the particles do not self-propel in either bulk, hence $\Delta\rho = 0$. For nonzero activity $\mathrm{Pe} > 0$, the density difference increases with the velocity asymmetry a, from $\Delta\rho = 0$ in the symmetric case ($a = 0$) to an asymptotic value in the limit $a \to \infty$. For high activity $\mathrm{Pe} \gg 1$, self-propulsion dominates over translational diffusion, and the density difference closely resembles the solution $\Delta\rho/\rho_\mathrm{f} = a$ found for the case with no translational diffusion.

We also obtained analytical solutions, by solving the moment equations (4.7) in steady state with the closure of no nematic order, i.e. $S_{\alpha\beta} = 0$. This closure is exact in the limit $\mathrm{Pe} \ll 1$. The derivation of the solutions is given in appendix 4.A; here, we simply give the resulting density profile

$$\rho(x) = \begin{cases} \rho_\mathrm{f} + A\mathrm{Pe}_\mathrm{f}\dfrac{\lambda_\mathrm{f}}{\ell}\exp(x/\lambda_\mathrm{f}) & \text{for } x \leq 0, \\ \rho_\mathrm{s} - A\mathrm{Pe}_\mathrm{s}\dfrac{\lambda_\mathrm{s}}{\ell}\exp(-x/\lambda_\mathrm{s}) & \text{for } x \geq 0, \end{cases} \tag{4.12}$$

and polarization profile

$$\mathbf{m}(x) = \begin{cases} A\exp(x/\lambda_\mathrm{f})\hat{\mathbf{x}} & \text{for } x \leq 0, \\ A\exp(-x/\lambda_\mathrm{s})\hat{\mathbf{x}} & \text{for } x \geq 0. \end{cases} \tag{4.13}$$

In Eqs. (4.12) and (4.13) we explicitly distinguished the Péclet number on the fast side $\mathrm{Pe}_\mathrm{f} \equiv \mathrm{Pe}$ and the Péclet number on the slow side $\mathrm{Pe}_\mathrm{s} \equiv \mathrm{Pe}/(1+a)$, and we defined the length scales $\lambda_\mathrm{f/s} \equiv (1 + \mathrm{Pe}_\mathrm{f/s}^2/2)^{-1/2}\ell$. The constant A, which depends on Pe and a, is given explicitly in appendix 4.A. Finally, the analytical solution for the slow bulk density is

$$\rho_\mathrm{s} = \rho_\mathrm{f}\sqrt{\frac{1 + \frac{1}{2}\mathrm{Pe}_\mathrm{f}^2}{1 + \frac{1}{2}\mathrm{Pe}_\mathrm{s}^2}}. \tag{4.14}$$

The analytical profiles (4.12) and (4.13) are shown in Fig. 4.2(d), for the same parameter values as the numerical solution, i.e. for $\mathrm{Pe} = 3$ and $a = 3$. Even though the closure is only exact for $\mathrm{Pe} \ll 1$, the agreement is still very good, and in fact remains very good - at least for these profiles - up to Péclet numbers as high as 100. The analytical solutions (4.12) and (4.13) show that the width of the interface is set by the length scales λ_f and λ_s. For large activity, these length scales are inversely proportional to the Péclet numbers Pe_f and Pe_s, respectively. Therefore: the higher the activity, the sharper the interface, another feature that is also displayed by the interface of MIPS [25]. The differences in

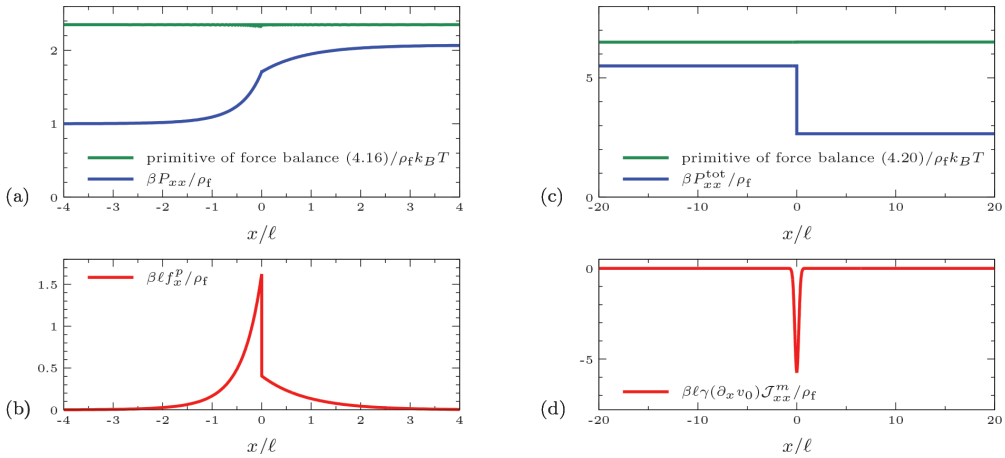

Figure 4.4: (a-b) Illustration of the force balance (4.15) for activity $\mathrm{Pe} = 3$ and asymmetry $a = 3$. (a) The normal pressure $P_{xx}(x) = \rho(x)k_BT$ (blue line) and (b) the propulsion force density $f_x^p = \gamma v_0(x) m_x(x)$. The green line in (a) is the primitive of the force balance (4.15) $\left(\int_{x_b^f}^{x} \mathrm{d}x' f_x^p(x') - P_{xx}(x)\right)/\rho_f k_B T$, shifted for clarity; the fact that is independent of x confirms that the force balance is satisfied. (c-d) Illustration of the rewritten force balance (4.20), again for $\mathrm{Pe} = a = 3$. (c) The total normal pressure $P_{xx}^{\mathrm{tot}}(x)$ (blue line) is constant as long as $v_0(x)$ is constant, but its value jumps at $x = 0$. (d) The $\partial_x v_0$-term takes the form of a delta function, as suggested by the red line. The green line in (c) is the primitive of the force balance (4.20) $\left(\int_{x_b^f}^{x} \mathrm{d}x' \gamma(\partial_{x'} v_0)(x')\mathcal{J}_{xx}^m(x') - P_{xx}^{\mathrm{tot}}(x)\right)/\rho_f k_B T$, shifted for clarity; the fact that it is independent of x confirms that the rewritten force balance is satisfied.

bulk density $\Delta\rho$ that follow from Eq. (4.14) are plotted as the solid lines in Fig. 4.3, again displaying excellent agreement with the numerical data. Finally, we point out that the ratio in bulk densities (4.14) agrees with the bulk densities that were obtained by Magiera and Brendel, who account for the position-dependent activity by using an effective, position-dependent diffusion coefficient [142].

Now that we have characterized the interface, the next question is: what is its interfacial tension? Before we can address this question, we first need to discuss the various forces and pressures at play in the interface.

4.5 Force balances

The force balance follows from multiplying Eq. (4.8a) by the friction coefficient γ, which results in

$$\mathbf{0} = \mathbf{f}^f(\mathbf{r}) + \mathbf{f}^p(\mathbf{r}) + \mathbf{f}^e(\mathbf{r}) - \boldsymbol{\nabla} \cdot \mathbf{P}(\mathbf{r}). \tag{4.15}$$

Here $\mathbf{f}^f \equiv -\gamma \mathbf{J}$ is the frictional force density, $\mathbf{f}^p \equiv \gamma v_0 \mathbf{m}$ is the propulsion force density, $\mathbf{f}^e \equiv -(\boldsymbol{\nabla} V)\rho$ is the external force density, and $\mathbf{P}(\mathbf{r}) \equiv \rho(\mathbf{r}) k_B T \mathbb{I}$ is the 'bare' local

pressure tensor that represents the momentum flux of our active ideal gas particles[f] [83, 97]. Furthermore, to obtain an expression for the pressure that is familiar from equilibrium thermodynamics, we defined a temperature from the Einstein relation, i.e. $k_BT \equiv \gamma D_t$.

Far from any walls (where $\mathbf{f}^e = \mathbf{0}$), and in our steady state that is flux-free (such that $\mathbf{f}^f = \mathbf{0}$), the force balance (4.15) in the direction normal to the interface simplifies to

$$0 = f_x^p(x) - \partial_x P_{xx}(x), \tag{4.16}$$

where $P_{xx}(x) = \rho(x)k_BT$ is the xx-component of the tensor $\mathbf{P}$. This normal pressure is plotted as the blue line in Fig. 4.4(a). As it is proportional to the density, it is higher in the slow bulk than in the fast bulk, and hence gives rise to a pressure gradient force directed towards the fast bulk. This pressure gradient should be balanced by the propulsion force $f_x^p(x)$, shown as the red line in Fig. 4.4(b). The propulsion force points - just like the polarization - towards the slow bulk. To explicitly check that these forces indeed balance each other, the green line in Fig. 4.4(a) shows the integrated force balance $\int^x \mathrm{d}x' f_x^p(x') - P_{xx}(x)$. The fact that this expression is independent of x confirms that the force balance is indeed satisfied.

A convenient way to rewrite the propulsion force balance (4.15) is by employing the evolution equation (4.7b) for the polarization $\mathbf{m}$. When multiplied by $\gamma v_0(x)$, it becomes the following evolution equation for the propulsion force density $\mathbf{f}^p(\mathbf{r}, t)$.

$$\partial_t f_\alpha^p = -\partial_\beta \mathcal{J}_{\beta\alpha}^p - D_r f_\alpha^p + \gamma \left(\partial_\beta v_0\right) \mathcal{J}_{\beta\alpha}^m, \tag{4.17}$$

where we defined the propulsion force flux $\mathcal{J}_{\alpha\beta}^p(x,t) \equiv \gamma v_0(x) \mathcal{J}_{\alpha\beta}^m(x,t)$. When there is reason to assume that $\partial_t f_\alpha^p = 0$, e.g. in steady state, or when the polarization can be considered a fast variable on the time scale of interest, then Eq. (4.17) can be solved for the propulsion force as

$$f_\alpha^p = -\partial_\beta P_{\beta\alpha}^{\mathrm{swim}} + \frac{\gamma}{D_r} \left(\partial_\beta v_0\right) \mathcal{J}_{\beta\alpha}^m. \tag{4.18}$$

Here we defined the swim pressure tensor $P_{\alpha\beta}^{\mathrm{swim}} \equiv \mathcal{J}_{\alpha\beta}^p / D_r$ [g], a quantity that is also called the flux of 'active impulse' [132], and that is thus proportional to the propulsion force flux $\mathcal{J}_{\alpha\beta}^p$ [42]. With Eq. (4.18), the force balance (4.15) can be rewritten as

$$0 = f_\alpha^f + f_\alpha^e - \partial_\beta P_{\beta\alpha}^{\mathrm{tot}} + \frac{\gamma}{D_r} (\partial_\beta v_0) \mathcal{J}_{\beta\alpha}^m, \tag{4.19}$$

[f] For the overdamped motion considered here, the momentum flux tensor of active particles has the same form as the one for passive particles. Generally, the propulsion force does give additional contributions to the momentum flux, but these contributions disappear in the overdamped limit [83, 97].

[g] Actually, other authors reserve the term 'swim pressure' (or 'active pressure') solely for the contribution to $P_{\alpha\beta}^{\mathrm{swim}}$ that comes from the density term in the orientation current $\mathcal{J}_{\alpha\beta}^m$ (see Eq. (4.8b)) [30, 42, 85]. We point out that the swim pressure was originally derived as a property of a homogeneous and isotropic bulk [84–86]. In such a bulk, the other contributions to $\mathcal{J}_{\alpha\beta}^m$ vanish, such that the swim pressure as defined here agrees with other definitions. We find the definition used here, $P_{\alpha\beta}^{\mathrm{swim}}(\mathbf{r}) = \mathcal{J}_{\alpha\beta}^p(\mathbf{r})/D_r$, a natural extension of the notion of swim pressure to a local property of inhomogeneous and anisotropic regions. Having said that, the difference in convention is purely semantic, and the results of this chapter do not depend on it.

where $\mathbf{P}^{\text{tot}} = \mathbf{P} + \mathbf{P}^{\text{swim}}$ has the form of a total pressure tensor that now includes the swim pressure. One reason why Eq. (4.19) is convenient to work with, is that in a homogeneous and isotropic bulk the total pressure tensor $\mathbf{P}^{\text{tot}}(\mathbf{r}) = P^{\text{tot}}\mathbb{I}$ reduces to a constant scalar quantity P^{tot} that equals the pressure exerted onto a (planar [143]) wall that confines the bulk. This wall pressure P^{tot} usually exceeds the bare bulk pressure $P = \frac{1}{2}\text{Tr}(\mathbf{P})$. The reason is that active particles tend to persistently self-propel 'into' the wall, and thereby exert an additional pressure on it. This additional pressure is precisely equal to the value of the swim pressure evaluated in the bulk [83, 132]. We point out that the force balance (4.19) is derived here only for an active ideal gas, but it can be generalized to systems with isotropic particle-particle interactions: for these systems Eq. (4.19) remains valid, but with generalized expressions for the total pressure tensor $P^{\text{tot}}_{\alpha\beta}$ (see e.g. [144]) and orientation flux $\mathcal{J}^m_{\alpha\beta}$ [141].

Rewriting the force balance (4.15) into (4.19) is by now standard [66, 132], but because we consider a position-dependent propulsion speed $v_0(x)$, we pick up an additional term proportional to its gradient $\partial_\beta v_0$. To illustrate the effect of this term, we again consider the force balance in a flux-free steady state away from any walls, such that $\mathbf{f}^f = \mathbf{f}^e = \mathbf{0}$. The component of the force balance (4.19) in the direction normal to the interface then simplifies to

$$0 = -\partial_x P^{\text{tot}}_{xx}(x) + \frac{\gamma(\partial_x v_0)}{D_r}\left[v_0\left(S_{xx} + \frac{\rho}{2}\right) - D_t \partial_x m_x\right], \tag{4.20}$$

where we used Eq. (4.8b). The force balance (4.20) is illustrated in Figs. 4.4(c-d). The normal component of the total pressure, $P^{\text{tot}}_{xx}(x)$, is plotted as the blue line in Fig. 4.4(c). It is constant as long as $v_0(x)$ is constant, i.e. $P^{\text{tot}}_{xx}(x) = P^{\text{tot}}_{\text{f}}$ for $x < 0$, and $P^{\text{tot}}_{xx}(x) = P^{\text{tot}}_{\text{s}}$ for $x > 0$, where $P^{\text{tot}}_{\text{f}}$ and $P^{\text{tot}}_{\text{s}}$ represent the total pressure of the fast and slow bulk, respectively. However, as Fig. 4.4(c) shows, the value of $P^{\text{tot}}_{xx}(x)$ jumps at $x = 0$, such that $P^{\text{tot}}_{\text{f}} \neq P^{\text{tot}}_{\text{s}}$. According to the discussion above, this implies that the fast bulk and slow bulk exert different pressures on their surrounding walls, a feature that was already observed in [88]. This difference is a consequence of the fact that both the densities and propulsion speeds differ between the two bulks, and, consequently, so do both the bare pressure and the swim pressure. The overall result is that the total pressure is higher in the slow bulk than in the fast bulk. We show here that the force balance is nonetheless satisfied. Indeed, for our velocity profile $v_0(x)$ given by Eq. (4.3), the $\partial_x v_0$-term in Eq. (4.20) takes the form of a delta function, which is represented by the red line in Fig. 4.4(d). This delta function restores the force balance, as again made explicit by the fact that the integral up to x of both terms in Eq. (4.20), shown as the green line in Fig. 4.4(c), is independent of x.

4.6 Mechanical interfacial tension

Having established the force and pressures at play in the interface, we now aim to find the interfacial tension. First, we must answer the question how to extend the equilibrium concept of interfacial tension to active systems. We consider two possible extensions, both of which deserve their own section.

In this section, we define the *mechanical* interfacial tension σ_{m}, that follows from the

equilibrium concept of interfacial tension σ in the following way. For an equilibrium phase coexistence, the interfacial tension σ is defined as the free energy cost of an interface of unit length. Note that we speak of a unit *length* because we consider a two-dimensional system; in three dimensions it would be the cost of an interface of unit *area*. This definition implies that if one increases the interfacial length by an infinitesimal amount $\mathrm{d}L$, the free energy increases by an amount $dF = \sigma \mathrm{d}L$, provided that one keeps other system parameters constant, such as the system's total area (or, in 3D, its volume). For a system in a rectangular box, such a transformation can be achieved by lengthening the box in the direction tangential to the interface, while simultaneously shortening the box in the normal direction in such a way that its area remains constant. This box deformation is indicated by the orange arrows in Figs. 4.5(a) and (b). Note that our interface points along the y-axis, such that $\mathrm{d}L = \mathrm{d}L_y$. If the deformation is performed quasi-statically, the work required for the deformation $\mathrm{d}W$ equals the increase in the system's free energy dF, which implies

$$\mathrm{d}W = \sigma \mathrm{d}L_y. \tag{4.21}$$

Now, by itself, Eq. (4.21) is a purely mechanical equation for the interfacial tension σ, and can therefore directly be applied to active systems, in which case we denote the resulting interfacial tension by σ_m.

We thus obtain the mechanical interfacial tension σ_m by first calculating the work $\mathrm{d}W$ required for the constant-volume box deformation, and subsequently applying Eq. (4.21). Actually, the situation is a bit more involved than outlined above, and the entire calculation is presented in Appendix 4.B. Nonetheless, the essential idea is the same, and the result of the derivation in Appendix 4.B is as follows. The interfacial tension σ_m equals the work per increase in interface length, i.e. $\sigma_\mathrm{m} = \mathrm{d}W/\mathrm{d}L_y$, where $\mathrm{d}W$ is the work required for a constant-area box deformation of the actual system *minus* the work required for the same deformation of a *reference* system that has a 'trivial' interface. This reference system is defined as the combination of a fast and slow *bulk* that exist all the way up and down to $x = 0$, respectively, and is schematically depicted in Fig. 4.5(a). The actual system, illustrated in Fig. 4.5(b), differs from the reference system by the existence of a nontrivial interface in between the bulks. Thus, the interfacial tension σ_m equals the difference between Figs. 4.5(b) and (a) in the force that is exerted vertically onto the upper (or lower) wall. The difference in this force comes from the difference between the systems in the region where their interface meets the wall. This region is marked by the upper (or lower) yellow rectangle in Figs. 4.5(a) and (b). For definiteness, in this discussion we stick to the upper wall, and upper yellow rectangle, whose enclosed area we denote by S_up. Hence, by Newton's third law, the interfacial tension reads

$$\sigma_\mathrm{m} = -\int_{S_\mathrm{up}} \mathrm{d}S (f^e_{y,\mathrm{ref}} - f^e_y). \tag{4.22}$$

The subscript 'ref' refers to the reference system of Fig. 4.5(a). The surface integral is defined as $\int_{S_\mathrm{up}} \mathrm{d}S = \int_{x_\mathrm{b}^\mathrm{f}}^{x_\mathrm{b}^\mathrm{s}} \mathrm{d}x \int_{y_\mathrm{b}}^{L_y} \mathrm{d}y$, where it is understood that the boundary $y = L_y$ (the upper boundary of S_up) lies just *above* the upper wall, such that no particles are present at $y = L_y$. The reason that a *surface* integral appears is because we consider a two-dimensional system; in three dimensions it would be a volume integral.

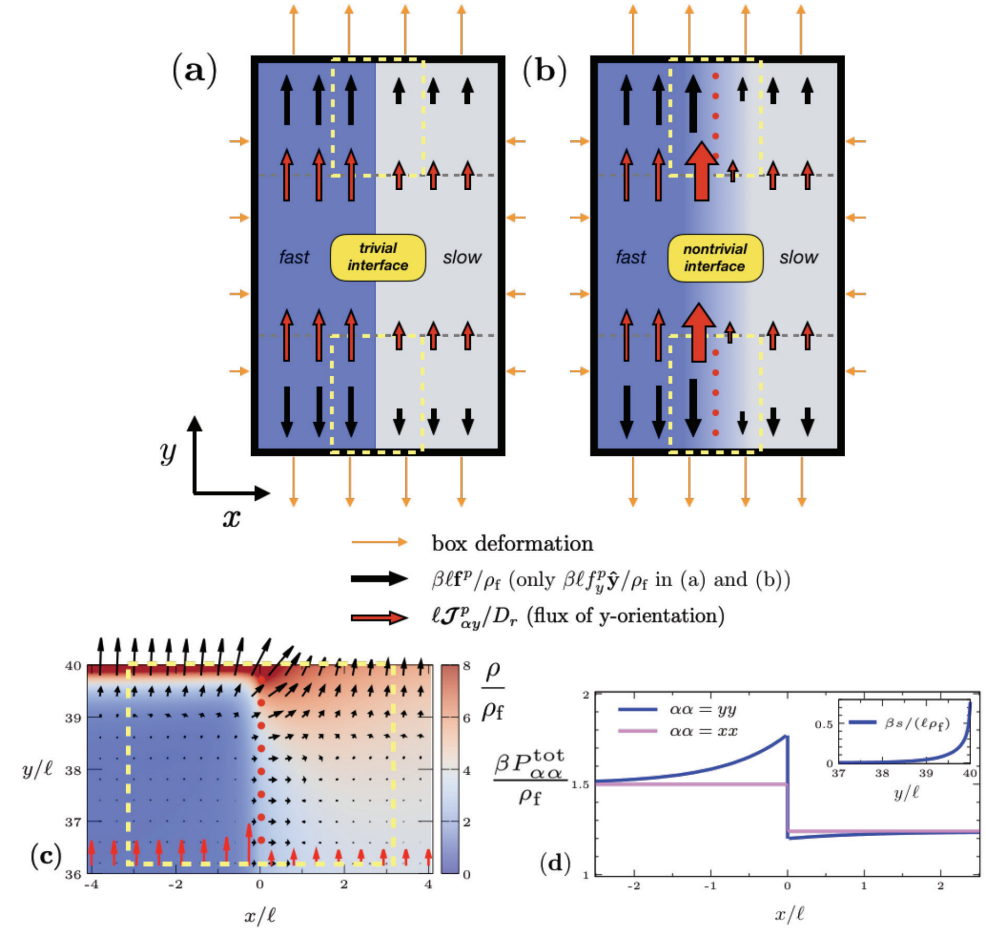

Figure 4.5: Sketch of (a) a fictional reference system that consists of a fast and slow bulk simply glued together at $x = 0$ and (b) the actual system with a nontrivial interface. (c) Numerical solution of the actual system in the region where the interface meets the wall, obtained under the closure $\mathbf{S} = \mathbf{0}$ for $\mathrm{Pe} = a = 5$. The orange arrows in (a-b) indicate a constant-volume box deformation that increases the interfacial length by $\mathrm{d}L_y$. The background color in (a-c) indicates the bare pressure $P = \rho k_B T$, black arrows indicate the propulsion force $\mathbf{f}^{\mathrm{p}}$ (or, actually, only the vertical component $f_y^p\hat{\mathbf{y}}$ in (a-b)), and red arrows indicate the flux of propulsion force $\mathcal{J}^p_{yy}$. (d) Total pressure profile P^{tot}_{yy} over the lower boundary of the upper yellow box in (a) for the actual system (blue line) and for the reference system (violet line), under the same closure but for $\mathrm{Pe} = 1$ and $a = 5$. The area under the difference of these curves gives a negative contribution to the mechanical interfacial tension σ_{m}. Inset: The profile of the source term $s(y)$ - that is due to $v_0(x)$ being position dependent - over the dotted red line in (a), again for $\mathbf{S} = \mathbf{0}$, $\mathrm{Pe} = 1$ and $a = 5$. The area under this curve gives a contribution to σ_{m} that is positive and exactly opposite to the contribution from the total pressure difference. Therefore, $\sigma_{\mathrm{m}} = 0$.

A closeup of the region $S_{\rm up}$ is shown in Fig. 4.5(c) for a numerical solution of the actual system. The numerical solution is obtained under the closure $\mathbf{S} = \mathbf{0}$, i.e. by solving Eqs. (4.7) and (4.8), in steady state, and in a box with lengths $L_x = L_y = 80\ell$ enclosed by hard walls. The solution is shown for $\mathrm{Pe} = 5$ and $a = 5$. The choice for $\mathrm{Pe} = 5$ may seem strange, since the closure $\mathbf{S} = \mathbf{0}$ is only expected to be reasonable for $\mathrm{Pe} \lesssim 1$. However, it is made only for illustrational purposes: the purpose of Fig. 4.5(c) is to illustrate the qualitative features that we discuss below, and while these features are also present for $\mathrm{Pe} \lesssim 1$, they are smaller, and therefore not clearly visible in that case.

To rewrite Eq. (4.22) into a more useful form, we utilize the force balance of Eq. (4.15) to substitute the external forces $f^e_{y,\rm ref}$ and f^e_y. Of the several terms that follow, the contribution from the frictional force $f^f_y = -\gamma J_y$ vanishes: for the reference system of Fig. 4.5(a), the reason is simply that the particle flux $\mathbf{J}_{\rm ref}$ is zero everywhere; for the actual system of Fig. 4.5(b), it turns out that there *is* a nonzero current $\mathbf{J}$ in the region where the interface meets the wall, but this vector field is a pure rotation, and therefore its contribution the integral vanishes, as shown in Appendix 4.C. The remaining contributions to the interfacial tension are

$$\sigma_{\rm m} = \int_{x_{\rm b}^{\rm f}}^{x_{\rm b}^{\rm s}} \mathrm{d}x \left(P_{yy,\rm ref}(x, y_{\rm b}) - P_{yy}(x, y_{\rm b})\right) + \int_{S_{\rm up}} \mathrm{d}S \left(f^p_{y,\rm ref}(x, y) - f^p_y(x, y)\right). \tag{4.23}$$

Here we used Gauss' theorem to rewrite the integral over the pressure term as an integral over the boundary $\delta S_{\rm up}$. Of this boundary integral, only the integral over the lower side of $\delta S_{\rm up}$ (at $y = y_{\rm b}$) contributes: the contributions from the vertical sides (at $x = x_{\rm b}^{\rm f}$ and at $x = x_{\rm b}^{\rm s}$) vanish due to the fact that $\mathbf{P}$ is diagonal, whereas the contribution from the upper side (at $y = L_y$) vanishes because it is understood to lie just above the upper wall, where there are no particles such that $P_{yy,\rm ref}(x, L_y) = P_{yy}(x, L_y) = 0$.

Eq. (4.23) shows that the mechanical interfacial tension $\sigma_{\rm m}$ is the sum of two contributions. The first contribution is the difference in the bare pressure P_{yy} integrated over the lower boundary of $\delta S_{\rm up}$, i.e. integrated through the interface at fixed $y = y_{\rm b}$. The bare pressure $P_{yy}(x, y_{\rm b}) = \rho(x, y_{\rm b}) k_B T$ is proportional to the local density $\rho(x, y_{\rm b})$, which is shown by the background color in Figs. 4.5(a-c). Because the density profile in the interface is different for the actual and reference systems, the first contribution of Eq. (4.23) to $\sigma_{\rm m}$ is nonzero, and can be either positive or negative, depending on Pe and a. The second contribution to Eq. (4.23) comes from the y-component of the propulsion force f^p_y. The propulsion force field is shown as the black arrows in Figs. 4.5(a-c). A nonzero propulsion force $f^p_y = \gamma v_0(x) m_y$ forms close to the horizontal walls, because, as already alluded to in section 4.5, active particles tend to persistently propel 'into' walls, and thereby form a polarization m_y pointed towards the wall. Note that Figs. 4.5(a) and (b) only (schematically) show the y-component of the propulsion force, which is the only component that contributes to the interfacial tension. In contrast, Fig. 4.5(c) shows the profile of the full propulsion force $\mathbf{f}^p$, and therefore also displays the horizontal propulsion force f^p_x that forms in the interface (see section 4.5).

Rather than evaluating the two contributions to Eq. (4.23) directly, we choose to further rewrite them by employing Eq. (4.18). The result is

$$\sigma_{\rm m} = \sigma_0 + \sigma_{\rm mg}, \tag{4.24}$$

where

$$\sigma_0 \equiv \int_{x_\mathrm{b}^\mathrm{f}}^{x_\mathrm{b}^\mathrm{s}} \mathrm{d}x \left(P_{yy,\mathrm{ref}}^{\mathrm{tot}}(x, y_\mathrm{b}) - P_{yy}^{\mathrm{tot}}(x, y_\mathrm{b}) \right) \tag{4.25}$$

and

$$\sigma_\mathrm{mg} \equiv -\frac{\gamma}{D_r} \int_{S_\mathrm{up}} \mathrm{d}S (\partial_x v_0)(x) \mathcal{J}_{xy}^m(x, y). \tag{4.26}$$

The subscript "mg" stands for "motility gradient", for reasons we discuss below. In deriving Eq. (4.24), we used the fact that the $\partial_x v_0$-term is absent for the trivial interface of the reference system, simply because this is how the reference system is defined. In fact, Appendix 4.B only derives Eq. (4.24) where $P_{yy,\mathrm{ref}}^{\mathrm{tot}}(x, y_\mathrm{b})$ is *defined* to be given by $P_\mathrm{f}^{\mathrm{tot}}$ for $x < 0$ and by $P_\mathrm{s}^{\mathrm{tot}}$ for $x > 0$. Indeed, these are the total bulk pressures of the fast and slow bulk, and thus of the reference system of Fig. 4.5(a). Nonetheless, strictly speaking, Eqs. (4.22)-(4.23) and the comparison with the reference system only constitute an *interpretation* of the result derived in appendix 4.B.

Eq. (4.24) again shows the interfacial tension σ_m as the sum of two contributions: σ_0, whose expression (4.25) does not explicitly depend on the velocity profile $v_0(x)$, and σ_mg, whose expression (4.26) involves $\partial_x v_0(x)$ such that σ_mg is only nonzero for systems with a motility gradient. We discuss these contributions one by one.

4.6.1 The contribution σ_0

The first contribution (4.25) comes from the difference in the yy-component of the total pressure tensor, again integrated through the interface (at fixed $y = y_\mathrm{b}$). This contribution can be rewritten into a form that only involves the actual system. To this end, we point out that the *reference* system's total pressure *tangential* to the interface coincides with the *actual* system's total pressure *normal* to the interface, i.e. $P_{yy,\mathrm{ref}}^{\mathrm{tot}}(x, y_\mathrm{b}) = P_{xx}^{\mathrm{tot}}(x, y_\mathrm{b})$. Indeed, Sec. 4.5 showed that $P_{xx}^{\mathrm{tot}}(x, y_\mathrm{b})$ is also given by $P_\mathrm{f}^{\mathrm{tot}}$ for $x < 0$ and by $P_\mathrm{s}^{\mathrm{tot}}$ for $x > 0$. Therefore,

$$\sigma_0 = \int_{x_\mathrm{b}^\mathrm{f}}^{x_\mathrm{b}^\mathrm{s}} \mathrm{d}x \left(P_{xx}^{\mathrm{tot}}(x, y_\mathrm{b}) - P_{yy}^{\mathrm{tot}}(x, y_\mathrm{b}) \right). \tag{4.27}$$

Now, Eq. (4.27) is precisely the expression for the mechanical interfacial tension that has been found for MIPS [25, 26]. Thus, whereas for our system σ_0 is only one of two contributions to the mechanical interfacial tension σ_m of Eq. (4.24), for MIPS it constitutes *full* mechanical interfacial tension $\sigma_\mathrm{m} = \sigma_0$ [25, 26]. Of course, in the latter case it is understood that the total pressure tensor includes the appropriate contributions from particle-particle interactions [26, 144].

The two pressure components that appear in Eq. (4.27) are plotted in Fig. 4.5(d), this time for $\mathrm{Pe} = 1$ and $a = 5$. As already discussed in Sec. 4.5, the component normal to the interface $P_{xx}^{\mathrm{tot}}(x)$ jumps at $x = 0$, but is otherwise constant and equal to the bulk pressures $P_\mathrm{f/s}^{\mathrm{tot}}$. The component tangential to the interface $P_{yy}^{\mathrm{tot}}(x)$ behaves differently. On the fast side of the interface, i.e. for $x < 0$, it exceeds the bulk pressure $P_\mathrm{f}^{\mathrm{tot}}$, whereas on the slow side of the interface ($x < 0$) it is lower than the corresponding bulk pressure P_s^{tot}, but by a lesser amount. The overall result is that the integral of Eq. (4.27), given as

the area under the difference of the two curves, is *negative*. Hence, σ_0, which forms the full - negative [26] - interfacial tension for MIPS, is already negative in our simple ideal gas system!

And precisely because our system is a simple active ideal gas, we can also understand *why* it is negative. We explain it for the form that σ_0 takes in Eq. (4.25), i.e. by comparing the interfacial profiles $P_{yy}^{\rm tot}$ of the actual and the reference system. As explained in Sec. 4.5, the total pressure $P_{yy}^{\rm tot}$ is the sum of the bare pressure P_{yy} and the swim pressure $P_{yy}^{\rm swim}$. We already explained below Eq. (4.23) that the bare pressure P_{yy} differs between the two systems, and that this gives a contribution to the interfacial tension $\sigma_{\rm m}$ that can be either positive or negative. As we will explain below, the contribution from the swim pressure $P_{yy}^{\rm swim}$ to Eq. (4.25) is *always* negative. Moreover, it turns out that the sum of the contributions from the bare and swim pressure is *also* always negative, such that indeed $\sigma_0 < 0$. In fact, for small Péclet numbers (Pe $\ll 1$), Appendix 4.D derives that

$$\sigma_0 = -\ell k_B T \mathrm{Pe} \frac{a}{1+a} m_x(0), \tag{4.28}$$

where the polarization $m_x(0) = m_x(x = 0, y = y_{\rm b})$ is positive (see Fig. 4.2(b)), such that Eq. (4.28) is indeed manifestly negative. In the opposite limit, i.e. for Pe $\gg 1$, the contribution from the swim pressure dominates the contribution from the bare pressure, such that the result is also negative.

So why is the contribution to Eq. (4.25) from the swim pressure $P_{yy}^{\rm swim}$ negative? Physically, the reason is that this contribution represents a propulsion force f_y^p in the interface-wall region that is *larger* in the actual system than in the reference system. Because this propulsion force *helps* in doing the box deformation, its contribution to the interfacial tension is *negative*. We now explain this in more technical terms. The reason that the interfacial profile $P_{yy}^{\rm swim}(x, y_{\rm b})$ contributes to the interfacial tension $\sigma_{\rm m}$ in the first place is that, as explained in Sec. 4.5, it is proportional to the flux of y-component of propulsion force $\mathcal{J}_{yy}^p$. In turn, the flux $\mathcal{J}_{yy}^p(x, y_{\rm b})$ contributes to the total amount of propulsion force in $S_{\rm up}$, and thus, via the second term of Eq. (4.23), to the interfacial tension $\sigma_{\rm m}$. To understand the sign of this contribution, we compare the flux $\mathcal{J}_{yy}^p(x, y_{\rm b})$ between the actual and the reference system. This flux is shown as the red arrows in Figs. 4.5(a-c). For the reference system, the flux $\mathcal{J}_{yy}^p$ into $S_{\rm up}$ simply equals its fast bulk value for $x < 0$ and its slow bulk value for $x > 0$ (see Fig. 4.5(a)). The actual system, however, has a higher influx $\mathcal{J}_{yy}^p$ on the fast side of the interface, and a lower influx on the slow side of the interface[h] (see Figs. 4.5(b) and (c)). Importantly, the difference between the actual and reference system is of larger magnitude on the fast side than on the slow side[i], such that the overall effect is that the actual system has a *higher* influx $\mathcal{J}_{yy}^p$ into

[h]The excess influx on the fast side can be traced back to the fact that, compared to the reference system, the actual system has a density and tangential nematic alignment $S_{yy} = 1 - S_{xx}$ that are *higher* on this side (see Fig. 4.2). By Eq. (4.8b), this leads to a higher orientation flux $\mathcal{J}_{yy}^m$ - which means that particles are more mobile along the interface - and thus to a higher flux of propulsion force $\mathcal{J}_{yy}^p = \gamma v_0(x) \mathcal{J}_{yy}^m$. Conversely, on the *slow* side the actual system's density and nematic alignment S_{yy} are *lower*, which makes particles *less* mobile along that side of the interface and thus leads to a *lower* value of $\mathcal{J}_{yy}^p$.

[i]The reason is the factor $v_0(x)$ that appears in $\mathcal{J}_{yy}^p = \gamma v_0(x) \mathcal{J}_{yy}^m$: the change in particle mobility along the interface $\mathcal{J}_{yy}^m$ has a larger impact on the flux of propulsion force $\mathcal{J}_{yy}^p$ on the fast side of the interface than on the slow side.

$S_{\rm up}$ than the reference system. If we ignore the "mg"-contribution from the $\partial_x v_0$-term in Eq. (4.18) for the moment, the result is indeed that the actual system has a larger propulsion force f_y^p in the interface-wall region than the reference system. As emphasized above, this propulsion force *helps* in doing the box deformation, and this is (largely) the reason that $\sigma_0 < 0$.

4.6.2 The contribution $\sigma_{\rm mg}$

Finally, we discuss the effect of the motility gradient, which gives rise to the contribution $\sigma_{\rm mg}$ in Eq. (4.24). Eq. (4.26) shows that $\sigma_{\rm mg}$ is proportional to an integral over $\partial_x v_0(x)\mathcal{J}^m_{xy}(x,y)$. Since $\partial_x v_0(x) = -(v_f - v_s)\delta(x)$ (see Eq. (4.3)), this integrand only contributes at $x = 0$, i.e. on the line marked by the red dots in Fig. 4.5(b). Consequently, the integral over x can be performed, which yields - using Eq. (4.8b) and treating the discontinuities at $x = 0$ carefully -

$$\sigma_{\rm mg} = \int_{y_{\rm b}}^{L_y} \frac{{\rm d}y}{\ell} s(y), \tag{4.29}$$

with

$$\frac{\beta s(y)}{\ell} \equiv \frac{\rm Pe}{(1+a)^2}\Big(- a(1+a)\ell\overline{\partial_x m_y}(y) + {\rm Pe}\, a(2+a)S_{xy}(0,y)\Big). \tag{4.30}$$

Here $\beta \equiv (k_B T)^{-1}$ and $\overline{\partial_x m_y}(y) \equiv 1/2(\partial_x m_y(0^+,y) + \partial_x m_y(0^-,y))$, where $0^\pm \equiv \lim_{\epsilon\downarrow 0}(0 \pm \epsilon)$. $\overline{\partial_x m_y}$ is the 'mean value' of $\partial_x m_y$, which is discontinous, at $x = 0$. Here we defined $0^\pm \equiv \lim_{\epsilon\downarrow 0}(0 \pm \epsilon)$. Generally, calculating the function $s(y)$ requires the full numerical solution of the system sketched in Fig. 4.5(b), including the y-dependence near the horizontal wall. Since we were not able to obtain this solution to the required accuracy for general Pe, instead we used the closure $\mathbf{S} = \mathbf{0}$ to simplify the equations. The resulting solution $s(y)$ is shown in the inset of Fig. 4.5(d), for ${\rm Pe} = 1$ and $a = 5$. Clearly, $s(y)$ is positive, and therefore so is $\sigma_{\rm mg}$. In fact, under this closure $\sigma_{\rm mg}$ can be calculated analytically, which is done in Appendix 4.D. The result is

$$\sigma_{\rm mg} = \ell k_B T {\rm Pe}\frac{a}{1+a} m_x(0). \tag{4.31}$$

Remarkably, comparing Eq. (4.31) with Eq. (4.28) shows that $\sigma_{\rm mg} = -\sigma_0$, such that, by Eq. (4.83), $\sigma_{\rm m} = 0$!

We conclude that in the limit ${\rm Pe} \ll 1$ the mechanical interfacial tension $\sigma_{\rm m} = 0$. This means that the presence of the interface neither makes the box deformation of Figs. 4.5(a-b) cost more work, nor less.

4.7 Tensile force in the interface

For an equilibrium phase coexistence, the interfacial tension σ also plays the role of the tensile force in the interface. Thereby, it stabilizes the interface against perturbations. In this section we extend this definition to active systems, for which we call it $\sigma_{\rm t}$. Moreover,

we investigate the stability of the interface.

To this end, we slightly perturb the interface, and see how it responds. The perturbation consists of shifting the interface at coordinate y in the x-direction by an amount $h(y)$. Thus, the perturbed density profile $\rho(x, y, t)$ is initially given by

$$\rho(x, y, t = 0) = \rho_0(x - h(y)), \tag{4.32}$$

where $\rho_0(x)$ denotes the unperturbed density profile. For simplicity, we assume

$$h(y) = \mathcal{A}\cos(ky) \tag{4.33}$$

for a given wavenumber k and amplitude $\mathcal{A}$. We assume that $h(y)$, $h'(y)$ and $h''(y)$ all can be considered 'small', which means that B must be much smaller than any internal length scale, while k must not be much larger than the reciprocal of any internal length scale. The perturbation $h(y)$ is sketched in Fig. 4.6.

Eq. (4.32) does not fully specify the perturbed probability density $\psi(\mathbf{r}, \theta, t = 0)$, since it states nothing about the change in the higher angular moments $\mathbf{m}$, $\mathbf{S}$ etc. To specify the perturbation fully, we assume that these higher angular moments are adiabatically enslaved to the density. In other words, we assume that they attain their steady-state values at the fixed density profile (4.32). This assumption is valid only if all gradients are 'small' [66], i.e. if $|\boldsymbol{\nabla}\psi| \ll \psi/\max(\ell, \ell_p)$, where we recall that ℓ is the diffusive length scale and ℓ_p the persistence length. This assumption is not justified for the solutions of Sec. 4.4, which correspond to the step function profile (4.3) of the propulsion speed. Therefore, in the current section, instead we assume a profile $v_0(x)$ that varies slowly from one bulk to the other. 'Slowly' means over a distance W much larger than any internal length scale, such that the interface width is much larger than ℓ and ℓ_p. Appendix 4.F derives the perturbations of the higher angular moments that follow from this assumption.

In order to track the response of the interface over time, we define its location by the Gibbs dividing line $x_G(y, t)$. The definition of $x_G(y, t)$ is given in appendix 4.E. Actually, the most interesting quantity is the deviation of the Gibbs dividing line $\delta x_G(y, t) \equiv x_G(y, t) - x_{G,0}(y, t)$ from its unperturbed value $x_{G,0}(y, t)$. In the following, we consider this displacement $\delta x_G(y, t)$ of an interface segment of infinitesimal width δy along the interface. An example of such a segment (but of finite width) is drawn in Fig. 4.6. As shown in Appendix 4.E, the displacement of this segment changes according to

$$\partial_t \delta x_G(y, t) = \frac{1}{\Delta\rho}\frac{1}{\delta y}\int_{\delta S_{\text{segm}}} \mathrm{d}\ell \mathbf{J}\cdot\hat{\mathbf{n}}. \tag{4.34}$$

Here $\delta S_{\text{segment}}$ denotes the boundary of the segment's surface area S_{segm} and $\hat{\mathbf{n}}$ its outward-pointing normal vector. Also, recall that $\Delta\rho = \rho_{\text{s}} - \rho_{\text{f}}$ is the difference in bulk densities, which remain unchanged by the perturbation. Eq. (4.34) shows that particles that flow out of the segment ($\mathbf{J}\cdot\hat{\mathbf{n}} > 0$) cause the interface to displace towards the right ($\partial_t \delta x_G > 0$), which is towards the dense phase, as expected. Similarly, particles flowing into the segment ($\mathbf{J}\cdot\hat{\mathbf{n}} < 0$) cause the interface to displace towards the dilute phase on the left ($\partial_t \delta x_G < 0$). The particle flux $\mathbf{J}\cdot\hat{\mathbf{n}}$ can either come from the adjoining bulks through the normal faces of the segment, or from the adjoining part of the interface through the lateral faces. Indeed,

as shown in appendix 4.E, Eq. (4.34) can also be written as

$$\partial_t \delta x_G(y,t) = \frac{1}{\Delta\rho}\Big(J_x(x_{\rm b}^{\rm s},t) - J_x(x_{\rm b}^{\rm f},t) + \int_{x_{\rm b}^{\rm f}}^{x_{\rm b}^{\rm s}} {\rm d}x \partial_y J_y \Big), \tag{4.35}$$

where $J_x(x_{\rm b}^{\rm s},t) - J_x(x_{\rm b}^{\rm f},t)$ represents the outflux through the normal faces, and where $\int_{x_{\rm b}^{\rm f}}^{x_{\rm b}^{\rm s}} {\rm d}x \partial_y J_y(x,y,t)$ represents the outflux through the lateral faces. As we will show in Sec. 4.7.2, a lateral flux is only present if the interfacial tension $\sigma_{\rm t}$ - that we will define in Sec. 4.7.1 - depends on the location y in the interface. Before we discuss this possibility, we first focus on the case that $\sigma_{\rm t}$ is uniform, such that fluxes tangential to the interfaces are absent.

4.7.1 Interface response in absence of tangential currents

If tangential currents are absent, it seems likely that the fluxes through the normal faces, $J_x(x_{\rm b}^{\rm f})$ and $J_x(x_{\rm b}^{\rm f})$, are related to the change in center-of-mass position of the interface segment. Indeed, if one approximates the interface segment as a rigid object of $n \equiv \int_{S_{\rm segm}} {\rm d}S \rho_0(x)$ particles, then its center-of-mass velocity $\bar{v}_x \equiv \int_{S_{\rm segm}} {\rm d}S J_x/n$ equals the local velocity at the normal faces. Therefore, the fluxes through these faces are given by $J_x(x_{\rm b}^{\rm f}) = \rho_{\rm f}\bar{v}_x$ and $J_x(x_{\rm b}^{\rm s}) = \rho_{\rm s}\bar{v}_x$, and Eq. (4.35) becomes

$$\partial_t h(y,t) = \bar{v}_x = \frac{1}{n\gamma}\int_{S_{\rm segm}} {\rm d}S \gamma J_x. \tag{4.36}$$

Here we replaced $\delta x_G(y,t)$ by $h(y,t)$, because the assumption that the interface consists of rigid segments implies that the density profile remains of the form (4.32), but with a shift $h(y,t)$ that now depends on time and that equals the change in Gibbs dividing surface $\delta x_G(y,t)$. Eq. (4.36) shows that the change in the perturbation $\partial_t h(y,t)$ is proportional to the particle flux J_x - and thereby to the frictional force $f_x^f = -\gamma J_x$ - integrated over the interface segment. According to the force balance (4.19), any change in $h(y,t)$ thus results from the sum of the non-frictional forces integrated over the segment, which is an intuitive result.

We now calculate the integral $\int_{S_{\rm segm}} {\rm d}S\gamma J_x$. Integrating the force balance (4.19) over the interface segment gives

$$\int_{S_{\rm segm}} {\rm d}S \gamma J_\alpha = -\int_{\delta S_{\rm segm}} {\rm d}\ell P_{\alpha\beta}^{\rm tot} n_\beta + \frac{\gamma}{D_r}\int_{S_{\rm segm}} {\rm d}S (\partial_x v_0)\mathcal{J}_{x\alpha}^m, \tag{4.37}$$

where we used that $\partial_y v_0 = 0$. In order to obtain a more useful form, we slightly rewrite Eq. (4.37). We make use of the fact that the undeformed interface satisfies the force balance

$$0 = -\partial_\alpha P_{0,xx}^{\rm tot} + \frac{\gamma}{D_r}(\partial_x v_0)\mathcal{J}_{0,x\alpha}^m, \tag{4.38}$$

where $P_{0,\alpha\beta}^{\rm tot}$ is the total normal pressure of the unperturbed system, and $\mathcal{J}_{0,\alpha\beta}^m$ its orientation current. To see that Eq. (4.38) is indeed correct, note that for $\alpha = x$ it

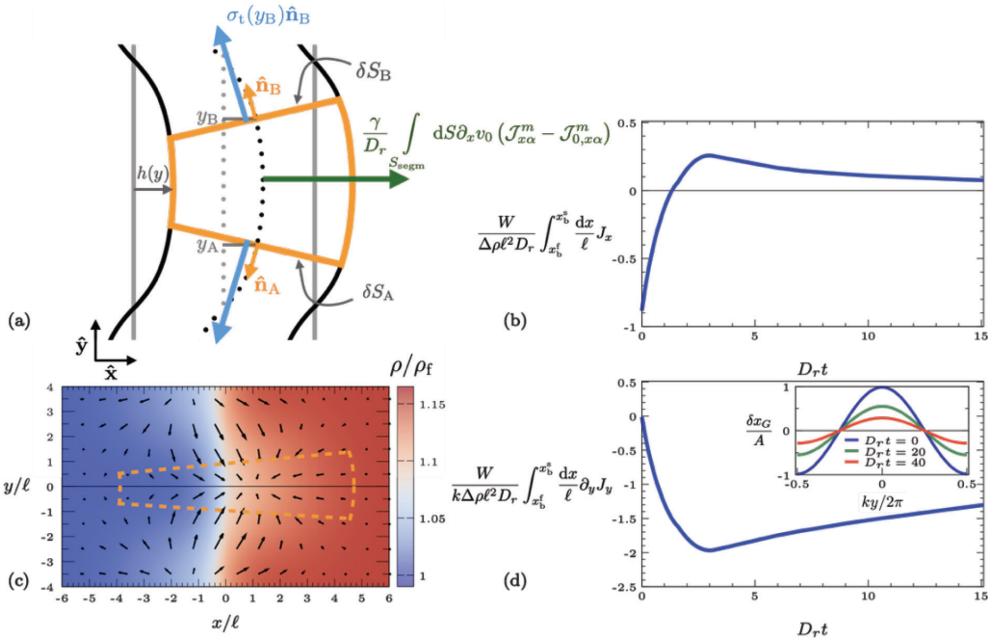

Figure 4.6: (a) Sketch of the forces that act on a perturbed interface segment. The interface, in black, is perturbed by the function $h(y)$ from its original position in gray. Marked orange is an interface segment whose lower (upper) boundary δS_A (δS_B) is located at $y = y_A$ ($y = y_B$) and has normal vector $\hat{\mathbf{n}}_A$ ($\hat{\mathbf{n}}_B$). Blue arrows denote the tensile forces $\sigma_t(y_A)\hat{\mathbf{n}}_A$ and $\sigma_t(y_B)\hat{\mathbf{n}}_B$ that act on the upper and lower boundary (the sketch assumes $\sigma_t(y_{A/B}) > 0$). Green arrow denotes the force due to the motility gradient, $\gamma/D_r\partial_x v_0(\mathcal{J}^m_{x\alpha} - \mathcal{J}^m_{0,x\alpha})$, integrated over the segment. In (b-d) we specialize to an interface segment centered at $y = 0$, where $h(y)$ is positive and maximal. (b) The normal flux J_x integrated over the segment is, after an initial transient, positive. This *seems* to make the perturbation grow. (c) Typical snapshot of an interface perturbation. Colors indicate density, arrows indicate particle flux. A tangential current through the interface increases the number of particles in the orange segment. (d) The tangential derivative of this current, $\partial_y J_y$, integrated over the segment, is negative. As a result, (inset) the interface position, represented by the offset in Gibbs dividing surface $\delta x_G(y,t)$, is restored over time. Parameter values used for (b) and (d) are $\mathrm{Pe} = 1$, $a = 1$, $W = 10$, $\mathcal{A} = 0.1$, and $k = 2\pi/40$, while for (c) $\mathrm{Pe} = 1$, $a = 1$, $W = 0.5$, $\mathcal{A} = 2$, $k = 2\pi/8$ and $D_r t = 0.8$. The values for (c) do not satisfy the assumptions that the perturbation and spatial gradients are small, but these values are chosen only to obtain a snapshot for which the perturbation and tangential currents are visible with the naked eye.

reduces to Eq. (4.20), while for $\alpha = y$ it is trivially satisfied since $\partial_y P^{\rm tot}_{0,xx} = 0$ and $\mathcal{J}^m_{0,xy} = 0$. We integrate Eq. (4.38) over $S_{\rm segm}$, and rewrite the pressure term by using $-\partial_\alpha P^{\rm tot}_{0,xx} = -\partial_\beta (P^{\rm tot}_{0,xx}\delta_{\alpha\beta})$ and Gauss' theorem. The result we subtract from Eq. (4.37), which yields

$$\int\limits_{S_{\rm segm}} {\rm d}S \gamma J_\alpha = -\int\limits_{\delta S_{\rm segm}} {\rm d}\ell \left(P^{\rm tot}_{\alpha\beta} - P^{\rm tot}_{0,xx}\delta_{\alpha\beta}\right) n_\beta + \frac{\gamma}{D_r}\int\limits_{S_{\rm segm}} {\rm d}S (\partial_x v_0)\left(\mathcal{J}^m_{x\alpha} - \mathcal{J}^m_{0,x\alpha}\right). \quad (4.39)$$

The integral over the pressure terms in Eq. (4.42) does not contribute on the left and right boundaries of the segment, because these boundaries are assumed to lie in the unperturbed isotropic bulk systems, where $P^{\rm tot}_{\alpha\beta} = P^{\rm tot}_{0,xx}\delta_{\alpha\beta}$. Therefore, the integral only contributes on the lower and upper boundary. These boundaries are located at $y = y_{\rm A}$ and $y = y_{\rm B}$, and denoted by $\delta S_{\rm A}$ and $\delta S_{\rm B}$, respectively (see Fig. 4.6(a)). Their contributions are assumed to point in the direction of their normal vectors $\hat{\mathbf{n}}_{\rm A}$ and $\hat{\mathbf{n}}_{\rm B}$, such that

$$\int_{\delta S_{\rm A}} {\rm d}\ell \left(P^{\rm tot}_{0,xx}\delta_{\alpha\beta} - P^{\rm tot}_{\alpha\beta}\right) n_\beta \equiv \sigma_{\rm t}(y_{\rm A}, t)\hat{\mathbf{n}}_{\rm A} \quad (4.40)$$

for the lower boundary, and the same expression holds for the upper boundary with the subscripts 'A' replaced by 'B'. Physically, the contribution of Eq. (4.40) represents a tensile force in the interface. Thereby, it defines our second extension of the equilibrium concept of interfacial tension: $\sigma_{\rm t}$. The subscript 't' is for 'tension'. Since the perturbation $h(y,t)$ is assumed to be small, the leading order contribution to the tension $\sigma_{\rm t}$ follows from Eq. (4.40) evaluated for the unperturbed interface. For the unperturbed interface, $\mathbf{P}^{\rm tot}$ is diagonal and $\hat{\mathbf{n}}_{\rm A} = -\hat{\mathbf{y}}$, such that the tension $\sigma_{\rm t}$ reduces to the quantity σ_0 of Eq. (4.27). Note that σ_0 does not depend on y (or time). Additionally, the tension $\sigma_{\rm t}$ can have subleading contributions that depend on the perturbation $h(y,t)$ (or its derivatives), and that we denote by $\sigma_1(y,t)$. Therefore, the tensile force

$$\sigma_{\rm t}(y,t) = \sigma_0 + \sigma_1(y,t) \quad (4.41)$$

can only depend on the position in the interface y through $\sigma_1(y,t)$. With Eq. (4.40) - and its equivalent for the upper boundary - the integrated flux (4.39) becomes

$$\int_{S_{\rm segm}} {\rm d}S \gamma J_\alpha = \sigma_{\rm t}(y_{\rm A},t)\hat{\mathbf{n}}_{\rm A} + \sigma_{\rm t}(y_{\rm B},t)\hat{\mathbf{n}}_{\rm B} + \frac{\gamma}{D_r}\int_{S_{\rm segm}} {\rm d}S (\partial_x v_0)\left(\mathcal{J}^m_{x\alpha} - \mathcal{J}^m_{0,x\alpha}\right). \quad (4.42)$$

Before we address the right-hand side terms of Eq. (4.42) for our system, we discuss them for a case that is more familiar: a phase coexistence of interacting particles with homogeneous propulsion speed. This includes equilibrium phase coexistences (for which the propulsion speed is zero), but also MIPS. Since $\partial_x v_0 = 0$ for these systems, the final term in Eq. (4.42) vanishes. Moreover, the dominant contribution to $\sigma_{\rm t}$ is simply σ_0, which, as discussed in section 4.6, equals the mechanical interfacial tension. Hence, $\sigma_{\rm t} = \sigma_0 = \sigma_{\rm m}$, such that the two definitions for the interfacial tension $\sigma_{\rm t}$ and $\sigma_{\rm m}$ coincide (for an interface with small spatial gradients). Since the directions of the tensile forces in

Eq. (4.42) add up as $\hat{\mathbf{n}}_\mathrm{A} + \hat{\mathbf{n}}_\mathrm{B} = h''(y_\mathrm{A}, t)\delta y\hat{\mathbf{x}}$ (see appendix 4.F), the change in interface location (4.36) reads

$$\partial_t h(y,t) = \frac{\delta y}{n\gamma}\sigma_0 h''(y,t). \tag{4.43}$$

We use primes to denote derivatives with respect to y, i.e. $h''(y,t) \equiv \partial^2 h/(\partial y)^2$. Since, $h''(y,t)$ has the opposite sign of our perturbation $h(y,t)$ of Eq. (4.33), Eq. (4.43) shows that a positive interfacial tension σ_0 results in a particle flux that restores the original interface, whereas a negative interfacial tension makes the perturbation grow. Hence, for interfaces of interacting particles with homogeneous propulsion speed, under the assumption that there are no tangential currents, the sign of the interfacial tension controls whether small perturbations grow or shrink.

For MIPS, the finding that $\sigma_0 < 0$ [25, 26] then seems to imply that the interface is unstable. However, Ref. [25] shows that significant tangential currents *do* exist in the interface. Therefore, the term $\int_{x_\mathrm{b}^\mathrm{f}}^{x_\mathrm{b}^\mathrm{s}} \mathrm{d}x\partial_y J_y(x,y,t)$ in Eq. (4.35) cannot be neglected, and Eq. (4.43) is not valid. We discuss this term in Sec. 4.7.2, and discuss its implications for MIPS in Sec. 4.7.3.

We now discuss the terms on the right hand side of Eq. (4.42) for our active ideal gas with position dependent propulsion speed. First, we discuss the tensile forces. In Sec. 4.6.1, we saw that the unperturbed interface gave rise to a tension σ_0 that was negative. However, as shown in appendix 4.F, an interface with small spatial gradients has $\sigma_0 = 0$. Therefore, the leading contribution to the tension σ_t comes from σ_1, which appendix 4.F derives to be

$$\sigma_\mathrm{t}(y,t) = \sigma_1(y,t) = \mathcal{M}h(y,t). \tag{4.44}$$

Here $\mathcal{M}$ is a positive constant whose value is given in the appendix. Since Eq. (4.44) is linear in the perturbation h, the sum $\sigma_\mathrm{t}(y_\mathrm{A},t)\hat{\mathbf{n}}_\mathrm{A} + \sigma_\mathrm{t}(y_\mathrm{B},t)\hat{\mathbf{n}}_\mathrm{B}$ yields a normal component that is quadratic in the perturbation (see appendix 4.F). Therefore, the dominant contribution to the integrated normal flux of Eq. (4.42) comes from the $\partial_x v_0$-term. As appendix 4.F shows, this term is given by

$$\frac{\gamma}{D_r}\int_{S_\mathrm{segm}} \mathrm{d}S(\partial_x v_0)\left(\mathcal{J}^m_{xx} - \mathcal{J}^m_{0,xx}\right) = \mathcal{K}h(y,t)\delta y. \tag{4.45}$$

Here $\mathcal{K}$ is again a positive constant whose value is given in the appendix. Thus, as sketched in Fig. 4.6(a), the $\partial_x v_0$-term plays the role of a body force that acts in the same direction as the perturbation. Inserting Eq. (4.45) into Eqs. (4.42) and (4.36) now yields

$$\partial_t h(y,t) = \frac{\mathcal{K}\delta y}{n\gamma}h(y,t), \tag{4.46}$$

which predicts that the perturbation $h(y,t)$ grows! Thus, the assumption of having rigid interface segments predicts perturbations that grow, both for MIPS and for the active ideal gas considered here.

To check this prediction, we solved the time evolution of a small interface perturbation

numerically. The time evolution of the normal flux J_x, integrated over an interface segment with $h(y,t) > 0$, is shown in Fig. 4.6(b). After an initial transient - that corresponds to the time it takes the fast variables $\mathbf{m}$, $\mathbf{S}$, etc. to adapt to the slow density profile ρ - the integrated flux $\int_{x_\mathrm{b}^\mathrm{f}}^{x_\mathrm{b}^\mathrm{s}} \mathrm{d}x J_x$ is indeed positive. Nonetheless, the interface displacement $\delta x_G(y,t)$, shown in the inset of Fig. 4.6(d), *decays* in time. The reason for this apparent discrepancy is, again, that tangential currents *are* present in the interface. Therefore, Eq. (4.46) is not valid, and the effect of the term $\int_{x_\mathrm{b}^\mathrm{f}}^{x_\mathrm{b}^\mathrm{s}} \mathrm{d}x \partial_y J_y(x,y,t)$ in Eq. (4.35) has to be taken into account. We discuss this term now.

4.7.2 Interface response in the presence of tangential currents

Tangential currents through the interface are generated by spatial gradients in the interfacial tension $\sigma_\mathrm{t}(y,t)$. Indeed, appendix 4.F derives that the transverse flux integrated over a cross section through the interface is given by

$$\int_{x_\mathrm{b}^\mathrm{f}}^{x_\mathrm{b}^\mathrm{s}} \mathrm{d}x J_y(x,y,t) = \frac{1}{\gamma}\sigma_\mathrm{t}'(y,t). \tag{4.47}$$

Eq. (4.47) shows that a tangential current forms from regions of low to regions of high interfacial tension. This effect is known as the Marangoni effect [33]. Usually, the gradients in the tension σ_t are caused by gradients in the tension σ_0 of the unperturbed interface, due to e.g. a gradient in temperature or in concentration. In our case, however, $\sigma_0 = 0$, and the gradients come instead from the higher order terms $\sigma_1(y,t)$. Indeed, Eq. (4.44) shows that $\sigma_\mathrm{t} = \sigma_1 \propto h$, which means that the transverse flux is directed towards maxima of the perturbation h. This is confirmed by Fig. 4.6(c), which shows a typical snapshot of the perturbed interface. The orange box in the figure marks an interface segment where $h(y)$ has a maximum, and, indeed, particles flow through the lateral faces into the segment. This flux increases the number of particles in the segment, and consequently shifts the interface location δx_G towards the left. Thereby, the tangential particle flux diminishes the perturbation!

Moreover, the snapshot shows that the fluxes through the normal faces are zero, i.e. $J_x(x_\mathrm{b}^\mathrm{f}) = J_x(x_\mathrm{b}^\mathrm{s}) = 0$. The reason is that for our ideal gas the effect of the density perturbation remains localized in the interface. Therefore, the transverse currents are the *only* contribution to the change in interface location $\partial_t \delta x_G$, and Eq. (4.35) simplifies to

$$\partial_t \delta x_G(y,t) = \frac{1}{\Delta\rho}\int_{x_\mathrm{b}^\mathrm{f}}^{x_\mathrm{b}^\mathrm{s}} \mathrm{d}x \partial_y J_y(x,y,t), \tag{4.48}$$

Fig. 4.6(d) shows the time evolution of $\int_{x_\mathrm{b}^\mathrm{f}}^{x_\mathrm{b}^\mathrm{s}} \mathrm{d}x \partial_y J_y(x,y,t)/\Delta\rho$ for the same interface segment. Clearly, this term is negative for all times, which confirms that the transverse flux is the restoring mechanism for our interface perturbation.

Finally, we can use Eqs. (4.48), (4.47), and (4.44) to find that our interface location

changes initially [j] according to

$$\partial_t \delta x_G(y, t = 0) = \frac{\mathcal{M}}{\delta \rho \gamma} h''(y). \tag{4.49}$$

Since $h''(y)$ has the opposite sign of the perturbation $h(y)$ of Eq. (4.33), Eq. (4.49) again shows that the perturbation initially shrinks.

4.7.3 Discussion

From Eq. (4.35) we distinguished two mechanisms by which the displacement $\delta x_G(y, t)$ of an interface segment can change: either by a net flux through the normal faces of the segment, or by a net flux through its lateral faces. Subsequently, we argued that for 'rigid' interface segments only the normal fluxes are important - where we had in mind the case of a classic solid-gas or liquid-gas interface, for which the Marangoni-effect plays no role. Then, we argued that for our active ideal gas only the tangential fluxes are important, and that they are entirely caused by a Marangoni-like effect.

Actually, however, the distinction between the two effects is somewhat arbitrary. The distinction depends on where one locates the left and right boundary of the interface segment: where does the interface end and the bulk begin? A proper treatment would probably define these boundaries by a threshold in density. For example, one could identify the interface as the region where the density ρ satisfies $\rho_{\mathrm{f}} + c\Delta\rho < \rho < \rho_{\mathrm{s}} - c\Delta\rho$, for, say, $c = 0.05$. Then indeed for a classic liquid-gas interface the flux through the normal faces should dominate over the flux through the lateral faces. In contrast, if instead one takes the boundaries of the segment extremely far into the bulks, then certainly the normal fluxes through these faces will be zero, and any in- or outflux will be through the (very long) lateral faces. In fact, for the classic liquid-gas coexistence one expects that the restoring movement of the interface is accompanied by a 'circular' particle flux in the bulk regions next to the interface, whereby particles in the dense phase move from interface bulges to interface depressions, while particles in the dilute phase move in the opposite direction. Locating the normal faces of the segment far into the bulks would (partly) identify this circular flux as a tangential flux through the interface, and thus, by Eq. (4.47), as the Marangoni-effect. Therefore, this choice of interface boundaries does not provide a proper definition of the interface segment.

Yet, in Eq. (4.48) we used precisely this definition for our interface segment. However, while a proper treatment is beyond the scope of this chapter, we point out that the tangential current is clearly different from the aforementioned 'circular motion', as it has the same direction on both sides of the interface (see Fig. 4.6(c)). Moreover, the same figure shows that the tangential currents in the interface are clearly larger than any normal currents. Therefore, it is safe to say that these currents are indeed generated by the Marangoni effect.

Finally, we discuss the stabilizing mechanism for MIPS. Patch et al. [25] show that significant tangential currents are present in the MIPS interface. They substantiate the claim

[j] Without the assumption of having rigid interface segments, Eq. (4.44) is only valid at $t = 0$, because at later times the density profile is not anymore of the form (4.32).

that these currents are due to a Marangoni-like effect, and that they restore the perturbed interface to its original state. The facts that our perturbed interface shows all of these features and that our interface qualitatively resembles the MIPS interface (see Sec. 4.4) support the idea that this is indeed the stabilizing mechanism.

Lee [29] argues that the stability of the MIPS interface is caused by the fact that particles in an interface bulge can escape more easily into the dilute phase than particles in an interface depression. He relates this effect to an effective interfacial tension that is positive and constant throughout the interface, and therefore different from the interfacial tensions that are considered here and in [25]. Because it is likely that escaping particles give rise to tangential currents, the different proposed stability mechanisms are likely related, yet at this point we do not see more precisely how Lee's argument fits into the framework presented here.

Hermann et al. [31] also propose that the stability is governed by an interfacial tension that is non-negative. Their definition of the interfacial tension is based on the structural force components, which are defined as minus the sum of the ideal diffusive force and the adiabatic[k] interaction force components. Since *all* forces - including the propulsion force - play an important role in the stability analysis presented in this section, at this point we do not see how the interfacial tension presented in [31] and the stability analysis presented here can be related.

4.8 Conclusions

We studied the interface formed by an active ideal gas in two half-spaces with different propulsion speeds. We characterized the interfacial profiles of density, polarization, and nematic order, and identified the relevant forces and pressures. We showed that the total pressure differs between the two bulks, but that the force balance is nonetheless satisfied due to an additional 'body force' that appears because the propulsion speed depends on position. Moreover, we proposed two ways to extend the equilibrium concept of interfacial tension to active systems. The first definition, which we called the mechanical interfacial tension σ_{m}, represents the work required to deform the system in a way that changes the interfacial area but not the system volume. The second definition, σ_{t}, is the tensile force in the interface.

We found that the system considered here shares important qualitative features with MIPS. Firstly, the interface has polarization towards the dense side, an effect which does thus not require having particle interactions, nor particle anisotropy. Secondly, σ_0, the anisotropy of the total pressure tensor integrated through the interface, is negative - an effect that we explained microscopically. While for MIPS $\sigma_0 = \sigma_{\mathrm{m}}$ forms the full mechanical interfacial tension, in our case the additional force term also contributes and, for $\mathrm{Pe} \ll 1$, precisely cancels the contribution from σ_0, such that $\sigma_{\mathrm{m}} = 0$. Thirdly, an analysis of an interface perturbation, under the assumption of small spatial gradients,

[k]Somewhat confusingly, in this context the term 'adiabatic' does not refer to the assumption made in the beginning of Sec. 4.7, i.e. that the higher angular moments are adiabatically enslaved to the density. Instead, the adiabatic interaction forces are the interaction force components that can be written as the gradient of a free energy derivative in the Density Functional Theory framework [145].

shows that the normal force on an interface segment acts in the same direction as the perturbation. While the responsible force is different - for MIPS it is the tension $\sigma_{\mathrm{t}} = \sigma_{\mathrm{m}} = \sigma_0$, which is negative, while for our model it is the additional body force - the result is the same, and the analysis seems to imply that the perturbation *grows*, at least at first sight.

Nonetheless, we showed that the interface of our system is stable. The reason is that the tension $\sigma_{\mathrm{t}}(y)$ depends on the position y in the interface. This leads to the Marangoni effect, which causes tangential currents through the interface that restore the interface to its original state. This finding supports the idea of Patch et al. [25] that a Marangoni-like effect similarly stabilizes the interface of MIPS.

4.9 Acknowledgements

This chapter is part of a collaboration with Liesbeth Janssen and René van Roij. While all the presented results have been obtained by the author of this thesis, Liesbeth Janssen performed particle-based computer simulations on the same system (whose results are not shown), and has been involved in the design and structuring of the presented research. René van Roij helped with critically examining all results and identifying future directions throughout the research process.

Appendices

Appendix 4.A Derivation of analytical solutions

In this appendix, we derive the analytical solution given in the main text, i.e. we derive Eqs. (4.12) and (4.13). The approach is to solve the moment equations (4.7) and (4.8) by using the closure $S_{\alpha\beta} = 0$. We consider the region far from any walls, where $V(\mathbf{r}) = 0$, and where there is invariance in the y-direction. Furthermore, we consider a steady state, such that $\partial_t \rho = \partial_t m_x = 0$.

First, we take the propulsion speed to be a constant, i.e. $v_0(x) = v_0$, which holds true for the regions $x < 0$ and $x > 0$ separately. In order to write the equations in dimensionless form, in this appendix we use a definition for the Péclet number slightly different from the main text, namely $\mathrm{Pe} \equiv v_0/\sqrt{D_t D_r}$. Whenever we wish to specify the activity of the fast or slow region explicitly, we shall use $\mathrm{Pe}_{\mathrm{f/s}} \equiv v_{\mathrm{f/s}}/\sqrt{D_t D_r}$. Eqs. (4.12) and (4.13) of the main text then take the form

$$0 = -\ell\partial_x \left(\mathrm{Pe} m_x - \ell\partial_x \rho\right), \tag{4.50a}$$

$$0 = -\ell\partial_x \left(\mathrm{Pe}\rho/2 - \ell\partial_x m_x\right) - m_x, \tag{4.50b}$$

which are to be solved for $\rho(x)$ and $m_x(x)$. Eq. (4.50a) implies that the term in between brackets, which represents the horizontal particle flux, is constant. Since there can be no constant particle flux in steady state due to the presence of walls around the system, this constant equals zero. Therefore,

$$\mathrm{Pe} m_x - \ell\partial_x \rho = 0. \tag{4.51}$$

Eq. (4.51) can be used to substitute $\ell\partial_x\rho$ in Eq. (4.50b), which yields

$$0 = \partial_{xx} m_x - \lambda^{-2} m_x, \tag{4.52}$$

where $\lambda \equiv \ell/(1 + \mathrm{Pe}^2/2)^{1/2}$. Eq. (4.52) is solved by

$$m_x(x) = Be^{x/\lambda} + Ce^{-x/\lambda}, \tag{4.53}$$

where B and C are integration constants. Solution (4.53), in turn, can be substituted in Eq. (4.51), which can subsequently be solved for the density as

$$\rho(x) = \rho_0 + B\,\mathrm{Pe}\frac{\lambda}{\ell}e^{-x/\lambda} - C\,\mathrm{Pe}\frac{\lambda}{\ell}e^{-x/\lambda}, \tag{4.54}$$

where ρ_0 is an additional integration constant.

The solutions (4.53) and (4.54) hold for the fast region ($x < 0$) and the slow region ($x > 0$) separately. We now make this explicit by writing

$$\rho(x) = \begin{cases} \tilde{\rho}_\mathrm{f} + B_\mathrm{f}\,\mathrm{Pe}_\mathrm{f}\dfrac{\lambda_\mathrm{f}}{\ell}e^{x/\lambda_\mathrm{f}} - C_\mathrm{f}\,\mathrm{Pe}_\mathrm{f}\dfrac{\lambda_\mathrm{f}}{\ell}e^{-x/\lambda_\mathrm{f}} & \text{for } x < 0, \\ \rho_\mathrm{s} + B_\mathrm{s}\,\mathrm{Pe}_\mathrm{s}\dfrac{\lambda_\mathrm{s}}{\ell}e^{x/\lambda_\mathrm{s}} - C_\mathrm{s}\,\mathrm{Pe}_\mathrm{s}\dfrac{\lambda_\mathrm{s}}{\ell}e^{-x/\lambda_\mathrm{s}} & \text{for } x > 0, \end{cases} \tag{4.55}$$

and

$$m_x(x) = \begin{cases} B_\mathrm{f}e^{x/\lambda_\mathrm{f}} + C_\mathrm{f}e^{-x/\lambda_\mathrm{f}} & \text{for } x < 0, \\ B_\mathrm{s}e^{x/\lambda_\mathrm{s}} + C_\mathrm{s}e^{-x/\lambda_\mathrm{s}} & \text{for } x > 0. \end{cases} \tag{4.56}$$

The solutions (4.55) and (4.56) contain six integration constants, namely $\tilde{\rho}_\mathrm{f}$, ρ_s, B_f, B_s, C_f, and C_s. These are to be determined from boundary conditions. First, we apply boundary condition 1 of the main text, which translates to $m_x(-\infty) = 0$ and $\rho(-\infty) = \rho_\mathrm{f}$. This yields $C_\mathrm{f} = 0$ and $\tilde{\rho}_\mathrm{f} = \rho_\mathrm{f}$. Next, we apply boundary condition 2 of the main text, which translates to $m_x(\infty) = 0$. This yields $B_\mathrm{s} = 0$. The three remaining constants, ρ_s, B_f, and C_s, are to be determined from the requirements that the density $\rho(x)$, the polarization $m_x(x)$, and orientation current $\mathcal{J}^m_{xx}(x)$ all need to be continuous at $x = 0$. The continuity requirement for the polarization yields $B_\mathrm{f} = C_\mathrm{s} \equiv A$. Using the values obtained so far for the integration constants in Eqs. (4.55) and (4.56) yields the solutions (4.12) and (4.13) given in the main text. The values for the constants ρ_s and A follow from the two remaining continuity conditions. The result for ρ_s is given by Eq. (4.14), whereas

$$A = \frac{c_\mathrm{ff}}{c_\mathrm{ff}c_\mathrm{ss} + c_\mathrm{fs}^2}\frac{\mathrm{Pe}_\mathrm{f} - \mathrm{Pe}_\mathrm{s}}{2}\rho_\mathrm{f}, \tag{4.57}$$

where $c_\mathrm{ff} \equiv (1 + \mathrm{Pe}_\mathrm{f}^2/2)^{1/2} = \ell/\lambda_\mathrm{f}$, $c_\mathrm{ss} \equiv (1 + \mathrm{Pe}_\mathrm{s}^2/2)^{1/2} = \ell/\lambda_\mathrm{s}$, and $c_\mathrm{fs} \equiv (1 + \mathrm{Pe_f Pe_s}/2)^{1/2}$.

Appendix 4.B Derivation of the mechanical interfacial tension

In this appendix, we derive the mechanical interfacial tension σ_m as given by Eq. (4.24) in the main text. In order to do so, the essential idea, explained in section 4.6, is to calculate the work required for a constant-area box deformation, and subsequently apply Eq. (4.21). Actually, the situation is a bit more involved than outlined in the main text, for two reasons. Firstly, our system contains two bulks with *different* pressures, and therefore the proper box deformation is one that keeps the areas of *both* bulks constant. Secondly, in Eq. (4.21) we ignored the fact that the required box deformation also modifies the lengths of the container walls, and that these have line tensions associated with them as well. Again, we speak of *line* tensions rather than surface tensions because our system is 2D instead of 3D. Consequently, the box deformation that keeps both bulk areas constant requires the work

$$\mathrm{d}W = \sigma_\mathrm{m}\mathrm{d}L_y + \sigma_\mathrm{f}\mathrm{d}L_\mathrm{f} + \sigma_\mathrm{s}\mathrm{d}L_\mathrm{s}, \tag{4.58}$$

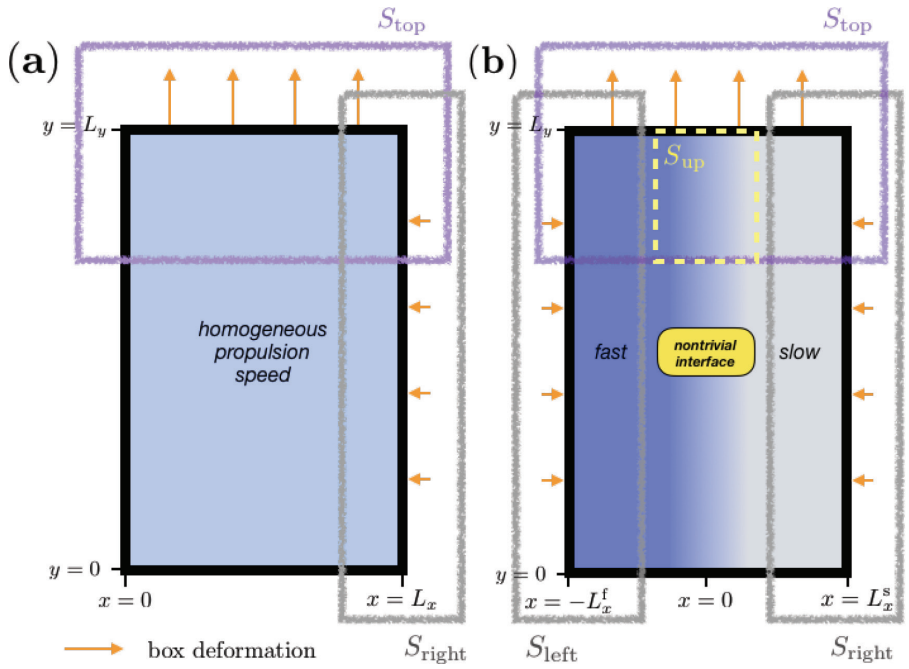

Figure 4.B.1: Illustration of the setting and box deformation considered in appendix 4.B (a) for the calculation of the wall line tension, and (b) for the calculation of the interfacial tension. It is understood that the integration areas S_{left}, S_{right} and S_{top} cross the interior of the system far from the wall that they enclose, i.e. at a bulk value of the coordinate normal to that wall.

where $\mathrm{d}L_{\text{f/s}}$ is the increase in the length of the wall that surrounds the fast/slow bulk, and where $\sigma_{\text{f/s}}$ is the associated line tension. Our strategy is as folows. First, we determine the wall line tensions $\sigma_{\text{s/f}}$, by calculating the work required for a constant-area box deformation of a *homogeneous* system, with single propulsion speed and single bulk density. Then, we calculate the work required for the box deformation of our system with a fast *and* slow bulk, and use Eq. (4.58) to obtain the interfacial tension σ_{m}.

To determine the wall line tensions $\sigma_{\text{s/f}}$, we consider a steady state of an active ideal gas with a uniform propulsion speed in a rectangular box. This system is depicted in Fig. 4.B.1(a). It forms a single, homogeneous bulk, that we characterize by the coordinate $(x_{\text{b}}, y_{\text{b}})$. The walls are located at $x = 0$, $x = L_x$, $y = 0$ and $y = L_y$, and they are assumed to be identical, in the sense that they all exert the same external potential on the particles. The box deformation that we consider is one that shifts the right wall to $x = L_x + \mathrm{d}L_x$ and the top wall to $y = L_y + \mathrm{d}L_y$, but under the restriction that system area remains constant, i.e. that

$$L_x \mathrm{d}L_y + L_y \mathrm{d}L_x = 0. \tag{4.59}$$

This implies that if $\mathrm{d}L_y > 0$, such as in Fig. 4.B.1(a), then $\mathrm{d}L_x < 0$. The line tension σ_w of the wall is defined as

$$\mathrm{d}W = \sigma_\mathrm{w}\mathrm{d}L_\mathrm{w}, \tag{4.60}$$

where $\mathrm{d}W$ is the work required for the box deformation, and where

$$\mathrm{d}L_\mathrm{w} = 2(\mathrm{d}L_x + \mathrm{d}L_y) \tag{4.61}$$

is the change in total length of wall that surrounds the system. We first calculate $\mathrm{d}W$, and then obtain the line tension σ_w of the wall via Eq. (4.60).

$$\mathrm{d}W = -(F_\mathrm{right}\mathrm{d}L_x + F_\mathrm{top}\mathrm{d}L_y). \tag{4.62}$$

Here, F_right is the total horizontal force exerted by the system onto the right wall, and F_top the total force exerted onto the top wall. We first calculate F_right. Note that only particles in the vicinity of the right wall contribute to F_right, and that all these particles are contained in S_right, an area that extends from the bulk system to the right wall (see Fig. 4.B.1(a)). By Newton's third law, F_right equals minus the horizontal external force exerted onto the particles in S_right. Therefore,

$$F_\mathrm{right} = -\int\limits_{S_\mathrm{right}} \mathrm{d}S f_x^e(x,y) \overset{(4.19)}{=} -\int\limits_{S_\mathrm{right}} \mathrm{d}S \partial_\beta P_{\beta x}^\mathrm{tot}(x,y) = -\int\limits_{\delta S_\mathrm{right}} \mathrm{d}\ell P_{\beta x}^\mathrm{tot} n_\beta = \int\limits_0^{L_y} \mathrm{d}y P_{xx}^\mathrm{tot}(x_\mathrm{b},y). \tag{4.63}$$

For the second equality we used Gauss' theorem, for the third equality we defined δS_right to be the boundary of S_right and $\mathbf{n}$ to be an outward-pointing normal vector, and for the last equality we used that $\mathbf{P}^\mathrm{tot} = \mathbf{0}$ outside of the walls. In order to proceed, we point out that the total pressure tensor in the bulk of the system is constant and isotropic, such that $P_{xx}^\mathrm{tot}(x_\mathrm{b},y_\mathrm{b}) = P_{yy}^\mathrm{tot}(x_\mathrm{b},y_\mathrm{b}) \equiv P_\mathrm{b}^\mathrm{tot}$. The integrand in the last line of Eq. (4.63), $P_{xx}^\mathrm{tot}(x_\mathrm{b},y)$, only differs from $P_\mathrm{b}^\mathrm{tot}$ near the horizontal walls. We make this explicit by rewriting the last term of Eq. (4.63) as

$$F_\mathrm{right} = L_y P_\mathrm{b}^\mathrm{tot} - 2\int_{y_\mathrm{b}}^{L_y} \mathrm{d}y \left(P_\mathrm{b}^\mathrm{tot} - P_{xx}^\mathrm{tot}(x_\mathrm{b},y)\right), \tag{4.64}$$

where we used the top-down mirror symmetry of the system. In a completely analogous way - but using the area S_top instead of S_right - we obtain the force exerted onto the top wall as

$$F_\mathrm{top} = L_x P_\mathrm{b}^\mathrm{tot} - 2\int_{x_\mathrm{b}}^{L_x} \mathrm{d}x \left(P_\mathrm{b}^\mathrm{tot} - P_{yy}^\mathrm{tot}(x,y_\mathrm{b})\right). \tag{4.65}$$

Because the walls are assumed to be identical, and due to the symmetry of the system, the integrals that appear in Eqs. (4.64) and (4.65) are actually identical. Both represent an integral from the bulk to a wall, and can be represented as

$$\tilde{\sigma}_\mathrm{w} \equiv \int_{n_\mathrm{b}}^{L_n} \mathrm{d}n \left(P_\mathrm{b}^\mathrm{tot} - P_T^\mathrm{tot}(n)\right), \tag{4.66}$$

where $n \in \{x, y\}$ is the coordinate perpendicular to the wall, where $P_T^{\text{tot}}(n)$ is the total pressure component tangential to the wall, and where it is understood that the integration takes place away from any other walls, i.e. at a 'bulk value of the tangential coordinate'. With Eq. (4.66), inserting the forces (4.64) and (4.65) into Eq. (4.62) yields

$$\begin{aligned} \mathrm{d}W &= -P_{\mathrm{b}}^{\text{tot}} \left(L_y \mathrm{d}L_x + L_x \mathrm{d}L_y\right) + 2\tilde{\sigma}_{\mathrm{w}}(\mathrm{d}L_x + \mathrm{d}L_y) \\ &\overset{(4.59),(4.61)}{=} \tilde{\sigma}_{\mathrm{w}} \mathrm{d}L_{\mathrm{w}}. \end{aligned} \tag{4.67}$$

Comparing Eq. (4.67) with Eq. (4.60) readily shows that $\sigma_{\mathrm{w}} = \tilde{\sigma}_{\mathrm{w}}$. Therefore, we conclude that the line tension of a wall that surrounds a bulk system is given by

$$\sigma_{\mathrm{w}} = \int_{n_{\mathrm{b}}}^{L_n} \mathrm{d}n \left(P_{\mathrm{b}}^{\text{tot}} - P_T^{\text{tot}}(n)\right). \tag{4.68}$$

Evaluating Eq. (4.68) for the pressure profile $P_{\mathrm{b}}^{\text{tot}} - P_T^{\text{tot}}(n)$ next to a wall for a system with propulsion speed v_{f} yields σ_{f}, whereas evaluating the same quantity for propulsion speed v_{s} yields σ_{s}.

Next, in order to calculate the interfacial tension σ_{m}, we consider a box deformation of our original system that keeps the areas of both the fast and slow bulk constant. We recall that the horizontal walls are located at $y = 0$ and $y = y_{\mathrm{b}}$, that the interface is located at $x = 0$ and stretches vertically, and the the vertical walls are located at $x = -L_x^{\mathrm{f}}$ and $x = L_x^{\mathrm{s}}$. This setting is depicted in Fig. 4.B.1(b). The deformation shifts the top wall to $y = L_y + \mathrm{d}L_y$, the left wall to $x = -(L_x^{\mathrm{f}} + \mathrm{d}L_x^{\mathrm{f}})$, and the right wall to $x = L_x^{\mathrm{s}} + \mathrm{d}L_x^{\mathrm{s}}$. Note that in Fig. 4.B.1(b) $\mathrm{d}L_y > 0$ and $\mathrm{d}L_x^{\mathrm{f}}, \mathrm{d}L_x^{\mathrm{s}} < 0$. The requirement that the areas of the fast and slow bulks remain constant implies

$$L_y \mathrm{d}L_x^{\mathrm{f/s}} + L_x^{\mathrm{f/s}} \mathrm{d}L_y = 0. \tag{4.69}$$

The interfacial tension follows from Eq. (4.58), where

$$\mathrm{d}L_{\mathrm{f/s}} = 2\mathrm{d}L_x^{\mathrm{f/s}} + \mathrm{d}L_y \tag{4.70}$$

is the change in total length of wall that surrounds the fast/slow bulk, and where $\mathrm{d}W$ is the work required for the box deformation. This work can be calculated as

$$\mathrm{d}W = -(F_{\text{left}} \mathrm{d}L_x^{\mathrm{f}} + F_{\text{right}} \mathrm{d}L_x^{\mathrm{s}} + F_{\text{top}} \mathrm{d}L_y), \tag{4.71}$$

where $F_{\text{left/right}}$ is the magnitude of the total horizontal force exerted onto the left/right wall, and F_{top} the magnitude of the total vertical force on the top wall. We calculate these forces one by one. The integration areas S_{left}, S_{right}, and S_{top} that appear in these calculations are depicted in Fig. 4.B.1(b).

$$F_{\text{left}} = \int_{S_{\text{left}}} \mathrm{d}S f_x^e \overset{(4.19)}{=} \int_{\delta S_{\text{left}}} \mathrm{d}\ell P_{\beta x}^{\text{tot}} n_\beta = \int_0^{L_y} \mathrm{d}y P_{xx}^{\text{tot}}(x_{\mathrm{b}}^{\mathrm{f}}, y). \tag{4.72}$$

Next, in the integrand in the last line of Eq. (4.72) we add and substract the total fast bulk pressure $P_{\rm f}^{\rm tot}$. Note that the term $P_{xx}^{\rm tot}(x_{\rm b}^{\rm f}, y) - P_{\rm f}^{\rm tot}$ only contributes near the upper and horizontal walls, and that we recognize both these contributions from Eq. (4.68) as $-\sigma_{\rm f}$. The result is

$$F_{\rm left} = L_y P_{\rm f}^{\rm tot} - 2\sigma_{\rm f}. \tag{4.73}$$

In a similar way, the force on the right wall follows as

$$F_{\rm right} = L_y P_{\rm s}^{\rm tot} - 2\sigma_{\rm s}. \tag{4.74}$$

The force on the top wall can be calculated as

$$F_{\rm top} = -\int_{S_{\rm top}} {\rm d}S f_y^e \overset{(4.19)}{=} \int_{S_{\rm top}} {\rm d}S \left(-\partial_\beta P_{\beta y}^{\rm tot} + f_y^f + \frac{\gamma}{D_r}(\partial_x v_0)\mathcal{J}_{xy}^m \right). \tag{4.75}$$

As shown in appendix 4.C, the frictional force f_y^f is nonzero in the region where the interface meets the wall, but its contribution to the integral disappears. Therefore, two terms remain. The first we rewrite by similar manipulations as before, as follows.

$$-\int_{S_{\rm up}} {\rm d}S \partial_\beta P_{\beta y}^{\rm tot} = \int_{-L_x^{\rm f}}^{L_x^{\rm s}} {\rm d}x P_{yy}^{\rm tot}(x, y_{\rm b}) = \int_{-L_x^{\rm f}}^{0} {\rm d}x P_{yy}^{\rm tot}(x, y_{\rm b}) + \int_{0}^{L_x^{\rm s}} {\rm d}x P_{yy}^{\rm tot}(x, y_{\rm b}). \tag{4.76}$$

In the first integrand in the last line of Eq. (4.76) we add and substract the total fast bulk pressure $P_{\rm f}^{\rm tot}$. The term $P_{yy}^{\rm tot}(x, y_{\rm b}) - P_{\rm f}^{\rm tot}$ then contributes near the left wall, where its integral gives $-\sigma_{\rm f}$, and near the interface. In the second integrand in the last line of Eq. (4.76) we add and substract the total slow bulk pressure $P_{\rm s}^{\rm tot}$. The term $P_{yy}^{\rm tot}(x, y_{\rm b}) - P_{\rm s}^{\rm tot}$ then contributes as $-\sigma_s$ near the right wall, and additionally near the interface. The result is

$$-\int_{S_{\rm up}} {\rm d}S \partial_\beta P_{\beta y}^{\rm tot} = L_x^{\rm f} P_{\rm f}^{\rm tot} + L_x^{\rm s} P_{\rm s}^{\rm tot} - \sigma_{\rm f} - \sigma_{\rm s} - \sigma_0, \tag{4.77}$$

where we defined

$$\sigma_0 \equiv \int_{x_{\rm b}^{\rm f}}^{0} {\rm d}x \left(P_{\rm f}^{\rm tot} - P_{yy}^{\rm tot}(x, y_{\rm b}) \right) + \int_{0}^{x_{\rm b}^{\rm s}} {\rm d}x \left(P_{\rm s}^{\rm tot} - P_{yy}^{\rm tot}(x, y_{\rm b}) \right), \tag{4.78}$$

which is equivalent to Eq. (4.25) of the main text. With Eq. (4.77), Eq. (4.75) becomes

$$F_{\rm top} = L_x^{\rm f} P_{\rm f}^{\rm tot} + L_x^{\rm s} P_{\rm s}^{\rm tot} - \sigma_{\rm f} - \sigma_{\rm s} - \sigma_0 - \sigma_{\rm mg}, \tag{4.79}$$

where

$$\sigma_{\rm mg} = -\frac{\gamma}{D_r} \int_{S_{\rm up}} {\rm d}S (\partial_x v_0)\mathcal{J}_{xy}^m, \tag{4.80}$$

in accordance with Eq. (4.26). We used the fact that the integrand $(\partial_x v_0)\mathcal{J}_{xy}^m$ only contributes near the interface, and therefore only in the area $S_{\rm up} \subset S_{\rm top}$ defined in section 4.6. Inserting the expressions for the forces (4.73), (4.74) and (4.79) into Eq. (4.71) yields

$$\begin{aligned} {\rm d}W = &- P_{\rm f}^{\rm tot}(L_y {\rm d}L_x^{\rm f} + L_x^{\rm f} {\rm d}L_y) - P_{\rm s}^{\rm tot}(L_y {\rm d}L_x^{\rm s} + L_x^{\rm s} {\rm d}L_y) \\ &+ \sigma_{\rm f}(2{\rm d}L_x^{\rm f} + {\rm d}L_y) + \sigma_{\rm s}(2{\rm d}L_x^{\rm s} + {\rm d}L_y) \\ &+ \Big(\sigma_0 + \sigma_{\rm mg}\Big){\rm d}L_y, \end{aligned} \tag{4.81}$$

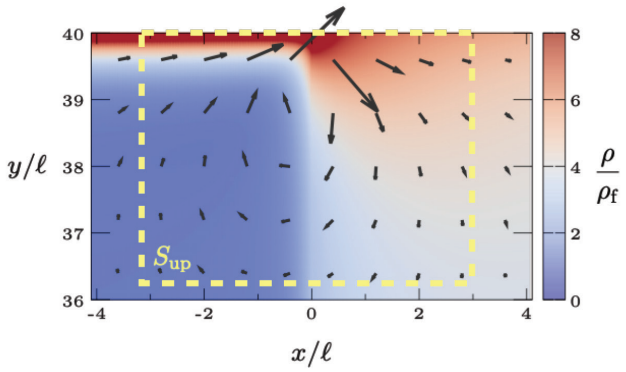

Figure 4.C.1: Same as Fig. 4.5(c), but now the arrows denote the (dimensionless) particle flux $\ell\mathbf{J}/D_r$. A nonzero, rotating flux exists in S_{up}, the region where the interface meets the wall. Although not strictly true in the figure, it is understood that S_{up} extends to x- and y-values far from the interface-wall intersection, such that $\mathbf{J} = \mathbf{0}$ at its boundary δS_{up}.

which, by Eqs. (4.69) and (4.70), simplifies to

$$\mathrm{d}W = \sigma_{\mathrm{f}}\mathrm{d}L_{\mathrm{f}} + \sigma_{\mathrm{s}}\mathrm{d}L_{\mathrm{s}} + \Big(\sigma_0 + \sigma_{\mathrm{mg}}\Big)\mathrm{d}L_y. \tag{4.82}$$

Comparing Eq. (4.82) with Eq. (4.58) shows that the interfacial tension is given by

$$\sigma_{\mathrm{m}} = \sigma_0 + \sigma_{\mathrm{mg}}, \tag{4.83}$$

which indeed is Eq. (4.24) of the main text.

Appendix 4.C Particle flux in the interface-wall region

In this appendix, we show that there is a nonzero particle current $\mathbf{J}$, and thus frictional force $\mathbf{f}^f = -\gamma\mathbf{J}$, in the region S_{up} where the interface meets the wall. Also, we show that $\int_{S_{\mathrm{up}}} \mathrm{d}S f_y^f = 0$. This integral appears in Eq. (4.75), and in Eq. (4.22) upon using the force balance (4.15).

First of all, we point out that in steady state, Eq. (4.7a) implies that $\boldsymbol{\nabla}\cdot\mathbf{J} = \mathbf{0}$. In most regions of our setting, the symmetry and boundary conditions of the problem then dictate that $\mathbf{J} = \mathbf{0}$. However, in principle, a nonzero 'rotation' $\partial_x J_y - \partial_y J_x$ is not ruled out, and indeed appears in the region S_{up}, as shown by the numerical solution depicted in Fig. 4.C.1.

To understand that $\int_{S_{\mathrm{up}}} \mathrm{d}S f_y^f = 0$ nonetheless, we first employ the fact that the current $\mathbf{J}$ is divergenceless. This implies that it can be specified by a scalar function $B(x, y)$ as $J_x = \partial_y B$ and $J_y = -\partial_x B$, just as, in hydrodynamics, a divergenceless two-dimensional flow can be specified by a stream function [146]. On δS_{up}, the boundary of S_{up}, the particle

flux $\mathbf{J}$ is zero, and therefore $\partial_x B = \partial_y B = 0$. This implies that $B(x,y) =$ constant over $\delta S_{\rm up}$. In particular, $B(x_{\rm b}^{\rm f}, y) = B(x_{\rm b}^{\rm s}, y)$ for $y_{\rm b} \leq y \leq L_y$. Then

$$\int_{S_{\rm up}} {\rm d}S J_y = -\int_{x_{\rm b}^{\rm f}}^{x_{\rm b}^{\rm s}} {\rm d}x \int_{y_{\rm b}}^{L_y} {\rm d}y \partial_x B(x,y) = -\int_{y_{\rm b}}^{L_y} {\rm d}y \left(B(x_{\rm b}^{\rm s}, y) - B(x_{\rm b}^{\rm f}, y) \right) = 0. \quad (4.84)$$

Hence also $\int_{S_{\rm up}} {\rm d}S f_y^f = 0$, which is what we wanted to prove.

Appendix 4.D Mechanical interfacial tension for small activity

In this appendix, we show that for ${\rm Pe} \ll 1$, i.e. when the closure $\mathbf{S} = \mathbf{0}$ is fully justified, the mechanical interfacial tension $\sigma_{\rm m}$ equals 0. In order to do so, we calculate the two contributions to $\sigma_{\rm m}$ in Eq. (4.24) separately. We prove that the first contribution is given by Eq. (4.28), and the second by Eq. (4.31).

We start with the first contribution σ_0, and calculate it via Eq. (4.27). The integrand in the last line of Eq. (4.27), $P_{xx}^{\rm tot}(x, y_{\rm b}) - P_{yy}^{\rm tot}(x, y_{\rm b})$, is the difference of the diagonal elements of the total pressure tensor. Since $\mathbf{P}^{\rm tot} = \mathbf{P} + \mathbf{P}^{\rm swim}$, and since the bare pressure $\mathbf{P}$ is proportional to the identity, this difference only comes from the components of the swim pressure:

$$\sigma_0 = \int_{x_{\rm b}^{\rm f}}^{x_{\rm b}^{\rm s}} {\rm d}x \left(P_{xx}^{\rm swim}(x, y_{\rm b}) - P_{yy}^{\rm swim}(x, y_{\rm b}) \right). \quad (4.85)$$

From Sec. 4.5 we know that $P_{\alpha\beta}^{\rm swim} = \mathcal{J}_{\alpha\beta}^p / D_r = \gamma v_0(x) \mathcal{J}_{\alpha\beta}^m / D_r$. Using this in Eq. (4.85) yields

$$\begin{aligned} \sigma_0 &= \frac{\gamma}{D_r} \int_{x_{\rm b}^{\rm f}}^{x_{\rm b}^{\rm s}} {\rm d}x v_0(x) \left(\mathcal{J}_{xx}^m(x, y_{\rm b}) - \mathcal{J}_{yy}^m(x, y_{\rm b}) \right) \\ &\overset{(4.8b)}{=} -\frac{k_B T}{D_r} \int_{x_{\rm b}^{\rm f}}^{x_{\rm b}^{\rm s}} {\rm d}x v_0(x) \partial_x m_x(x, y_{\rm b}). \end{aligned} \quad (4.86)$$

In the last line we used the closure $\mathbf{S} = \mathbf{0}$, as well as the fact that the integral runs through the interface far from any walls, i.e. over positions for which $V(\mathbf{r}) = 0$ and $m_y = 0$. Next, we suppress the label $y = y_{\rm b}$, and calculate the integral in the last line of Eq. (4.86).

$$\begin{aligned} \sigma_0 &= -\frac{k_B T}{D_r} \left\{ v_{\rm f} \int_{x_{\rm b}^{\rm f}}^{0} {\rm d}x \partial_x m_x(x) + v_{\rm s} \int_{0}^{x_{\rm b}^{\rm s}} {\rm d}x \partial_x m_x(x) \right\} \\ &= -\frac{k_B T}{D_r} (v_{\rm f} - v_{\rm s}) m_x(0), \end{aligned} \quad (4.87)$$

where in the last line we used that $m_x(x_{\rm b}^{\rm f}) = m_x(x_{\rm b}^{\rm s}) = 0$. Upon using $v_{\rm s} = v_{\rm f}/(1+a)$, $v_{\rm f} = \sqrt{D_t D_r}{\rm Pe}$, and $\ell = \sqrt{D_t / D_r}$, Eq. (4.87) indeed becomes Eq. (4.28) of the main text.

Next, we calculate the second contribution $\sigma_{\rm mg}$.

$$\begin{aligned}\sigma_{\rm mg} &\overset{(4.26)}{=} -\frac{\gamma}{D_r}\int_{S_{\rm up}} {\rm d}S(\partial_x v_0)(x)\mathcal{J}^m_{xy}(x,y)\\ &\overset{(4.3),(4.8b)}{=} -\frac{k_BT}{D_r}\int_{x_{\rm b}^{\rm f}}^{x_{\rm b}^{\rm s}}{\rm d}x\int_{y_{\rm b}}^{L_y}{\rm d}y(v_{\rm f}-v_{\rm s})\delta(x)\partial_x m_y(x,y)\\ &= -\frac{k_BT}{D_r}(v_{\rm f}-v_{\rm s})\int_{y_{\rm b}}^{L_y}{\rm d}y\partial_x m_y(0,y). \end{aligned} \tag{4.88}$$

At this point, it seems that, in order to calculate the integral in the last line of Eq. (4.88), one needs the full solution of the polarization $m_y(x,y)$ near the horizontal wall - which we do not have analytically. However, it turns out that is sufficient to only know the interfacial profile far from any walls (i.e., the solution for $x_{\rm b}^{\rm f} < x < x_{\rm b}^{\rm s}$ at fixed $y = y_{\rm b}$), which we *do* have analytically for ${\rm Pe} \ll 1$. The trick is to write Eq. (4.88) as

$$\sigma_{\rm mg} = -\frac{k_BT}{D_r}(v_{\rm f}-v_{\rm s})I'(0), \tag{4.89}$$

where $I'(x) \equiv \partial_x I(x)$ and $I(x) \equiv \int_{y_{\rm b}}^{L_y}{\rm d}y m_y(x,y)$, and to subsequently derive a differential equation for $I(x)$. This differential equation is found from the evolution equation (4.7b) for m_y. Together with Eq. (4.8b), this evolution equation in steady state reads

$$0 = D_t\partial_{xx}m_y - \partial_y\left(\frac{1}{2}v_0(x)\rho - D_t\partial_y m_y\right) - D_r m_y. \tag{4.90}$$

Bringing the first and last term to the left and dividing by D_r yields

$$(1-\ell^2\partial_{xx})m_y(x,y) = -\ell\partial_y\Big(\frac{1}{2}{\rm Pe}(x)\rho(x,y) - \ell\partial_y m_y(x,y)\Big), \tag{4.91}$$

where we defined ${\rm Pe}(x) \equiv v_0(x)/\sqrt{D_tD_r}$. Integrating Eq. (4.91) over y, from $y = y_{\rm b}$ to $y = L_y$, then gives

$$(1-\ell^2\partial_{xx})I(x) = \frac{1}{2}{\rm Pe}(x)\rho(x,y_{\rm b}). \tag{4.92}$$

Here we used that ρ and $\partial_y m_y$ are zero inside the wall (which is where $y = L_y$ is), and that $\partial_y m_y = 0$ at $y = y_{\rm b}$. Eq. (4.92) is the differential equation for $I(x)$ that we were looking for. Indeed, it only depends on the interfacial profile $\rho(x,y_{\rm b})$. In principle, Eq. (4.92) can be solved for $I(x)$, since we know the analytical solution for $\rho(x,y_{\rm b})$ (see Eq. (4.12)). However, there is an easier way to obtain $I'(0)$. The first step is to take the derivative of Eq. (4.92) with respect to x. This gives the following differential equation for $I'(x)$.

$$(1-\ell^2\partial_{xx})I'(x) = \partial_x\Big(\frac{1}{2}{\rm Pe}(x)\rho(x,y_{\rm b})\Big). \tag{4.93}$$

The next step is to recognize that the same differential equation is satisfied by $-m_x(x,y_{\rm b})$. To see this, we find the steady-state equation for $m_x(x,y_{\rm b})$ far from any walls. According to Eqs. (4.7b) and (4.8b), $m_x(x,y_{\rm b})$ satisfies

$$0 = -\partial_x\Big(\frac{1}{2}v_0(x)\rho(x,y_{\rm b}) - D_t\partial_x m_x(x,y_{\rm b})\Big) - D_r m_x(x,y_{\rm b}), \tag{4.94}$$

which can be rewritten as

$$(1-\ell^2\partial_{xx})\left(-m_x(x,y_\mathrm{b})\right)=\ell\partial_x\Big(\frac{1}{2}\mathrm{Pe}(x)\rho(x,y_\mathrm{b})\Big). \tag{4.95}$$

Comparing Eqs. (4.95) and (4.93) shows that $I'(x)$ and $-m_x(x,y_\mathrm{b})$ indeed satisfy the same differential equation, and in particular that

$$(1-\ell^2\partial_{xx})I'(x)=(1-\ell^2\partial_{xx})\left(-m_x(x,y_\mathrm{b})\right). \tag{4.96}$$

Eq. (4.96) implies that $I'(x)$ and $-m_x(x)$ can only differ by a function that vanishes by applying the operator $(1-\ell^2\partial_{xx})$. Therefore, the general solution for $I'(x)$ is

$$I'(x)=-m_x(x)+D_1e^{x/\ell}+D_2e^{-x/\ell}, \tag{4.97}$$

where D_1 and D_2 are integration constants. Since $x=x_\mathrm{b}^\mathrm{f}$ and $x=x_\mathrm{b}^\mathrm{s}$ correspond to bulks where everything is x-invariant, $I'(x_\mathrm{b}^\mathrm{f})=I'(x_\mathrm{b}^\mathrm{s})=0$. Since also $m_x(x_\mathrm{b}^\mathrm{f})=m_x(x_\mathrm{b}^\mathrm{s})=0$, Eq. (4.97) then implies that $D_1=D_2=0$. Therefore $I'(x)=-m_x(x)$, and in particular $I'(0)=-m_x(0)$. Using this in Eq. (4.89) yields

$$\sigma_\mathrm{mg}=\frac{k_BT}{D_r}(v_\mathrm{f}-v_\mathrm{s})m_x(0). \tag{4.98}$$

This is indeed the opposite of the first contribution (4.87). Therefore, Eq. (4.31) - being the opposite of Eq. (4.27) - is indeed correct, and both contributions cancel, such that indeed $\sigma_\mathrm{m}=0$ for $\mathrm{Pe}\ll 1$.

Appendix 4.E Gibbs dividing line

In this appendix, we define the Gibbs dividing line used in Sec. 4.7, and we derive Eqs. (4.34) and (4.35). We start by considering a fixed time t, and fixed coordinate y - or, actually, a bin of infinitesimal width δy centered at y. In this bin, the density profile $\rho(x)$ interpolates between the fast bulk density ρ_f at $x=x_\mathrm{b}^\mathrm{f}$ and the slow bulk density ρ_s at $x=x_\mathrm{b}^\mathrm{s}$. One could imagine rearranging the particles in this bin in such a way that the density suddenly jumps from ρ_f to ρ_s, i.e. in such a way that $\rho(x)=\rho_\mathrm{f}$ for x smaller than some x_G, while $\rho(x)=\rho_\mathrm{s}$ for $x>x_G$. Performing this rearrangement for all y and t defines a line $x_G(y,t)$, known as the Gibbs dividing line, usually called Gibbs dividing surface in three dimensions [2]. The Gibbs dividing line $x_G(y,t)$ is defined by the equation

$$\int_{x_\mathrm{b}^\mathrm{f}}^{x_\mathrm{b}^\mathrm{s}}\mathrm{d}x\rho(x,y,t)=\rho_\mathrm{f}\left(x_G(y,t)-x_\mathrm{b}^\mathrm{f}\right)+\rho_\mathrm{s}\left(x_\mathrm{b}^\mathrm{s}-x_G(y,t)\right), \tag{4.99}$$

which expresses that the number of particles in the bin does not change during the rearrangement. We are mostly interested in the offset of $x_G(y,t)$ from its unperturbed value $x_{G,0}$, i.e. in $\delta x_G(y,t)\equiv x_G(y,t)-x_{G,0}$. Since Eq. (4.99) forms a linear relationship between x_G and ρ, this offset δx_G follows from (4.99) as

$$\delta x_G(y,t)=-\frac{1}{\Delta\rho}\int_{x_\mathrm{b}^\mathrm{f}}^{x_\mathrm{b}^\mathrm{s}}\mathrm{d}x\delta\rho(x,y,t), \tag{4.100}$$

where $\delta\rho(x,y,t) \equiv \rho(x,y,t) - \rho_0(x)$ is the change in density with respect to its unperturbed profile $\rho_0(x)$, and where $\Delta\rho = \rho_\mathrm{s} - \rho_\mathrm{f}$. Taking the time-derivative of Eq. (4.100) and using $\partial_t \delta\rho = \partial_t \rho \overset{(4.7a)}{=} -\boldsymbol{\nabla}\cdot\mathbf{J}$ yields

$$\partial_t \delta x_G(y,t) = \frac{1}{\Delta\rho}\int_{x_\mathrm{b}^\mathrm{f}}^{x_\mathrm{b}^\mathrm{s}} \mathrm{d}x \boldsymbol{\nabla}\cdot\mathbf{J}(x,y,t). \tag{4.101}$$

On one hand, by using $\boldsymbol{\nabla}\cdot\mathbf{J} = \partial_x J_x + \partial_y J_y$ and subsequently performing the integral over $\partial_x J_x$, Eq. (4.101) becomes Eq. (4.35) of the main text. On the other hand, we can integrate Eq. (4.101) over our bin of infinitesimal width, i.e. from y_A to $y_\mathrm{B} = y_\mathrm{A} + \delta y$. This yields

$$\partial_t \delta x_G(y,t) = \frac{1}{\Delta\rho\delta y}\int_{x_\mathrm{b}^\mathrm{f}}^{x_\mathrm{b}^\mathrm{s}} \mathrm{d}x \int_{y_\mathrm{A}}^{y_\mathrm{B}} \mathrm{d}y \boldsymbol{\nabla}\cdot\mathbf{J}(x,y,t). \tag{4.102}$$

Since the slope of the perturbation $h'(y) \ll 1$, the integration over the rectangular area $\int_{x_\mathrm{b}^\mathrm{f}}^{x_\mathrm{b}^\mathrm{s}} \mathrm{d}x \int_{y_\mathrm{A}}^{y_\mathrm{B}} \mathrm{d}y(\dots)$ can be replaced by the integration over an interface segment $\int_{S_\mathrm{segm}} \mathrm{d}S(\dots)$. Subsequently using Gauss' theorem to rewrite the integral then yields Eq. (4.34) of the main text.

Appendix 4.F Response to an interface perturbation

In sections 4.7.1 and 4.7.2 we used several results without derivation. In this appendix, we present their derivations. We calculate the integrated flux of Eq. (4.42) that results from a perturbation of the interface for our active ideal gas with position dependent propulsion speed. We show that the tension σ_t is given by Eq. (4.44), and that the normal component of the sum $\sigma_\mathrm{t}(y_\mathrm{A},t)\hat{\mathbf{n}}_\mathrm{A} + \sigma_\mathrm{t}(y_\mathrm{B},t)\hat{\mathbf{n}}_\mathrm{B}$ is indeed quadratic in the perturbation. We prove Eqs. (4.45) and (4.47). Also, along the way, we show that $\hat{\mathbf{n}}_\mathrm{A} + \hat{\mathbf{n}}_\mathrm{B} = h''(y_\mathrm{A})\mathrm{d}y\hat{\mathbf{x}}$, which was used in the main text above Eq. (4.43).

First, we make use of the approximation that all spatial gradients are small (in the sense described in section 4.7). By Eq. (4.7a), this implies that the density ρ is a slow variable, whereas according to Eq. (4.7b) the polarization $\mathbf{m}$ is then a fast variable. Therefore, on the timescale at which the density evolves, we can assume that for any density profile the polarization reaches its steady-state value immediately. In other words, we can set $\partial_t \mathbf{m} = \mathbf{0}$ in Eq. (4.7b). As explained in Sec. 4.5, this justifies the use of the force balance (4.19) in Sec. 4.7. Another consequence of the assumption of small spatial gradients is that the orientation current $\mathcal{J}^m_{\alpha\beta}$ of Eq. (4.8b) simplifies to

$$\mathcal{J}^m_{\alpha\beta} = \frac{1}{2}\rho(x)v_0(x)\delta_{\alpha\beta}. \tag{4.103}$$

Here we used that we are far from any walls, such that $V(\mathbf{r}) = \mathbf{0}$, and that the nematic order $S_{\alpha\beta}$ can be neglected, as was shown in section 2.3.2 of this thesis. An immediate consequence of Eq. (4.103) is that the swim pressure tensor is given by $P^\mathrm{swim}_{\alpha\beta} = \mathcal{J}^p_{\alpha\beta}/D_r = \gamma v_0(x)\mathcal{J}^m_{\alpha\beta}/D_r = \frac{1}{2}\gamma(v_0(x))^2/D_r\delta_{\alpha\beta}$, such that the total pressure tensor reads

$$P^\mathrm{tot}_{\alpha\beta} = P_{\alpha\beta} + P^\mathrm{swim}_{\alpha\beta} = \rho k_B T\left(1 + \frac{1}{2}\mathrm{Pe}^2(x)\right)\delta_{\alpha\beta}. \tag{4.104}$$

Here we defined $\mathrm{Pe}(x) \equiv v_0(x)/\sqrt{D_t D_r}$, a notation that we use throughout this section, but that is not used in the main text to avoid confusion with the Péclet number on the fast side $\mathrm{Pe} \equiv \mathrm{Pe_f}$. Note that total pressure tensor of Eq. (4.104) satisfies $P^{\mathrm{tot}}_{xx} = P^{\mathrm{tot}}_{yy}$. By Eq. (4.27), this implies that the tension σ_0 of the unperturbed interface is zero, as was claimed in Sec. 4.7.1.

We now calculate the contributions to the integrated flux $\int_{S_{\mathrm{segm}}} \mathrm{d}S \gamma J_\alpha$ as given by Eq. (4.42). We start with the tensile force on the lower boundary of the segment.

$$\begin{aligned}\sigma_{\mathrm{t}}(y_{\mathrm{A}})\hat{\mathbf{n}}_{\mathrm{A}} &\overset{(4.40)}{=} \int_{\delta S_{\mathrm{A}}} \mathrm{d}\ell \left(P^{\mathrm{tot}}_{0,xx}\delta_{\alpha\beta} - P^{\mathrm{tot}}_{\alpha\beta}\right) n_\beta \\ &\overset{(4.104)}{=} \hat{\mathbf{n}}_{\mathrm{A}} \int_{\delta S_{\mathrm{A}}} \mathrm{d}\ell \left[\rho_0(x) - \rho(x,y)\right] k_B T \left(1 + \mathrm{Pe}^2(x)\right).\end{aligned} \tag{4.105}$$

We now use the fact that $h(y)$ and $h'(y)$ are small (in the sense explained in the main text) to simplify Eq. (4.105). Firstly, the fact that $h(y)$ is small implies that

$$\rho(x,y) \overset{(4.32)}{=} \rho_0(x - h(y)) = \rho_0(x) - h(y)\rho_0'(x) \tag{4.106}$$

to leading order in $h(y)$. Secondly, the fact that $h'(y)$ is small implies that α_{A}, the angle that $\hat{\mathbf{n}}_{\mathrm{A}}$ makes with the negative y-axis (see Fig. 4.6), is small. Therefore, the integration $\int_{\delta S_{\mathrm{A}}} \mathrm{d}\ell(\dots)$ in Eq. (4.106) can be replaced by the purely horizontal integration $\int_{x_{\mathrm{b}}^{\mathrm{f}}}^{x_{\mathrm{b}}^{\mathrm{s}}} \mathrm{d}x(\dots)$. With these simplifications, Eq. (4.105) becomes

$$\sigma_{\mathrm{t}}(y_{\mathrm{A}})\hat{\mathbf{n}}_{\mathrm{A}} = \mathcal{M} h(y_{\mathrm{A}})\hat{\mathbf{n}}_{\mathrm{A}}, \tag{4.107}$$

where

$$\mathcal{M} \equiv \int_{x_{\mathrm{b}}^{\mathrm{f}}}^{x_{\mathrm{b}}^{\mathrm{s}}} \mathrm{d}x \rho_0'(x) k_B T \left(1 + \frac{1}{2}\mathrm{Pe}^2(x)\right). \tag{4.108}$$

Note that $\rho_0'(x) > 0$, and hence $\mathcal{M} > 0$, as claimed in the main text. The tensile force on the upper side of the segment can be calculated in an analogous way, and reads

$$\sigma_{\mathrm{t}}(y_{\mathrm{B}})\hat{\mathbf{n}}_{\mathrm{B}} = \mathcal{M} h(y_{\mathrm{B}})\hat{\mathbf{n}}_{\mathrm{B}}. \tag{4.109}$$

Eqs. (4.107) and (4.109) identify the tension as

$$\sigma_{\mathrm{t}}(y) = \mathcal{M} h(y), \tag{4.110}$$

and thus prove Eq. (4.44) of the main text. In order to add the tensile forces $\sigma_{\mathrm{t}}(y_{\mathrm{A}})\hat{\mathbf{n}}_{\mathrm{A}}$ and $\sigma_{\mathrm{t}}(y_{\mathrm{B}})\hat{\mathbf{n}}_{\mathrm{B}}$, we again use the fact that $h'(y)$ is small, which implies that

$$\hat{\mathbf{n}}_{\mathrm{A}} = -\left(h'(y_{\mathrm{A}})\hat{\mathbf{x}} + \hat{\mathbf{y}}\right) \tag{4.111}$$

and

$$\hat{\mathbf{n}}_{\mathrm{B}} = h'(y_{\mathrm{B}})\hat{\mathbf{x}} + \hat{\mathbf{y}} \tag{4.112}$$

to linear order in $h'(y)$. The difference in sign between Eqs. (4.107) and (4.109) comes from the different orientation of the normal vectors $\hat{\mathbf{n}}_{\mathrm{A}}$ and $\hat{\mathbf{n}}_{\mathrm{B}}$. As an aside, since $y_{\mathrm{B}} = y_{\mathrm{A}} + \delta y$, where δy is assumed to be infinitesimal, Eqs. (4.111) and (4.112) imply that

$$\hat{\mathbf{n}}_{\mathrm{A}} + \hat{\mathbf{n}}_{\mathrm{B}} = h''(y_{\mathrm{A}})\mathrm{d}y\hat{\mathbf{x}}, \tag{4.113}$$

which is the identity that was used in the main text above Eq. (4.43). We proceed by calculating the sum $\sigma_{\mathrm{t}}(y_{\mathrm{A}})\hat{\mathbf{n}}_{\mathrm{A}} + \sigma_{\mathrm{t}}(y_{\mathrm{B}})\hat{\mathbf{n}}_{\mathrm{B}}$. By Eqs. (4.111) and (4.111), this yields

$$\sigma_{\mathrm{t}}(y_{\mathrm{A}})\hat{\mathbf{n}}_{\mathrm{A}} + \sigma_{\mathrm{t}}(y_{\mathrm{B}})\hat{\mathbf{n}}_{\mathrm{B}} = \left(\sigma_{\mathrm{t}}' h' + \sigma_{\mathrm{t}} h''\right)\delta y \hat{\mathbf{x}} + \sigma_{\mathrm{t}}' \delta y \hat{\mathbf{y}}, \tag{4.114}$$

where the right hand side line is to be evaluated at $y = y_{\mathrm{A}}$. Note that, since σ_{t} is linear in the perturbation (see Eq. (4.110)), the x-component of the sum (4.114) is indeed quadratic in the perturbation, as was claimed in the main text.

Next, we calculate the contribution from the $\partial_x v_0$-term in Eq. (4.42).

$$\frac{\gamma}{D_r}\int_{S_{\mathrm{segm}}} \mathrm{d}S \partial_x v_0 \left(\mathcal{J}^m_{x\alpha} - \mathcal{J}^m_{0,x\alpha}\right) \overset{(4.103)}{=} \frac{\gamma}{2D_r}\int_{S_{\mathrm{segm}}} \mathrm{d}S \left(\rho - \rho_0\right) v_0(x)\partial_x v_0(x)\delta_{x\alpha}. \tag{4.115}$$

To simplify Eq. (4.115), we use Eq. (4.106), as well as the fact that the slopes $h'(y)$ is small. The latter fact implies that the interface segment can be approximated to be rectangular, such that the integration $\int_{S_{\mathrm{segm}}} \mathrm{d}S(\dots)$ can be replaced by $\int_{x_{\mathrm{b}}^{\mathrm{f}}}^{x_{\mathrm{b}}^{\mathrm{s}}} \mathrm{d}x \int_{y_{\mathrm{A}}}^{y_{\mathrm{b}}} \mathrm{d}y(\dots)$. Consequently,

$$\frac{\gamma}{D_r}\int_{S_{\mathrm{segm}}} \mathrm{d}S \partial_x v_0 \left(\mathcal{J}^m_{x\alpha} - \mathcal{J}^m_{0,x\alpha}\right) = \mathcal{K}\int_{y_{\mathrm{A}}}^{y_{\mathrm{B}}} \mathrm{d}y h(y)\delta_{x\alpha}, \tag{4.116}$$

where

$$\mathcal{K} \equiv -\frac{\gamma}{2D_r}\int_{x_{\mathrm{b}}^{\mathrm{f}}}^{x_{\mathrm{b}}^{\mathrm{s}}} \mathrm{d}x \rho_0'(x) v_0(x)\partial_x v_0(x). \tag{4.117}$$

Since regions of high propulsion speed v_0 correspond to a low density ρ_0 and vice versa, $\partial_x v_0$ and ρ_0' are expected to have opposite sign. Therefore, $\mathcal{K} > 0$, as was claimed in the main text. Since the width of the interface segment is infinitesimal, $\int_{y_{\mathrm{A}}}^{y_{\mathrm{B}}} \mathrm{d}y h(y) = h(y_{\mathrm{A}})\delta y$. Using this in Eq. (4.116), and adding the result to the tensile forces (4.114) gives the following integrated flux of Eq. (4.42),

$$\int_{S_{\mathrm{segm}}} \mathrm{d}S \gamma \mathbf{J} = \left(\mathcal{K} h \hat{\mathbf{x}} + \sigma_{\mathrm{t}}' \hat{\mathbf{y}}\right)\delta y, \tag{4.118}$$

to leading order in the perturbation strength. Note that the x-component of this flux is indeed given by Eq. (4.45), and that this component is only due to the $\partial_x v_0$-term. The x-components of the tensile forces are subleading, since, as we saw in Eq. (4.114), they are quadratic in the perturbation strength.

Finally, we slightly rewrite the y-component of Eq. (4.118). Again replacing the integration $\int_{S_{\mathrm{segm}}} \mathrm{d}S(\dots)$ by $\int_{x_{\mathrm{b}}^{\mathrm{f}}}^{x_{\mathrm{b}}^{\mathrm{s}}} \mathrm{d}x \int_{y_{\mathrm{A}}}^{y_{\mathrm{b}}} \mathrm{d}y(\dots)$, and using that the width δy of the segment is infinitesimal, yields

$$\int_{x_{\mathrm{b}}^{\mathrm{f}}}^{x_{\mathrm{b}}^{\mathrm{s}}} \mathrm{d}x J_y(x, y_{\mathrm{A}}, t) = \frac{1}{\gamma}\sigma_{\mathrm{t}}'(y_{\mathrm{A}}, t), \tag{4.119}$$

which proves Eq. (4.47) of the main text.

5

Chemical potential in active systems: predicting phase equilibrium from bulk equations of state?

In this chapter, we focus on the simplest ABPs considered so far - isotropic ABPs with homogeneous propulsion speed - and address the remaining thermodynamic variable: the chemical potential.

We derive a microscopic expression for a quantity μ that plays the role of chemical potential for ABPs in steady state and in a planar geometry with normal Cartesian coordinate z. This quantity μ is not to be confused with the solvent chemical potential μ_s introduced in chapter 3. We confirm that $\mu(z)$ is spatially constant for several inhomogeneous active fluids, and also use it to study phase coexistences of ABPs. We show that these phase coexistences satisfy not only mechanical but also diffusive equilibrium, and test whether the coexisting densities can be found by equating the bulk chemical potentials and bulk pressures obtained from bulk simulations. While this works well for a coexistence of weakly active Lennard Jones particles, the predicted densities are found to be inaccurate for the highly active MIPS. We show that the discrepancy can be traced back to interfacial contributions to μ.

This chapter is part of a collaboration with Siddharth Paliwal, Marjolein Dijkstra and René van Roij. It is based on chapter 4 of Siddharth Paliwal's PhD thesis [21], as well as on the publication that carries the same title as this chapter [141]. Siddharth Paliwal performed all computer simulations, whereas the author of this thesis was responsible for the Fokker-Planck calculations of the active ideal gas, and, together with Marjolein Dijkstra and René van Roij, for the conceptualization of the swim potential.

5.1 Remarks on notation

We warn the reader that the various pressures appearing in this chapter have slightly different notation than in chapter 4. The most important difference is that the total pressure P^{tot} of chapter 4 is denoted in this chapter by P. In chapter 4, P was the bare pressure, and followed from the trace of the bare pressure tensor $\mathbf{P}$; in the current chapter, only the normal component of the bare pressure tensor enters, and is called P_N. The swim pressure P^{swim} of chapter 4 still corresponds to the swim pressure P_{swim} of this chapter.

Furthermore, whereas in the other chapters the orientation of an active Brownian particle is denoted by $\hat{\mathbf{e}}$, in this chapter it is called $\hat{\mathbf{u}}$.

5.2 Introduction

Coexisting phases in thermodynamic equilibrium are, apart from thermal, also in mechanical and chemical equilibrium with each other. These conditions mean that, for a certain temperature, both phases have equal pressure as well as equal chemical potential. If the pressure and chemical potential are known for a homogeneous system as a function of the density, then these two conditions can be used to solve for the densities of the two coexisting phases. This is a powerful technique, and a feat that would truly show the usefulness of thermodynamic variables for ABPs, would be to show that they can predict the coexisting densities of MIPS in a similar fashion.

The variable pressure for ABPs has already been discussed in chapters 3 and 4. These chapters did show some surprises: chapter 3 showed that in systems with torque the pressure on the wall depends on the wall potential, while chapter 5 showed that two phases with different propulsion speeds "coexist" at different pressure. However, for the simple case of isotropic particles with homogeneous propulsion speed, the situation is just like in equilibrium: the total pressure exerted on the wall is well-defined (as shown by Eqs. (3.8) and (3.6)), and two phases coexist at equal total pressure [92] (see Eq. (4.19)[a]). Therefore, in the remainder of this thesis we focus on isotropic particles with homogeneous propulsion speed. For these systems, the question that remains is: can we define a chemical potential? And can it, together with the pressure, be used to predict the coexisting densities of MIPS?

A chemical potential has already been introduced in the literature using phenomenological arguments [41, 46, 57, 89, 147]. For instance, Takatori and Brady [41] introduced a chemical potential using micromechanical arguments, of similar form to the one that we will derive by a different approach in this chapter. The same authors even proceed and calculate binodals on the basis of either a Gibbs-Duhem-like equation or a free energy for the case of an incompressible solvent. However, a quantitative comparison with simulated data later showed that a Maxwell construction on the simulated equation of state does *not* yield the correct coexistence densities [70]. Recently, Hermann et al. [148] also introduced a different non-equilibrium chemical potential. With the help of an ansatz for the crucially unknown chemical potential component, they were able to find the coexisting

[a] Actually, in chapter 4 we considered only an active ideal gas. However, the same equality holds for a suitable generalization of the pressure to interacting systems, as we show in this chapter.

densities to good accuracy. While all of these efforts provide valuable insight, none of the proposed chemical potentials is fully microscopic, which means that they cannot be measured unambiguously (yet) in computer simulations of homogeneous bulk systems.

In this chapter, we aim to view the problem from a different perspective, by introducing a chemical potential-like quantity that *is* fully microscopic. While our Fokker-Planck approach is similar in spirit to that of Refs. [46, 70], it sheds new light on the problem by explicitly defining an expression for the local chemical potential in terms of the new concept of a "swim potential".

The outline of this chapter is as follows. First, we derive a microscopic expression for the local chemical potential $\mu(z)$ of active Brownian particles in a spatially inhomogeneous steady state in a planar geometry, for simplicity, with z the normal Cartesian direction. Next, we confirm using Brownian Dynamics simulations that $\mu(z)$ is spatially constant for active fluids in contact with a soft planar wall, in a gravitational field, and in two-phase coexistence with a planar interface. Subsequently, we show that the coexistence is described by diffusive and mechanical equilibrium with equal bulk pressure and bulk chemical potential of the coexisting phases, provided the swim potential that we introduce in this chapter, is properly taken into account. However, we conclude that the swim potential and hence the chemical potential $\mu(z)$ is not a state function of the density for a macroscopic system.

5.3 Methods and Formulation

We consider a three-dimensional dispersion of N active Brownian particles (ABPs) with positions $\mathbf{r}_i = (x_i, y_i, z_i)$ and orientations $\mathbf{u}_i = (\sin\theta_i \cos\phi_i, \sin\theta_i \sin\phi_i, \cos\theta_i)$ with polar angle θ_i and azimuthal angle ϕ_i, interacting via an isotropic pair potential $U(|\mathbf{r}_i - \mathbf{r}_j|)$ and subject to an external field $V_e(\mathbf{r}_i)$ for $i = 1, \ldots, N$ at temperature T. Particle i experiences a constant self-propulsion force along its orientation $\mathbf{u}_i$. The motion of particle i is described by the overdamped Langevin equations

$$\dot{\mathbf{r}}_i = -\beta D_t \nabla_i \left[V_e(\mathbf{r}_i) + \sum_{j \neq i} U(|\mathbf{r}_i - \mathbf{r}_j|) \right] + v_0 \mathbf{u}_i + \sqrt{2D_t}\boldsymbol{\Lambda}_i^t, \tag{5.1}$$

$$\dot{\mathbf{u}}_i = \sqrt{2D_r}(\mathbf{u}_i \times \boldsymbol{\Lambda}_i^r), \tag{5.2}$$

where D_t and D_r are the translational and rotational diffusion coefficients, $\beta = 1/k_B T$ with k_B the Boltzmann constant, and v_0 is the self-propulsion speed. The collisions with the solvent are described by a stochastic force and torque characterised by random vectors $\boldsymbol{\Lambda}_i^t$ and $\boldsymbol{\Lambda}_i^r$ with $\langle \boldsymbol{\Lambda}_i^t \rangle = \langle \boldsymbol{\Lambda}_i^r \rangle = \mathbf{0}$ and $\langle \Lambda_{i,\alpha}^t(t) \Lambda_{j,\beta}^t(t') \rangle = \langle \Lambda_{i,\alpha}^r(t) \Lambda_{j,\beta}^r(t') \rangle = \delta_{\alpha\beta}\delta_{ij}\delta(t - t')$ with $\alpha, \beta = x, y, z$ [149].

Starting from (5.1) and (5.2), we average over the noise to derive the deterministic Fokker-Planck equation [70, 149, 150]

$$\frac{\partial \psi(\mathbf{r}, \mathbf{u}, t)}{\partial t} = -\nabla \cdot \mathbf{j}(\mathbf{r}, \mathbf{u}, t) - \nabla_{\mathbf{u}} \cdot \mathbf{j}_{\mathbf{u}}(\mathbf{r}, \mathbf{u}, t) \tag{5.3}$$

for the time evolution of the probability distribution function

$$\psi(\mathbf{r},\mathbf{u},t) \equiv \left\langle \sum_{i=1}^{N} \delta(\mathbf{r}-\mathbf{r}_i)\delta(\mathbf{u}-\mathbf{u}_i) \right\rangle$$

with $\langle \cdots \rangle$ denoting the averaging over the random noise. Here we defined the translational and rotational fluxes

$$\begin{aligned} \mathbf{j}(\mathbf{r},\mathbf{u},t) =& -\beta D_t \int \mathrm{d}\mathbf{r}' \int \mathrm{d}\mathbf{u}' \psi^{(2)}(\mathbf{r},\mathbf{u},\mathbf{r}',\mathbf{u}',t)\nabla U(|\mathbf{r}-\mathbf{r}'|) \\ &+ \psi(\mathbf{r},\mathbf{u},t)\left(-\beta D_t \nabla V_e(\mathbf{r}) + v_0\mathbf{u}\right) - D_t\nabla\psi(\mathbf{r},\mathbf{u},t); \qquad (5.4) \\ \mathbf{j}_{\mathbf{u}}(\mathbf{r},\mathbf{u},t) =& -D_r\nabla_{\mathbf{u}}\psi(\mathbf{r},\mathbf{u},t). \qquad (5.5) \end{aligned}$$

We introduced here the instantaneous full two-body correlation function

$$\psi^{(2)}(\mathbf{r},\mathbf{u},\mathbf{r}',\mathbf{u}',t) \equiv \left\langle \sum_{i=1}^{N}\sum_{j\neq i}^{N} \delta(\mathbf{r}-\mathbf{r}_i)\delta(\mathbf{u}-\mathbf{u}_i)\delta(\mathbf{r}'-\mathbf{r}_j)\delta(\mathbf{u}'-\mathbf{u}_j) \right\rangle, \qquad (5.6)$$

which can be formally related to higher n-body correlation functions using a BBGKY-like hierarchy of Fokker-Planck equations or approximated by applying a closure relation such as the mean-field approximation $\psi^{(2)}(\mathbf{r},\mathbf{u},\mathbf{r}',\mathbf{u}',t) \simeq \psi(\mathbf{r},\mathbf{u},t)\psi(\mathbf{r}',\mathbf{u}',t)$. In our formulation we do not make such an approximation and rather calculate $\psi^{(2)}(\mathbf{r},\mathbf{u},\mathbf{r}',\mathbf{u}',t)$ by simulating the particle dynamics explicitly for various setups as described in the subsequent sections.

We next define the first few angular moments of the probability distribution function $\psi(\mathbf{r},\mathbf{u},t)$

$$\begin{aligned} \rho(\mathbf{r},t) &= \int \mathrm{d}\mathbf{u}\ \psi(\mathbf{r},\mathbf{u},t) \\ \mathbf{m}(\mathbf{r},t) &= \int \mathrm{d}\mathbf{u}\ \psi(\mathbf{r},\mathbf{u},t)\mathbf{u} \\ \mathcal{S}(\mathbf{r},t) &= \int \mathrm{d}\mathbf{u}\ \psi(\mathbf{r},\mathbf{u},t)(\mathbf{u}\mathbf{u}-\mathbb{I}/d) \end{aligned} \qquad (5.7)$$

which are, respectively, the local particle density $\rho(\mathbf{r},t)$, the local polarization $\mathbf{m}(\mathbf{r},t)$ and the traceless alignment tensor $\mathcal{S}(\mathbf{r},t)$. $\mathbb{I}$ is the identity matrix and $d = 2, 3$ denotes the spatial dimension of interest.

The time evolution of the local particle density $\rho(\mathbf{r},t)$ is described by the continuity equation obtained from the zeroth moment of Eq. (5.3),

$$\frac{\partial\rho(\mathbf{r},t)}{\partial t} = -\nabla\cdot\mathbf{J}(\mathbf{r},t), \qquad (5.8)$$

with the particle flux $\mathbf{J}(\mathbf{r},t)$ given by

$$\mathbf{J}(\mathbf{r},t) = \int \mathrm{d}\mathbf{u}\ \mathbf{j}(\mathbf{r},\mathbf{u},t) \qquad (5.9)$$

which can be expressed using Eq. (5.4) as

$$\mathbf{J}(\mathbf{r},t) = -\beta D_t \int \mathrm{d}\mathbf{r}' \rho^{(2)}(\mathbf{r},\mathbf{r}',t)\nabla U(|\mathbf{r}-\mathbf{r}'|) \\ - \beta D_t\ \rho(\mathbf{r},t)\nabla V_e(\mathbf{r}) + v_0\mathbf{m}(\mathbf{r},t) - D_t\nabla\rho(\mathbf{r},t). \tag{5.10}$$

Here $\rho^{(2)}(\mathbf{r},\mathbf{r}',t)$ is the spatial two-body correlation function given by

$$\rho^{(2)}(\mathbf{r},\mathbf{r}',t) = \int \mathrm{d}\mathbf{u} \int \mathrm{d}\mathbf{u}' \psi^{(2)}(\mathbf{r},\mathbf{u},\mathbf{r}',\mathbf{u}',t).$$

An equation for the evolution of $\mathbf{m}(\mathbf{r},t)$ follows from the first moment of Eq. (5.3) which yields

$$\frac{\partial \mathbf{m}(\mathbf{r},t)}{\partial t} = -\nabla\cdot\mathcal{J}_m(\mathbf{r},t) - (d-1)D_r\mathbf{m}(\mathbf{r},t), \tag{5.11}$$

with the two-rank momentum flux tensor

$$\mathcal{J}_m(\mathbf{r},t) = -\beta D_t \int \mathrm{d}\mathbf{u}\ \mathbf{u} \int \mathrm{d}\mathbf{r}' \int \mathrm{d}\mathbf{u}' \psi^{(2)}(\mathbf{r},\mathbf{u},\mathbf{r}',\mathbf{u}',t)\nabla U(|\mathbf{r}-\mathbf{r}'|) \\ - \mathbf{m}(\mathbf{r},t)\beta D_t\nabla V_e(\mathbf{r}) + v_0\Big(\rho(\mathbf{r},t)\ \frac{\mathbb{I}}{d} + \mathcal{S}(\mathbf{r},t)\Big) - D_t\nabla\mathbf{m}(\mathbf{r},t). \tag{5.12}$$

We now assume that the system is only inhomogeneous in the z-direction, due to either an external potential $V_e(z)$ or due to coexistence of two phases separated by an interface parallel to the xy-plane. Without loss of generality, we consider a large, but finite system by setting $V_e(\pm\infty) = \infty$, such that $\rho(z \to \pm\infty) = 0$. From Eq. (5.10), we find that the particle flux in the z-direction is given by

$$J_z(z,t) = -\frac{\beta D_t}{L^{d-1}} \int \mathrm{d}\mathbf{r}^{d-1} \int \mathrm{d}\mathbf{r}' \rho^{(2)}(\mathbf{r},\mathbf{r}',t)\partial_z U(|\mathbf{r}-\mathbf{r}'|) \\ - \beta D_t\rho(z,t)\partial_z V_e(z) + v_0\mathrm{m}_z(z,t) - D_t\partial_z\rho(z,t), \tag{5.13}$$

where we spatially integrated over the direction(s) perpendicular to z-direction and divided by the surface area L^{d-1} in d-dimensions, so that $\rho(z,t) = L^{-d+1}\int \mathrm{d}\mathbf{r}^{d-1}\rho(\mathbf{r},t)$. When divided by βD_t, we interpret Eq. (5.13) as a force balance in a continuum picture rather than at the microscopic level, which assumes averaging over bins that contain enough colloids for the continuum picture to hold. In the following sections we ensure this by having bins that are very elongated in the direction(s) perpendicular to the z-direction.

The term $(\beta D_t)^{-1}v_0 m_z(z,t)$ has previously been interpreted as a contribution to the divergence of the stress tensor, which has led to a debate on pressure being a state function or not in active systems [150–152]. Here, however, we take another point of view, and regard this term as an activity-induced body force

$$-\rho(z,t)\frac{\partial}{\partial z}V_{\mathrm{swim}}(z,t) \equiv \frac{v_0}{\beta D_t}m_z(z,t), \tag{5.14}$$

that is exerted on the active particles by the solvent [83, 151]. This allows us to define the so-called swim potential

$$V_{\mathrm{swim}}(z,t) = V_{\mathrm{swim}}(z_0,t) - \frac{v_0}{\beta D_t}\int_{z_0}^{z} \frac{m_z(z',t)}{\rho(z',t)}\mathrm{d}z', \tag{5.15}$$

where $V_{\rm swim}(z_0,t)$ is a suitably chosen reference.

Clearly, for a homogeneous and isotropic bulk phase, for which the polarization $\mathbf{m}=0$ in a steady state, $V_{\rm swim}$ is a spatial constant. Interestingly, however, the value of this constant is determined by surfaces and interfaces, where $\mathbf{m}$ can be non-zero, not unlike the Donnan potential in inhomogeneous electrolyte solutions [153, 154]. This is a reflection of the fact that the activity-induced body force on the active particles only averages out in the bulk, but not near interfaces.

We now combine Eqs. (5.13)-(5.15) to construct, in the spirit of the simplest dynamic density functional theory [155, 156] with a density-independent diffusion coefficient D_t, a local chemical potential-like function $\mu(z,t)$ by

$$-\rho(z,t)\frac{\partial}{\partial z}\beta\mu(z,t) \equiv \frac{1}{D_t}J_z(z,t) \tag{5.16}$$

or more explicitly

$$\begin{aligned}\rho(z,t)\frac{\partial}{\partial z}\beta\mu(z,t) =& \frac{1}{L^{d-1}}\int \mathrm{d}\mathbf{r}^{d-1}\int \mathrm{d}\mathbf{r}'\rho^{(2)}(\mathbf{r},\mathbf{r}',t)\frac{\partial}{\partial z}\beta U(|\mathbf{r}-\mathbf{r}'|)\\ &+\rho(z,t)\frac{\partial}{\partial z}\beta V_e(z) - \frac{v_0}{D_t}\mathrm{m}_z(z,t) + \frac{\partial}{\partial z}\rho(z,t).\end{aligned} \tag{5.17}$$

The quantity $\mu(z)$ can then be interpreted as a sum of the swim potential ($V_{\rm swim}(z)$) and the equilibrium-like external ($V_e(z)$) and intrinsic ($\mu_{\rm int}(z)$) contributions such that:

$$\begin{aligned}\mu(z,t)-\mu(z_0,t) =& \mu_{\rm int}(z,t)-\mu_{\rm int}(z_0,t)\\ &+V_e(z)-V_e(z_0)+V_{\rm swim}(z,t)-V_{\rm swim}(z_0,t),\end{aligned} \tag{5.18}$$

where the intrinsic chemical potential $\mu_{\rm int}(z,t) = k_BT\ln\rho(z,t)+\mu_{\rm ex}(z,t)$. Here the 'excess' contribution $\mu_{\rm ex}(z,t)$ is defined using Eq. (5.13) as

$$\mu_{\rm ex}(z,t)=\mu_{\rm ex}(z_0,t)+\frac{1}{L^{d-1}}\int \mathrm{d}\mathbf{r}^{d-1}\int_{z_0}^{z}\mathrm{d}z''\frac{1}{\rho(z'',t)}\int \mathrm{d}\mathbf{r}'\rho^{(2)}(\mathbf{r}'',\mathbf{r}',t)\frac{\partial U(|\mathbf{r}''-\mathbf{r}'|)}{\partial z''}. \tag{5.19}$$

Eq. (5.18) reduces to the conventional chemical potential for a passive system, where $v_0=0$, and is constructed such that $J_z(z,t)=0$ if $\mu(z,t)$ is a spatial constant. The local chemical potential $\mu(z)$ is therefore a prime candidate to describe diffusive equilibrium of coexisting phases in stationary states of active systems. Interestingly, all terms in Eq. (5.18) can be determined in Brownian Dynamics (BD) simulations of ABPs.

The body-force interpretation of the polarization (5.14) can also be used to write the mechanical equilibrium condition of a stationary state in terms of a well-defined normal component of the stress tensor. Since the stationary state satisfies $\partial_t\rho(z,t)=0$, which from Eq. (5.8) is equivalent to $J_z(z)=0$ for a macroscopically large, but finite system, we can rewrite Eq. (5.13) as

$$\frac{\mathrm{d}P_N(z)}{\mathrm{d}z}+\rho(z)\frac{\partial V_{\rm swim}(z)}{\partial z} = -\rho(z)\frac{\partial V_e(z)}{\partial z} \tag{5.20}$$

where the standard equilibrium-like (intrinsic) normal pressure

$$P_N(z) = P_{\text{id}}(z) + P_{\text{vir}}(z)$$

with the ideal contribution $P_{\text{id}}(z) = \rho(z)k_BT$ and the 'virial' contribution $P_{\text{vir}}(z)$ given by:

$$\frac{\mathrm{d}P_{\text{vir}}(z)}{\mathrm{d}z} = \frac{1}{L^{d-1}} \int \mathrm{d}\mathbf{r}^{d-1} \int \mathrm{d}\mathbf{r}' \; \rho^{(2)}(\mathbf{r}, \mathbf{r}') \frac{\partial U(|\mathbf{r} - \mathbf{r}'|)}{\partial z}, \tag{5.21}$$

where we used Newton's third law and the symmetry of $\rho^{(2)}(\mathbf{r}, \mathbf{r}')$ under particle exchange. Eq. (5.21) gives us the virial contribution that describes the z-component of the interparticle forces across a plane at z, which can be measured in a BD simulation [157]. Note that we did *not* add a swim pressure [150, 151] to the "intrinsic" P_N, but instead treated the activity at the level of a swim potential V_{swim} in the force balance (5.20), which turns out to be crucial for interpreting the (osmotic) pressure as a state function [83]. However, in order to connect to existing literature, and for later reference, we do define

$$\begin{aligned} P_{\text{swim}}(z) - P_{\text{swim}}(z_0) &= \int_{z_0}^{z} \mathrm{d}z' \rho(z') \frac{\partial V_{\text{swim}}(z')}{\partial z'} \\ &= \frac{v_0 k_B T}{(d-1) D_t D_r} \left(\mathcal{J}_{m,zz}(z) - \mathcal{J}_{m,zz}(z_0) \right) \end{aligned} \tag{5.22}$$

with the zz-component of $\mathcal{J}_m$ given by

$$\begin{aligned} \mathcal{J}_{m,zz}(z) = \frac{v_0}{d}\rho(z) - m_z(z)\beta D_t \frac{\partial}{\partial z} V_e(z) + v_0 \mathcal{S}_{zz}(z) - D_t \frac{\partial}{\partial z} m_z(z) \\ - \frac{\beta D_t}{L^{d-1}} \int \mathrm{d}\mathbf{r}^{d-1} \int \mathrm{d}\mathbf{u} \int \mathrm{d}\mathbf{r}' \int \mathrm{d}\mathbf{u}' \psi^{(2)}(\mathbf{r}, \mathbf{u}, \mathbf{r}', \mathbf{u}', t) \frac{\partial}{\partial z} U(|\mathbf{r} - \mathbf{r}'|) \cos\theta, \end{aligned} \tag{5.23}$$

which reduces to the conventional swim pressure [41, 158]

$$P_{\text{swim}}(z_b) = \rho(z_b) \frac{v_0^2 k_B T}{d(d-1) D_t D_r}$$

in an ideal active bulk fluid at $z = z_b$. Note that our local swim pressure (5.22) deviates from previous expressions [86, 159] due to the gradient term $\partial_z m_z(z)$, which plays a non-negligible role in the force balance obtained from Eq. (5.20) when significant spatial variations are present, e.g. in the interface of a phase coexistence.

To summarize, we have introduced the concept of a swim potential here using a force balance for only the colloids. As we saw in chapter 3, this force balance can be combined with an additional force balance for the solvent, which provides an alternative interpretation, but identical expression, for the swim pressure as an excess solvent pressure.

With the definition (5.22) one can thus define a total pressure $P(z) = P_N(z) + P_{\text{swim}}(z)$, such that Eq. (5.20) can be written as $\mathrm{d}P/\mathrm{d}z = -\rho(z)\partial_z V_e(z)$; in the case where $V_e(z) = 0$

a steady state is then characterized by a spatially constant total pressure $P(z)$. The intrinsic chemical potential $\mu_{\rm int}(z)$ and intrinsic normal pressure $P_N(z)$, and the swim potential $V_{\rm swim}(z)$ and swim pressure $P_{\rm swim}(z)$ have thus been constructed such that

$$\frac{\mathrm{d}P_N(z)}{\mathrm{d}z} = \rho(z)\frac{\mathrm{d}\mu_{\rm int}(z)}{\mathrm{d}z}, \quad \text{and} \quad \frac{\mathrm{d}P_{\rm swim}(z)}{\mathrm{d}z} = \rho(z)\frac{\mathrm{d}V_{\rm swim}(z)}{\mathrm{d}z}. \tag{5.24}$$

If we now invoke a Local Density Approximation (LDA), i.e. assume that the local environment behaves as a bulk such that the local pressure and chemical potential are a function of only the local density $\rho(z)$, then Eq. (5.24) can be written in terms of bulk quantities as:

$$\frac{\mathrm{d}P_N(\rho)}{\mathrm{d}\rho} = \rho\frac{\mathrm{d}\mu_{\rm int}(\rho)}{\mathrm{d}\rho}, \quad \text{and} \quad \frac{\mathrm{d}P_{\rm swim}(\rho)}{\mathrm{d}\rho} = \rho\frac{\mathrm{d}V_{\rm swim}(\rho)}{\mathrm{d}\rho}, \tag{5.25}$$

allowing us to write

$$\frac{\mathrm{d}P(\rho)}{\mathrm{d}\rho} = \rho\frac{\mathrm{d}\mu(\rho)}{\mathrm{d}\rho} \tag{5.26}$$

with $\mu(\rho) = \mu_{\rm int}(\rho) + V_{\rm swim}(\rho)$, in a zero external potential. Here, we shall take care to distinguish the notation $\mu(\rho)$ for the chemical potential obtained via Eq. (5.26), from $\mu(z)$ which denotes the chemical potential calculated from Eq. (5.18). We recognize Eq. (5.26) as a generalization of the Gibbs-Duhem relation for equilibrium systems. Whereas in equilibrium (where $P_{\rm swim} = V_{\rm swim} = 0$) it holds true in general, we emphasize that in this case we had to make use of the LDA to derive it. This Gibbs-Duhem relation provides a way to obtain the chemical potential $\mu(\rho)$ from the bulk equation of state $P(\rho)$, whereas to obtain $\mu(z)$ from Eq. (5.18) we require complete spatial profiles. We test the applicability of Eq. (5.26) in simulations and show that it works well for cases with *low anisotropy* (e.g. low polarization). However, Eq. (5.26) does not hold true in general as $V_{\rm swim}(z) \neq V_{\rm swim}^{LDA}(\rho(z))$ for *high anisotropy* as we discuss later in Section 5.5.

We note that Eq. (5.26) is akin to the one in Ref. [41], apart from a factor that is equal to the (incompressible) solvent volume fraction. The equilibrium analogue of Eq. (5.26) follows naturally if the solvent is treated grand-canonically which we implicitly assume. Both approaches are also similar in the sense that they both identify the fluxes as being proportional to the gradient of a (scalar) chemical potential. In the next section we describe some of the details of the methodology and parameters used for numerical simulations.

5.3.1 Simulation details

Within a collaboration, Brownian Dynamics (BD) simulations were performed of non-interacting as well as interacting particles, by employing Eqs. (5.1) and (5.2) in three-dimensional and two-dimensional geometries in Sections 5.4.1-5.4.3 and Section 5.4.4, respectively. The Euler-Maruyama method was used to integrate the equations of motion (5.1) and (5.2) with a time step size $dt = 10^{-5}\tau$, where $\tau = 3Dr^{-1}$ is the unit of time. The translational and rotational diffusion coefficients (D_t and D_r respectively) are kept

fixed, v_0 is varied to change Pe, and the interaction strength ε is varied to change the temperature of the colloidal particles. We employ periodic boundary conditions in only x- and y-direction in Section 5.4.1 and 5.4.2, in all three directions in Section 5.4.3, and in both y- and z- directions in Section 5.4.4. We simulate system sizes of about 2500 particles in 3D and about 6500 particles in 2D within an elongated box. We measure the density profile $\rho(z)$ in the z-direction as $\rho(z) = \langle n(z)\rangle/L^2\Delta z$ by measuring the average of the number of particles $\langle n(z)\rangle$ in the slabs of volume $L^2\Delta z$ ($\rho(z) = \langle n(z)\rangle/L\Delta z$ in 2D) arranged parallel to xy plane (y-direction in 2D), where L is the length of the system in the x and/or y-direction, and where $\Delta z = 0.1\sigma$ is the width of the slab. In a similar manner we measure the polarization profile $m_z(z)$ by summing the particle orientations in the slab at location z. The density profiles $\rho(z)$ in the case of a phase coexistence in Sections 5.4.3 and 5.4.4 are fitted to a hyperbolic tangent function:

$$\rho(z) = \frac{1}{2}\left(\rho(z_l) + \rho(z_g)\right) + \frac{1}{2}\left(\rho(z_l) - \rho(z_g)\right)\tanh\left[\frac{2(z - z_0^*)}{w}\right], \tag{5.27}$$

where $\rho(z_l)$ and $\rho(z_g)$ are the corresponding bulk liquid and vapour phase coexisting densities, z_0^* is the location of the dividing plane and w represents the thickness of the interface.

The swim potential profile $V_{\text{swim}}(z)$ is obtained as

$$V_{\text{swim}}(z) = V_{\text{swim}}(z_0) - \frac{v_0}{\beta D_t}\int_{z_0}^{z}\frac{m_z(z')}{\rho(z')}\mathrm{d}z', \tag{5.28}$$

where we numerically integrate the mean-orientation profile $m_z(z)/\rho(z)$ as measured in the BD simulations and $V_{\text{swim}}(z_0)$ is a suitably chosen reference state. In addition, we measure the normal component $P_N(z)$ of the stress tensor using

$$P_N(z) = P_{\text{id}}(z) + P_{\text{vir}}(z) \tag{5.29}$$

with the ideal gas pressure $P_{\text{id}}(z)$ and the virial pressure $P_{\text{vir}}(z)$ given by:

$$P_{\text{id}}(z) = \rho(z)k_BT \tag{5.30}$$

$$P_{\text{vir}}(z) = \frac{1}{2L^2\Delta z}\left\langle\sum_{i=1}^{N}\sum_{j\neq i}^{N}\frac{z_{ij}}{r_{ij}}\frac{\mathrm{d}U(r_{ij})}{\mathrm{d}r_{ij}}\int_{C_{ij}}\mathrm{d}\mathbf{l}_z\right\rangle, \tag{5.31}$$

where $r_{ij} = |\mathbf{r}_{ij}| = |\mathbf{r}_j - \mathbf{r}_i|$ denotes the center-of-mass distance between particle i and j, $z_{ij} = z_j - z_i$ where z_i is the z position of particle i, C_{ij} is the intersection of $\mathbf{r}_{ij}$ and the slab of width Δz centered at z. The integral in Eq. (5.31) denotes that the virial contribution to the pressure of particle pair i and j is due to the part of $\mathbf{r}_{ij}$ that lies inside the respective slab at z within the coarse-grained Irving-Kirkwood approximation [157]. We also calculate the swim pressure using the expression

$$\begin{aligned}P_{\text{swim}}(z) = {} & \frac{v_0^2k_BT}{d(d-1)D_tD_r}\rho(z) - \frac{v_0m_z(z)}{(d-1)D_r}\partial_zV_e(z)\\ & - \frac{v_0}{(d-1)D_r}\frac{1}{L^{d-1}}\int\mathrm{d}\mathbf{r}^{d-1}\int\mathrm{d}\mathbf{u}\int\mathrm{d}\mathbf{r}'\mathrm{d}\mathbf{u}'\psi^{(2)}(\mathbf{r},\mathbf{u},\mathbf{r}',\mathbf{u}')\frac{\partial U(|\mathbf{r}-\mathbf{r}'|)}{\partial z}\cos\theta\\ & + \frac{v_0^2k_BT}{(d-1)D_tD_r}\mathcal{S}_{zz}(z) - \frac{v_0k_BT}{(d-1)D_r}\partial_zm_z(z),\end{aligned} \tag{5.32}$$

and the chemical potential profile $\mu(z)$ using Eq. (5.18) with the excess chemical potential $\mu_{\rm ex}(z)$ measured as

$$\mu_{\rm ex}(z) = \mu_{\rm ex}(z_0) + \int_{z_0}^{z} {\rm d}z' \left\langle \frac{1}{n(z')} \sum_{i=1}^{n(z')} \sum_{j\neq i}^{N} \frac{z'_{ij}}{r'_{ij}} \frac{{\rm d}U(r'_{ij})}{{\rm d}r'_{ij}} \right\rangle . \tag{5.33}$$

Here, the excess chemical potential at z with respect to a reference at z_0 is determined by integrating the averaged force that a particle feels due to the particle interactions with all other particles in the system over the distance z_0 to z.
Alternatively, if $V_e(z) = 0$, $\mu(z)$ can also be obtained using

$$\mu(z) = \mu(z_0) + \int_{z_0}^{z} {\rm d}z' \frac{1}{\rho(z')} \frac{{\rm d}P(z')}{{\rm d}z'} \tag{5.34}$$

with $P(z) = P_N(z) + P_{\rm swim}(z)$.

In the next Section, we discuss the results obtained by applying the formalism of Eqs. (5.15)-(5.22) to active fluids and consider four different scenarios. In Section 5.4.1 we study a non-interacting active fluid in contact with a short-ranged planar soft wall. We compare and verify that the stationary state is indeed described by constant $\mu(z)$ in both the Fokker-Planck calculations and particle based simulations. Next we present the results of BD simulations of an active fluid with Lennard-Jones (LJ) interactions subject to a gravitational field in Section 5.4.2. In Section 5.4.3 we consider an active Lennard-Jones fluid exhibiting gas-liquid coexistence with a planar interface and confirm mechanical and diffusive equilibrium. We perform a Maxwell equal-area construction to identify phase coexistence from bulk equations of state. We then attempt to apply the same formalism to active particles which undergo Motility Induced Phase Separation (MIPS) at high activity in Section 5.4.4.

5.4 Results

5.4.1 Active Ideal Gas

We first consider a three-dimensional active ideal gas (with $U(r) = 0$) at Péclet number ${\rm Pe} = v_0/\sigma D_r = 0$ (passive), 1, 3, 5, in the presence of an external potential

$$\beta V_e(z) = \begin{cases} (z/\sigma)^2 & \text{if } z < 0 \\ 0 & \text{if } z \geq 0 \end{cases}$$

where the unit of length $\sigma = \sqrt{3D_t/D_r}$ is chosen to be the particle diameter so that the Stokes-Einstein relation for spheres in three dimensions is satisfied. Note that Pe can also be perceived as the ratio of the persistence length v_0/D_r and the particle diameter[158]. For large but finite $z = z_b \gtrsim 3\sigma$, the active fluid reaches a bulk state with bulk density $\rho_b = \rho(z_b)$, and the normal pressure reduces to the bulk pressure $P_b = P_N(z_b) = \rho_b k_B T$. In Fig. 5.1(a) and (b) we show the time-averaged density profiles $\rho(z)$ and orientation

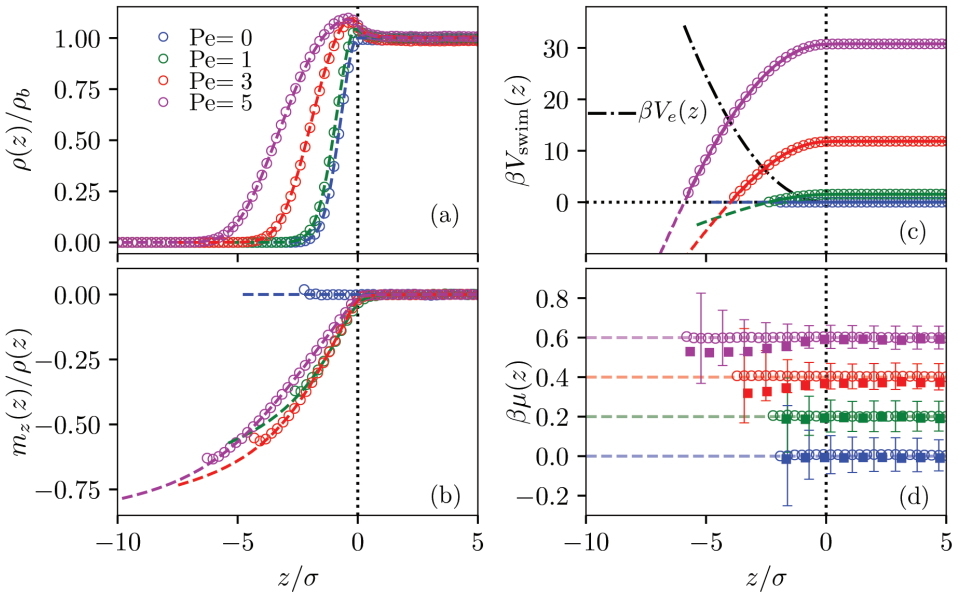

Figure 5.1: (a) Density profile $\rho(z)$, (b) polarization profile $m_z(z)/\rho(z)$, (c) swim potential $V_{\rm swim}(z)$ and the soft external potential $V_e(z)$ (see text), and (d) local chemical potential $\mu(z)$ (with error bars), all as a function of z for an active ideal gas in contact with a planar soft wall, as obtained from BD simulations (open circles) and Fokker-Planck calculations (dashed lines), for varying Péclet numbers as labeled. In (d) the open circles represent $\beta\mu(z)$ obtained by the integration of $J_z(z)/\rho(z)$, which fluctuates about zero, whereas the square symbols show the resultant from Eq. (5.18). The errorbars represent the error induced in $\beta\mu(z)$ due to the statistical error in $\rho(z)$. The deviation from the Fokker-Planck calculations deep into the wall for high Pe is due to the correlation of error upon numerical integration.

profiles $m_z(z)/\rho(z)$, respectively as measured in BD simulations (solid lines) as well as from Fokker-Planck calculations (dashed lines). We observe that the particles penetrate deeper into the wall at higher Pe resulting into a more extended $\rho(z)$ within the wall accompanied by a small adsorption (that was found in Ref. [160] as well) close to $z = 0$. In Fig. 5.1(b) we see no average polarization outside or inside the wall for the passive case. At finite Pe, however, Fig. 5.1(b) shows that the average orientation is zero in the bulk where $V_e(z) = 0$ and negative within the wall, corresponding to the particles oriented towards the wall. Fig. 5.1(c) and (d) show $V_{\rm swim}(z)$ and $\mu(z)$ as obtained from Eq. (5.15) and (5.18), respectively. We find that $V_{\rm swim}(z)$ is attractive towards the wall consistent with the polarization and extended density profile close to the wall. Finally, we also confirm that $\mu(z)$ is indeed constant within our statistical accuracy of $\sim 0.1 k_B T$. Clearly, for $\mu(z)$ to be constant it is crucial that $V_{\rm swim}(z)$ is included in Eq. (5.18) and ignoring this contribution of $10 - 30 k_B T$ would *not* have yielded a spatially constant chemical potential in the stationary state. Although $\mu(z)$ was constructed to be spatially

constant within the Fokker-Planck formalism, a confirmation from the simulations serves as a useful validation.

Additionally, we verify that the swim pressure (given by Eq. (5.22)) measured in the bulk reduces to $P_{\rm swim}(z_b) = k_B T v_0^2 \rho_b/(6 D_r D_t)$. $V_{\rm swim}$ can similarly be obtained as $V_{\rm swim}(z_b) = (k_B T v_0^2/6 D_r D_t) \ln \rho_b \sigma^3$. We use this bulk state at $z_b \gtrsim 3\sigma$ with $V_{\rm swim}(z_0 = z_b)$ as the reference point for the profiles of $V_{\rm swim}(z)$ and $\mu(z)$ in Fig. 5.1(c) and (d), respectively.

5.4.2 Sedimenting weakly active LJ-particles

We now consider simulations of weakly active Lennard-Jones (LJ) particles with an isotropic pair potential, $U_{LJ}(r) = 4\varepsilon((\sigma/r)^{12} - (\sigma/r)^6)$, at $k_B T/\varepsilon = 2.0$ in the gravitational potential $V_e(z) = Mgz$ for $z > 0$ with a hard 'bottom' at $z = 0$, with M the buoyant particle mass. These systems are supercritical in the passive case, and therefore even more so in the active cases since the 'critical temperature' decreases with increasing activity[128, 161]. We measure the density $\rho(z)\sigma^3$, polarization $m_z(z)/\rho(z)$, swim potential $\beta V_{\rm swim}(z)$, and chemical potential $\mu(z)$ for $\beta M g \sigma = 0.5$ and 1.0 for Pe=0, and $\beta M g \sigma = 3$ and 5 for Pe=10 and 20, all plotted in Fig. 5.2(a)-(d). In order to obtain a comparable length scale l over which variations are observed in the passive (where we choose $l = \sigma$) and in the active cases (where $l = v_0/D_r$), we used a smaller buoyant mass ($\beta M g \sigma$) of the particles in the passive case. We observe that the polarization $m_z(z)$ is positive for Pe=10 and 20, and hence the mean swimming direction is opposite to the gravitational field, consistent with the findings in Ref. [162]. Moreover, Fig. 5.2(b) shows that the polarization profile $m_z(z)/\rho(z)$ is surprisingly constant over a large regime of heights z. As a consequence, the swim potential profile $\beta V_{\rm swim}(z)$ essentially decreases linearly with height z for Pe = 10 and 20 and counteracts largely the gravitational field, as shown in Fig. 5.2(c), leading to an enormous increase in sedimentation length $(\beta M g)^{-1}$[163]. The chemical potential profile $\mu(z)$ is calibrated by $\mu(z_0) = 0$ at the reference point z_0 determined by the condition $\rho(z_0)\sigma^3 = 10^{-3}$. The chemical potential profile $\mu(z)$ is shown in Fig. 5.2(d) and is indeed spatially constant upto $\sim 0.3 k_B T$ within our statistical accuracy. It is important to note here that $V_{\rm swim}(z)$ decreases by a few hundred $k_B T$ and the external gravitational potential $V_e(z) = Mgz$ increases by a few hundred $k_B T$ in the z-range of interest as shown in Fig. 5.2(d).

In addition, we show in Fig. 5.2(e) and (f) both P_N and $\mu_{\rm int}$ as a function of ρ, obtained by eliminating z from $P_N(z)$ and $\rho(z)$, and $\mu_{int}(z)$ and $\rho(z)$, respectively. We observe that the data collapse at fixed Pe, and it is alluring to interpret that $P_N(\rho,{\rm Pe})$ and $\mu_{\rm int}(\rho,{\rm Pe})$ are state functions of the density in this regime.

5.4.3 Active-LJ phase coexistence

We now consider a weakly active LJ fluid without any external potential ($V_e(z) = 0$), and at subcritical temperatures such that coexistence of a gas and a liquid phase with bulk densities ρ_g and ρ_l, respectively, is to be expected at overall intermediate densities $\rho_g < \rho < \rho_l$ in an elongated simulation box with periodic boundary conditions [128, 161]. A temperature $k_B T/\varepsilon = 0.43$ and a Péclet number Pe= $v_0/\sigma D_r = 3.0$ are used in this

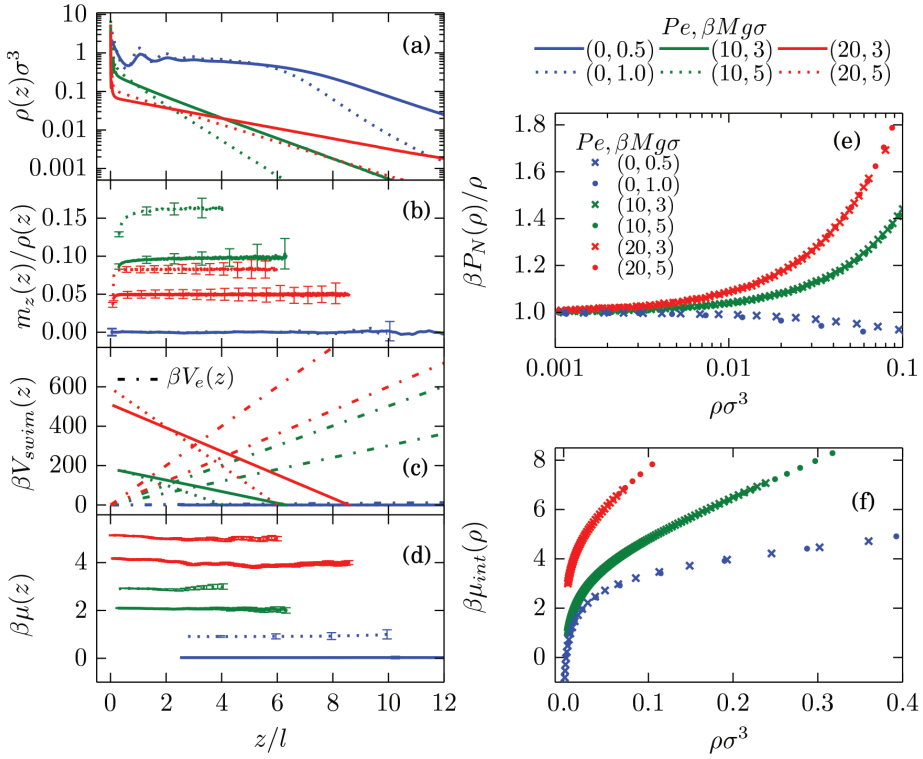

Figure 5.2: Height-dependence of (a) density $\rho(z)$, (b) polarization $m_z(z)/\rho(z)$, (c) swim potential $V_{\text{swim}}(z)$, and (d) chemical potential $\mu(z)$ (with an offset for clarity), all for an active LJ fluid in an external gravitational potential $V_e(z) = Mgz$ for various values of $\beta Mg\sigma$, and Péclet number Pe=0 (blue), 10 (green), 20 (red) as obtained from BD simulations. The height z is scaled with respect to l, where $l = v_0/D_r$ is the persistence length for Pe=10 and 20, and $l = \sigma$ is the particle diameter for Pe=0. The compressibility factor $P_N(\rho, \text{Pe})/\rho$ in (e) and the intrinsic chemical potential $\mu_{\text{int}}(\rho, \text{Pe})$ shown with an offset in (f) show a proper collapse in the dilute limit for different $\beta Mg\sigma$ but *not* for Pe.

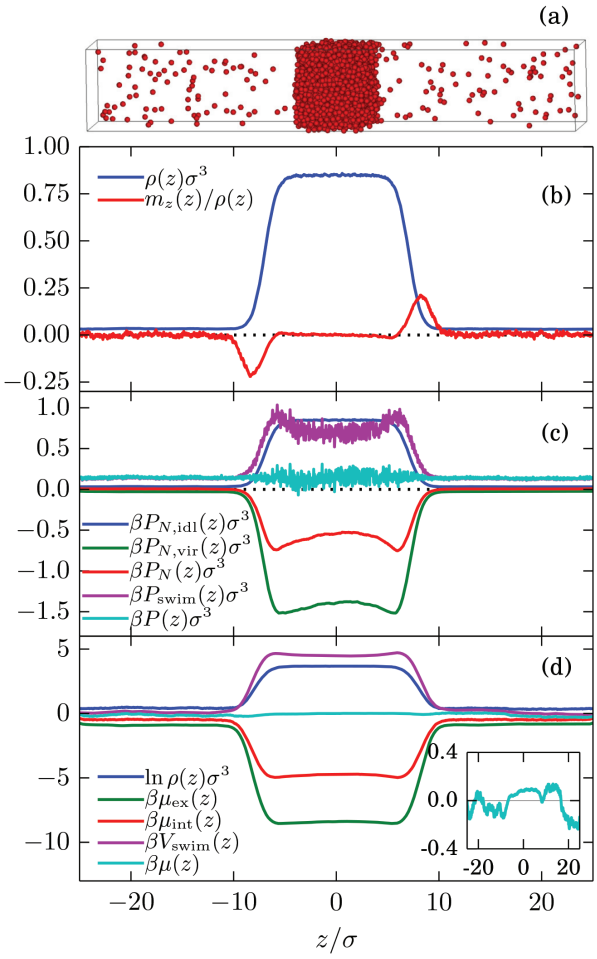

Figure 5.3: (a) A typical configuration of a three-dimensional gas-liquid coexistence of an active LJ fluid at Pe=3.0, and temperature $k_BT/\varepsilon = 0.43$, along with (b) the corresponding density profile $\rho(z)$ and polarization profile $m_z(z)/\rho(z)$, (c) total pressure $P(z) = P_N(z) + P_{\mathrm{swim}}(z)$ and the individual contributions, and (d) total chemical potential $\mu(z)$ obtained from Eq. (5.18), and individual contributions, along with an inset showing a magnified view of $\mu(z)$. Both $P(z)$ and $\mu(z)$ are spatially constant within numerical accuracy, demonstrating mechanical and diffusive equilibrium of the coexisting gas and liquid phase.

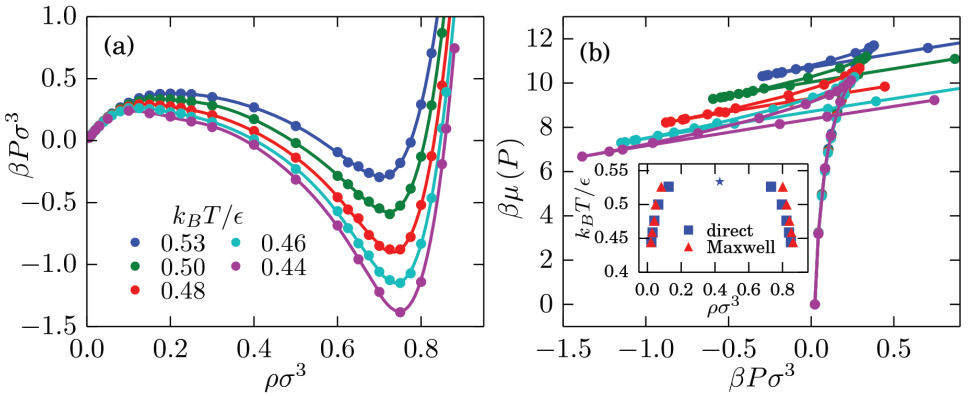

Figure 5.4: (a) Scaled pressure-density P-ρ, and (b) chemical potential-pressure μ-P relations of an active LJ fluid at several temperatures k_BT/ε and Péclet Pe= $v_0/\sigma D_r = 2.7$. The inset shows the temperature-density gas-liquid binodals as obtained from direct coexistence simulations (■) and from equating μ and P in the coexisting phases (▲) of an active LJ fluid.

case. In Fig. 5.3(a), we show a typical configuration of a liquid slab in the center of the simulation box in coexistence with a gas phase on either side. In Fig. 5.3(b) we plot the corresponding density profile $\rho(z)$ which can be fitted to a hyperbolic tangent function (Eq. (5.27)), independently for $z > 0$ and $z < 0$, to obtain the coexistence densities $\rho(z_g)$ and $\rho(z_l)$ of the two bulk phases as fit parameters, with z_g and z_l a position in the bulk gas and liquid respectively. In the same figure we also plot the polarization profile $m_z(z)/\rho(z)$, showing that the swimming direction of the particles at the liquid-gas interface is pointing from the liquid phase towards the gas phase, i.e., against the attractive interparticle forces from the liquid[128, 164].

In Fig. 5.3(c) and (d) we plot the profiles of total pressure $P(z)$ and chemical potential $\mu(z)$, respectively, which clearly show that both are spatially constant. We hence conclude that $P(z_g) = P(z_l)$ and $\mu(z_g) = \mu(z_l)$, demonstrating mechanical and diffusive equilibrium of the coexisting gas and liquid phase. For completeness, in Fig. 5.3(c) we also plot the individual contributions to the total pressure $P(z) = P_N(z) + P_{\text{swim}}(z)$, where $P_{\text{swim}}(z)$ is the swim pressure obtained from Eq. (5.22), and $P_N(z) = P_{N,\text{idl}}(z) + P_{N,\text{vir}}(z)$ is the normal pressure with the ideal pressure $P_{N,\text{idl}}(z)$ and the virial contribution to the normal pressure $P_{N,\text{vir}}(z)$ as obtained from Eq. (5.21). Similarly we plot the contributions to the chemical potential $\mu(z) = \mu_{\text{int}}(z) + V_{\text{swim}}(z)$ in Fig. 5.3(d), where the intrinsic chemical potential $\mu_{\text{int}}(z) = k_BT \ln \rho(z) + \mu_{\text{ex}}(z)$ represents the sum of ideal and excess chemical potential. The swim potential $V_{\text{swim}}(z)$ is calculated from the measured polarization profiles using Eq. (5.15).

In order to investigate if we can predict phase coexistence solely from bulk quantities, we perform BD simulations of bulk states of ABPs at several temperatures k_BT/ε and Péclet number Pe=2.7. We measure the bulk pressure P as a function of density ρ in a simulation box small enough to prevent phase separation and plot the equations of state

$P(\rho)$ for several subcritical temperatures in Fig. 5.4(a). Now, within a Local Density Approximation (LDA), we apply the Gibbs-Duhem relation Eq. (5.26) and obtain $\mu(P)$ by integrating the equation of state $P(\rho)$ for several T's as shown in Fig. 5.4(b). We emphasize here that we refer to $\mu(\rho)$ as the μ obtained by applying Eq. (5.26) which is not to be confused with $\mu(z)$. The intersection of the curve $\mu(P)$ gives the coexistence $\mu_g = \mu_l$ and $P_g = P_l$. In the inset of Fig. 5.4(b) we compare the binodals in the (scaled) temperature-density plane as obtained from the density profiles from direct coexistence simulations ($\rho(z_g)$ and $\rho(z_l)$) and from the bulk $\mu(P)$ intersections (ρ_g and ρ_l). We find good agreement between the two results and thus conclude that the corresponding coexistence densities ρ_g and ρ_l could, in this (low Pe) case at least, be determined from the bulk equations of state. Note that the activity has a huge effect on the gas-liquid binodals (shown in the inset of Fig. 5.4(b)) as the critical temperature shifts from $k_BT/\varepsilon \approx 1.15$ in the passive case to $k_BT/\varepsilon \approx 0.54$ in the active case for Pe=2.7 (see Ref. [128] for full comparison).

5.4.4 Motility Induced Phase Separation

In this section we discuss the swim potential and the chemical potential in a two-dimensional system of strongly active particles exhibiting motility induced phase separation at high Pe. We choose our planar geometry in the yz plane and assume homogeneity in the y direction to be consistent with previous definitions. The particles interact with the WCA potential given by $U_{WCA}(r) = U_{LJ}(r) + \varepsilon$, with a cut-off beyond $r \geq r_c = 2^{1/6}\sigma$ to make the particles purely repulsive. The particle orientations can be described in terms of the angle θ_i as $\mathbf{u}_i = (\cos\theta_i, \sin\theta_i)$. The translational equation of motion in 2D is similar to Eq. (5.1) and the rotational diffusion follows $\dot{\theta}_i = \sqrt{2D_r}\Lambda_i^r$, with Λ_i^r a zero-mean unit-variance Gaussian random variable.

As before, we fix rotational and translation diffusion coefficients to correspond to the particle interaction length scale $\sigma = \sqrt{3D_t/D_r}$ and change the self-propulsion speed v_0 to vary Pe. At high Pe, we find that the system phase separates into a gas phase and a dense phase, both of well-defined densities, separated by a planar interface in an elongated simulation box[40]. For Pe=50 the typical density and polarization profiles are shown in Fig. 5.5(a). Notably, the polarization profiles are now reversed with respect to Fig. 5.3(b) as the particles at the interfaces are now pointing towards the dense phase. We measure the normal component of the total pressure $P(z)$ and the chemical potential $\mu(z)$ by summing the individual contributions, and plot them in Fig. 5.5(c) and (d), respectively for $z > 0$. We clearly observe that both the quantities $P(z)$ and $\mu(z)$ are spatially constant, demonstrating mechanical and diffusive equilibrium of the coexisting phases. With the polarization profiles reversed, $P_{\text{swim}}(z)$ and $V_{\text{swim}}(z)$ are now higher in the gas phase as compared to the denser phase.

Further, we perform a Maxwell equal-area construction on the equation of state. The $P - \rho$ curves shown in Fig. 5.5(b) are obtained again using a small system size for which there is no global phase separation at intermediate densities. We confirm the results of the homogeneous states with larger system sizes and find that the agreement is satisfactory for our analysis. Performing a Maxwell construction on P as a function of $1/\rho$ gives the equal-area pressure P_{Maxwell} shown as the dashed horizontal line in Fig. 5.5(b). In the same

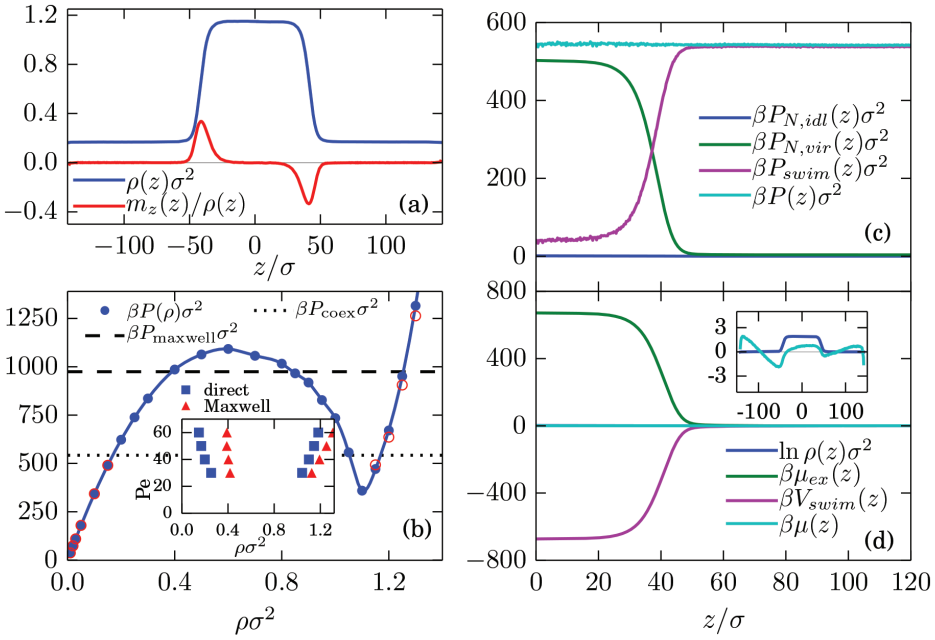

Figure 5.5: (a) Density $\rho(z)\sigma^2$ and polarization $m_z(z)/\rho(z)$ profiles of an active fluid with WCA interactions exhibiting MIPS at Pe = 50, and temperature $k_BT/\varepsilon = 0.1$. (b) Pressure $\beta P(\rho)\sigma^2$ vs. density $\rho\sigma^2$ curve obtained from bulk simulations of small systems (solid circles) and large systems (open circles), together with Maxwell equal-area pressure (dashed line) and coexistence pressure $P_{\rm coex} = P(z)$ (dotted line) as measured in (c). The inset shows a comparison of bulk densities from direct coexistence simulations (■) and the Maxwell equal-area construction (▲) for various Pe. (c) Total pressure $P(z) = P_N(z) + P_{\rm swim}(z)$ profile, with the ideal, virial and swim contributions, and (d) total chemical potential $\mu(z)$ profile with individual contributions, for $z > 0$, corresponding to the system described in (a). The inset shows the ideal contribution $\beta\mu_{\rm id}(z) = \ln \rho(z)\sigma^2$ and that $\mu(z)$ is constant within an accuracy of $3k_BT$.

figure, we also show the coexistence pressure $P_{\rm coex}$ obtained from the direct coexistence simulation of the phases coexisting at the corresponding set of parameters. From the two curves it is evident that the coexistence densities predicted by the Maxwell construction and the direct-coexistence simulations do *not* agree. We perform the same procedure on a set of Pe in the range $30 - 60$ and plot the corresponding coexistence densities and the densities predicted by the Maxwell construction in the inset of Fig. 5.5(b). From the disagreement between the two binodals we conclude that the Maxwell equal-area construction does not correspond to the coexisting states as obtained from the direct coexistence simulations, noted previously as well in Refs. [46, 70]. We have checked that using our $P(\rho)$ data with the definition of the chemical potential introduced in Ref. [41] yields the same binodals as predicted here despite the difference of the factor concerning the solvent volume fraction.

5.5 Technical Discussion

The results from the previous section show that the Maxwell equal-area construction, and hence the Gibbs-Duhem equation (5.26), cannot be used in general to predict the coexisting densities ρ_g and ρ_l [46, 70] in systems of ABPs. In other words, even though $\mu(z_g) = \mu(z_l)$ in a phase-separated system (where z_g and z_l are locations far from interfaces such that the local densities are ρ_g and ρ_l, respectively) , the chemical potentials obtained from the Gibbs-Duhem equation (5.26) may not be equal, i.e. $\mu(\rho_g) \neq \mu(\rho_l)$. The nonzero difference between $\mu(\rho_g)$ and $\mu(\rho_l)$ is caused by the failure of the LDA assumed in the derivation of Eq. (5.26), as we will show below. In particular, the values of $V_{\text{swim}}(z)$ and $\mu_{\text{ex}}(z)$ in a bulk state at position z and density ρ_b do not only depend on ρ_b (and other system parameters such as Pe) but *also* on the interface between the bulk state and the reference state at z_0. This implies that neither V_{swim} nor μ_{ex} as expressed in Eqs. (5.15) and (5.19), respectively, are state functions of the density. Below we show an example for $V_{\text{swim}}(z)$ which demonstrates this breakdown of the LDA in the case of a 2D active ideal gas (for which $\mu_{\text{ex}}(z) \equiv 0$) in a particular external potential.

The setup consists of a ramp-like external potential $\beta V_e(z) = \lambda z/\sigma$ in the region $0 < z < 5\sigma$ which separates a bulk region at the left (where $\beta V_e(z) = 0$ for $z < 0$) from the bulk on the right (where $\beta V_e(z) = 5\lambda$ for $z > 5\sigma$). These external potentials are plotted in Fig. 5.6(a) as dash-dot lines for $\lambda = 0, 0.5, 1$, and 2. The probability density $\psi(z, \theta)$ is obtained by solving Eq. (5.3) for $U(r) = 0$ numerically, at Pe = 1 with a fixed density boundary condition $\rho\sigma^2 = 1.0$ for $z_0 = -10\sigma$ and with a hard wall placed at $z = 15\sigma$. The density and polarization profiles for increasing λ are plotted in Fig. 5.6(a) and (b), respectively.

In order to determine $V_{\text{swim}}(z)$ for this non-interacting system (with $U(r) \equiv 0$,) we substitute $\mathrm{m}_z(z)$ from Eq. (5.11) with $\partial_t \mathrm{m}_z(z) = 0$ into Eq. (5.14) to obtain

$$V_{\text{swim}}(z) - V_{\text{swim}}(z_0) = \frac{v_0^2}{2\beta D_t D_r} \ln\left(\frac{\rho(z)}{\rho(z_0)}\right) + \frac{v_0}{\beta D_r} \int_{z_0}^{z} \mathrm{d}z' \frac{1}{\rho(z')} \frac{\mathrm{d}}{\mathrm{d}z'} \left[\frac{v_0}{D_t} \mathcal{S}_{zz}(z') - \beta m_z(z') \frac{\partial V_e(z')}{\partial z'} - \frac{\partial m_z(z')}{\partial z'}\right]. \tag{5.35}$$

The $V_{\text{swim}}(z)$ profiles, obtained equivalently from Eq. (5.35) or from Eq. (5.15), are plotted as solid lines in Fig. 5.6(c) where we have taken $z_0 = -10\sigma$ as the reference state where $V_{\text{swim}}(z_0) = 0$. If we would approximate the vicinity of any point z' as an isotropic bulk with density $\rho(z')$ in evaluating the swim potential $V_{\text{swim}}(z')$, i.e. assume in Eq. (5.35) $\mathcal{S}_{zz}(z') \approx m_z(z') \approx 0$ such that the term in square brackets vanishes for every z', we obtain

$$\beta V_{\text{swim}}^{LDA}(\rho(z)) = \frac{v_0^2}{2D_t D_r} \ln \rho(z)\sigma^2$$

which we refer to as the local density approximation (LDA) of Eq. (5.35). Note that Eq. (5.35) follows from the Fokker-Planck formalism, and this LDA does not refer to an approximation of a free-energy functional. This $V_{\text{swim}}^{LDA}(\rho(z))$, plotted as dotted lines in Fig. 5.6(c), is equal to $V_{\text{swim}}(\rho)$ obtained from the swim component of the Gibbs-Duhem-like relation (5.26). We find that $V_{\text{swim}}(z)$ and $V_{\text{swim}}^{LDA}(\rho(z))$ start to deviate at high λ

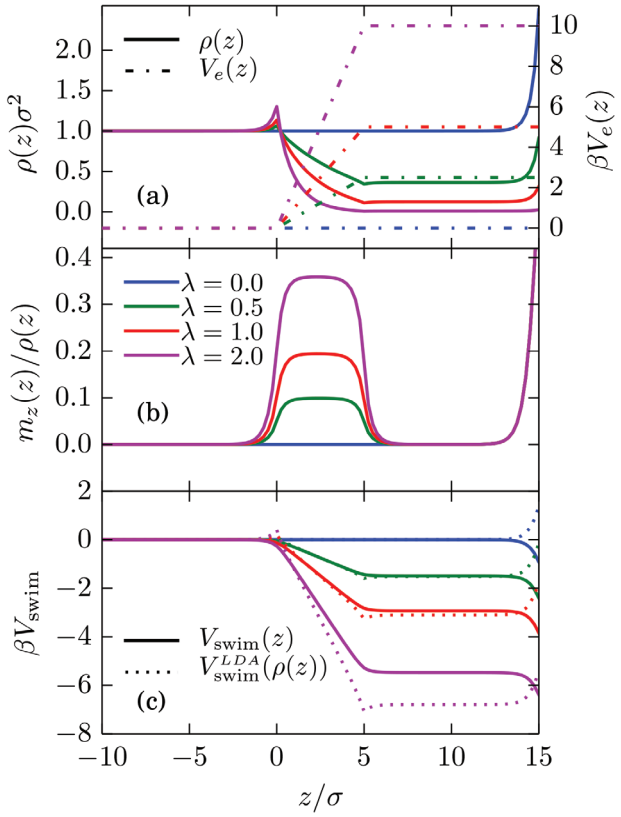

Figure 5.6: (a) Density profiles $\rho(z)$ and (b) mean-orientation profiles $m_z(z)/\rho(z)$ of a non-interacting active fluid at Pe=1 in a ramp-shaped external potential with slope $\lambda = 0, 0.5, 1, 2$ shown as broken lines in (a). (c) Comparison of $V_{\rm swim}(z)$ obtained using Eq. (5.15) and $\beta V_{\rm swim}^{LDA}(\rho(z)) = (v_0^2/2D_tD_r)\ln\rho(z)\sigma^2$ obtained using LDA.

and do not coincide in the right bulk. Hence, we can conclude that the values for $V_{\rm swim}^{LDA}$ obtained from the Gibbs-Duhem equation are not correct in general. This is due to the failure of LDA, i.e. due to the *anisotropy* in the interface that renders the integral on the right hand side in Eq. (5.35) non-negligible as compared to the first term. In Fig. 5.6(b) we see that the polarization within the interface increases with λ, consistent with this idea of increasing anistropy. For an interacting system the forces between particles would add another contribution to $m_z(z)/\rho(z)$, which could also become a source of failure for the LDA.

In Section 5.4.3 we observed that the Maxwell construction was able to predict the coexistence densities for the active LJ case with reasonable accuracy, but was in disagreement at higher activity in Section 5.4.4 for MIPS. We now assert that the error made in the chemical potential by assuming the LDA translates into an error in the predicted

coexisting densities that is small for the active LJ particles, but significant for MIPS. We define the error in predicted coexistence densities of the gas and the dense phase, respectively, as $\Delta\rho_g^{\rm err} = \rho(z_g) - \rho_g$ and $\Delta\rho_l^{\rm err} = \rho(z_l) - \rho_l$, where $\rho(z_g)$ and $\rho(z_l)$ are the bulk coexistence densities and ρ_g and ρ_l denote the estimates obtained by performing a Maxwell construction. If we define the gas state as the reference state for the chemical potential, i.e. $\mu(z_0) = \mu(\rho_g)$ in Eq. (5.18) with $z_0 = z_g$, then the error made in determining the chemical potential of the dense phase by using the Gibbs-Duhem equation (5.26) is $\Delta\mu_l^{\rm err} = \mu(\rho_l) - \mu(z_l)$, where we recall that $\mu(\rho_l)$ is the chemical potential of the dense phase obtained from the Gibbs-Duhem relation, whereas $\mu(z_l)$ is the true chemical potential determined in the coexistence simulation. From $\Delta\mu_l^{\rm err}$ the relative error in the predicted density of the dense phase can be estimated as

$$\frac{\Delta\rho_l^{\rm err}}{\rho(z_l)} \approx \frac{1}{\rho(z_l)} \frac{\Delta\mu_l^{\rm err}}{(d\mu/d\rho)_l}.$$

Similarly, the error in the predicted density of the gas phase can be estimated by using the dense phase as the reference state ($\mu(z_0) = \mu(\rho_l)$). The relative density error estimated in this manner is less than 5% for the active LJ case, whereas it is of the order of 100% for the MIPS case, which agrees with our findings in Fig. 5.4(b) and 5.5(b), respectively.

We wish to make a note that the *anisotropy* terms identified here resemble the interfacial contributions discussed in Ref. [46] for pairwise-interacting particles. Although it requires explicit measurement of these interfacial contributions by performing phase coexistence simulations, Solon et al. were able to suggest a modified Maxwell construction for estimating the binodals in Ref. [46].

Moreover, our elongated simulation box in Section 5.4.3 and 5.4.4 forces the system to phase separate with a planar interface. Only for such a geometry $J_z(z) = 0$, allowing us to write explicit expressions for mechanical and diffusive equilibrium. In other geometries the stationary state condition $\nabla \cdot \mathbf{J} = 0$ still allows for swirls that correspond to non-zero $\nabla \times \mathbf{J}$, for which our expressions for mechanical and diffusive equilibrium break down and a whole new framework is needed. Furthermore, the regime of applicability of Eq. (5.18) is limited by the underlying dynamic DFT relation, where a ρ-independent diffusion coefficient D_t is assumed; an extension to account for a ρ-dependent diffusion coefficient is left for a future study.

5.6 Conclusions & Discussion

In conclusion, we have constructed expression (5.17) for the local chemical potential $\mu(z)$ for active fluids in a planar geometry, which includes the swim potential $V_{\rm swim}(z)$ defined by Eq. (5.15) in addition to ideal, excess, and external contributions well-known from equilibrium. Our BD simulations confirm that $\mu(z)$ is spatially constant in steady states of several inhomogeneous ideal and interacting fluids of active particles, with $V_{\rm swim}(z)$ an important contribution that counteracts either the external potential $V_e(z)$ or the excess contribution $\mu_{\rm ex}(z)$. In the low activity regime studied for active LJ fluid, the chemical potential provides a method to predict the coexisting densities from bulk simulations. At high activity the *anisotropy* in the interface causes the Gibbs-Duhem relation to be

invalid, which which is similar to the finding of Ref. [46], where interfacial contributions are also required to determine the coexisting bulk densities.

The question that remains is this: have we been considering the wrong bulk equations of state, and can the coexisting densities be found from bulk quantities *other* than $\mu(\rho)$ and $P(\rho)$ (possiblity 1)? Or is it *generally* impossible to find the coexisting densities from bulk equations of state, and is information about the interface *always* required (possibility 2)?

Support for possibility 1 is provided by the work by van der Meer et al. [131]. For a phase coexistence of a mixture of active particles, they connect both coexisting phases to a (separate) reservoir via a membrane that is permeable to a single species only. Remarkably, they find that the two reservoirs attain equal densities in steady state. This equality - together with the equality of pressure $P(\rho)$ - allows them to correctly predict the coexisting densities. The finding that the reservoir densities are equal is a striking and nontrivial result. Yet, it is unclear *why* they are equal, and whether this translates into the equality of a quantity that can be measured in the bulk of the coexisting *phases* - rather than in the reservoirs - is still an open question.

The recent work by Hermann et al. [148] also provides support for possibility 1. This work defines a non-equilibrium chemical potential different from the one in this chapter, and proposes an ansatz for the crucial component of this chemical potential, which is the component that generates the ideal forces and adiabatic[b] interaction forces [31, 148]. With the help of two fit parameters, that represent the jamming density and the strength of the said chemical potential component, they find the coexisting densities to good accuracy. To the author of this thesis, this seems to be an impressive result. Yet, the proposed chemical potential is not fully microscopic, and a definite proof that possibility 1 rather than possiblity 2 is true would require a statistical proof that the agreement between the predicted and simulated coexisting densities is significant when taking the usage of the fit parameters into account.

As for possibility 2: one may think it very unlikely that the bulk densities of the coexisting phases are influenced by the interface. After all, the bulks can be very large[c], so that would mean that the interface affects the steady-state density profile at very large distances away. However, such an effect is not unheard of in active systems: in chapter 6, we give an example of a system where the steady-state density profile depends on the details of an external potential that is located an arbitrarily large distance away. Even though this effect is due to an *external* influence - rather than an internal one - it illustrates that such 'long-range dependencies' are possible, and therefore that possibility 2 cannot be ruled out - at least not on the grounds that the distance between the interface and (parts of the) bulks can be very large.

[b] See the footnote on p. 76 for an explanation of this term.

[c] In square-box computer simulations well into the MIPS regime, Siddharth Paliwal always found one dense cluster, rather than several clusters (provided the box is not too small) [165]. This suggests that there is no maximum cluster size. The largest cluster he obtained filled approximately 70% of a $250\sigma \times 250\sigma$ box, where the box size was limited by the required computation time. This cluster size corresponds to approximately three times the persistence length $\ell_p = v_0/D_r$, since the Péclet number was $\mathrm{Pe} = \ell_p/\sigma \approx 70$. Therefore, even though the author of this thesis sees no reason why a maximum cluster size should exist, it cannot be ruled out that there is a maximum cluster size larger than approximately $3\ell_p$.

5.7 Acknowledgements

This chapter is part of a collaboration with Siddharth Paliwal, Marjolein Dijkstra and René van Roij. Siddharth Paliwal performed all computer simulations and their analysis, whereas the author of this thesis was responsible for the Fokker-Planck calculations of the active ideal gas, and, together with Marjolein Dijkstra and René van Roij, for the conceptualization of the swim potential. We thank Vasileios Prymidis for providing initial estimates and configurations for simulating MIPS in 2D, and Laura Filion and Julien Tailleur for stimulating discussions.

6

The effect of an external potential: ratchet-induced variations in bulk states of an active ideal gas

In this chapter, we present another effect that makes the statistical physics of ABPs challenging: the steady-state density profile of ABPs can depend on the external potential arbitrarily far away.

In order to illustrate this effect in the simplest setting possible, we study the distribution of noninteracting ABPs over two bulk states separated by a ratchet potential. We show that, in a flux-free setting, the ratchet potential affects the steady-state distribution of particles over the bulks, which can be of arbitrarily large size. We characterize how the difference in bulk densities depends on activity and on the ratchet potential, and identify power law dependencies in several limiting cases. We rationalize our results by a simple transition state model that presumes particles to cross the potential barrier by Arrhenius rates modified for activity. While this model does not quantitatively describe the difference in bulk densities for feasible parameter values, it does reproduce - in its regime of applicability - the complete power law behavior correctly.

This chapter is based on the publication *"Ratchet-induced variations in bulk states of an active ideal gas"* [166], and is part of a collaboration with Siddharth Paliwal, Marjolein de Jager, Peter Bolhuis (University of Amsterdam), Marjolein Dijkstra and René van Roij. While the author of this thesis obtained all the results presented in this chapter, Siddharth Paliwal validated the density and polarization profiles using particle-based computer simulations, Marjolein de Jager validated the same profiles using a lattice model and first obtained the power laws of section 6.3.2, and Peter Bolhuis conceptualized the transition state model of section 6.5.

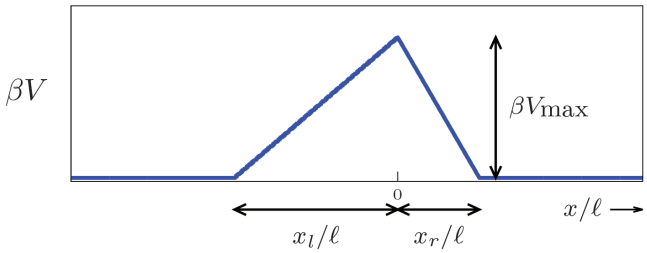

Figure 6.1: (Dimensionless) ratchet potential βV, as a function of the Cartesian x-coordinate in units of the diffusive length scale ℓ. The ratchet can be characterized by its height $\beta V_{\max}$, the width of its left side x_l/ℓ, and its asymmetry $a = (x_l - x_r)/x_r$.

6.1 Introduction

In chapter 5, we saw that it proved difficult to find the coexisting densities of the highly active MIPS, but also that they *could* be found for weakly active Lennard-Jones coexistences. This fits a trend: at small activity, active system are well understood by effective equilibrium approaches [130, 167–170]. In particular, it is well established that noninteracting particles at small activity can be described as an equilibrium system at an effective temperature [36, 130, 171–173]. For example, inserting the effective temperature in the Einstein relation yields the enhanced diffusion coefficient of an active particle, and using the effective temperature in the Boltzmann distribution gives the distribution of weakly active particles in a gravitational field [91, 91, 120, 173–177].

However, even weakly active systems can display behavior very different from equilibrium systems [99, 178–185]. For instance, a single array of funnel-shaped barriers, that is more easily crossed from one lateral direction than from the other, can induce a steady state with ratchet currents that span the entire system [181]. Alternatively, when the boundary conditions deny such a system-wide flux, the result is a steady state with a higher density on one side of the array than on the other [179, 181]. As the system can be arbitrarily long in the lateral direction, the presence of the funnels influences the steady-state density profile at arbitrarily large distance.

Characterizing such a long-range effect is a challenge, and the natural place to start is in a setting as simple as possible. As we shall show, having an external potential with a long-range influence on the steady-state density profile is only possible with the key ingredients of (1) activity, and (2) an external potential that is nonlinear. Therefore, a good candidate for a minimal model is to study the distribution of active particles over two bulks separated by a potential barrier that is only piecewise linear. Here, we focus on a sawtooth-shaped barrier, known as a ratchet potential (see Fig. 6.1). As we will see, the asymmetry of the ratchet induces a flux-free steady state with different densities in both bulks. Since the bulk sizes can be arbitrarily large, the ratchet potential indeed influences the steady-state density profile at arbitrarily large distance away. This system has actually already been studied, both experimentally [186] and theoretically [187]. However, the former study was performed at high degree of activity, and the latter study neglected

Brownian fluctuations, such that the degree of activity could not be quantified. Thereby, the regime of weak activity, where the statistical physics generally seems best understood [130, 141, 167–170], remains largely unexplored.

In this work, we study the effect of an external potential on arbitrarily large bulk regions with as few complications as possible. To this end, we investigate how a ratchet potential affects active particles that also undergo translational Brownian motion, such that the degree of activity can be quantified. We ask the questions: can we characterize how the external potential influences the density distribution as a function of activity? And can we understand this distribution in the limit of weak activity?

This chapter is organized as follows. In section 6.2, we introduce two active particle models, as well as the ratchet potential. In section 6.3, we numerically solve the density and polarization profiles of these active particles in the ratchet potential, and we study how the difference in bulk densities depends on activity, and on the ratchet potential. In section 6.4, we specialize to the limit of weak activity, and provide an analytical solution that explicitly shows that the nonzero difference in bulk densities cannot be understood by the use of an effective temperature. Instead, in section 6.5, we propose to understand the density difference in terms of a simple transition state model. We end with a discussion, in section 6.6, on what ingredients are necessary to have the external potential affect the densities in such a (highly) nonlocal way, and with concluding remarks in section 6.7.

6.2 Models

6.2.1 2D active Brownian particles

In order to investigate the behavior of active particles in a ratchet potential, we consider the widely employed model of active Brownian particles [109] (ABPs) in two dimensions. For simplicity, we consider spherical, noninteracting particles. Every particle is represented by its position $\mathbf{r}(t) = x(t)\hat{\mathbf{x}} + y(t)\hat{\mathbf{y}}$, where $\hat{\mathbf{x}}$ and $\hat{\mathbf{y}}$ are Cartesian unit vectors and t is time, as well as by its orientation $\hat{\mathbf{e}}(t) \equiv \cos\theta(t)\hat{\mathbf{x}} + \sin\theta(t)\hat{\mathbf{y}}$. Its time evolution is governed by the overdamped Langevin equations

$$\partial_t \mathbf{r}(t) = v_0\hat{\mathbf{e}}(t) - \gamma^{-1}\boldsymbol{\nabla}V(\mathbf{r}) + \sqrt{2D_t}\boldsymbol{\eta}_t(t), \tag{6.1a}$$

$$\partial_t \theta(t) = \sqrt{2D_r}\eta_r(t). \tag{6.1b}$$

Eq. (6.1a) expresses that a particle's position changes in response to (i) a propulsion force, that acts in the direction of $\hat{\mathbf{e}}$, and that gives rise to a propulsion speed v_0, (ii) an external force, generated by the external potential $V(\mathbf{r})$, and (iii) the unit-variance Wiener process $\boldsymbol{\eta}_t(t)$, that gives rise to translational diffusion with diffusion coefficient D_t. Here γ is the friction coefficient. Note that $\beta \equiv (\gamma D_t)^{-1}$ is an inverse energy scale, and that in thermodynamic equilibrium the Einstein relation implies $\beta = (k_B T)^{-1}$, where k_B is the Boltzmann constant and T the temperature. Eq. (6.1b) expresses that the orientation of a particle changes due to the unit-variance Wiener process $\eta_r(t)$, which leads to rotational diffusion with diffusion coefficient D_r.

The stochastic Langevin equations (6.1) induce a probability density $\psi(\mathbf{r},\theta,t)$, whose time evolution follows the Smoluchowski equation

$$\partial_t\psi = -\boldsymbol{\nabla}\cdot\Big(v_0\hat{\mathbf{e}}\psi - \frac{1}{\gamma}(\boldsymbol{\nabla}V)\psi - D_t\boldsymbol{\nabla}\psi\Big) + D_r\partial_{\theta\theta}\psi. \tag{6.2}$$

Here $\boldsymbol{\nabla} = (\partial_x,\partial_y)^T$ is the two-dimensional spatial gradient operator. Two useful functions to characterize the probability density $\psi(\mathbf{r},\theta,t)$ are the density $\rho(\mathbf{r},t) \equiv \int \mathrm{d}\theta\psi(\mathbf{r},\theta,t)$ and the polarization $\mathbf{m}(\mathbf{r},t) \equiv \int \mathrm{d}\theta\psi(\mathbf{r},\theta,t)\hat{\mathbf{e}}(\theta)$. Their time-evolutions follow from the Smoluchowski equation (6.2) as

$$\begin{aligned}\partial_t\rho &= -\boldsymbol{\nabla}\cdot\Big\{v_0\mathbf{m} - \frac{1}{\gamma}(\boldsymbol{\nabla}V)\rho - D_t\boldsymbol{\nabla}\rho\Big\},\\ \partial_t\mathbf{m} &= -\boldsymbol{\nabla}\cdot\Big\{v_0\Big(\boldsymbol{\mathcal{S}} + \frac{\mathbb{I}}{2}\rho\Big) - \frac{1}{\gamma}(\boldsymbol{\nabla}V)\mathbf{m} - D_t\boldsymbol{\nabla}\mathbf{m}\Big\} - D_r\mathbf{m},\end{aligned} \tag{6.3}$$

where $\mathbb{I}$ is the 2×2 identity matrix, and where $\boldsymbol{\mathcal{S}}(\mathbf{r},t) \equiv \int \mathrm{d}\theta\psi(\mathbf{r},\theta,t)(\hat{\mathbf{e}}(\theta)\hat{\mathbf{e}}(\theta) - \mathbb{I}/2)$ is the 2×2 nematic alignment tensor. Due to the appearance of $\boldsymbol{\mathcal{S}}$, Eqs. (6.3) are not closed. Therefore, solving Eqs. (6.3), rather than the full Smoluchowski Eq. (6.2), requires a closure, an example of which we discuss in section 6.2.2.

We consider a planar geometry that is invariant in the y-direction, i.e. $V(\mathbf{r}) = V(x)$, such that $\psi(\mathbf{r},\theta,t) = \psi(x,\theta,t)$, $\rho(\mathbf{r},t) = \rho(x,t)$, $\mathbf{m}(\mathbf{r},t) = m_x(x,t)\hat{\mathbf{x}}$ etc. The geometry consists of two bulks, located at $x \ll 0$ and $x \gg 0$. These bulk systems are separated by the ratchet potential

$$V(x) = \begin{cases} 0, & \text{for} \quad x < -x_l,\\ V_{\max}\Big(\dfrac{x}{x_l} + 1\Big), & \text{for} \quad -x_l < x < 0,\\ V_{\max}\Big(1 - \dfrac{x}{x_r}\Big), & \text{for} \quad 0 < x < x_r,\\ 0, & \text{for} \quad x_r < x, \end{cases} \tag{6.4}$$

where x_l and x_r are both positive. This sawtooth-shaped potential is illustrated in Fig. 6.1. Note that the potential is generally asymmetric, the degree of which is characterized by the asymmetry factor $a \equiv (x_l - x_r)/x_r$. Without loss of generality, we only consider ratchets for which $x_l > x_r$, such that $a > 0$.

The complete problem is specified by four dimensionless parameters. We use the rotational time D_r^{-1}, and the diffusive length scale $\ell \equiv \sqrt{D_t/D_r}$, which is proportional to the size of a particle undergoing free translational and rotational diffusion, to obtain the Péclet number

$$\begin{aligned} &\mathrm{Pe} \equiv \frac{1}{\sqrt{2}}\frac{v_0}{D_r\ell}, && \text{as a measure for the degree of activity,}\\ &\beta V_{\max}, && \text{the barrier height,}\\ &\frac{x_l}{\ell}, && \text{the width of the ratchet's left side,}\\ &a, && \text{the asymmetry of the ratchet.} \end{aligned} \tag{6.5}$$

We caution the reader that the factor $1/\sqrt{2}$ is often omitted from the definition of the Péclet number; it is included here to connect to the model described below.

6.2.2 1D Run-and-Tumble particles

The fact that there is only one nontrivial dimension in the problem suggests a simpler, one-dimensional model with the same physical ingredients. In this model, which we refer to as the 1D Run-and-Tumble (RnT) model, particles are characterized by a position $x(t)$, as well as by an orientation $e_x(t)$ that points in either the positive or the negative x-direction, i.e. $e_x = \pm 1$. The orientation e_x can flip with probability D_r per unit time. Every particle performs overdamped motion driven by (i) a propulsion force, that acts in the direction of its orientation, (ii) an external force, generated by the ratchet potential (6.4), and (iii) Brownian motion, with associated diffusion constant D_t. The problem can be specified in terms of probability density functions $\psi_\pm(x,t)$ to find particles with orientation $e_x = \pm 1$. For our purposes, it is more convenient to consider the density $\rho(x,t) \equiv \psi_+(x,t) + \psi_-(x,t)$, and polarization $m_x(x,t) \equiv [\psi_+(x,t) - \psi_-(x,t)]/\sqrt{2}$. These fields evolve as

$$\begin{aligned} \partial_t \rho &= -\partial_x \Big\{ \sqrt{2} v_0 m_x - \frac{1}{\gamma}(\partial_x V)\rho - D_t \partial_x \rho \Big\}, \\ \partial_t m_x &= -\partial_x \Big\{ \frac{v_0}{\sqrt{2}}\rho - \frac{1}{\gamma}(\partial_x V) m_x - D_t \partial_x m_x \Big\} - D_r m_x. \end{aligned} \tag{6.6}$$

Note the similarity of Eqs. (6.6) with Eqs. (6.3) of the 2D ABP model. In fact, if we define the Péclet number for the 1D RnT model as $\mathrm{Pe} \equiv v_0/(D_r \ell)$, then supplying the 2D ABP model with the closure $\boldsymbol{\mathcal{S}}(\mathbf{r},t) = 0$ maps Eqs. (6.3) to the 1D RnT model. The mapping is such that if one uses the same values for the dimensionless parameters Pe, $\beta V_{\max}$, x_l/ℓ, and a, then both models yield equal density profiles $\rho(x)$ and polarization profiles $m_x(x,t)$. As the closure $\boldsymbol{\mathcal{S}}(\mathbf{r},t) = 0$ is exact in the limit of weak activity, i.e. $\mathrm{Pe} \ll 1$, this mapping is expected to give good agreement between the two models for small values of the Péclet number Pe.

6.3 Numerical solutions

6.3.1 Density and mean orientation profiles

We study steady state solutions of both 2D ABPs and 1D RnT particles in the ratchet potential (6.4). To find the solutions, for the 2D ABP model we numerically solve Eq. (6.2) with $\partial_t \psi = 0$, whereas for the 1D model we numerically solve Eqs. (6.6) with $\partial_t \rho = \partial_t m_x = 0$. We impose the following three boundary conditions.

1. To the left of the ratchet, we imagine an infinitely large reservoir that fixes the density to be ρ_l at $x_{\mathrm{res}} \ll -x_l$, i.e. we impose $\psi(x_{\mathrm{res}}, \theta) = (2\pi)^{-1}\rho_l$ for the 2D case, and $\rho(x_{\mathrm{res}}) = \rho_l$, $m_x(x_{\mathrm{res}}) = 0$ for the 1D case.

2. To the right of the ratchet, we assume an isotropic bulk that is thermodynamically large, yet finite, such that its density follows from the solution of the equations. In technical terms, at $x_{\max} \gg x_r$ we impose $\partial_x \psi(x_{\max}, \theta) = 0$ for the 2D case, and $\partial_x \rho(x_{\max}) = 0$, $m_x(x_{\max}) = 0$ for the 1D case.

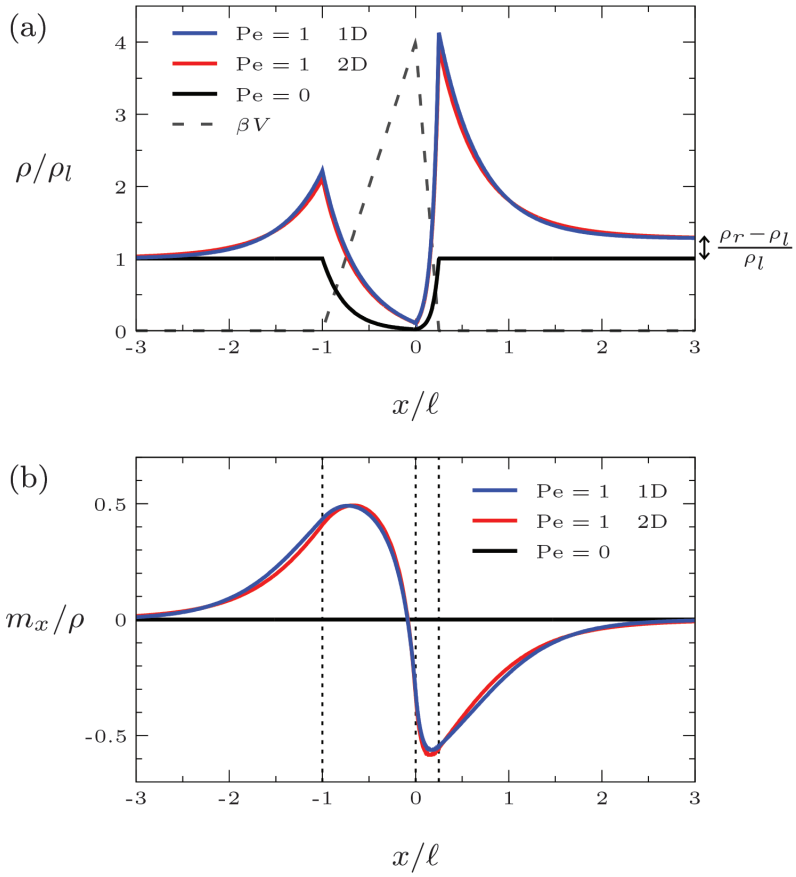

Figure 6.2: (a) Density profiles $\rho(x)/\rho_l$ and (b) mean orientation profiles $m_x(x)/\rho(x)$ of 2D ABPs, and 1D RnT particles, as indicated, in a ratchet potential $V(x)$ of height $\beta V_{\max} = 4$, width $x_l/\ell = 1$, and asymmetry $a = 3$. The dashed, vertical lines indicate the positions of the barrier peak ($x = 0$) and the ratchet sides ($x = -x_l$ and $x = x_r$). The bulk density to the left of the ratchet is $\rho(x \ll -x_l) = \rho_l$. Passive particles (Pe = 0) are distributed isotropically ($m_x = 0$), with a density profile given by the Boltzmann weight $\rho(x) = \rho_l \exp(-\beta V(x))$. Consequently, the densities ρ_l and ρ_r in the bulks on either side of the ratchet are equal. Active particles (Pe = 1) display much richer behaviour, with an accumulation of particles at either side of the ratchet, with a mean orientation towards the barrier peak, with a depletion of particles near the top of the ratchet, and with the right bulk density ρ_r exceeding the left bulk density ρ_l.

3. Additionally, for the 2D case we identify $\theta = 0$ with $\theta = 2\pi$, i.e. $\psi(x, 0) = \psi(x, 2\pi)$ and $\partial_\theta \psi(x, 0) = \partial_\theta \psi(x, 2\pi)$ for all x.

In order to allow the profiles to decay to their bulk values specified by boundary conditions 1 and 2, in our numerical calculations we always ensure the distance between x_{res} (or x_{max}) and the ratchet potential to be at least a multitude of the most significant length scale.

Typical solutions are shown in Fig. 6.2. The considered ratchet potential, with height $\beta V_{\text{max}} = 4$, width $x_l/\ell = 1$, and asymmetry $a = 3$, is shown as the dashed line in Fig. 6.2(a). We consider both a passive system (Pe = 0) and an active system (Pe = 1), using $x_{\text{res}} = -11l$ and $x_{\text{max}} = 10.25l$ in this case. The resulting density profiles and mean orientation profiles are shown in Fig. 6.2(a) and Fig. 6.2(b), respectively. For the passive system, the solution is isotropic (i.e. $\psi(x, \theta) \propto \rho(x)$ and $m_x(x) = 0$ everywhere), and given by the Boltzmann weight $\rho(x) = \rho_l \exp(-\beta V(x))$. One checks that these solutions indeed solve Eqs. (6.2) and (6.6) when the propulsion speed v_0 equals 0. Thus, in accordance with this Boltzmann distribution, the density in the passive system is lower in the ratchet region than in the left bulk, and its value $\rho_r \equiv \rho(x_{\text{max}})$ in the right bulk satisfies $\rho_r = \rho_l$, with ρ_l the density in the left bulk. This is a necessity in thermodynamic equilibrium, even for interacting systems: the equality of the external potential implies equal densities of the bulks.

For the active case (Pe = 1), the behavior is much richer. Firstly, the solution is anisotropic in the ratchet region, even though the external potential is isotropic. Indeed, Fig. 6.2(b) shows a mean orientation of particles directed towards the barrier on either side of the ratchet. This is consistent with the finding that active particles tend to align against a constant external force [174, 188], but is also reminiscent of active particles near a repulsive wall. Indeed, at walls particles tend to accumulate with a mean orientation towards the wall [114, 189], and a similar accumulation is displayed by the density profiles of Fig. 6.2(a) at the ratchet sides $x = -x_l$ and $x = x_r$. The overall result is an accumulation of particles at the ratchet sides, a depletion of particles near the center of the ratchet, and, remarkably, a density ρ_r in the right bulk that is higher than the density ρ_l in the left bulk.

The fact that the difference in bulk densities $\Delta\rho \equiv \rho_r - \rho_l$ is positive is caused by the asymmetry of the ratchet: due to their propulsion force, particles can cross the potential barrier more easily from the shallower, left side than from the steeper, right side. This argument is easily understood in the absence of translational Brownian motion ($D_t = 0$), i.e. when the only force that makes particles move (apart from the external force) is the propulsion force. Indeed, in this case, one can even think of ratchet potentials whose asymmetry is such that particles *can* climb it from the shallow side, but *not* from the steep side [187]. For such a ratchet potential, *all* particles eventually end up on the right side of the ratchet, such that clearly the right bulk density ρ_r exceeds the left bulk density ρ_l. The effect of having nonzero translational Brownian motion ($D_t > 0$) is that particles always have *some* probability to climb also the steep side of the ratchet. This leads to a density difference $\Delta\rho$ that is smaller than in the $D_t = 0$ case. Yet, as long as the ratchet is asymmetric, the density difference *always* turns out positive for *any* positive activity Pe.

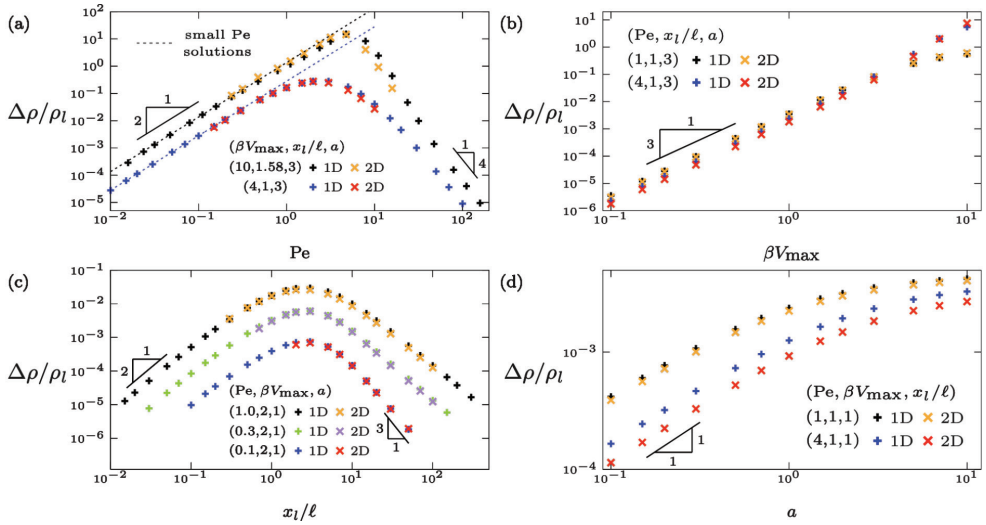

Figure 6.3: Normalized density difference $\Delta\rho/\rho_l$ as a function of (a) activity Pe, (b) barrier height $\beta V_{\max}$, (c) barrier width x_l/ℓ, and (d) barrier asymmetry a. Results are shown for both the 2D ABP and 1D RnT models, as indicated. In the limiting cases of small and large values of its arguments, the density difference shows power law behavior. The corresponding exponents are listed in Table 6.1. Additionally, (a) shows the density difference obtained analytically in the limit of weak activity (see section 6.4), for the same ratchet parameters as used for the numerical solutions. The analytical and numerical solutions show good agreement up to $\mathrm{Pe} \approx 0.5$.

We stress that the fact that $\rho_r > \rho_l$ is actually quite remarkable. The reason is that, whereas the ratchet potential is localized around $x = 0$, the right bulk can be arbitrarily large. Since our results clearly show that the right bulk density ρ_r is influenced by the ratchet, this means that the steady-state density profile depends on the details of the external potential at arbitrarily large distance.

Note that the *instantaneous* profile is, according to Eq. (6.2), only influenced by the external potential *locally*. What is happening is that the ratchet potential acts as a particle 'pump': if one starts with equal and homogeneous densities on either side of the ratchet potential, then the ratchet will locally generate a particle current. This particle current will change the density profile immediately adjacent to the ratchet. These density perturbations, in turn, will spread over the adjacent bulks. If the bulks are indeed arbitrarily large, then the time it takes the density perturbations to spread over the entire bulks will also be arbitrarily large, and the same will be true for the time it takes the system to reach its final steady state. Nonetheless, if one wants to find the final steady-state density at a given location, then one needs to know the details of the external potential at arbitrarily large distance away[a] - and this makes it much harder to find the steady-state density profile for an active than for a passive system.

[a] and/or solve for the complete history of the system.

		exponent		
base	limit	numerical solution	$\mathrm{Pe} \ll 1$ solution	transition state model
Pe	$\mathrm{Pe} \ll 1$	2	2	2
	$\mathrm{Pe} \gg 1$	-4		
$\beta V_{\max}$	$\beta V_{\max} \ll 1$	3	3	
	$\beta V_{\max} \gg 1$	0	0	0
x_l/ℓ	$x_l/\ell \ll 1$	2	2	2
	$x_l/\ell \gg 1$	*	-3	
a	$a \ll 1$	1	1	1
	$a \gg 1$	0	0	0

*depends on Pe. For $\mathrm{Pe} \ll 1$, this exponent equals -3.

Table 6.1: Power laws $\Delta\rho \propto \text{base}^{\text{exponent}}$, for limiting values of the base. Here the base denotes either the activity Pe, the barrier height $\beta V_{\max}$, the barrier width x_l/ℓ, or the barrier asymmetry a. Exponents were obtained numerically for the 1D RnT and 2D ABP models (yielding consistent exponents), analytically for the case of small activity $\mathrm{Pe} \ll 1$, and for a simple transition state model. Exponents are shown only in limits where the corresponding solution is applicable.

6.3.2 Scaling of the bulk density difference $\Delta\rho$

Next, we examine, one by one, how the density difference $\Delta\rho$ depends on activity Pe, the barrier height $\beta V_{\max}$, the barrier width x_l/ℓ, and on the barrier asymmetry a. The results are shown in Figs. 6.3(a)-(d), for both the 2D ABP and the 1D RnT models. In all cases, both models give density differences that are quantitatively somewhat different, but qualitatively similar, as they are both consistent with identical power laws[b].

Fig. 6.3(a) shows the density difference as a function of activity Pe, for two different ratchet potentials. For small Pe, the figure shows that the density difference increases as Pe^2. For large Pe, the density difference decreases again, to decay to 0 in the limit $\mathrm{Pe} \to \infty$. The reason for this decrease is that particles with high activity can easily climb either side of the ratchet potential, such that they hardly notice the presence of the barrier at all. As shown by Fig. 6.3(a), this decay follows the power law $\Delta\rho \propto \mathrm{Pe}^{-4}$. Whereas the prefactors of these power laws are different for the two different ratchet potentials considered, the exponents were found to be independent of the ratchet parameters, which was tested for many more values of $\beta V_{\max}$, x_l/ℓ, and a.

Fig. 6.3(b) shows the density difference as a function of the barrier height $\beta V_{\max}$. The barrier width, $x_l/\ell = 1$, and asymmetry, $a = 3$, are kept fixed, and two levels of activity, $\mathrm{Pe} = 1$ and $\mathrm{Pe} = 4$, are considered. For all cases, we find the power law $\Delta\rho \propto (\beta V_{\max})^3$, up to values of the barrier height $\beta V_{\max} \approx 3$. Exploring the behavior for large values of the barrier height $\beta V_{\max}$ was numerically not feasible, but the fact that the curves for ac-

[b]For numerical reasons, fewer results were obtained for the 2D ABP model than for the 1D RnT model. Therefore, not all of the power laws obtained for the 1D model could be tested for the 2D model. Yet, all 2D results seem consistent with all of the power laws.

tivity $\mathrm{Pe} = 1$ level off for barrier heights $\beta V_{\max} \geq 5$ seems consistent with the asymptotic behavior for $\beta V_{\max} \gg 1$ that we shall obtain, in section 6.4, in the limit of weak activity.

Fig. 6.3(c) shows the density difference as a function of the width x_l/ℓ of the left side of the ratchet. Here the barrier height and asymmetry are fixed, at $\beta V_{\max} = 2$ and $a = 1$, respectively, whereas the degree of activity is varied as $\mathrm{Pe} = 0.1, 0.3$, and 1. For small barrier widths, i.e. for $x_l/\ell \ll 1$, the curves show the power law $\Delta\rho \propto (x_l/\ell)^2$, independent of the activity Pe. For very wide barriers, i.e. for $x_l/\ell \gg 1$, the curves show power law behavior with an exponent that does depend on the activity Pe. For the smallest degree of activity, $\mathrm{Pe} = 0.1$, this exponent is found to equal -3. This scaling, $\Delta\rho \propto (x_l/\ell)^{-3}$ for large widths $x_l/\ell \gg 1$, will also be obtained analytically in section 6.4 for the case of weak activity.

Finally, Fig. 6.3(d) shows the density difference as a function of the barrier asymmetry a. The barrier height and width are fixed, at $\beta V_{\max} = 1$ and $x_l/\ell = 1$, respectively, and the degree of activity is varied as $\mathrm{Pe} = 1$ and $\mathrm{Pe} = 4$. For nearly symmetric ratchets, i.e. for $a \ll 1$, all curves show $\Delta\rho \propto a$, whereas for large asymmetries $a \gg 1$ the curves suggest asymptotic behavior, i.e. $\Delta\rho \propto a^0$. This asymptotic behavior can be understood on physical grounds, as the limit $a \to \infty$ corresponds to a ratchet whose right slope is vertical, a situation that we expect to lead to a finite density difference indeed.

All discussed scalings are summarized in Table 6.1. Of these, the scaling $\Delta\rho \propto \mathrm{Pe}^2$ for small activity $\mathrm{Pe} \ll 1$ can be regarded as trivial. The reason is that, in an expansion of the density difference $\Delta\rho$ around $\mathrm{Pe} = 0$, the quadratic term is the first term to be expected on general grounds: (i) Eqs. (6.2) and (6.6) are invariant under a simultaneous inversion of the self-propulsion speed ($v_0 \to -v_0$) and the orientation ($\hat{\mathbf{e}} \to -\hat{\mathbf{e}}$, and hence $m_x \to -m_x$), such that the expansion of the density difference $\Delta\rho$ contains only even powers of Pe, and (ii) for the passive case ($\mathrm{Pe} = 0$), the density difference $\Delta\rho$ equals 0, such that the zeroth order term is absent. Similarly, the obtained scaling $\Delta\rho \propto a$ is as expected: since a symmetric ratchet ($a = 0$) leads to the density difference $\Delta\rho = 0$, the leading order term one expects in an expansion of the density difference $\Delta\rho$ around $a = 0$ is linear in the asymmetry a. However, all other scalings listed in Table 6.1 cannot be predicted by such general arguments, and are therefore nontrivial findings.

We emphasize that these results have been obtained and verified by multiple approaches independently. While the presented results have been obtained by numerically solving the differential equations (6.2) and (6.6) as explained above, both the 2D ABP model and the 1D RnT model were also solved by separate approaches. For the 2D ABP model, results were additionally obtained by numerically integrating the Langevin equations (6.1) in particle-based computer simulations. For the 1D RnT model, results were also obtained by solving a lattice model, where particles can hop to neighbouring lattice sites, and change their orientation, with probabilities that reflect the same physical processes of self-propulsion, external forcing, translational Brownian motion, and tumbling[190]. For both the 2D ABP and the 1D RnT model, the two alternative approaches showed full agreement with the presented results.

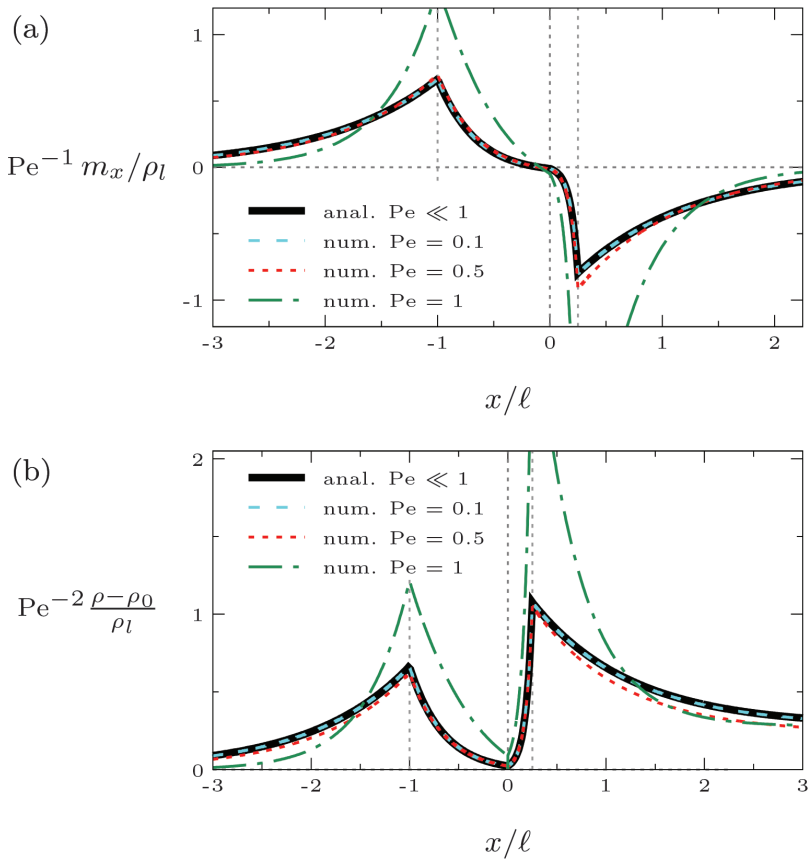

Figure 6.4: (a) Normalized polarization profiles $m_x(x)/\rho_l$ and (b) deviations of the density $\rho(x)$ from the passive solution $\rho_0(x)$, for a ratchet potential of height $\beta V_{\max} = 4$, width $x_l/\ell = 1$, and asymmetry $a = 3$. The dashed, vertical lines indicate the positions of the barrier peak ($x = 0$) and the ratchet sides ($x = -x_l$ and $x = x_r$). Results are shown for the analytical $\mathrm{Pe} \ll 1$ solution, and for the numerical solutions to the 1D RnT model, for activity levels $\mathrm{Pe} = 0.1, 0.5$ and 1. The polarizations and density deviations are divided by Pe and Pe^2, respectively, such that the curves for the analytical solution are independent of Pe.

6.4 Weak activity limit

Having characterized how the ratchet potential influences the densities of the adjoining bulks, we now turn to the question whether we can better understand this effect. We first try to answer this question for the simplest case possible, and therefore focus on the limit of weak activity, i.e. $\mathrm{Pe} \ll 1$. Recall that in this limit the 2D ABP model and the 1D RnT model are equivalent. In this section, we present an analytical solution for the $\mathrm{Pe} \ll 1$ limit. In the next section, we propose to rationalize its results by a simple transition state model, that is valid for, but not limited to, weak activity.

In case of a small propulsion force, i.e. of $\mathrm{Pe} \ll 1$, the density can be expanded as $\rho(x) = \rho_0(x) + \mathrm{Pe}^2\rho_2(x) + \mathcal{O}(\mathrm{Pe}^4)$, and the polarization as $m_x(x) = \mathrm{Pe}\, m_1(x) + \mathcal{O}(\mathrm{Pe}^3)$. Here $\rho_0(x)$, $\rho_2(x)$ and $m_1(x)$ are assumed to be independent of Pe. We used the arguments that the density $\rho(x)$ is an even function of Pe, and the polarization $m_x(x)$ an odd function of Pe, as explained in section 6.3.2. With these expansions, Eqs. (6.6) can be solved perturbatively in Pe, separately for each region where the ratchet potential (6.4) is defined. As shown in the appendix, the solutions within one region are

$$\begin{aligned}
\rho_0(x) =& A_0 e^{-\beta V(x)},\\
m_1(x) =& -\frac{A_0}{\sqrt{2}} f e^{-\beta V(x)} + B_+ e^{c_+ x/\ell} + B_- e^{c_- x/\ell},\\
\rho_2(x) =& \left[A_2 - A_0 f \frac{x}{\ell}\right] e^{-\beta V(x)}\\
&+ \frac{\sqrt{2}B_+}{c_+ - f} e^{c_+ x/\ell} + \frac{\sqrt{2}B_-}{c_- - f} e^{c_- x/\ell}.
\end{aligned} \tag{6.7}$$

Here we defined the non-dimensionalized external force $f(x) \equiv -\beta\ell\partial_x V(x)$, such that $f = 0$ for $x < -x_l$, $f = -\beta V_{\max}\ell/x_l$ for $-x_l < x < 0$, $f = \beta V_{\max}\ell/x_r$ for $0 < x < x_r$, and $f = 0$ for $x > x_r$, in accordance with Eq. (6.4). Furthermore, we defined $c_\pm \equiv (f \pm \sqrt{f^2+4})/2$. The integration constants A_0, A_2, B_+, and B_- are found separately for each region, by applying the boundary conditions $\rho(-\infty) = \rho_l$, $m(\infty) = m(-\infty) = 0$, and the appropriate continuity conditions at the region boundaries $x = -x_l$, $x = 0$ and $x = x_r$. Applying these conditions to the solutions $\rho_0(x)$ in Eq. (6.7) shows that the leading order solution is given by the Boltzmann weight, i.e. $\rho_0(x) = \rho_l \exp(-\beta V(x))$ for all x. Clearly, this is the correct passive solution. The higher order solutions that follow, i.e. the polarization profile $m_1(x)$ and the density correction $\rho_2(x)$, are plotted in Fig. 6.4. Qualitatively, these plots show the same features as displayed by the numerical solutions in Fig. 6.2: an accumulation of particles facing the barrier at the ratchet sides $x = -x_l$ and $x = x_r$, and a right bulk density ρ_r that exceeds the left bulk density ρ_l. To allow for a quantitative comparison, Fig. 6.4 also shows polarization profiles $m_x(x)$ and density corrections $\rho(x) - \rho_0(x)$ that were obtained for the 1D RnT model numerically. While the ratchet potential is fixed, with barrier height $\beta V_{\max} = 4$, width $x_l/\ell = 1$, and asymmetry $a = 3$, the comparison is made for several degrees of activity, namely $\mathrm{Pe} = 0.1, 0.5,$ and 1. The analytical and numerical results show good agreement for $\mathrm{Pe} = 0.1$, reasonable agreement for $\mathrm{Pe} = 0.5$, and deviate significantly for $\mathrm{Pe} = 1$. All of these observations are as expected, since the analytical solutions (6.7) are obtained under the assumption $\mathrm{Pe} \ll 1$.

The most interesting part of solution (6.7) is the density correction $\rho_2(x)$, as this

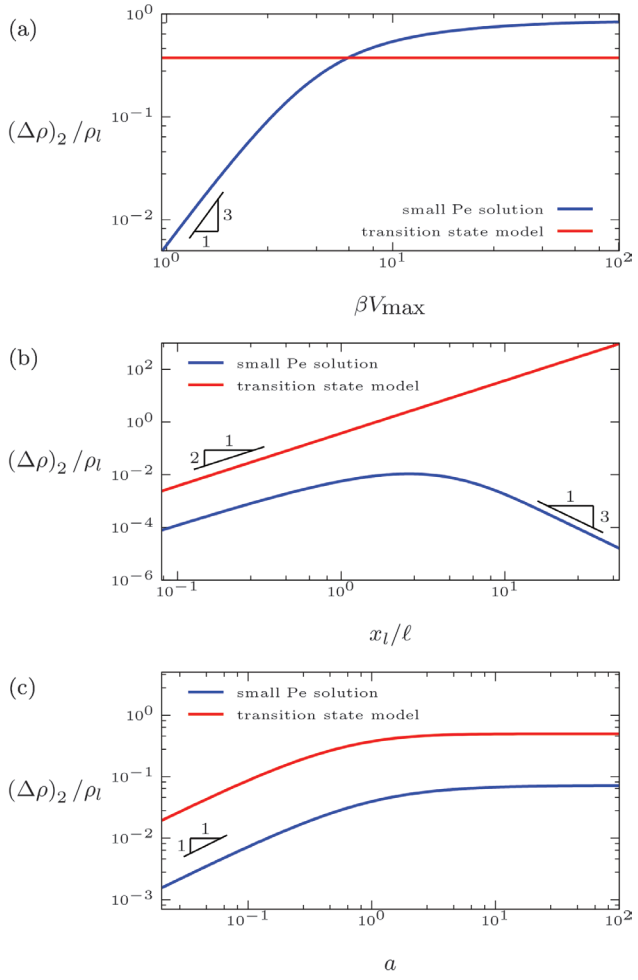

Figure 6.5: Normalized leading order coefficient $(\Delta\rho)_2$ in the expansion of the density difference $\Delta\rho$ for small activity Pe, as found from the analytical Pe $\ll 1$ solution and as predicted by the transition state model, (a) as a function of the barrier height $\beta V_{\max}$, at fixed barrier width $x_l/\ell = 1$ and asymmetry $a = 1$, (b) as a function of the barrier width x_l/ℓ, at fixed barrier height $\beta V_{\max} = 1$ and asymmetry $a = 1$, and (c) as a function of the asymmetry a, at fixed barrier height $\beta V_{\max} = 2$ and barrier width $x_l/\ell = 1$. The power laws shown by the transition state model in its regime of applicability, i.e. for $\beta V_{\max} \gg 1$ and $x_l/\ell \ll 1$, have exponents that agree with the power laws of the analytical solution. These exponents can be found in Table 6.1. The analytical and transition state solution do not agree quantitavely for these parameter values.

correction contains the leading order contribution to the difference in bulk densities $\Delta\rho$. To gain some understanding for the meaning of the various terms contributing to $\rho_2(x)$, we point out that for small activity, i.e. for $\mathrm{Pe} \ll 1$, active particles are often understood as passive particles at an effective temperature [36, 120, 130, 171–173]. In our convention, this effective temperature reads $T_{\text{eff}} = T(1 + \mathrm{Pe}^2)$. Therefore, one might think that for our weakly active system the density profile is given by Boltzmann weight at this effective temperature, i.e. by $\rho(x) = A \exp(-V(x)/k_B T_{\text{eff}})$ within one region. Here the prefactor A can depend on the activity Pe. Expanding this effective Boltzmann weight for small Pe yields the passive solution $\rho_0(x)$, and the terms on the first line of $\rho_2(x)$ in Eq. (6.7). However, it does *not* reproduce the final two terms that contribute to $\rho_2(x)$ in Eq. (6.7). Precisely these last two terms are crucial to obtain a nonzero difference $\Delta\rho$ in bulk densities. Indeed, a density profile given solely by the effective Boltzmann weight necessarily yields equal bulk densities $\rho_l = \rho_r$, as the external potential $V(x)$ is equal on either side of the ratchet.

The analytical expression for the difference in bulk densities $\Delta\rho$, implied by the solutions (6.7), is rather lengthy and intransparent, and is therefore not shown here. Instead, we show the dependence of $\Delta\rho$ on the activity Pe graphically, in Fig. 6.3(a), for the same two ratchet potentials as used for the numerical solutions. As the density difference $\Delta\rho$ follows from the correction $\rho_2(x)$, it scales as Pe^2, just like the numerical solutions for $\mathrm{Pe} \ll 1$. As shown by Fig. 6.3(a), the analytical and numerical solutions agree quantitatively up to $\mathrm{Pe} \approx 0.5$, as also found in Fig. 6.4. Before we illustrate how the density difference $\Delta\rho$ depends on the ratchet potential, we extract its dependence on activity Pe by considering $(\Delta\rho)_2 = \Delta\rho/\mathrm{Pe}^2$, i.e. the leading order coefficient in an expansion of $\Delta\rho$ around $\mathrm{Pe} = 0$. The coefficient $(\Delta\rho)_2$ is independent of Pe, but still depends on the barrier height $\beta V_{\max}$, the barrier width x_l/ℓ, and the asymmetry a. Its dependence on these ratchet parameters is plotted in Figs. 6.5(a)-(c), respectively. These figures display all the power law behavior that was obtained numerically in section 6.3. The power laws are summarized in Table 6.1.

6.5 Transition State Model

As argued in the previous section, the nonzero difference in bulk densities $\Delta\rho$ cannot be accounted for by the effective temperature that is often employed in the weak activity limit. Instead, to understand the behavior of the bulk density difference $\Delta\rho$ better, we propose the following simple transition state model. The model consists of four states, designed to mimic the 1D RnT model in a minimal way. Particles in the bulk to the left of the ratchet, with an orientation in the positive (negative) x-direction, are said to be in state $l_+(l_-)$, whereas particles in the bulk to the right of the ratchet, with positive (negative) x-orientation, are in state $r_+(r_-)$. This setting is illustrated in Fig. 6.6. Particles can change their orientation, i.e. transition from $l_\pm$ to $l_\mp$, and from $r_\pm$ to $r_\mp$, with a rate D_r. Furthermore, particles can cross the potential barrier and transition between the l- and r-states. The associated rate constants are assumed to be given by modified Arrhenius rates [191–193], where the effect of self-propulsion is to effectively increase or

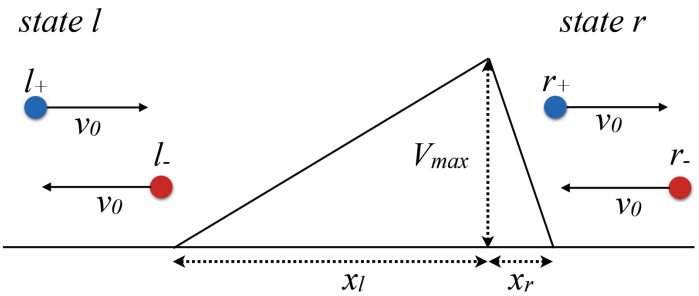

Figure 6.6: Illustration of the states in the transition state model. Particles in the left bulk with positive (negative) x-orientation are in state $l_+(l_-)$. Similarly, particles in the right bulk are in state r_+ or r_-. Within one bulk, particles can change their orientation with rate constant D_r. Between the bulks, particles can transition by crossing the potential barrier with the effective Arrhenius rates of Eqs. (6.8) and (6.9), where the effect of self-propulsion is to shift the potential barrier $V_{\max}$ by the work $\gamma v_0 x_l$ ($\gamma v_0 x_r$) performed by the propulsion force when a particles climbs the left (right) slope of the ratchet.

decrease the potential barrier. For example, the rate to transition from l_+ to r_+ is

$$k_{l_+\to r_+} = \frac{\nu_l}{L_l} \exp\left[-\beta(V_{\max} - \gamma v_0 x_l)\right]. \tag{6.8}$$

As the propulsion force helps the particle to cross the barrier, it effectively lowers the potential barrier $V_{\max}$ by the work $\gamma v_0 x_l$ that the propulsion force performs when the particle climbs the left slope of the ratchet. This modified Arrhenius rate is expected to be valid under the assumptions (a) of a large barrier height $\beta V_{\max} \gg 1$, which is a condition for the Arrhenius rates to be valid even for passive systems [194], (b) of a ratchet potential that is typically crossed faster than a particle reorients, which can be achieved by making the barrier width x_l/ℓ sufficiently small, and (c) that the work $\gamma v_0 x_l$ performed by the propulsion force is much smaller than the barrier height $V_{\max}$. We point out that assumption (c) can be rewritten as $\mathrm{Pe} \ll \beta V_{\max}\ell/x_l$. This means that if assumptions (a) and (b) are satisfied, which imply that $\beta V_{\max}\ell/x_l \gg 1$, then assumption (c) is not much further restrictive on the activity Pe. The remaining rate constants follow along a similar reasoning as

$$\begin{aligned} k_{l_-\to r_-} &= \frac{\nu_l}{L_l} \exp\left[-\beta(V_{\max} + \gamma v_0 x_l)\right], \\ k_{r_+\to l_+} &= \frac{\nu_r}{L_r} \exp\left[-\beta(V_{\max} + \gamma v_0 x_r)\right], \\ k_{r_-\to l_-} &= \frac{\nu_r}{L_r} \exp\left[-\beta(V_{\max} - \gamma v_0 x_r)\right]. \end{aligned} \tag{6.9}$$

For large bulks on either side of the ratchet, the attempt frequencies in the rate expressions (6.8) and (6.9) are inversely proportional to the size of the bulk that is being transitioned from. This size is denoted by L_l for the left bulk, and by L_r for the right bulk. Therefore, the factors ν_l and ν_r are independent of the bulk sizes L_l and L_r, and can only depend on the shape of the rachet potential, i.e. on its height $\beta V_{\max}$, on its width x_l/ℓ, and on

its asymmetry a.

We denote the number of particles in the $l_\pm$ and $r_\pm$ states by $N_{l_\pm}(t)$ and $N_{r_\pm}(t)$, respectively. The time evolution of these particle numbers follows from the rates outlined above. For example, the number of particles $N_{l_+}(t)$ in state l_+ evolves according to the rate equation

$$\partial_t N_{l_+} = -\Big(D_r + k_{l_+\to r_+}\Big) N_{l_+} + D_r N_{l_-} + k_{r_+\to l_+} N_{r_+}. \tag{6.10}$$

Similar equations hold for the particle numbers $N_{l_-}(t)$, $N_{r_+}(t)$ and $N_{r_-}(t)$. These rate equations can be solved in steady state, i.e. when $\partial_t N_{l_\pm} = \partial_t N_{r_\pm} = 0$, for the particle numbers $N_{l_\pm}$ and $N_{r_\pm}$. We consider infinitely large bulks, i.e. $L_l, L_r \to \infty$. In this case, the solutions show that $N_{l_+} = N_{l_-}$ and $N_{r_+} = N_{r_-}$, such that the l and r states correspond to isotropic bulks. Furthermore, the solution shows that the bulk densities $\rho_l = (N_{l_+} + N_{l_-})/L_l$ and $\rho_r = (N_{r_+} + N_{r_-})/L_r$ differ by an amount $\Delta\rho = \rho_r - \rho_l$ given by

$$\frac{\Delta\rho}{\rho_l} = \frac{\nu_l}{\nu_r} \frac{\cosh\left(\mathrm{Pe}\, x_l/\ell\right) - \cosh\left(\mathrm{Pe}\, x_r/\ell\right)}{\cosh\left(\mathrm{Pe}\, x_r/\ell\right)}, \tag{6.11}$$

where we recall that $x_r = (1+a)^{-1} x_l$. We point out that the ratio ν_l/ν_r can generally depend on the ratchet parameters $\beta V_{\max}$, x_l/ℓ, and a. However, in the following we simply assume $\nu_l/\nu_r = 1$, which is justified for nearly symmetric ratchets.

To enable a comparison with the analytical solution of the previous section, we now focus on the limit of weak activity, i.e. of $\mathrm{Pe} \ll 1$. This ensures assumption (c) to be satisfied, but we emphasize that the transition state model is not limited to weak activity. We expand the density difference (6.11) as $\Delta\rho = (\Delta\rho)_2\, \mathrm{Pe}^2 + \mathcal{O}(\mathrm{Pe}^4)$, and compare the coefficient $(\Delta\rho)_2$ with the same coefficient obtained in section 6.3 for the analytical solution in the weak activity limit. The coefficient $(\Delta\rho)_2$ is plotted in Figs. 6.5(a)-(c), as a function of the of the barrier height $\beta V_{\max}$, the barrier width x_l/ℓ, and the barrier asymmetry a, respectively. Fig. 6.5(a) merely illustrates that the density difference (6.11) is independent of the barrier height $\beta V_{\max}$. This independency agrees with the asymptotic behavior displayed by the analytical solution for large barrier heights $\beta V_{\max} \gg 1$. Note that the regime $\beta V_{\max} \gg 1$ is indeed assumed for the modified Arrhenius rates (assumption (b)). Fig. 6.5(b) illustrates that the density difference predicted by the transition state model scales quadratically with the barrier width, i.e. that $\Delta\rho \propto (x_l/\ell)^2$. This scaling agrees with the scaling of the analytical solution for the regime of small barrier widths $x_l/\ell \ll 1$. Again, this regime is assumed for the modified Arrhenius rates, as having a small barrier width is required for having particles cross the ratchet faster than they typically reorient (assumption (c)). Finally, Fig. 6.5(c) illustrates that the density difference predicted by the transition state model scales linearly with the barrier asymmetry for nearly symmetric ratchets, i.e. $\Delta\rho \propto a$ for $a \ll 1$, and asymptotically for very asymmetric ratchets, i.e. $\Delta\rho \propto a^0$ for $a \gg 1$. Both scalings are also displayed by the analytical solution. All these power laws can again be found in Table 6.1.

Of course, the transition state model reproduces only the power laws that lie inside its regime of applicability. However, the fact this simple model *does* reproduce all these power laws is quite remarkable, since, as discussed in section 6.3, most of these scalings are nontrivial. Furthermore, we note that the transition state model can also be solved

for finite bulk sizes, which in fact predicts a turnover of the density difference $\Delta\rho$ as a function of activity Pe, as observed in Fig. 6.3(a).

Quantitatively, Fig. 6.5 clearly shows that the predictions of the transition state model typically differ from the analytical solution by an order of magnitude. A possible reason for this disagreement is that these plots are made for parameters values that do not satisfy assumptions (a) and (b) that underly the modified Arrhenius rates. In fact, it turned out to be impossible to satisfy these assumptions simultaneously with feasible parameter values. The root of the difficulty is that the time it takes a particle to cross the potential barrier increases with the barrier height $\beta V_{\max}$. As a consequence, having a barrier that is simultaneously very high (assumption (a)), and typically crossed faster than a particle reorients (assumption (b)), turns out to require unrealistically small barrier widths x_l/ℓ. The quantitative mismatch of the transition state model with the full solution for small activity might also be attributed to the assumption that the prefactors ν_l and ν_r in the rate expressions (6.8) and (6.9) are not exactly identical, but in fact might depend on the precise shape of the barrier. However, this possibility goes beyond the current scope of this chapter, and we leave it for future study.

We conclude that, whereas it was not possible to test the predictions of the transition state model in its regime of applicability quantitatively, the model *does* reproduce the complete power law behavior of this regime correctly.

6.6 Discussion

The most interesting aspect of the studied system is that the external potential has a long-range influence on the steady-state density profile. This is in sharp contrast to an ideal gas in equilibrium, whose density profile is only a function of the *local* external potential. So what ingredients are necessary to obtain this effect? To answer this question, we consider the 1D RnT model subject to a general external potential $V(x)$. Furthermore, we introduce the particle current $J(x)$ and the orientation current $J_m(x)$ that appear in the evolution equations (6.6), i.e.

$$\begin{aligned} J(x) &= \sqrt{2}v_0 m_x - \frac{1}{\gamma}(\partial_x V)\rho - D_t\partial_x\rho, \\ J_m(x) &= \frac{v_0}{\sqrt{2}}\rho - \frac{1}{\gamma}(\partial_x V)m_x - D_t\partial_x m_x. \end{aligned} \tag{6.12}$$

We focus on a state that is steady, such that $J(x) = \text{constant} \equiv J$, and flux-free, such that $J = 0$. Then Eqs. (6.6) and (6.12) can be recast into the first order differential equation

$$\ell\partial_x \mathbf{Y}(x) = \boldsymbol{\mathcal{M}}(x)\mathbf{Y}(x) \tag{6.13}$$

for the three (non-dimensionalized) unknowns $\mathbf{Y}(x) \equiv (\ell\rho(x), \ell m_x(x), J_m(x)/D_r)^T$. The coefficient matrix in Eq. (6.13) is given by

$$\boldsymbol{\mathcal{M}}(x) = \begin{bmatrix} f(x) & \sqrt{2}\mathrm{Pe} & 0 \\ \mathrm{Pe}/\sqrt{2} & f(x) & -1 \\ 0 & -1 & 0 \end{bmatrix}, \tag{6.14}$$

where $f(x) \equiv -\beta\ell\partial_x V(x)$ is the dimensionless external force, that is now a function of position x. For a passive system (Pe = 0), Eqs. (6.13) and (6.14) show that the density equation decouples. In this case, the density profile is solved by the Boltzmann weight, i.e. $\rho(x) \propto \exp(-\beta V(x))$, as required in thermodynamic equilibrium. For the general case, we observe that, *if* the coefficient matrix $\boldsymbol{\mathcal{M}}(x)$ commutes with its integral $\int_{x_0}^{x} \mathrm{d}x' \boldsymbol{\mathcal{M}}(x')$, *then* Eq. (6.13) is solved by

$$\mathbf{Y}(x) = \exp\left(\frac{1}{\ell}\int_{x_0}^{x} \mathrm{d}x' \boldsymbol{\mathcal{M}}(x')\right) \cdot \begin{pmatrix} c_1 \\ c_2 \\ c_3 \end{pmatrix}, \tag{6.15}$$

where the integration constants c_1, c_2 and c_3 are to be determined from boundary conditions. Here x_0 is an arbitrary reference position. By virtue of $\int_{x_0}^{x} \mathrm{d}x' f(x') = -\beta\ell V(x)$, the solution (6.15) *is* a local function of the external potential. An explicit calculation of the commutator shows that $[\boldsymbol{\mathcal{M}}(x), \int_{x_0}^{x} \mathrm{d}x' \boldsymbol{\mathcal{M}}(x')] = 0$ if and only if $\beta(V(x) - V(x_0)) = -f(x)\,(x - x_0)/\ell$, i.e. if the external potential is a linear function of x. Therefore, for linear potentials, the density profile *is* a local function of the external potential. This explains why in a gravitational field the density profile *can* be found as a local function of the external potential, and why sedimentation profiles stand a chance to be described in terms of an effective temperature in the first place[35, 91, 120, 173–177, 188, 195–197]. However, for nonlinear external potentials, e.g. for the ratchet studied here that is only piecewise linear, the solution (6.15) is *not* valid, and a nonlocal dependence on the external potential is to be expected. Therefore, for the ratchet potential (6.4), the kinks at $x = -x_l$, $x = 0$ and $x = x_r$ are crucial to have a density that depends nonlocally on the external potential. Indeed, in the analytical solution for weak activity, presented in section 6.4, the nonlocal dependence of the right bulk density ρ_r on the external potential enters through the fact that the integration constants in Eq. (6.7) are found from continuity conditions that are applied precisely at the positions of these kinks.

Summarizing, in order to have the external potential influence the steady-state density of ideal particles in a nonlocal way, one needs to have (1) particles that are active (such that the system is out of thermodynamic equilibrium), and (2) an external potential that is nonlinear. Thereby, the 1D RnT particles in the ratchet potential (6.4) illustrate the nonlocal, and even long-range, influence of the external potential in a most minimal way.

In the discussion above, we have only shown that a linear external potential yields a density profile that is a strictly local function of the potential. Thereby, a nonlinear potential is not guaranteed to influence the density (arbitrarily) far away, and indeed other criteria have been discussed in the literature. For example, in the context of active Ornstein-Uhlenbeck particles, approximate locality was shown for a wide class of nonlinear potentials [93, 130], and it was argued that in order to lose this property it is crucial to have an external potential with nonconvex regions [198]. More generally, the fact that the potential barrier is more easily crossed from one side than from the other is a rectification effect, and it has been shown that such effects can occur when the dynamics break time-reversal symmetry, while also the spatial mirror symmetry is broken [199, 200]. In our case, these criteria are met by the presence of activity, and by having a ratchet that is asymmetric ($a \neq 0$), respectively.

Our results are also fully consistent with the work by Baek et al. [185], who study the

effect of placing a nonspherical body in a two-dimensional fluid of ABPs. They show that such an inclusion leads to a steady state with a density perturbation that scales in the far field as $1/r$, where r is the distance to the body. Repeating their derivation for the 1D RnT model in our setting yields a far-field density perturbation that is simply constant, i.e. independent of r. This is consistent with our findings. Furthermore, under suitable conditions, in particular that the external potential is small everywhere, the authors of [185] derive that the far-field density perturbation scales as $(V_{\max})^3$. This confirms our finding of the powerlaw $\Delta\rho \propto (\beta V_{\max})^3$ for small potential barriers $\beta V_{\max} \ll 1$. Moreover, it suggests that this scaling is not limited to the sawtooth-shaped potential barrier considered here, but also holds for external potentials of more general shape.

6.7 Conclusions

We have studied the distribution of noninteracting, active particles over two bulks separated by a ratchet potential. The active particles were modelled both as two-dimensional ABPs, and as one-dimensional RnT particles. Our numerical solutions to the steady state Smoluchowski equations show that the ratchet potential influences the distribution of particles over the bulks, even though the potential is short-ranged itself. Thus, the external potential influences the steady-state density profile at large distance away. We have shown that such a (highly) nonlocal influence can occur for noninteracting particles only when they are (1) active, and (2) subject to an external potential that is nonlinear. Thereby, the piecewise linear setup considered in this chapter captures this long-range influence in a most minimal way.

To characterize the influence of the external potential, we have described how the difference in bulk densities depends on activity, as well as on the ratchet potential itself. Both models of active particles showed consistent power law behavior that is summarized in Table 6.1.

To understand the "long-range influence" of the potential in the simplest case possible, we focussed on the limit of weak activity. While weakly active systems are often described by an effective temperature, our analytical solution explicitly shows that the influence of the ratchet potential cannot be rationalized in this way. Instead, we propose a simple transition state model, in which particles can cross the potential barrier by Arrhenius rates with an effective barrier height that depends on the degree of activity. While the model could not be tested quantitatively, as its underlying assumptions could not be simultaneously satisfied for feasible parameter values, it does reproduce - in its regime of applicability - the complete power law behavior of the distribution of particles over the bulks.

Future questions are whether the power law behavior can be understood also outside the regime where the transition state model applies, and whether the power laws also hold for potential barriers of more generic shape than the sawtooth of Fig. 6.1. Our work illustrates that even weakly active, noninteracting particles pose challenges that are fundamental to nonequilibrium systems, and, moreover, that an external potential can affect the steady-state profile arbitrarily far away in such systems. We express the hope that

such long-range and nonlocal effects can be incorporated into a more generic statistical mechanical description of nonequilibrium systems.

6.8 Acknowledgements

This chapter is part of a collaboration with Siddharth Paliwal, Marjolein de Jager, Peter Bolhuis, Marjolein Dijkstra and René van Roij. The author of this thesis obtained and analyzed all presented results; Siddharth Paliwal validated the density and polarization profiles using particle-based computer simulations; Marjolein de Jager validated the same profiles using a lattice model, and first obtained the power laws of section 6.3.2; Peter Bolhuis conceptualized the transition state model of section 6.5; and Marjolein Dijkstra and René van Roij helped by critically examining all results and identifying future directions throughout the research process.

Appendices

Appendix 6.A Weak Activity Solution

In this appendix, we derive the analytical solutions (6.7), i.e. the steady state solutions to the 1D RnT Eqs. (6.6) in the limit of weak activity. First, we define the particle flux $J(x) \equiv \sqrt{2}v_0 m_x - \gamma^{-1}(\partial_x V)\rho - D_t \partial_x \rho$, such that the evolution equation for the density, given by Eq. (6.6), reads $\partial_t \rho = -\partial_x J(x)$. Having a steady state ($\partial_t \rho = 0$) implies that $J(x) \equiv J$ is constant, i.e. independent of x. The boundary condition of having a bulk at $x = x_{\max}$ that is homogeneous and isotropic, and hence flux-free, then implies $J = 0$. The equation $J(x) = 0$ has to be solved together with the steady state condition for the polarization implied by Eq. (6.6). In dimensionless form, these equations read

$$\begin{aligned} 0 &= \sqrt{2}\mathrm{Pe}\, m_x + f(x)\rho - \ell\partial_x \rho, \\ 0 &= -\ell\partial_x \left\{ \frac{\mathrm{Pe}}{\sqrt{2}}\rho + f(x)m_x - \ell\partial_x m_x \right\} - m_x. \end{aligned} \tag{6.16}$$

Here, we defined the non-dimensionalized external force $f(x) \equiv -\beta\ell\partial_x V(x)$. We shall solve Eqs. (6.16) separately for every region where the ratchet potential (6.4) is a linear function. Within one such region, $f(x) = f$ is constant, namely $f = 0$ to the left and to the right of the potential barrier, $f = -\beta V_{\max}\ell/x_l$ on the left slope of the barrier, and $f = -\beta V_{\max}\ell/x_r$ on the right slope. We treat these cases simultaneously by simply writing $f(x) = f$, and keeping in mind that the solution holds only within one region. Furthermore, we focus on the limit of weak activity, i.e. of $\mathrm{Pe} \ll 1$, and expand the density as $\rho(x) = \rho_0(x) + \mathrm{Pe}^2\rho_2(x) + \mathcal{O}(\mathrm{Pe}^4)$, and the polarization as $m_x(x) = \mathrm{Pe}\, m_1(x) + \mathcal{O}(\mathrm{Pe}^3)$, as explained in the main text. We insert these expansions into Eqs. (6.16), and solve order by order in Pe. To zeroth order in Pe, the equations read $f\rho_0 - \ell\partial_x\rho_0 = 0$, and are solved by

$$\rho_0(x) = A_0 e^{fx/\ell}, \tag{6.17}$$

where A_0 is an integration constant. Note that Eq. (6.17) is the Boltzmann weight, and hence the correct passive solution for noninteracting particles. To linear order in Pe, the equations read

$$-\ell\partial_x \left(f m_1 - \ell\partial_x m_1 \right) - m_1 = \frac{1}{\sqrt{2}}\ell\partial_x \rho_0, \tag{6.18}$$

where $\rho_0(x)$ is given by Eq. (6.17). The solution to Eq. (6.18) is

$$m_1(x) = -\frac{A_0}{\sqrt{2}} f e^{fx/\ell} + B_+ e^{c_+ x/\ell} + B_- e^{c_- x/\ell}, \tag{6.19}$$

where B_+ and B_- are integration constants, and where $c_\pm \equiv (f \pm \sqrt{f^2+4})/2$. To quadratic order in Pe, the equations read

$$f\rho_2 - \ell\partial_x\rho_2 = -\sqrt{2}m_1, \tag{6.20}$$

where $m_1(x)$ is given by Eq. (6.19). The solution to Eq. (6.20) is given by

$$\begin{aligned}\rho_2(x) = [A_2 - A_0 f x/\ell]\, e^{fx/\ell} + \frac{\sqrt{2}B_+}{c_+ - f}e^{c_+ x/\ell} \\ + \frac{\sqrt{2}B_-}{c_- - f}e^{c_- x/\ell},\end{aligned} \tag{6.21}$$

where A_2 is another integration constant. Together, Eqs. (6.17), (6.19) and (6.21) constitute the solution (6.7) of the main text.

As emphasized above, these solutions hold within every region separately. Therefore, the values of the integration constants A_0, A_2, B_+, and B_- can differ per region. These values are determined from the boundary conditions outlined in section 6.3.1, i.e. $\rho(-\infty) = \rho_l$, $m_x(-\infty) = 0$, and $m_x(\infty) = 0$ (we take $x_{\text{res}} \to -\infty$ and $x_{\max} \to \infty$), and from the requirements that the density $\rho(x)$, the polarization $m_x(x)$, and the orientation flux $J_m(x) \equiv \text{Pe}\,\rho/\sqrt{2} + f(x)m_x - \ell\partial_x m_x$ all be continuous at the region boundaries $x = -x_l$, $x = 0$ and $x = x_r$. The conditions that $\rho(-\infty) = \rho_l$ and that the the density $\rho(x)$ be continuous straightforwardly imply that $A_0 = \rho_l$ everywhere. However, the values that follow for the other integration constants A_2, B_+, and B_- are mostly lengthy, and intransparent, and therefore not shown. The same is true for the leading order difference in bulk densities $\Delta\rho = \rho_r - \rho_l = \text{Pe}^2 A_2|_{x>x_r}$, whose dependence on the parameters of the problem is instead depicted graphically, in Figs. 6.3(a) and 6.5(a)-(c).

7

Conclusions

In this chapter, we summarize the research of this thesis, and discuss what we have learnt from the research as a whole. Also, we provide directions for future research.

7.1 Summary

In this thesis we studied the thermodynamic variables pressure, chemical potential and surface tension for active Brownian particles (ABPs). The motivation comes largely from the motility-induced phase separation (MIPS) that purely repulsive particles at high enough density can undergo when they are made sufficiently active. MIPS was introduced in **chapter 2**. We presented phase diagrams, and explained its onset from a stability analysis of the homogeneous isotropic phase. Additionally, we studied the influence of particle shape on MIPS, and showed that the phase separation disappears when perfectly isotropic particles are turned into slightly elongated rods.

The phenomenon of MIPS inspired two research questions that are central to this thesis. The first question is: can the coexisting densities be found by equating the pressure and chemical potentials of the two phases?

Since ABPs are out of equilibrium, a pressure and chemical potential first need to be defined. **Chapters 3, 4 and 5** studied the definition of pressure. While complications arise for particles that are anisotropic (**chapter 3**), or whose propulsion speed is spatially dependent (**chapter 4**), the situation is relatively straightforward for isotropic particles with homogeneous propulsion speed: the total pressure of the system is the sum of the 'bare' pressure, which has the same functional form as the equilibrium pressure, and the swim pressure, which is induced by the activity. If one takes into account the fact that the ABPs swim in a solvent (**chapter 3**), then the bare pressure is associated with the colloids, while the swim pressure is identified as the pressure of the solvent. Their sum is then indeed the total pressure of the suspension.

For these isotropic particles with homogeneous propulsion speed, **chapter 5** studied the definition of a chemical potential. It used a Gibbs-Duhem-like equation to define a quantity that plays the role of chemical potential, and tested whether, together with the pressure, it could be used to predict the coexisting densities. While the densities could be accurately predicted for a coexistence of weakly active Lennard-Jones particles, this was not the case for the highly active MIPS. The discrepancy is a consequence of the fact that the chemical potential-like quantity is not a state function, and that its bulk value depends on the profiles in the interface.

The second question concerns the interface of MIPS. In Ref. [26] it was found that its interfacial tension is negative. What does this precisely mean, and why is the interface nonetheless stable? These questions were studied in **chapter 4**. This chapter did not directly study the MIPS interface, but a simpler system that we showed to share important qualitative features: the interface formed by an active ideal gas in between two bulks with different propulsion speeds. We proposed two possible definitions of the interfacial tension, and investigated the stability of the interface. Remarkably, just like for MIPS, the normal force on a piece of perturbed interface acts in the same direction as the perturbation, and thus seems to have a destabilizing effect. Nonetheless, we found the interface to be stable. The reason is that the interfacial tension depends on the lateral position in the interface. This leads, by a Marangoni-like effect, to tangential currents that restore

the interface to its original state.

Finally, in **chapter 6**, we studied another effect that makes the statistical physics of ABPs challenging: in the presence of an external potential, the steady-state density profile can depend on the details of the external potential at locations arbitrarily far away. We studied this effect in a minimal setting, by applying an external "sawtooth" potential in between two bulks of an active ideal gas. We showed that the steady-state densities in the two bulks, which can be arbitrarly large size, indeed depend on the parameters of the sawtooth potential. To explain this dependence we proposed a simple transition state model, which, in its regime of applicability, indeed captures the correct trends.

7.2 Concluding remarks

A priori, it may not be clear how thermodynamic variables, defined in thermodynamic equilibrium, can be extended to active systems. The route to follow is most clear for the pressure and surface tension, for they have a mechanical interpretation, that can be extended to active systems. However, correctly interpreting their meaning requires a careful analysis, and simply applying equations that are valid in equilibrium does generally not suffice. For example, whereas in equilibrium the pressure exerted on the wall always equals the pressure that follows from the trace of the local stress tensor [88, 129], this is not true for ABPs that are anisotropic. As another example, an interfacial tension that is negative does not necessarily imply that the interface is unstable, and the stabilizing mechanism in chapter 4 was found only after analyzing carefully how the interface responds to a perturbation.

In contrast to the pressure and surface tension, the chemical potential cannot be defined mechanically. Therefore, its extension to active systems is more challenging. As a result, the literature shows a variety of definitions that sometimes seem difficult to relate [41, 46, 57, 89, 131, 147, 201], and we simply presented the definition that seemed most natural us: the chemical potential as the scalar function along whose gradient particles move.

So how useful are these thermodynamic variables for ABPs? A certain benefit is that they provide extra intuition. For example, the fact that in MIPS the dense phase of repulsive particles does not simply expand into the dilute phase, can be understood from the fact that the particles effectively move slower in the dense phase, such that the swim pressure is lower than in the dilute phase. As another example, the fact that active particles in a gravitational field have a larger sedimentation length than passive particles can be understood from the fact that the gravitational potential is counteracted by the swim potential.

On the other hand, the fact that the pressure and chemical potential could not predict the coexising densities of MIPS shows that they are not as effective as their equilibrium counterparts. This was confirmed in chapter 6: whereas for an ideal gas in equilibrium the density is a local function of the chemical potential, for and active ideal gas the density depends on values of the external potential - and thus of the chemical potential -

at locations arbitrarily far away. In the author's opinion, this does not as much reflect on the use of thermodynamic variables for active systems, as on their effectiveness for equilibrium systems. In fact, performing this research made the author appreciate how strong the thermodynamic framework in equilibrium really is.

In hindsight, it is perhaps not so surprising that the highly non-equilibrium phenomenon of MIPS cannot be described by the variables pressure and chemical potential, since they are, in principle, equilibrium concepts. Seen in this light, the fact that they *do* describe the coexistence of weakly active Lennard-Jones particles is already quite an achievement. An interesting future question is whether active system can be described by other thermodynamic variables that explicitly account for the 'non-equilibriumness' of the system. For example, there have already been studies on the entropy production of active systems [202–205], but is it also *minimized* [206] for active steady states? Another interesting approach is to note that the forces that do not map to an equilibrium system are the non-conservative ones. Since the conservative and non-conservative forces are separately accounted for in power functional theory [207], we deem the application of power functional theory to active systems [148, 208, 209] an interesting direction for future research as well.

References

[1] S. J. Blundell and K. M. Blundell. *Concepts in Thermal Physics*. Oxford University Press, 2006.

[2] J.-P. Hansen and I. R. McDonald. *Theory of Simple Liquids (Fourth Edition)*. Academic Press, fourth edition edition, 2013.

[3] M. P. Allen and D. J. Tildesley. *Computer Simulation of Liquids*. Oxford University Press, 1987.

[4] H. B. Callen. *Thermodynamics and an introduction to Thermostatistics*. Wiley, New York, 1960.

[5] J. G. Kirkwood and I. Oppenheim. *Chemical Thermodynamics*. McGraw-Hill Book Company, New York, 1961.

[6] R. Haase. *Physical Chemistry. An Advanced Treatise*. Academic Press, New York, 1971.

[7] W. Ebeling and I. M. Sokolov. *Statistical Thermodynamics and Stochastic Theory of Nonequilibrium Processes*. World Scientific, 2005.

[8] M. C. Marchetti, J. F. Joanny, S. Ramaswamy, T. B. Liverpool, J. Prost, M. Rao, and R. A. Simha, *Hydrodynamics of soft active matter*. Rev. Mod. Phys., 85:1143–1189, 2013.

[9] T. Vicsek and A. Zafeiris, *Collective motion*. Phys. Rep., 517:71, 2012.

[10] J. Elgeti, R. G. Winkler, and G. Gompper, *Physics of microswimmers-single particle motion and collective behavior: a review*. Rep. Prog. Phys., 78:056601, 2015.

[11] C. Bechinger, R. Di Leonardo, H. Löwen, C. Reichhardt, G. Volpe, and G. Volpe, *Active particles in complex and crowded environments*. Rev. Mod. Phys., 88:045006, 2016.

[12] H. C. Berg. *E. coli in motion*. Springer, 2004.

[13] R. M. Macnab, *Bacterial flagella rotating in bundles: a study in helical geometry*. Proc. Natl. Acad. Sci. U.S.A., 74:221, 1977.

[14] J. Arlt, V. A. Martinez, A. Dawson, T. Pilizota, and W. C. K. Poon, *Painting with light-powered bacteria*. Nat. Comm., 9:768, 2018.

[15] P. G. Moerman, H. W. Moyses, E. B. van der Wee, D. G. Grier, A. van Blaaderen, W. K. Kegel, J. Groenewold, and J. Brujic, *Solute-mediated interactions between active droplets*. Phys. Rev. E, 96:032607, 2017.

[16] H. H. Wensink, V. Kantsler, R. E. Goldstein, and J. Dunkel, *Controlling active self-assembly through broken particle-shape symmetry*. Phys. Rev. E, 89:010302, 2014.

[17] V. Prymidis, H. Sielcken, and L. Filion, *Self-assembly of active attractive spheres*. Soft Matter, 21:4158, 2015.

[18] U. K. Cheang, F. Meshkati, H. Kim, K. Lee, H. C. Fu, and M. J. Kim, *Versatile microrobotics using simple modular subunits*. Sci. Rep., 6:30472, 2016.

[19] A. Snezhko and I. S. Aranson, *Magnetic manipulation of self-assembled colloidal asters*. Nat. Mater., 10:698, 2011.

[20] L. Baraban, M. Tasinkevych, M. N. Popescu, S. Sanchez, S. Dietrich, and O. G. Schmidt, *Transport of cargo by catalytic janus micro-motors*. Soft Matter, 8:48, 2012.

[21] S. Paliwal. *Collective behaviour of self-propelled particles*. PhD thesis, Utrecht University, 2019.

[22] W. J. D., C. D., and A. H. C., *Role of repulsive forces in determining equilibrium structure of simple liquids*. J. Chem. Phys., 54:5237, 1971.

[23] G. S. Redner, M. F. Hagan, and A. Baskaran, *Structure and dynamics of a phase-separating active colloidal fluid*. Phys. Rev. Lett., 110(5):55701, 2013.

[24] R. van Roij. *Soft Condensed Matter*. Lecture Notes. Utrecht University, 2018.

[25] A. Patch, D. Sussman, D. Yllanes, and M. C. Marchetti, *Curvature-dependent tension and tangential flows at the interface of motility-induced phase separation*. Soft Matter, 14:7435, 2018.

[26] J. Bialké, J. T. Siebert, H. Löwen, and T. Speck, *Negative interfacial tension in phase-separated active brownian particles*. Phys. Rev. Lett., 115:098301, 2015.

[27] T. Speck, *Stochastic thermodynamics for active matter*. Europhys. Lett., 114:30006, 2016.

[28] G. S. Redner, C. G. Wagner, A. Baskaran, and M. F. Hagan, *Classical nucleation theory description of active colloid assembly*. Phys. Rev. Lett., 117:148002, 2016.

[29] C. F. Lee, *Interface stability, interface fluctuations, and the gibbs-thomson relationship in motility-induced phase separations*. Soft Matter, 13:376, 2016.

[30] A. P. Solon, J. Stenhammar, M. E. Cates, Y. Kafri, and J. Tailleur, *Generalized thermodynamics of motility-induced phase separation: phase equilibria, laplace pressure, and change of ensembles*. New Journal of Physics, 20(7):075001, 2018.

[31] S. Hermann, D. de las Heras, and M. Schmidt, *Non-negative interfacial tension in phase-separated active brownian particles*. Phys. Rev. Lett., 123:268002, 2019.

[32] L. F. Cugliandolo, G. Gonnella, and I. Petrelli, *Effective temperature in active brownian particles*. Fluctuation Noise Lett., 18:1940008, 2019.

[33] L. E. Scriven and C. V. Sternling, *The marangoni effects*. Nature, 1960.

[34] R. van Damme, J. Rodenburg, R. van Roij, and M. Dijkstra, *Interparticle torques suppress motility-induced phase separation for rodlike particles*. J. Chem. Phys., 150:164501, 2019.

[35] J. Tailleur and M. E. Cates, *Statistical Mechanics of Interacting Run-and-Tumble Bacteria*. Phys. Rev. Lett., 100(21):218103, 2008.

[36] Y. Fily and M. C. Marchetti, *Athermal phase separation of self-propelled particles with no alignment*. Phys. Rev. Lett., 108(23):235702, 2012.

[37] G. S. Redner, M. F. Hagan, and A. Baskaran, *Structure and Dynamics of a Phase-Separating Active Colloidal Fluid*. Phys. Rev. Lett., 110(5):055701, 2013.

[38] Y. Fily, A. Baskaran, and M. F. Hagan, *Dynamics of self-propelled particles under strong confinement*. Soft Matter, 10(30):5609–5617, 2014.

[39] J. Bialké, J. T. Siebert, H. Löwen, and T. Speck, *Negative Interfacial Tension in Phase-Separated Active Brownian Particles*. Phys. Rev. Lett., 115(9):098301, 2015.

[40] M. E. Cates and J. Tailleur, *Motility-Induced Phase Separation*. Annu. Rev. Condens. Matter Phys., 6(1):219–244, 2015.

[41] S. C. Takatori and J. F. Brady, *Towards a thermodynamics of active matter*. Phys. Rev. E, 91(3):032117, 2015.

[42] M. C. Marchetti, Y. Fily, S. Henkes, A. Patch, and D. Yllanes, *Minimal model of active colloids highlights the role of mechanical interactions in controlling the emergent behavior of active matter.* Current Opinion in Colloid & Interface Science, 21:34 – 43, 2016.

[43] G. S. Redner, C. G. Wagner, A. Baskaran, and M. F. Hagan, *Classical Nucleation Theory Description of Active Colloid Assembly.* Phys. Rev. Lett., 117(14):148002, 2016.

[44] A. Patch, D. Yllanes, and M. C. Marchetti, *Kinetics of motility-induced phase separation and swim pressure.* Phys. Rev. E, 95(1):012601, 2017.

[45] D. Levis, J. Codina, and I. Pagonabarraga, *Active Brownian Equation of State: Metastability and Phase Coexistence.* Soft Matter, 13:8113–8119, 2017.

[46] A. P. Solon, J. Stenhammar, M. E. Cates, Y. Kafri, and J. Tailleur, *Generalized thermodynamics of phase equilibria in scalar active matter.* Phys. Rev. E, 97:020602, 2018.

[47] J. Barré, R. Chétrite, M. Muratori, and F. Peruani, *Motility-Induced Phase Separation of Active Particles in the Presence of Velocity Alignment.* J. Stat. Phys., 158(3):589–600, 2015.

[48] E. Sese-Sansa, I. Pagonabarraga, and D. Levis, *Velocity alignment promotes motility-induced phase separation.* EPL, 124:30004, 2018.

[49] F. Peruani, A. Deutsch, and M. Bär, *Nonequilibrium clustering of self-propelled rods.* Phys. Rev. E, 74:030904, 2006.

[50] F. Ginelli, F. Peruani, M. Bär, and H. Chaté, *Large-Scale Collective Properties of Self-Propelled Rods.* Phys. Rev. Lett., 104(18):184502, 2010.

[51] F. Peruani, *Active Brownian rods.* Eur. Phys. J. Spec. Top., 225(11-12):2301–2317, 2016.

[52] S. Weitz, A. Deutsch, and F. Peruani, *Self-propelled rods exhibit a phase-separated state characterized by the presence of active stresses and the ejection of polar clusters.* Phys. Rev. E, 92(1):012322, 2015.

[53] C. Abaurrea Velasco, M. Abkenar, G. Gompper, and T. Auth, *Collective behavior of self-propelled rods with quorum sensing.* Phys. Rev. E, 98(2):022605, 2018.

[54] C. Vega and S. Lago, *A fast algorithm to evaluate the shortest distance between rods.* Comput. Chem., 18(1):55–59, 1994.

[55] B. Bet, G. Boosten, M. Dijkstra, and R. van Roij, *Efficient shapes for microswimming: From three-body swimmers to helical flagella.* J. Chem. Phys., 146(8):084904, 2017.

[56] F. Perrin, *Mouvement brownien d'un ellipsoide - I. Dispersion diélectrique pour des molécules ellipsoidales.* J. Phys. Radium, 5:497–511, 1934.

[57] J. Stenhammar, D. Marenduzzo, R. J. Allen, and M. E. Cates, *Phase behaviour of active Brownian particles: the role of dimensionality.* Soft Matter, 10(10):1489–1499, 2014.

[58] J. Bialké, H. Löwen, and T. Speck, *Microscopic theory for the phase separation of self-propelled repulsive disks.* EPL, 103(3):30008, 2013.

[59] A. Suma, G. Gonnella, D. Marenduzzo, and E. Orlandini, *Motility-induced phase separation in an active dumbbell fluid.* EPL, 108(5):56004, 2014.

[60] T. Speck, *Collective behavior of active Brownian particles: From microscopic clustering to macroscopic phase separation.* Eur. Phys. J. Spec. Top., 225(11-12):2287–2299, 2016.

[61] I. R. Bruss and S. C. Glotzer, *Phase separation of self-propelled ballistic particles.* Phys. Rev. E, 97(4):042609, 2018.

[62] I. Buttinoni, J. Bialké, F. Kümmel, H. Löwen, C. Bechinger, and T. Speck, *Dynamical Clustering and Phase Separation in Suspensions of Self-Propelled Colloidal Particles.* Phys. Rev. Lett., 110(23):238301, 2013.

[63] V. Prymidis, S. Samin, and L. Filion, *State behaviour and dynamics of self-propelled Brownian squares: a simulation study.* Soft Matter, 12(19):4309–4317, 2016.

[64] G. S. Redner, A. Baskaran, and M. F. Hagan, *Reentrant phase behavior in active colloids with attraction.* Phys. Rev. E, 88:012305, 2013.

[65] M. E. Cates and J. Tailleur, *When are active Brownian particles and run-and-tumble particles equivalent? Consequences for motility-induced phase separation.* EPL, 101(2):20010, 2013.

[66] T. Speck, A. M. Menzel, J. Bialké, and H. Löwen, *Dynamical mean-field theory and weakly non-linear analysis for the phase separation of active Brownian particles.* J. Chem. Phys., 142(22):224109, 2015.

[67] M. A. Bates and D. Frenkel, *Phase behavior of two-dimensional hard rod fluids.* J. Chem. Phys., 112(22):10034–10041, 2000.

[68] P. Digregorio, D. Levis, A. Suma, L. F. Cugliandolo, G. Gonnella, and I. Pagonabarraga, *Full Phase Diagram of Active Brownian Disks: From Melting to Motility-Induced Phase Separation.* Phys. Rev. Lett., 121(9):098003, 2018.

[69] T. Speck, J. Bialké, A. M. Menzel, and H. Löwen, *Effective Cahn-Hilliard Equation for the Phase Separation of Active Brownian Particles.* Phys. Rev. Lett., 112(21):218304, 2014.

[70] A. P. Solon, J. Stenhammar, R. Wittkowski, M. Kardar, Y. Kafri, M. E. Cates, and J. Tailleur, *Pressure and Phase Equilibria in Interacting Active Brownian Spheres.* Phys. Rev. Lett., 114(19):198301, 2015.

[71] X.-q. Shi and H. Chaté, *Self-Propelled Rods: Linking Alignment-Dominated and Repulsion-Dominated Active Matter.* preprint, 2018.

[72] J. Stenhammar, A. Tiribocchi, R. J. Allen, D. Marenduzzo, and M. E. Cates, *Continuum Theory of Phase Separation Kinetics for Active Brownian Particles.* Phys. Rev. Lett., 111(14):145702, 2013.

[73] Y. Fily, S. Henkes, and M. C. Marchetti, *Freezing and phase separation of self-propelled disks.* Soft Matter, 10(13):2132–2140, 2014.

[74] A. Baskaran and M. Cristina Marchetti, *Nonequilibrium statistical mechanics of self-propelled hard rods.* J. Stat. Mech. Theory Exp., 2010(04):P04019, 2010.

[75] E. Bertin, A. Baskaran, H. Chaté, and M. C. Marchetti, *Comparison between Smoluchowski and Boltzmann approaches for self-propelled rods.* Phys. Rev. E, 92(4):042141, 2015.

[76] S. E. Ilse, C. Holm, and J. de Graaf, *Surface roughness stabilizes the clustering of self-propelled triangles.* J. Chem. Phys., 145(13):134904, 2016.

[77] L. F. Cugliandolo, P. Digregorio, G. Gonnella, and A. Suma, *Phase Coexistence in Two-Dimensional Passive and Active Dumbbell Systems.* Phys. Rev. Lett., 119(26):268002, 2017.

[78] A. Zöttl and H. Stark, *Hydrodynamics Determines Collective Motion and Phase Behavior of Active Colloids in Quasi-Two-Dimensional Confinement.* Phys. Rev. Lett., 112(11):118101, 2014.

[79] R. Matas-Navarro, R. Golestanian, T. B. Liverpool, and S. M. Fielding, *Hydrodynamic suppression of phase separation in active suspensions.* Phys. Rev. E, 90(3):032304, 2014.

[80] J. Blaschke, M. Maurer, K. Menon, A. Zöttl, and H. Stark, *Phase separation and coexistence of hydrodynamically interacting microswimmers.* Soft Matter, 12(48):9821–9831, 2016.

[81] N. Oyama, J. J. Molina, and R. Yamamoto, *Purely hydrodynamic origin for swarming of swimming particles.* Phys. Rev. E, 93(4):043114, 2016.

[82] N. Oyama, J. J. Molina, and R. Yamamoto, *Do hydrodynamically assisted binary collisions lead to orientational ordering of microswimmers?* Eur. Phys. J. E, 40(11):95, 2017.

[83] J. Rodenburg, M. Dijkstra, and R. van Roij, *Van't Hoff's law for active suspensions: the role of the solvent chemical potential.* Soft Matter, 13:8957, 2017.

[84] X. Yang, M. L. Manning, and M. C. Marchetti, *Aggregation and segregation of confined active particles.* Soft Matter, 10:6477, 2014.

[85] S. C. Takatori, W. Yan, and J. F. Brady, *Swim pressure: Stress generation in active matter.* Phys. Rev. Lett., 113:028103, 2014.

[86] R. G. Winkler, A. Wysocki, and G. Gompper, *Virial pressure in systems of spherical active brownian particles.* Soft Matter, 11:6680, 2014.

[87] J.-P. Hansen and I. R. McDonald. *Theory of Simple Liquids.* Academic Press, 4 edition, 2013.

[88] A. P. Solon, Y. Fily, A. Baskaran, M. E. Cates, Y. Kafri, M. Kardar, and J. Tailleur, *Pressure is not a state function for generic active fluids.* Nature Phys., 11:673–678, 2015.

[89] R. Wittkowski, A. Tiribocchi, J. Stenhammar, R. J. Allen, D. Marenduzzo, and M. E. Cates, *Scalar ϕ^4 theory for active-particle phase separation.* Nat. Commun., 5:4351, 2014.

[90] S. C. Takatori and J. F. Brady, *Swim stress, motion, and deformation of active matter: effect of an external field.* Soft Matter, 10:9433, 2014.

[91] F. Ginot, I. Theurkauff, D. Levis, C. Ybert, L. Bocquet, L. Berthier, and C. Cottin-Bizonne, *Nonequilibrium equation of state in suspensions of active colloids.* Phys. Rev. X, 5:011004, 2015.

[92] A. P. Solon, J. Stenhammar, R. Wittkowski, M. Kardar, Y. Kafri, M. E. Cates, and J. Tailleur, *Pressure and phase equilibria in interacting active brownian spheres.* Phys. Rev. Lett., 114:198301, 2015.

[93] C. Maggi, U. M. B. Marconi, N. Gnan, and R. Di Leonardo, *Multidimensional stationary probability distribution for interacting active particles.* Sci. Rep., 5:10742, 2015.

[94] W. Yan and J. F. Brady, *The swim force as a body force.* Soft Matter, 11:6235, 2015.

[95] W. Yan and J. F. Brady, *The force on a boundary in active matter.* J. Fluid Mech., 785:R1, 2015.

[96] M. Joyeux and E. Bertin, *Pressure of a gas of underdamped active dumbbells.* Phys. Rev. E, 93:032605, 2016.

[97] T. Speck and R. L. Jack, *Ideal bulk pressure of active brownian particles.* Phys. Rev. E, 93:062605, 2016.

[98] S. C. Takatori, R. D. Dier, J. Vermant, and J. F. Brady, *Acoustic trapping of active matter.* Nat. Commun., 7:10694, 2016.

[99] N. Nikola, A. P. Solon, Y. Kafri, M. Kardar, J. Tailleur, and R. Voituriez, *Active particles with soft and curved walls: Equation of state, ratchets, and instabilities.* Phys. Rev. Lett., 117:098001, 2016.

[100] G. Falasco, F. Baldovin, K. Kroy, and M. Baiesi, *Mesoscopic virial equation for nonequilibrium statistical mechanics.* New J. Phys., 18:093043, 2016.

[101] J. Blaschke, M. Maurer, K. Menon, A. Zöttl, and H. Stark, *Phase separation and coexistence of hydrodynamically interacting microswimmers.* Soft Matter, 12:9821, 2016.

[102] S. Steffenoni, G. Falasco, and K. Kroy, *Microscopic derivation of the hydrodynamics of active-brownian-particle suspensions.* Phys. Rev. E, 95:052142, 2017.

[103] G. Junot, G. Briand, R. Ledesma-Alonso, and O. Dauchot, *Active vs. passive hard disks against a membrane: Mechanical pressure and instability.* Phys. Rev. Lett., 119:028002, 2017.

[104] S. C. Takatori and J. F. Brady, *Inertial effects on the stress generation of active fluids.* Phys. Rev. Fluids, 2:094305, 2017.

[105] T. W. Lion and R. J. Allen, *Osmosis with active solutes.* Europhys. Lett., 106:34003, 2014.

[106] J. van't Hoff, *Die rolle osmotischen drucks in der analogie zwischen losungen und gasen.* Z. Phys. Chem., 1:481, 1887.

[107] J. van't Hoff, *The function of osmotic pressure in the analogy between solutions and gases.* Phil. Mag., 26:81, 1888.

[108] J. van't Hoff. *The Role of Osmotic Pressure in the Analogy between Solutions and Gases*, page 11. Harper & Brothers Publishers, New York and London, 1899.

[109] P. Romanczuk, M. Bär, W. Ebeling, and B. Lindner, *Active brownian particles, from individual to collective stochastic dynamics.* Eur. Phys. J. ST, 202:1, 2012.

[110] M. C. Marchetti, Y. Fily, S. Henkes, A. Patch, and D. Yllanes, *Minimal model of active colloids highlights the role of mechanical interactions in controlling the emergent behavior of active matter.* Curr. Op. Colloid Interface Sci., 21:34, 2016.

[111] L. Rothschild, *Non-random distribution of bull spermatozoa in a drop of sperm suspension.* Nature, 198:1221, 1963.

[112] A. P. Berke, L. Turner, H. C. Berg, and E. Lauga, *Hydrodynamic attraction of swimming microorganisms by surfaces.* Phys. Rev. Lett., 101:038102, 2008.

[113] G. Li and J. X. Tang, *Accumulation of microswimmers near a surface mediated by collision and rotational brownian motion.* Phys. Rev. Lett., 103:078101, 2009.

[114] J. Elgeti and G. Gompper, *Wall accumulation of self-propelled spheres.* Europhys. Lett., 101:48003, 2013.

[115] C. Lee, *Active particles under confinement: aggregation at the wall and gradient formation inside a channel.* New J. Phys., 15:055007, 2013.

[116] Y. Fily, A. Baskaran, and M. F. Hagan, *Dynamics and density distribution of strongly confined noninteracting nonaligning self-propelled particles in a nonconvex boundary.* Phys. Rev. E, 91:012125, 2015.

[117] J. Vicario, R. Eelkema, W. R. Browne, A. Meetsma, R. M. L. Crois, and B. L. Feringa, *Catalytic molecular motors: fuelling autonomous movement by a surface bound synthetic manganese catalase.* Chem. Commun., 31:3936, 2005.

[118] D. A. Wilson, R. J. M. Nolte, and J. C. M. van Hest, *Autonomous movement of platinum-loaded stomatocytes.* Nat. Chem., 4:212, 2012.

[119] J. R. Howse, R. A. L. Jones, A. J. Ryan, T. Gough, R. Vafabakhsh, and R. Golestanian, *Self-motile colloidal particles: From directed propulsion to random walk.* Phys. Rev. Lett., 99:048102, 2007.

[120] J. Palacci, C. Cottin-Bizonne, C. Ybert, and L. Bocquet, *Sedimentation and effective temperature of active colloidal suspensions.* Phys. Rev. Lett., 105:088304, 2010.

[121] G. Volpe, I. Buttinoni, D. Vogt, H. Kümmerer, and C. Bechinger, *Microswimmers in patterned environments.* Soft Matter, 7:8810, 2011.

[122] M. Mussler, S. Rafaï, P. Peyla, and C. Wagner, *Effective viscosity of non-gravitactic chlamydomonas reinhardtii microswimmer suspensions.* Euro. Phys. Lett., 101:54004, 2013.

[123] K. Drescher, J. Dunkel, L. H. Cisneros, S. Ganguly, and R. E. Goldstein, *Fluid dynamics and noise in bacterial cell-cell and cell-surface scattering.* Proc. Natl. Acad. Sci. U.S.A., 108:10940, 2011.

[124] E. Lauga, W. R. DiLuzio, G. M. Whitesides, and H. A. Stone, *Swimming in circles: motion of bacteria near solid boundaries.* Biophys. J., 90:400, 2006.

[125] V. Prymidis, S. Samin, and L. Filion, *State behaviour and dynamics of self-propelled brownian squares: a simulation study.* Soft Matter, 12:4309, 2016.

[126] V. Prymidis. private communication, 2017.

[127] S. C. Takatori and J. F. Brady, *Forces, stresses and the (thermo?) dynamics of active matter.* Curr. Op. Colloid Interface Sci., 21:24, 2016.

[128] V. Prymidis, S. Paliwal, M. Dijkstra, and L. Filion, *Vapour-liquid coexistence of an active lennard-jones fluid.* J. Chem. Phys., 145:124904, 2016.

[129] J. S. Rowlinson and B. Widom. *Molecular Theory of Capillarity.* Dover Publications, 1982.

[130] U. M. B. Marconi and C. Maggi, *Towards a statistical mechanical theory of active fluids.* Soft Matter, 11:8768, 2015.

[131] B. van der Meer, V. Prymidis, M. Dijkstra, and L. Filion, *Mechanical and chemical equilibrium in mixtures of active spherical particles: predicting phase behaviour from bulk properties alone.* arXiv:1609.03867, 2017.

[132] Y. Fily, Y. Kafri, A. P. Solon, J. Tailleur, and A. Turner, *Mechanical pressure and momentum conservation in dry active matter.* Journal of Physics A: Mathematical and Theoretical, 51(4):044003, 2017.

[133] J. R. Blake, *A spherical envelope approach to ciliary propulsion.* J. Fluid Mech., 46:199, 1971.

[134] J. L. Anderson, *Colloid transport by interfacial forces.* Ann. Rev. Fluid Mech., 21:61, 1989.

[135] A. Zöttl and H. Stark, *Emergent behavior in active colloids.* J. of Phys.: Cond. Mat., 28:253001, 2016.

[136] S. Kim and S. J. Karrila. *Microhydrodynamics, Principles and Selected Applications.* Dover Publications, Mineola, New York, 2015.

[137] S. Paliwal, V. Prymidis, L. Filion, and M. Dijkstra, *Non-equilibrium surface tension of the vapour-liquid interface of active lennard-jones particles.* J. Chem. Phys., 147:084902, 2017.

[138] A. Marchand, J. H. Weijs, J. H. Snoeijer, and B. Andreotti, *Why is surface tension a force parallel to the interface?* Am. J. Phys., 79(October):999, 2011.

[139] J. Grauer, H. Löwen, and L. M. C. Janssen, *Spontaneous membrane formation and self-encapsulation of active rods in an inhomogeneous motility field.* Phys. Rev. E, 97:022608, 2018.

[140] M. E. Cates and J. Tailleur, *Motility-induced phase separation.* Annu. Rev. Condens. Matter Phys., 6:219, 2015.

[141] S. Paliwal, J. Rodenburg, R. van Roij, and M. Dijkstra, *Chemical potential in active systems: predicting phase equilibrium from bulk equations of state?* New J. Phys., 20:015003, 2018.

[142] M. P. Magiera and L. Brendel, *Trapping of interacting propelled colloidal particles in inhomogeneous media.* Phys. Rev. E, 92:012304, 2015.

[143] F. Smallenburg and H. Löwen, *Swim pressure on walls with curves and corners.* Phys. Rev. E, 92:032304, 2015.

[144] V. Prymidis. *Active matter in silico.* PhD thesis, Utrecht University, 2017.

[145] R. Evans, *The nature of the liquid-vapour interface and other topics in the statistical mechanics of non-uniform, classical fluids.* Adv. Phys., 28(2):143–200, 1979.

[146] G. K. Batchelor. *An Introduction to Fluid Dynamics.* Cambridge University Press, 1967.

[147] S. C. Takatori and J. F. Brady, *A theory for the phase behavior of mixtures of active particles.* Soft Matter, 11(40):7920–7931, 2015.

[148] S. Hermann, P. Krinninger, D. de las Heras, and M. Schmidt, *Phase coexistence of active brownian particles.* Phys. Rev. E, 100:052604, 2019.

[149] J. Bialké, H. Löwen, and T. Speck, *Microscopic theory for the phase separation of self-propelled repulsive disks.* Europhys. Lett., 103:30008, 2013.

[150] A. P. Solon, Y. Fily, A. Baskaran, M. E. Cates, Y. Kafri, M. Kardar, and J. Tailleur, *Pressure is not a state function for generic active fluids.* Nat. Phys., 11(August):673–678, 2015.

[151] W. Yan and J. F. Brady, *The swim force as a body force.* Soft Matter, 11(31):6235, 2015.

[152] T. Speck and R. L. Jack, *Ideal bulk pressure of active brownian particles.* Phys. Rev. E, 93(6):062605, 2016.

[153] E. Verwey and K. Niessen, *Xl. the electrical double layer at the interface of two liquids.* The London, Edinburgh, and Dublin Philosophical Magazine and Journal of Science, 28(189):435, 1939.

[154] M. Bier, J. Zwanikken, and R. van Roij, *Liquid-liquid interfacial tension of electrolyte solutions.* Phys. Rev. Lett., 101(4):046104, 2008.

[155] U. M. B. Marconi and P. Tarazona, *Dynamic density functional theory of fluids.* J. Chem. Phys., 110(16):8032, 1999.

[156] A. J. Archer, *Dynamical density functional theory for molecular and colloidal fluids: A microscopic approach to fluid mechanics.* J. Chem. Phys., 130(1):014509, 2009.

[157] T. Ikeshoji, B. Hafskjold, and H. Furuholt, *Molecular-level Calculation Scheme for Pressure in Inhomogeneous Systems of Flat and Spherical Layers.* Mol. Simul., 29(2):101–109, 2003.

[158] S. C. Takatori, W. Yan, and J. F. Brady, *Swim Pressure: Stress Generation in Active Matter.* Phys. Rev. Lett., 113(2):028103, 2014.

[159] X. Yang, M. L. Manning, and M. C. Marchetti, *Aggregation and segregation of confined active particles.* Soft Matter, 10(34):6477, 2014.

[160] W. Yan and J. F. Brady, *The swim force as a body force.* Soft Matter, 11(31):6235–6244, 2015.

[161] T. F. F. Farage, P. Krinninger, and J. M. Brader, *Effective interactions in active Brownian suspensions.* Phys. Rev. E, 91(4):042310, 2015.

[162] M. Enculescu and H. Stark, *Active colloidal suspensions exhibit polar order under gravity.* Phys. Rev. Lett., 107(5):058301, 2011.

[163] J. Palacci, C. Cottin-Bizonne, C. Ybert, and L. Bocquet, *Sedimentation and effective temperature of active colloidal suspensions.* Phys. Rev. Lett., 105(8):088304, 2010.

[164] S. Paliwal, V. Prymidis, L. Filion, and M. Dijkstra, *Non-equilibrium surface tension of the vapour-liquid interface of active Lennard-Jones particles.* J. Chem. Phys., 147(8):084902, 2017.

[165] S. Paliwal. private communication, 2020.

[166] J. Rodenburg, S. Paliwal, M. de Jager, P. G. Bolhuis, M. Dijkstra, and R. van Roij, *Ratchet-induced variations in bulk states of an active ideal gas.* J. Chem. Phys., 149:174910, 2019.

[167] T. F. F. Farage, P. Krinninger, and J. M. Brader, *Effective interactions in active brownian suspensions.* Phys. Rev. E, 91:042310, 2015.

[168] M. Rein and T. Speck, *Applicability of effective pair potential for active brownian particles.* Eur. Phys. J. E, 39:84, 2016.

[169] U. M. B. Marconi, M. Paoluzzi, and C. Maggi, *Effective potential method for active particles.* Mol. Phys., 114:2400, 2016.

[170] B. Trefz, S. K. Das, S. A. Egorov, P. Virnau, and K. Binder, *Activity mediated phase separation: Can we understand phase behavior of the nonequilibrium problem from an equilibrium approach?* J. Chem. Phys., 144:144902, 2016.

[171] D. Loi, S. Mossa, and L. F. Cugliandolo, *Effective temperature of active matter.* Phys. Rev. E, 77:051111, 2008.

[172] S. Wang and P. G. Wolynes, *Communication: Effective temperature and glassy dynamics of active matter.* The Journal of Chemical Physics, 135:051101, 2011.

[173] G. Szamel, *Self-propelled particle in an external potential: Existence of an effective temperature.* Phys. Rev. E, 90:012111, 2014.

[174] M. Enculescu and H. Stark, *Active colloidal suspensions exhibit polar order under gravity.* Phys. Rev. Lett., 107:058301, 2011.

[175] K. Wolff, A. M. Hahn, and H. Stark, *Sedimentation and polar order of active bottom-heavy particles.* The European Physical Journal E, 36:43, 2013.

[176] A. P. Solon, M. E. Cates, and J. Tailleur, *Active brownian particles and run-and-tumble particles: a comparative study.* Eur. Phys. J. ST, 224:1231, 2015.

[177] H. Stark, *Swimming in external fields.* Eur. Phys. J. ST, 225:2369, 2016.

[178] B. Lindner, L. Schimansky-Geier, P. Reimann, P. Hänggi, and M. Nagaoka, *Inertia ratchets: A numerical study versus theory.* Phys. Rev. E, 59:1417, 1999.

[179] P. Galajda, J. Keymer, P. Chaikin, and R. Austin, *A wall of funnels concentrates swimming bacteria.* Journal of Bacteriology, 189:8704, 2007.

[180] L. Angelani, A. Constanzo, and R. Di Leonardo, *Active ratchets.* EPL, 96:68002, 2011.

[181] A. O. Reichhardt and C. Reichhardt, *Ratchet effects in active matter systems.* Annu. Rev. Condens. Matter Phys., 8:51, 2016.

[182] D. McDermott, C. J. O. Reichhardt, and C. Reichhardt, *Collective ratchet effects and reversal for active matter particles on quasi-one-dimensional asymmetric substrates.* Soft Matter, 12:8606, 2016.

[183] B.-Q. Ai and F.-G. Li, *Transport of underdamped active particles in ratchet potentials.* Soft Matter, 13:2536, 2017.

[184] C. G. Wagner, M. F. Hagan, and A. Baskaran, *Steady-state distributions of ideal active brownian particles under confinement and forcing.* J. Stat. Mech. Theory Exp., 2017:043203, 2017.

[185] Y. Baek, A. P. Solon, X. Xu, N. Nikola, and Y. Kafri, *Generic long-range interactions between passive bodies in an active fluid.* Phys. Rev. Lett., 120:058002, 2018.

[186] N. Koumakis, A. Lepore, C. Maggi, and R. Di Leonardo, *Targeted delivery of colloids by swimming bacteria.* Nat. Comm., 4:2588, 2013.

[187] N. Koumakis, C. Maggi, and R. Di Leonardo, *Directed transport of active particles over asymmetric energy barriers.* Soft Matter, 10:5695, 2014.

[188] F. Ginot, A. Solon, Y. Kafri, C. Ybert, J. Tailleur, and C. Cottin-Bizonne, *Sedimentation of self-propelled janus colloids: polarization and pressure.* New. J. Phys., 2018.

[189] R. Ni, M. A. Cohen Stuart, and P. G. Bolhuis, *Tunable long range forces mediated by self-propelled colloidal hard spheres.* Phys. Rev. Lett., 114:018302, 2015.

[190] M. de Jager. *Steady state of an ideal active lattice gas: Accumulation at boundaries and ratchet potentials*, 2017. Bachelor's Thesis, Utrecht University.

[191] R. W. Friddle, *Unified model of dynamic forced barrier crossing in single molecules.* Phys. Rev. Lett., 100:138302, 2008.

[192] H. E. A. Tobolsky, *Mechanical properties of polymeric materials.* J. Chem. Phys., 11:125, 1943.

[193] G. Bell, *Models for the specific adhesion of cells to cells.* Science, 200:618, 1978.

[194] H. Kramers, *Brownian motion in a field of force and the diffusion model of chemical reactions.* Physica, 7:284, 1940.

[195] J. Tailleur and M. E. Cates, *Sedimentation, trapping, and rectification of dilute bacteria.* EPL, 86:60002, 2009.

[196] R. W. Nash, R. Adhikari, J. Tailleur, and M. E. Cates, *Run-and-tumble particles with hydrodynamics: Sedimentation, trapping, and upstream swimming.* Phys. Rev. Lett., 104:258101, 2010.

[197] S. Hermann and M. Schmidt, *Active ideal sedimentation: exact two-dimensional steady states.* Soft Matter, 14:1614, 2018.

[198] Y. Fily, A. Baskaran, and M. F. Hagan, *Equilibrium mappings in polar-isotropic confined active particles.* The European Physical Journal E, 40:61, 2017.

[199] M. O. Magnasco, *Forced thermal ratchets.* Phys. Rev. Lett., 71:1477, 1993.

[200] J. Prost, J.-F. m. c. Chauwin, L. Peliti, and A. Ajdari, *Asymmetric pumping of particles.* Phys. Rev. Lett., 72:2652, 1994.

[201] A. Solon, J. Stenhammar, M. E. Cates, Y. Kafri, and J. Tailleur, *Generalized thermodynamics of motility-induced phase separation: phase equilibria, laplace pressure, and change of ensembles.* New Journal of Physics, 20:075001, 2018.

[202] D. Chaudhuri, *Active Brownian particles: Entropy production and fluctuation response.* Phys. Rev. E, 90(2):022131, 2014.

[203] C. Nardini, É. Fodor, E. Tjhung, F. van Wijland, J. Tailleur, and M. E. Cates, *Entropy Production in Field Theories without Time-Reversal Symmetry: Quantifying the Non-Equilibrium Character of Active Matter.* Phys. Rev. X, 7(2):021007, 2017.

[204] P. Pietzonka and U. Seifert, *Entropy production of active particles and for particles in active baths.* J. Phys. A-Math. Theor., 51:01LT01, 2017.

[205] S. Shankar and M. C. Marchetti, *Hidden entropy production and work fluctuations in an ideal active gas.* Phys. Rev. E, 98:020604, 2018.

[206] S. R. de Groot and P. Mazur. *Non-equilibrium thermodynamics.* Courier Corporation, 1984.

[207] M. Schmidt and J. M. Brader, *Power functional theory for Brownian dynamics.* J. Chem. Phys., 138:214101, 2013.

[208] P. Krinninger, M. Schmidt, and J. M. Brader, *Nonequilibrium phase behavior from minimization of free power dissipation.* Phys. Rev. Lett., 117:208003, 2016.

[209] P. Krinninger, M. Schmidt, and J. M. Brader, *Erratum: Nonequilibrium phase behavior from minimization of free power dissipation [phys. rev. lett. 117, 208003 (2016)].* Phys. Rev. Lett., 119:029902, 2017.

Samenvatting

Heeft u ooit de tijd genomen om een zwerm vliegende spreeuwen te bekijken? Een zwerm, die uit wel 100.000 vogels kan bestaan, vormt soms patronen die bijna hypnotiserend zijn om naar te kijken (voor een voorbeeld zie Fig. 1.1 in hoofdstuk 1). Als u dit wel eens gezien heeft, dan heeft u zich misschien ook wel afgevraagd *hoe* de vogels deze patronen vormen. De beweging wordt namelijk *niet* gecoördineerd door één of meerdere vogels die de leiding hebben. In plaats daarvan vormen de patronen *spontaan*: ze volgen op de één of andere manier uit de manier waarop elke individuele spreeuw vliegt en reageert op de aanwezigheid van andere vogels in de buurt. Maar *hoe* de patronen dan precies uit dat individuele gedrag volgen is geen eenvoudige vraag. Iets scherper gesteld luidt deze vraag als volgt. Stel we weten precies hoe elke individuele spreeuw beweegt en hoe zij interacteert met andere spreeuwen, kunnen we dan het gedrag van een grote groep spreeuwen voorspellen?

Het gedrag van een groep spreeuwen is onderdeel van een onderzoeksveld dat bekend staat als *actieve materie*. Andere voorbeelden van actieve materie zijn scholen vissen en mensenmassa's, maar hieronder vallen ook zwemmende bacteriën en zwemmende microdeeltjes die gecreëerd zijn in het laboratorium. Actieve materie heet *actief* omdat alle objecten energie verbruiken en deze meestal omzetten in beweging. Waarom het *materie* wordt genoemd is in eerste instantie misschien niet duidelijk, maar het suggereert dat we een dergelijke systeem kunnen beschrijven zoals we 'gewone' materie beschrijven, dus alsof het bijvoorbeeld een gas of een vloeistof is. Gewone materie bestaat namelijk ook uit een groot aantal éénheden: moleculen. Het verschil is dat de moleculen (meestal) geen energie verbruiken, en dus niet actief maar *passief* zijn.

Passieve materie in evenwicht wordt beschreven door de statistische fysica. Deze theorie doet voor passieve materie precies wat we voor actieve materie hopen te bereiken: gegeven hoe individuele moleculen met elkaar interacteren, voorspelt de statistische fysica hoe het geheel van alle moleculen tezamen zich gedraagt. Het collectief van de moleculen beschrijven we dan simpelweg als één stof, die we dan karakterizeren door, bijvoorbeeld, de druk en temperatuur te geven. De druk en temperatuur zijn voorbeelden van *thermodynamische variabelen*. De statistische fysica kan dan ook voorspellen bij welke waarden van de thermodyamische variabelen een stof in een bepaalde fase is: wanneer vormt een stof een gas, wanneer een vloeistof en wanneer een vaste stof? Zo kunnen we bijvoorbeeld berekenen bij welke temperatuur water kookt boven op de Mount Everest, maar uiteindelijk ligt deze theorie ook ten grondslag aan de motoren die onze auto's en vliegtuigen aandrijven.

In hoeverre kan actieve materie ook worden beschreven door thermodynamische variabelen? Die vraag staat centraal in dit proefschrift. Daarbij focussen we op de thermodynamische variabelen *druk*, *chemische potentiaal* en *oppervlaktespanning*. We hebben hun gebruik niet onderzocht voor actieve materie in het algemeen, maar voor het simpele model van actieve Brownse deeltjes. Actieve Brownse deeltjes zijn, kort gezegd, gelijk aan passieve deeltjes, maar met het extra ingrediënt dat elk deeltje een voortstuwingskracht voelt in een richting die willekeurig verandert in de tijd. Deze voorstuwingskracht maakt

dat de deeltjes niet passief maar actief zijn.

De motivatie voor dit onderzoek komt voor een belangrijk deel uit het fenomeen dat bekend staat als *motiliteitsgeïnduceerde fasescheiding*. Om uit te leggen wat dit inhoudt volgt nu eerst een korte uitleg over normale fasescheiding. Passieve moleculen, zoals watermoleculen, kunnen bij de juiste omstandigheden scheiden in twee fases. Deze fases bestaan dan tegelijkertijd naast elkaar. Zo kan bijvoorbeeld een gas naast een vloeistof bestaan. Voor het optreden van een dergelijke gas-vloeistof scheiding is het essentieel dat de deeltjes elkaar (op bepaalde afstand) aantrekken - deze aantrekkingskracht zorgt ervoor dat de deeltjes niet slechts één gasfase vormen, maar ook een fase met hogere dichtheid: de vloeistof. Deeltjes die elkaar enkel afstoten vormen daarentegen slechts één gasfase. Wat blijkt nu: deeltjes die elkaar enkel afstoten, maar *wel* voldoende actief zijn, vertonen *wel* weer een dergelijke fasescheiding. De fasescheiding wordt nu dus niet veroorzaakt door een aantrekkingskracht, maar door door het feit dat de deeltjes actief zijn - met andere woorden, doordat ze een hoge motiliteit hebben. Daarom heet dit verschijnsel motilitieitsgeïnduceerde fasescheiding. De engelse benaming is motility-induced phase separation; de afkorting daarvan - MIPS - zal ik ook hier gebruiken. **Hoofdstuk 2** beschrijft MIPS in detail.

MIPS heeft geleid tot twee belangrijke vragen die dit onderzoek probeert te beantwoorden. Om de eerste vraag te introduceren is het belangrijk om te weten hoe thermodynamische variabelen van nut zijn in de beschrijving van een 'normale' gas-vloeistof fasescheiding. Een gas en een vloeistof die naast elkaar bestaan hebben namelijk altijd, naast dezelfde temperatuur, ook 1) dezelfde druk en 2) dezelfde chemische potentiaal. Deze twee gelijkheden (bij vaste temperatuur) stellen ons in staat om de dichtheden van het gas en de vloeistof te voorspellen. De eerste vraag is dan: kunnen we ook voor actieve deeltjes een druk en chemische potentiaal definiëren, en kunnen we daarmee de dichtheden voorspellen van de twee fases die in MIPS naast elkaar bestaan?

De definitie van de *druk* wordt behandeld in de **hoofdstukken 3, 4 en 5**. Elk hoofdstuk behandelt verschillende aspecten. Wat gebeurt er als de deeltjes niet bolvormig zijn (**hoofdstuk 3**)? Wat is de invloed van de vloeistof waar actieve deeltjes vaak in zwemmen (**hoofdstuk 3**)? Wat gebeurt er als de voorstuwingskracht niet overal gelijk is (**hoofdstuk 4**)? En hoe komen interacties tussen de deeltjes tot uiting in de druk (**hoofdstuk 5**)? De situatie blijkt het éénvoudigst voor deeltjes die bolvormig zijn en overal een gelijke voorstuwingskracht ondervinden. Voor deze deeltjes zorgt de activiteit er simpelweg voor dat de druk een extra bijdrage krijgt die bekend staat als de zwemdruk.

En voor deze deeltjes onderzoekt **hoofdstuk 5** dan ook de definitie van de *chemische potentiaal*. Dit hoofdstuk onderzoekt ook of de chemische poteniaal samen met de druk kan worden gebruikt om de dichtheden te voorspellen van actieve fasescheidingen. Dit blijkt goed te werken voor fasescheidingen van attractieve deeltjes bij lage activiteit, maar niet bij de MIPS die gevormd wordt door repulsieve deeltjes bij hoge activiteit.

De tweede vraag gaat over het grensvlak dat de twee fases in MIPS scheidt. Eerder onderzoek [26] vond dat dat de *oppervlaktespanning* van dit grensvlak negatief is. Dit roept vragen op. Bijvoorbeeld: wat betekent een negatieve oppervlaktespanning eigenlijk precies? En: bij passieve deeltjes zorgt de - altijd positieve - oppervlaktespanning voor

de stabiliteit van het grensvlak, dus hoe kan het dat de grensvlakspanning van MIPS negatief is terwijl het grensvlak *wel* stabiel is? **Hoofdstuk 4** behandelt deze vragen. Het hoofdstuk bekijkt niet direct MIPS, maar een eenvoudiger systeem dat erop lijkt: het grensvlak dat gevormd wordt door actieve deeltjes zonder interacties tussen twee gebieden met verschillende voorstuwingskracht. Het hoofdstuk laat zien de stabiliteit van dit grensvlak *niet* bepaald wordt door het feit dat de oppervlaktespanning positief dan wel negatief is. In plaats daarvan wordt de stabiliteit gegarandeerd door het Marangoni effect. Bij een verstoring van het grensvlak leidt dit effect tot een deeltjesstroom langs het grensvlak op een dusdanige manier dat het grensvlak weer in zijn oorspronkelijke staat hersteld wordt.

Hoofdstuk 7 presenteert een slotbeschouwing. Hoe nuttig kunnen we nu zeggen dat thermodynamische variabelen zijn voor actieve Brownse deeltjes? Een zeker voordeel is dat ze extra intuïtie verschaffen voor het gedrag van actieve materie. Daarbij zijn ze voornamelijk bij lage activiteit ook kwantitatief nuttig. We hebben bijvoorbeeld gezien dat de druk en de chemische potentiaal gebruikt kunnen worden om de dichtheden van licht actieve fasescheidingen te voorspellen.

Er zijn echter nog wel grote uitdagingen in de beschrijving van actieve materie. Het is bijvoorbeeld tot op heden niet gelukt om thermodynamische variabelen (met een microscopische uitdrukking) te vinden die de dichtheden van MIPS voorspellen. Een ander voorbeeld is het gedrag van actieve deeltjes zonder interacties - een zogenaamd actief ideaal gas - in een extern veld. Waar het dichtheidsprofiel van een *passief* ideaal gas in stabiele toestand direct volgt uit de lokale waarde van de externe potentiaal, laat **hoofdstuk 6** zien dat dit dichtheidsprofiel voor een *actief* ideaal gas afhangt van de waarden van de externe potentiaal op willekeurig grote afstanden.

Dus, hoewel thermodynamische variabelen zeker extra inzicht verschaffen in actieve systemen, vormen ze (nog) geen theoretisch raamwerk dat vergelijkbaar is met de statische fysica van passieve systemen in evenwicht. Naar de bescheiden mening van de auteur benadrukt dit vooral hoe krachtig de laatstgenoemde theorie is.

Acknowledgements

A good friend told me that you learn something from the interaction with every person you meet. Seen in this light, a lot of people contributed to the completion of this PhD thesis, and hereby I would like to thank them.

Ten eerste wil ik mijn begeleider René van Roij bedanken. Vanaf het moment dat ik Statistische Fysica 1 van je volgde werd ik aangestoken door jouw enthousiasme voor je vak, waarbij je resultaten intuïtief kan begrijpen én rigoreus kan afleiden. Toen ik besloot om in het kader van het NWO Graduate Program een onderzoeksvoorstel te schrijven teneinde een PhD positie aan het ITF te bemachtigen, wist ik meteen dat ik jou als begeleider zou vragen. We deelden een liefde voor het analytisch doorrekenen van modelletjes, maar jij hield ook altijd de grote lijn in de gaten zodat de nodige publicaties er ook kwamen. Verder bleek jij elke keer als dingen tegen zaten weer een begripvolle en flexibele begeleider. Bedankt voor dit alles.

I would also like to thank my collaborators Marjolein Dijkstra, Siddharth Paliwal, Vasileios Prymidis, Robin van Damme, Liesbeth Janssen, Rens de Haas, Marjolein de Jager and Peter Bolhuis. Marjolein (Dijkstra), bedankt voor je daadkracht, bijvoorbeeld in het zoeken naar nieuwe minimalizatieprincipes en in het publiceren van het paper over de chemische potentiaal. Siddharth, thanks for all our discussions where we tried to understand things as thoroughly as possible, they were among my favourite PhD activities. Robin and Vasileios, thanks for sharing all your insights from a simulators' perspective, they were very valuable. Liesbeth, bedankt dat je het initiatief nam om onze krachten te bundelen, onze bijeenkomsten gaven me altijd goede energie. I would also like to thank Sophie Hermann and Matthias Schmidt: our discussions about our - sometimes conflicting - points of view were always in-depth and at times passionate; I found them very exciting.

Next, I would like to thank my colleagues of the theoretical soft condensed matter group: Mathijs, Bram, Giuseppe, Jeffrey, Sela, Tara, Ben, Cheng, Peter, Willem and Alexander. You all had your own expertise that you were always willing to share with me, and together we formed a group I always felt at home in. Bram, bedankt voor een geweldige tijd in Cargese. Ben, bedankt voor het zijn van mijn PhD maatje en van een heel fijne gesprekspartner. Cheng, thanks for your good sense of humour, and for Haiping's great cooking skills. Willem, bedankt voor je goede vibe. Thanks also to my other colleagues at the ITP and the Debye institute, and to the friends I made during the various PhD schools and conferences. Olga, Wanda en Mariëlle: bedankt voor de gezellige praatjes, jullie waren een fijne afwisseling met al die wetenschappelijke figuren.

Verder wil ik mijn vrienden bedanken die niet onder bovenstaande categorieën vallen. Jacco, dank voor al onze gitaaravondjes. De natuurkundeboys, Melle, Evert, Qiao, Ben, Jaap en Gerwin, bedankt voor de gezellige avonden. Menno, bedankt voor onze fietstochtjes, hopelijk kunnen we die we weer eens oppakken. Dank aan mijn trainingsmaatjes van Phoenix, bij jullie kon ik niet alleen heel wat jaartjes mijn topsportdroom najagen, maar vond ik ook altijd een warm bad. In het bijzonder dank aan mijn trainer Joost Borm, ik heb in jou altijd een voorbeeld gezien, zowel als atleet maar vooral ook als mens. Ian and Rachel, thank you for making my trip to Taiwan so enjoyable at the time I could

use it the most. Dank ook aan Margot, Melie en het Veerkrachtteam, jullie hebben me geholpen om een heel nieuwe kant van mezelf te ontdekken.

Tot slot wil ik mijn familie bedanken. Pap, mam, Remco, Lisa, en ook Rutchanna en Jasper: dank voor jullie onvoorwaardelijke steun en liefde. Ik weet niet wat ik zonder jullie had gemoeten.

About the author

Jeroen Rodenburg was born on April 27th in 1991. Growing up in Amersfoort, he obtained his high school diploma cum laude at the Johan van Oldenbarneveldt gymnasium in 2008. During the last two years of high school he followed the science subjects at the Junior College Utrecht. In 2011, he obtained his bachelor degree cum laude in Earth Sciences. His thesis, supervised by prof. dr. Jeannot Trampert, was on seismic interferometry. For his master he changed subjects to Theoretical Physics, from which he graduated cum laude in 2015. His master thesis was supervised by prof. dr. Eric Laenen and studied the field theory of unstable elementary particles. Jeroen then continued his career as a physicist under supervision of prof. dr. René van Roij with the PhD study that you can read all about in this thesis.

In his spare time Jeroen enjoys doing track and field, specialized in the 800 metres. He participated in several editions of the national championships, won medals at the national students' championships, and is the current record holder in climbing the Dom Tower in Utrecht as fast as possible. He also likes playing the classical guitar, travelling and hiking.